Study of the effect of silica nanoparticles on the electrochemical analysis of ions at the liquid-liquid interface

Martha Collins

Sujet de thèse:

Etude des effets des nanoparticules de silice sur la détection électrochimique des ions à l'interface liquide-liquide

Par

Martha Collins

Pour l'obtention du titre de

Docteur de l'Université de Lorraine en Chimie

Directeur:

Prof. Marc Hébrant – Professeur à LCPME, Villers-lès-Nancy, France

Co-directeur :

Dr. Grégoire Herzog – Chargé de Recherche à LCPME, Villers-lès-Nancy, France

Rapporteurs:

Dr. Daniela Iacopino – Researcher à Tyndall National Institute, Ireland

Dr. Mark Platt – Senior Lecturer à Loughborough University, UK

Examinateurs:

Dr. Agnès Hagège – Chargé de Recherche à Institut des Sciences Analytiques, Lyon, France

Prof. Sabine Bouguet-Bonnet – Professeur à Université de Lorraine, France

Ecole Doctorale:

Synthèse, Simulations, Applications: de la Molécule aux Edifices Supramoléculaires (SESAMES) ED 412.

Date de soutenance: 21/09/18

Laboratoire de Chimie Physique et Microbiologie pour les Matériaux et l'Environnement (LCPME)
UMR 7564, CNRS / Université de Lorraine
405 Rue de Vandoeuvre, 54600, Villers-lès-Nancy, France

Title of thesis:

Study of the effect of silica nanoparticles on the electrochemical analysis of ions at the liquid-liquid interface

by

Martha Collins

To obtain the title of

Doctor of Chemistry from the University of Lorraine

Supervisor:

Prof. Marc Hébrant – Professor at LCPME, Villers-lès-Nancy, France

Co-supervisor:

Dr. Grégoire Herzog – Researcher at LCPME, Villers-lès-Nancy, France

Reviewers:

Dr. Daniela Iacopino – Researcher at Tyndall National Institute, Ireland

Dr. Mark Platt – Senior Lecturer at Loughborough University, UK

Examiners:

Dr. Agnès Hagège – Researcher at Institut des Sciences Analytiques, Lyon, France

Prof. Sabine Bouguet-Bonnet – Professor at University of Lorraine, France

PhD school:

Synthèse, Simulations, Applications: de la Molécule aux Edifices Supramoléculaires (SESAMES) ED 412.

Defence date: 21/09/18

Laboratoire de Chimie Physique et Microbiologie pour les Matériaux et l'Environnement (LCPME)
UMR 7564, CNRS / Université de Lorraine
405 Rue de Vandoeuvre, 54600, Villers-lès-Nancy, France

ACKNOWLEDGEMENTS:

Firstly I would like to express my deepest gratitude to my supervisors, Marc Hébrant and Grégoire Herzog, for their advice, support and the opportunities they have given me throughout my time in France. Their help and guidance during the course of this research has been invaluable and for that I am greatly appreciative.

I also wish to acknowledge those that have contributed to this work; Aurélien Renard for BET analysis, Céline Caillet for zeta potential measurements, Clare Genois for ICP analysis, Christelle Despas for elemental analysis, Guillaume Sautrey for capillary electrophoresis experiments. Furthermore I would like to thank Claire Genois, our lab technician for always ensuring chemical stocks were up to date. To the work shop team of Jean-Paul Moulin and Gérard Paquot, thank you for your technical support when mechanical problems arose during experiments. Thank you to Marie Tercier, Christelle Charbaut and Jacqueline Druon for their help with administration issues.

The multi-cultural ELAN team, forever evolving with students coming and going over the three years, has always been a lovely group to work with. Arriving here three and a half years ago to do my masters placement, I immediately made friends with Lukasz Poltorak, who was a final year PhD student at the time. He imparted so much information on the topic of liquid-liquid electrochemistry to me and also helped me with the experimental aspect of it, as did Alonso Gamero, a post doc researcher who started about the same time as me. Lin Zhang was a second year PhD student and Maciej Mierzwa, Tauqir Nasir and Cheryl Maria Karman were first year PhD students when I first arrived here. Najwa Jajuli did her masters placement with me and then came back for a year in 2017 for part of her PhD research. To say these people were just my friends would be an understatement. We were all so close and I really enjoyed spending time with them both in the lab and outside of it.

An extra special acknowledgement goes to Cheryl, not only was she my office buddy but also my house-mate for over two years. Going through all the ups and downs of life, both professionally and personally, was made so much easier knowing that we were always there to support each other. I made a friend for life, and I am blessed that she is one that can make amazing cakes and desserts too!

To Samuel and Christelle who started their PhD's the year after me, as well as ALL the first years who started last year – Ning, Wang, Deomila, Himanshu, Joanna, Wahid, Guofeng and Taisia, thank you for your friendship and for filling the lab with activity! Furthermore, Taisia, my new house-mate, I couldn't have found a nicer person to share the apartment with after Cheryl left, thank you for your friendship and kindness, and your ability to make great cakes too! To the rest of the LCPME and everyone else I met in France along the way, I just want to say thank you for being part of my story here.

And finally, to my family and friends back home who have helped me through these three and a half years, I am forever indebted to ye and ye will never know the extent of my gratitude. Megan and Hannah, I want to say thanks for being there for me, always ready for a chat, even though we rarely got to meet face to face! Donna, you get an honourable mention. I am so grateful for your help and support when I needed it most. To my brother Declan, thank you for being my brother! There aren't even words to express how thankful I am to my mom and dad, for all their love and support, on the good days and the bad, and for taking care of my three babies - Pet, Libby and Pippa (dog, cat and car!). Ivan, ma dude, you have been there every step of the way, your patience is incredible and I count my lucky stars every day that you are in my life. It's almost time for this chapter to end and the next one to begin… the excitement!! ☺

And of course, last but not least, I am grateful to the Ecole Doctorale SESAMES (ED 412, Université de Lorraine) for my PhD funding.

TABLE OF CONTENTS:

RESUME:

L'interface entre deux solutions électrolytiques immiscibles (ITIES) peut agir comme un support pour l'assemblage de nanoobjets. Cela présente de nombreux avantages : les particules ne requièrent pas d'ingénierie particulière pour leur obtention, peuvent s'assembler dans des conditions qui leur sont propres, sont pratiquement non dégradables et facilement renouvelables. Les recherches actuelles portent tant sur leur utilisation potentielle en tant que plateformes pour des appareils optiques ajustables, pour des capteurs ou encore pour de la catalyse.

L'adsorption de nanoparticules de silice, dense ou mésoporeuse, à l'interface liquide-liquide a été étudiée par voltammétrie en courant alternatif. L'interaction des nanoparticules de silice avec le bleu de méthylène et l'éosine B a été étudiée par voltammétrie cyclique et spectrophotométrie. Les constantes thermodynamiques d'adsorption du bleu de méthylène ont été déterminées à $1.66\ 10^5$ et $3.68\ 10^3$ sur les particules de silice dense et mésoporeuse respectivement. La variation de constante entre les deux types de silice repose essentiellement sur leur état d'ionisation respectif. L'énergie de Gibbs de transfert entre phase liquide est modifiée de 8.9 kJ mol^{-1} en présence de nanoparticules denses ce qui donne des indications sur le mécanisme de transfert du bleu de méthylène en présence de nanoparticules. Mettant à profit l'aptitude de la silice à accumuler le bleu de méthylène et à s'adsorber sur l'interface liquide il nous a été possible d'améliorer la sensibilité de la détection électrochimique. L'éosine B n'a aucune interaction avec les particules de silice.

Nos efforts ont ensuite porté sur l'amélioration de la sélectivité du transfert électrochimie par l'utilisation de nanoparticules de silice à empreinte moléculaire. Des nanoparticules de silice dense à empreinte moléculaire de Diclofénac (DIN) ont été synthétisées. Cette molécule est un anti-inflammatoire non stéroïdien très largement utilisé et figurant sur la liste européenne des polluants émergents. Les constantes d'affinité du Diclofénac pour les DIN et les particules équivalentes sans empreinte sont de $7.47\ 10^8$ et $2.96\ 10^7$ respectivement ce qui démontre clairement la présence d'empreintes ayant une forte affinité pour le diclofénac au sein des particules. Des molécules analogues (Diclofénac acide, Aceclofenac, acide 4 phenyl-azo benzoique) ont été testées et ont une affinité faible pour les DIN. En électrochimie, l'ajout de DIN bloque le transfert de Diclofénac à l'interface liquide-liquide.

ABSTRACT:

The interface between two immiscible electrolyte solutions (ITIES) can act as a scaffold for the assembly of nanometer-sized objects. The assembly of nanoparticles at liquid-liquid interfaces has numerous advantages – the nanoparticles do not require engineering, can assemble given proper conditions, are practically non-degrading and easily renewable. Research is ongoing into their use as a platform for tunable optical devices, sensors and catalysis.

The adsorption of both dense and mesoporous silica nanoparticles at the ITIES was studied by AC voltammetry. Their interactions with methylene blue (MB^+) and Eosin B (EB^-), selected as model ions, were studied by cyclic voltammetry and UV/Vis absorption spectroscopy. The thermodynamic constants of adsorption of MB^+ were found to be $1.66\ 10^5$ and $3.68\ 10^3$ onto dense and mesoporous silica nanoparticles respectively. The difference of adsorption constants for the two types of silica was explained by their differing ionisation states. The Gibbs energy of transfer of MB^+ is shifted by -8.9 kJ mol^{-1} in the presence of dense silica nanoparticles, giving some insights to the transfer mechanism of MB^+ in presence of nanoparticles. Combining the ability of silica to adsorb onto the ITIES and their affinity for MB^+, MB^+ was accumulated at the ITIES and so an increase in sensitivity of electrochemical detection was achieved. Eosin B demonstrated no affinity for the silica nanoparticles and its transfer at the ITIES was not influenced by their presence.

Next the focus was placed on improving the selectivity of the interaction by synthesising imprinted silica nanoparticles, more specifically, Diclofenac-imprinted dense silica nanoparticles. This drug was chosen as it is a commonly used nonsteroidal anti-inflammatory drug which has been placed on the European watch list of emerging pollutants. The thermodynamic constants were calculated as $7.47\ 10^8$ for Diclofenac-imprinted silica and only $2.96\ 10^7$ for non-imprinted silica. Thus the presence of imprint cavities greatly influences the affinity of diclofenac for the silica nanoparticles. The analogues of Diclofenac (Aceclofenac, Acid diclofenac, 4-phenyl azo benzoic acid) were shown to have a very limited affinity for the imprinted particles. Electrochemical experiments at the liquid-liquid interface revealed that the diclofenac transfer is blocked by the presence of imprinted particles.

1. INTRODUCTION:

This section gives an overview of the topics of my PhD, defining frequently used terms and introducing the three main concepts studied during the thesis. These are: 1. Interface between two immiscible electrolyte solutions, 2. Dense and mesoporous silica nanoparticles and 3. Molecularly imprinted silica nanoparticles.

1.1 ***Interface between Two Immiscible Electrolyte Solutions (ITIES)***

The term interface is defined as the boundary between two distinct phases [1]. The **L**iquid-**L**iquid **I**nterface (**LLI**) is thus the boundary between two immiscible liquids, for example oil and water. In this research, we work at the **I**nterface between **T**wo **I**mmiscible **E**lectrolyte **S**olutions, commonly referred to as the **ITIES**. The interface forms between two liquids of low mutual miscibility, generally an aqueous solution and a polar organic solvent, both of which contain an electrolyte salt that must be soluble in its respective phase but not the other. The aqueous phase contains a hydrophilic electrolyte (e.g. LiCl), whereas a hydrophobic electrolyte (e.g. Bis (triphenylphosphoranyldiene) ammonium chloride, $BTPPA^+$ $TPBCl^-$) is present in an organic solvent [2]. The organic solvent 1,2 – Dichloroethane, which was used during this research, has a moderate dielectric permittivity of 10.36 which allows for at least partial dissociation of the dissolved electrolyte(s) into ions [3,4].

Electrolyte solutions have ionic conductivity due to mobile charge carriers, thus allowing them to achieve equilibrium through ion transfer across this interface. The benefit of using electrolyte solutions at the ITIES is that the ionic conductivity of both phases imparts electrical potential difference on the interface. When correctly set up, it can behave, for electroanalytical purposes, like an electrode [1]. Thus, the normally solid conductor is replaced with an immiscible electrolyte phase and the polarization is an ionic process. Furthermore this set-up allows external reference electrodes to apply a potential between the two conductive phases thus making a polarizable interface. Ions in solution can transfer across the polarized interface and voltammetry is used to detect this via peaks on a cyclic voltammogram. This will be explained in further detail in section 1.1.2.

1.1.1 *Liquid-liquid interface structure*

The first attempts at studying the liquid-liquid interface date back to the 19th and 20th centuries, when ion partition equilibria at the ITIES was studied by Nernst [5]. The structure of the interface was first proposed by Verwey and Niessen in 1939 [6], whose theoretical model refers to the classical theory of Gouy [7] and Chapman [8]. The structure described an electrical double layer as two back-to-back electric double layers with opposite charge separated by a continuous boundary. Experimental evidence was reported by Gavach et al. almost 40 years later [9]. Further work developed the 'modified Verwey-Niessen' model which improved upon the original model by describing the interface as a 'compact layer' of oriented dipole molecules and assumed a very small potential drop across the interface. Furthermore, surface excess study of water at the interface between organic solvents of differing polarities, confirmed the presence of a mixed solvent layer, having a thickness of no more than two or three molecular diameter at the interface [10–12]. Each model is shown in Figure 1.1 below.

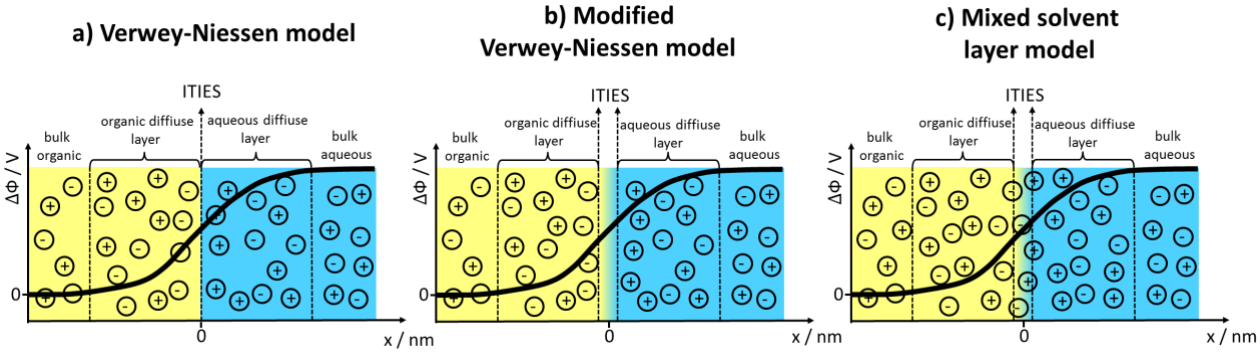

Figure 1.1 Different models for the ITIES structure. Black solid lines correspond to potential distribution across the polarized liquid – liquid interface [13].

Nernst and Riesenfeld were the first to investigate the effect of electric current flow across the ITIES in 1902. Using electrolysis, they visually observed the transfer of coloured ions from water to phenol [14]. Until the mid-1980's, research mainly focused on understanding fundamental phenomena. However in more recent times, it has shifted to studying electrochemistry at the ITIES with the aim of developing applications to answer specific needs. In this case, the ITIES replaces the working electrode, allowing the electrochemical detection of ionic species, which are normally not detectable by a redox process [15]. This is possible by monitoring the current generated when the ions transfer across the liquid-liquid interface, from one phase to the other.

1.1.2 *Charge transfer reactions at the ITIES*

Under open circuit potential, when no charge transfer is observed, the electrolyte ions stay in their respective phase, i.e. ions in the aqueous phase are too hydrophilic to transfer to the organic phase and those in the organic phase are too hydrophobic to transfer to the aqueous phase. However, when a potential difference is applied between the two reference electrodes, between the two immiscible phases, the equilibrium is disrupted. In order to restore balance at the ITIES ion transfer occurs [16]. Three main types of charge transfer reactions can occur at the ITIES: simple ion transfer, assisted ion transfer and electron transfer [17]. The principle of ion transfer reactions is to provide an ion with the energy it requires to go from one phase to another by polarizing the interface to create a potential difference which becomes re-equilibrated by the transfer of ions across the interface [1,17].

1.1.2.A Simple ion transfer reaction

Take for example a simple ion transfer reaction, the energy required to drive an ion (i) from one phase to the other is referred to as the Standard Gibbs energy of transfer ($\Delta G_{(i)}^{0,w\rightarrow o}$) and its value is dependent on the nature of the ion and solvents. It is defined as the difference between the Standard Gibbs energy of solvation ($\mu_{(i)}^{0,o}$) and hydration ($\mu_{(i)}^{0,w}$):

$$\Delta G_{(i)}^{0,w\rightarrow o} = \mu_{(i)}^{0,o} - \mu_{(i)}^{0,w} \qquad (1)$$

The Standard Gibbs energy of transfer can be converted to the Standard Galvani potential of ion transfer ($\Delta_o^w \phi_{(i)}^0$) by introducing z_i (ion charge) and F (Faraday constant):

$$\Delta_o^w \phi_{(i)}^0 = \frac{\Delta G_{(i)}^{0,w\rightarrow o}}{z_i F} \qquad (2)$$

The ion transfer equilibrium, at constant temperature and pressure, for the charged species (*i)* is given by:

$$\tilde{\mu}^{w}_{(i)} = \tilde{\mu}^{o}_{(i)} \quad (3)$$

From this the Electrochemical potential of the charged species ($\tilde{\mu}^{x}_{(i)}$) can be expressed, where *x* corresponds to the aqueous (w) or organic (o) phase, $\mu^{0}_{(i)}$ is the Standard Electrochemical potential and $a^{x}_{(i)}$ represents the activity of the charged species:

$$\tilde{\mu}^{x}_{(i)} = \mu^{0,x}_{(i)} + RTlna^{x}_{(i)} + z_{(i)}F\phi^{x} \quad (4)$$

Each of the immiscible phases at the ITIES can be characterized with its own Inner Galvani potential (ϕ^{x}) [1]. On equating the two previous equations (3 + 4) the following is obtained; which can be reshuffled to separate the Galvani potential difference on one side and the rest of the components on the other side of the equation:

$$\mu^{0,w}_{(i)} + RTlna^{w}_{(i)} + z_{(i)}F\phi^{w} = \mu^{0,o}_{(i)} + RTlna^{o}_{(i)} + z_{(i)}F\phi^{o} \quad (5)$$

$$\Delta^{w}_{o}\phi = \phi^{w} - \phi^{o} = \Delta^{w}_{o}\phi^{0}_{(i)} + \frac{RT}{z_{(i)}F} ln \frac{a^{o}_{(i)}}{a^{w}_{(i)}} \quad (6)$$

This yields a Nernst-like equation for ion transfer at the ITIES, where R is the gas constant (8.31 J mol^{-1} K) and T is the temperature:

$$\Delta^{w}_{o}\phi = \Delta^{w}_{o}\phi^{0}_{(i)} + \frac{RT}{z_{(i)}F} ln \frac{a^{o}_{(i)}}{a^{w}_{(i)}} \quad (7)$$

Thus the potential difference across the interface (Galvani potential difference, $\Delta^{w}_{o}\phi$) is controlled by the reference electrode in each phase and is linked to the activity of ionic species ($a_{(i)}$) distributed across the interface [3,16,18]. However, adaptions have to be made to the Nernst-like equation for simple ion transfer when describing assisted ion transfer, which will be described in the following section [19–21].

1.1.2.B Assisted ion transfer reaction

Assisted (facilitated) ion transfer involves the use of a ligand to 'assist' the transfer of the ion between phases, by employing a host-guest interaction between them. To describe the process, one assumes the ligand is in the organic phase, with the ion in the aqueous phase. Complexation occurs in the phase the ligand is present in (i.e. organic phase). An excess concentration of the ion is present in the aqueous phase compared with the organic phase and under open circuit potential, complex formation in the organic phase is high. Thus ion concentration in the organic phase and ligand concentration in the aqueous phase can be neglected. The complexation of the ligand with the ion in a 1:1 stoichiometry can be written as:

$$L_o + i_w \rightleftharpoons L - i_o \qquad (8)$$

With formation constant, β_1, given by:

$$\beta_1 = \frac{a^o_{L-(i)}}{a^o_L a^w_{(i)}} \qquad (9)$$

The Nernst-like equation is thus modified as follows:

$$\Delta^w_o \phi = \Delta^w_o \phi^0_{L-(i)} + \frac{RT}{z_{(i)}F} ln \frac{a^o_{L-(i)}}{a^w_{(i)}} \qquad (10)$$

With the Standard Galvani potential of ion transfer like so:

$$\Delta^w_o \phi^0_{L-(i)} = \Delta^w_o \phi^0_{(i)} + \frac{RT}{z_{(i)}F} ln(\beta_1 a^o_L) \quad (11)$$

Assisted ion transfer was reported by Koryta in 1979 [22]. He used ionophores in the organic phase to form a complex with ions in the aqueous phase, which allowed the transfer of these ions across the interface. Previously, those ions were unable to transfer as they were limited by the narrow range of the operating potential window between the phases (which will be discussed in Section 1.1.3). However, the presence of ionophores dissolved in the organic phase lowered the Gibbs energy of transfer and thus allowed the ions to transfer at lower interfacial potential difference values. Koryta used synthetic dibenzo-18-crown-6 ionophore, dissolved in nitrobenzene, which complexed with the potassium ion.

It facilitated the transfer of potassium from the aqueous to organic phase, and back again to the aqueous phase in reverse polarization, with a slight shift in the potential of potassium transfer. Koryta also worked with the antibiotics valinomycin and monensin as natural ionophores. The nature of assisted ion transfer reactions is quite complex but four mechanisms have been put forward to describe the processes occurring: **ACT** – aqueous complexation followed by transfer, **TOC** – transfer followed by complexation, **TIC** – transfer by interfacial complexation and **TID** – transfer by interfacial dissociation [23].

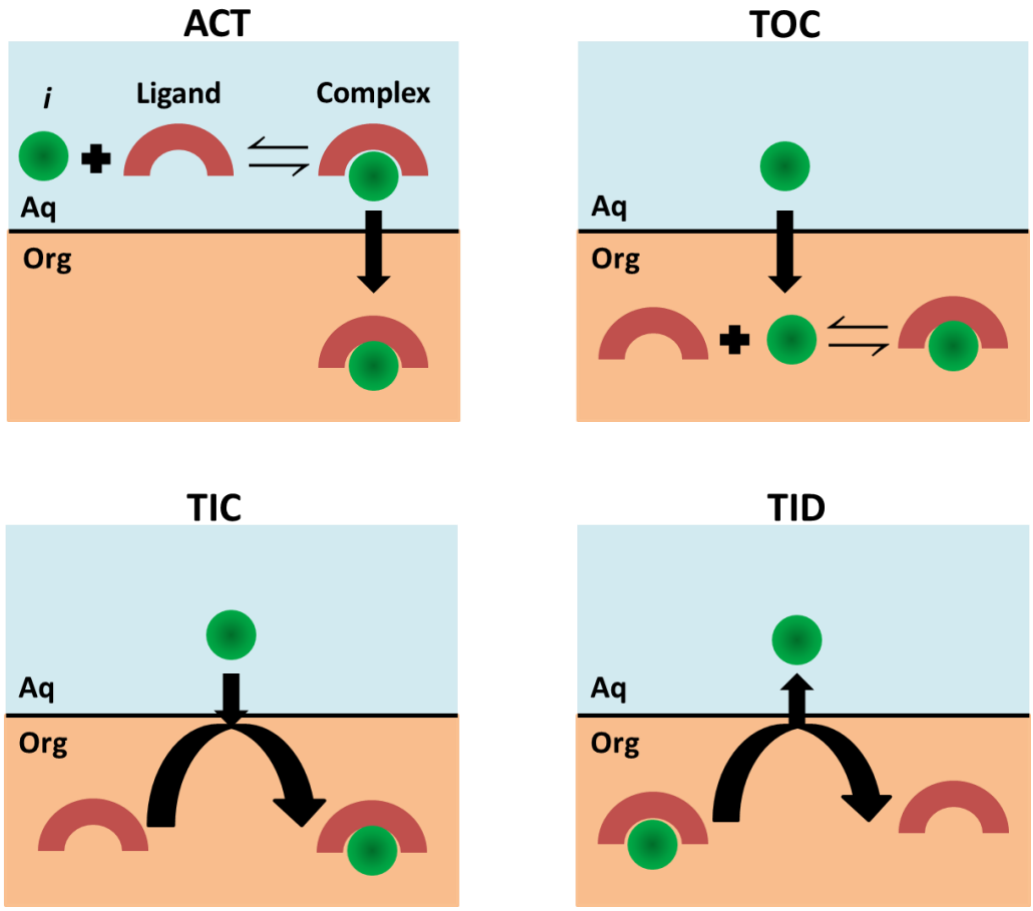

Figure 1.2: The four mechanisms of possible assisted ion (*i*) transfer reactions. ACT: aqueous complexation followed by transfer, TOC: transfer followed by complexation, TIC: transfer by interfacial complexation and TID: transfer by interfacial dissociation.

Since the pioneering work in 1979, others have used this approach to extract transition and other metal ions. For example, Fe(II) and (III), Ni(II) and Zn(II) transferred from water to nitrobenzene by complexing with bidentate nitrogen based ligands such as *o*-phenanthroline and *o,o*'-bipyridine [24]. The assisted transfer of heavy metal ions using ionophores has gained a lot of experimental attention. Lagger et al. used a series of hydrophobic cyclic thioether ligands as heavy metal ionophores, assisting the transfer of lead and cadmium at the polarized water|1,2-Dichloroethane interface [25].

1.1.2.C Electron transfer reaction

Finally, electron transfer reactions involve the study of charge transfer of redox-active species at the ITIES. It requires a redox reaction between an oxidized form of the redox couple in one phase and a reduced form in the other; however it is rarely used for sensing. The electrochemical study of ions at the ITIES, which are generally not detected by a redox process, is more interesting from an analytical point of view [15]. The study of the kinetics of electron transfer reactions can be achieved by using systems with a non-polarised interface [26]. A non-polarisable interface occurs when both immiscible phases contain at least one common ion. The common ion can freely cross the interface without inducing a change in interfacial potential difference.

1.1.3 *Potential window for ion transfer*

Voltammetry is used to detect ions in solution transferring across the interface, via peaks on a cyclic voltammogram. However, in order to observe this, the ion transfer must take place within the potential window in which the interface is polarizable. The size of the potential window is determined by the electrolyte salts chosen, as it is between the hydrophilic salt in the aqueous phase and lipophilic salt in the organic phase that the polarizable interface is assembled. The potential range available to observe the peak is further limited due to the transfer of the background electrolyte ions between the aqueous and organic phases at both ends of the potential window, e.g. $Li^+Cl^-_{aq}$ and $BTPPA^+TPBCl^-_{org.}$ The Li^+_{aq} and $TPBCl^-_{org}$ generate a current at the far right of the potential range when they transfer during the positive forward scan from *aqueous -> organic* and *organic -> aqueous* respectfully. Meanwhile the Cl^-_{aq} and $BTPPA^+_{org}$ generate a current at the far left of the potential range when they transfer

during the negative forward scan from *aqueous -> organic* and *organic -> aqueous* respectfully. This limits the potential window within which ion transfer of a probe ion can be investigated to the area between the dashed vertical lines shown in Figure 1.3.

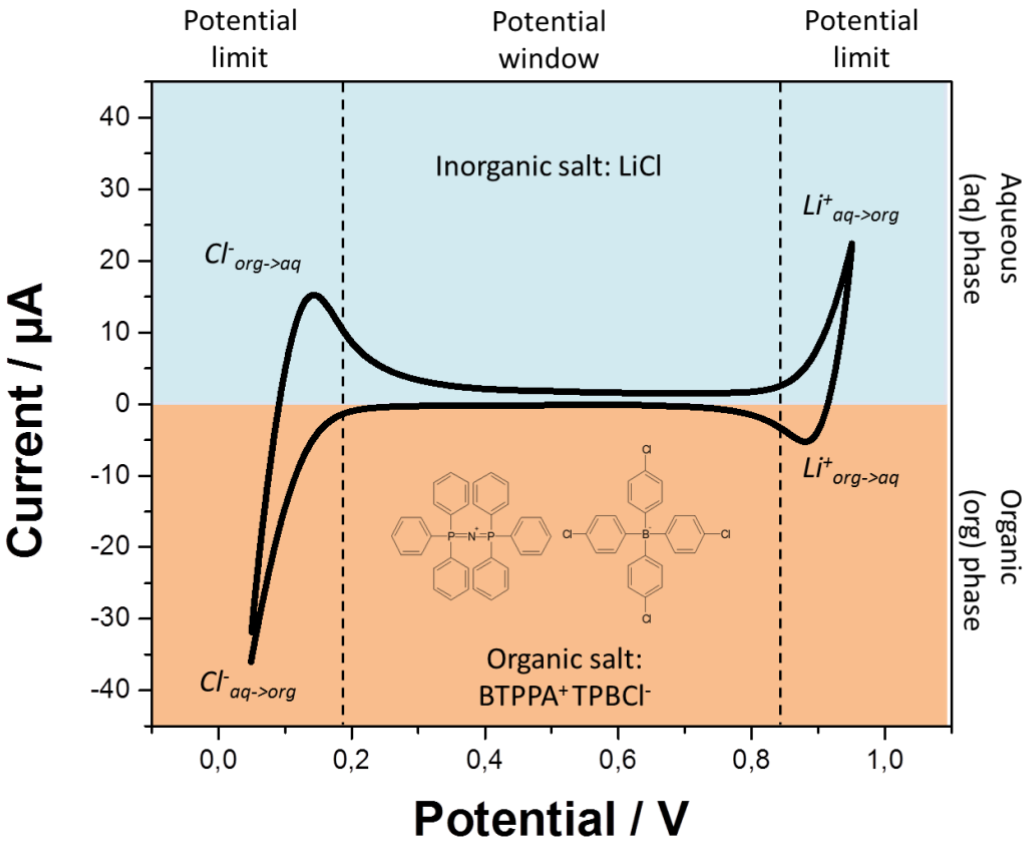

Figure 1.3: The limiting effect of transferring background electrolyte ions on the operating potential window

To sum, when monitoring the transfer of probe ions at the interface, their charge and direction of ion transfer determines where a peak will be visible on the voltammogram. The application of a Galvani potential ($\Delta_o^w\phi$) which is more positive than the standard value ($\Delta_o^w\phi^0$) results in cations transferring from the aqueous phase to the organic, and anions from the organic to aqueous phase during the positive forward scan [27]. In the opposite situation during the reverse scan, cations transfer from the *organic* to the *aqueous* phase, while anions transfer from the *aqueous* to *organic* phases. Both situations are shown in Figure 1.4.

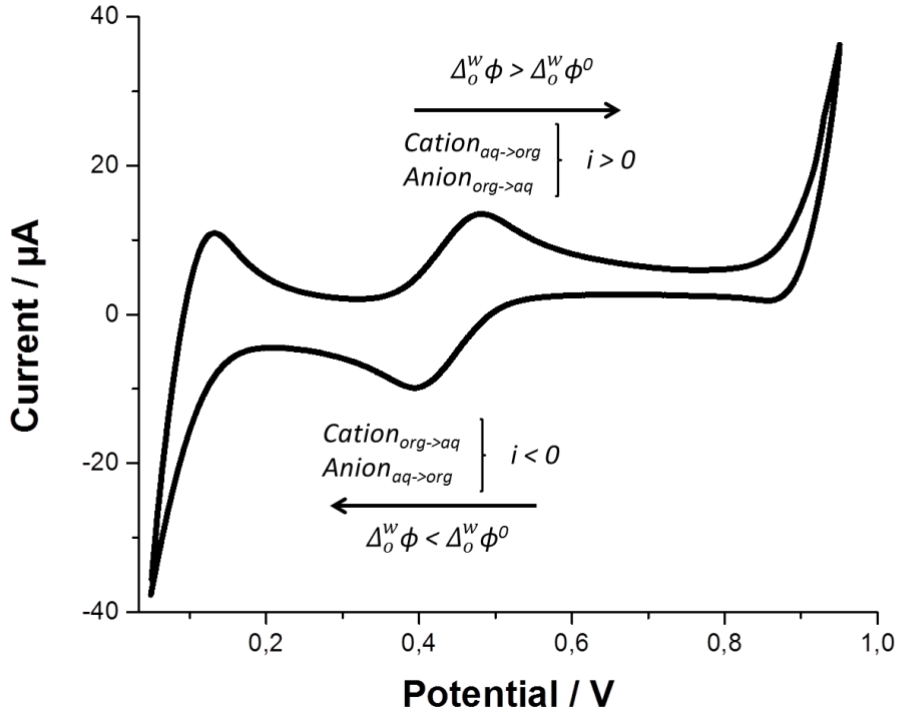

Figure 1.4: Direction of ion transfer and corresponding current (*i*) response

1.1.4 Sensitivity and selectivity at the ITIES

Along with the limitations of the potential window, two significant drawbacks with detection at the ITIES are poor sensitivity and selectivity.

Sensitivity is a quantitative parameter, a high sensitivity results in a low limit of detection, which is the most preferable result. Increasingly low limits of detection are sought after in the pharmaceutical industry and field of environmental analysis. Take for example pharmaceutical impurities that can be present in active pharmaceutical ingredients or drug product formulations. These unwanted substances can arise during drug synthesis or can be found in the starting materials, reagents, catalysts, and they can ultimately affect the safety of the final drug product. Their quantitation is a crucial part of the drug development process in pharmaceutical industries.

Electrochemistry at the ITIES has been frequently used as a sensing tool, as it allows non-redox active molecules to be detected, which may not possible with other analytical electrochemical sensing methods. Progress has been made to increase sensitivity, such as using microscopic ITIES and optimising hydrodynamic conditions in order to improve mass transport. Mass transport is the rate at which an analyte can get from the bulk solution to the position where it can be detected. The faster the rate, the higher the sensitivity. The rate of mass transport is affected by the diffusion profile of ionic species at the ITIES. As can be seen in Figure 1.5, the diffusion profile of the micro-ITIES has an asymmetric profile, versus a linear diffusion profile at macro-ITIES. The radial diffusion from the aqueous phase to the organic phase in the micro-ITIES generates a faster mass transport (as opposed to linear diffusion), thus giving a higher sensitivity, consequently allowing detection limits in the range of tens of nM [28]. Furthermore, using cyclic voltammetry and an array of nano-ITIES resulted in the detection of propranolol at values 5 – 10 times lower than the limit of detection achieved at the larger micro/macro interfaces [29]. Nano-ITIES have a diffusion profile similar to that of micro-ITIES and give a better electroanalytical response, as, under proper geometrical conditions, the array can be treated as a sum of individual ITIES, thereby maximizing the mass transport and thus greatly improving sensitivity.

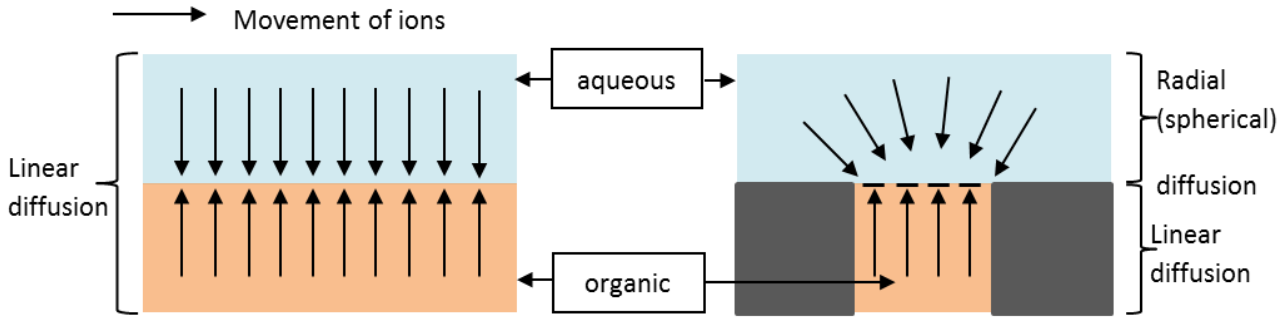

Figure 1.5: Linear diffusion profile in both directions at Macro-ITIES (left) Vs Radial diffusion into the pore and linear diffusion within the pore at Micro-ITIES (right).

On the other hand, selectivity is a qualitative parameter, with high selectivity allowing the detection of very specific target molecules in a complicated medium such as water, sediment, soil and biota. In the field of environmental analysis, these target molecules can be emerging pollutants. These are not necessarily new chemicals, rather chemicals that have just been discovered in the environment as a result of improved analytical detection techniques.

Thus these compounds need to be identified and their threat to both the environment and human health examined. In the pharmaceutical industry, assessing stereoselectivity in drug metabolism is highly important in order to produce safe, effective drug treatments. A technique with a very high degree of selectivity is needed to analyse racemic drugs and then eliminate the unwanted isomer. Recent developments to improve selectivity at the ITIES include the coupling of it with other analytical techniques, for example spectroscopy techniques, and using supported liquid membranes [15]. Using a porous membrane to support the ITIES has resulted in greater mechanical stability, which can help overcome limitations of linear diffusion of species and instability at the macro-ITIES. Matsui et al. studied the ion transfer of creatinine at a polarized nitrobenzene/water interface. A dialysis membrane covered the interface to prevent possible interference from urine proteins, while determining creatine in urine [30]. Furthermore, the modification of the ITIES can improve selectivity, by impacting the transfer of the analyte ions across the LLI. Modification via the assembly of particles and films at the interface is described in the following section.

1.1.5 *Particle assembly at the ITIES*

The ITIES has many advantageous properties from an electrochemical point of view. These include relative low cost, simple set up and short response time. The ability of the ITIES to be highly reproducible (due to its defect free nature) and self-healing (which allows self-assembly errors to be rapidly corrected), allows the assembly of a large variety of solid particles at the interface resulting in interfacial modification [31]. Certain materials can assemble automatically at the liquid-liquid interface, however for others electrochemistry at the ITIES acts as a driving force for the deposition of the materials at the interface. This can either occur *ex situ* (the material is first formed, then deposited) or *in situ* (the deposit forms during the interfacial reaction). Typical materials that can be assembled or deposited at the interface include phospholipids, organic polymers, carbon and metallic nanomaterials, as well as silica nanoparticles [32–35].

Single and multi-walled carbon nanotubes, graphene and graphite flakes can assemble at the liquid-liquid interface under proper conditions and due to their conductive properties they can improve chemical reactions and electron transfer kinetics by acting as conductive rafts [36–38]. Kane et al. used surfactants to direct single-walled carbon nanotubes (SWNTs) to the LLI.

These SWNTs can transport enzymes to the interface and enhance the rate of catalysis by almost 3 orders of magnitude compared with enzymes alone [39]. Dryfe et al. deposited Pd and Au nanoparticles on a graphene monolayer, which had been assembled at the LLI. Metal deposition then occurred spontaneously or via an electrochemically-controlled process [40]. Furthermore, Dryfe and co-workers reported a process for the controlled assembly of liquid exfoliated graphene and SWNTs at the ITIES [41]. The electroactivity of these free-standing carbon films was studied and Pd nanoparticles deposited on them via in situ electro-deposition at the liquid-liquid interface.

Metal deposition can occur with Au, Ag, Pd and Pt and can be in the form of nanoparticles or films. Gold nanoparticles have been injected onto the interface between [heptane + 1,2 – Dichloroethane] and water and formed a self-assembled monolayer surface coverage, which exhibits reflectance and electrical conductance [42]. Samec et al. deposited mercaptosuccinic acid-stabilised gold nanoparticles at the polarizable water and 1,2 – Dichloroethane interface, under potential controlled conditions. The gold nanoparticles, initially suspended in the aqueous phase, achieved reversible interfacial adsorption at the ITIES, under controlled Galvani potential difference [43]. Furthermore TiO_2 nanoparticles have been assembled at the polarizable interface between water and 1,2 – Dichloroethane, upon applying a potential bias [44,45].

Electrochemically induced interfacial adsorption at the ITIES has also been reported for amphiphilic ions, proteins and dendrimers. Amphiphilic molecules, e.g. phospholipids, have been adsorbed under applied potential conditions and studied via electrocapillary curve measurements [46–48]. Cyclic voltammetry was used to follow the adsorption of phosphatidylcholine phospholipid (which was present in the organic phase) and its interactions with ionic species that were present in the aqueous solution (K^+, H^+, Fe^{2+}, Fe^{3+}, $IrCl_6^{2-}$, $IrCl_6^{3-}$). A triangular signal in the cyclic voltammogram indicated the adsorption of the phospholipid. Contact angle measurements showed that values increased with the polarization towards more positive potential, when phospholipid adsorption occurred [49]. Dendrimers are large, multicharged species, which have applications as drug carriers [50], molecular gates [51] and soft templates [52]. At the electrified liquid-liquid interface, however, dendrimers with growing size and charge exhibit complex behaviour, thus electrochemistry at the ITIES has been used to study them [53,54].

Similarly, interfacial adsorption of biomolecules has been observed for insulin and hen egg-white lysozyme [55], as well as haemoglobin [56]. Haemoglobin not only adsorbed at the interface but due to its positive charge, interacted with the anionic part of the organic phase supporting electrolyte, facilitating its transfer by decreasing its Gibbs energy of transfer.

The assembly of silica materials at the LLI has found applications in a wide range of scientific disciplines due to their attractive physicochemical properties. A description of silica compounds, along with the synthesis of silica nanoparticles and their applications, are discussed in detail in the following section.

1.2 ***Nanoparticles***

Nanoparticles are defined as three-dimensional nanomaterials whose size spans the range between 1 and 100 nm in at least one dimension. Consequently, these particles show physical, chemical and biological properties that differ from those observed in their bulk or molecular counterparts [57,58].

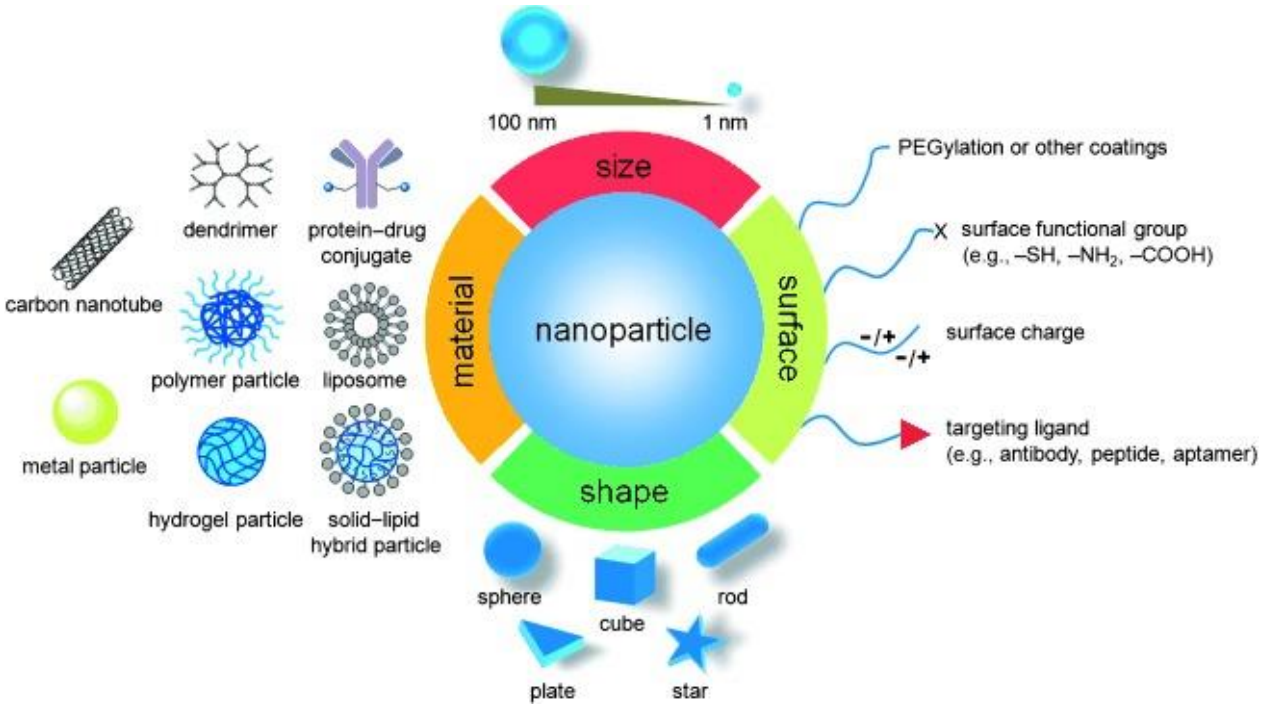

Figure 1.6: Summary of nanoparticles size, surface features, shapes and material [59].

Furthermore, as a result of this size range, nanoparticles also fall into the domain of colloidal particles. Colloid science is the study of colloid particles with a size or with one dimension between 1 nm and 1 µm [60]. It attempts to explain and predict the properties of substances based on their dimensions and surface features. Colloidal particles are sufficiently small to be unaffected by gravity but large enough to show differences from the properties of true solutions. They are made of associations or colonies of ~10^3 – 10^9 atoms, which are arranged in a crystalline or amorphous structure. Colloidal dispersions are defined as a multi-phase system where particles are dispersed/suspended in a solution. These dispersions can be stabilized against coagulation by steric effects or electrostatic repulsion. In this case, the stable dispersion of solid colloidal particles in the liquid phase is referred to as a sol [57,60].

Nanoscience and nanotechnology have become increasingly popular in recent years due to the benefits these areas have brought to research topics and their applications, in sectors such as information technology, medicine, energy, food and environmental science. However some nanomaterials are not without their disadvantages. Due to their small size, they have been found to have an adverse impact on health when inhaled and may have a negative, toxicological effect on the environment [58]. Conversely, silica nanoparticles have always been regarded as safe and authorized for use as an ingredient in food, due to the natural presence of silicon in the environment. Furthermore silica has been widely studied for decades and has applications in many fields. Silica compounds are amongst the most commonly used materials to synthesise nanoparticles due to their attractive properties such as physical rigidity, high thermal stability and negligible swelling in both aqueous and organic solutions [61].

1.2.1 *Nomenclature and physicochemical properties of silicon and silicon containing compounds*

Silicon (Si) is the second most abundant atom in the earth, after oxygen. It rarely occurs as a pure element in nature, but more frequently combines with other oxide materials in the environment. When combined with oxygen it is given the IUPAC name silicon dioxide (or silica), SiO_2, which forms amorphous and crystalline compounds such as quartz, flint, opal. Thus silica played an important role in civilization as it was used to make tools and pottery. The combination of silica with hydroxides generates silicic acid, with the general formula $[SiO_x(OH)_{4-2x}]_n$, which is found dissolved in the oceans.

Silica is also found in living organisms like sponges, grasses (which use it to stiffen stems for holding fruit) and animals (who use it to form bones, hair and teeth) [62–65]. Furthermore, SiH_4 is called silane and silicates are anionic species containing a silicon atom, e.g. SiO_4^{4-}. Silanols refer to a silicon atom which has at least one OH group attached. Organosilicon compounds occur when there is a covalent bond between a silicon and carbon atom. Finally, silicon alkoxides, or alkoxysilanes, are compounds of silicon and alcohol with the general formula $Si(OR)_4$, with R representing an organic group.

Table 1.1: Physiochemical properties of silicon atom [66]

IUPAC name	Silicon	**CAS no.**	7440-21-3
Discovery date	1824	**Melting point**	1414 °C, 1687 K
Discovered by	Jöns Jacob Berzelius	**Boiling point**	3265 °C, 3538 K
Allotropes	Amorphous, crystalline	**Atomic mass**	28.085
Atomic number	14	**Density**	2.3296 g cm^{-3}
Key isotopes	^{28}Si, ^{30}Si	**State at 20°C**	solid

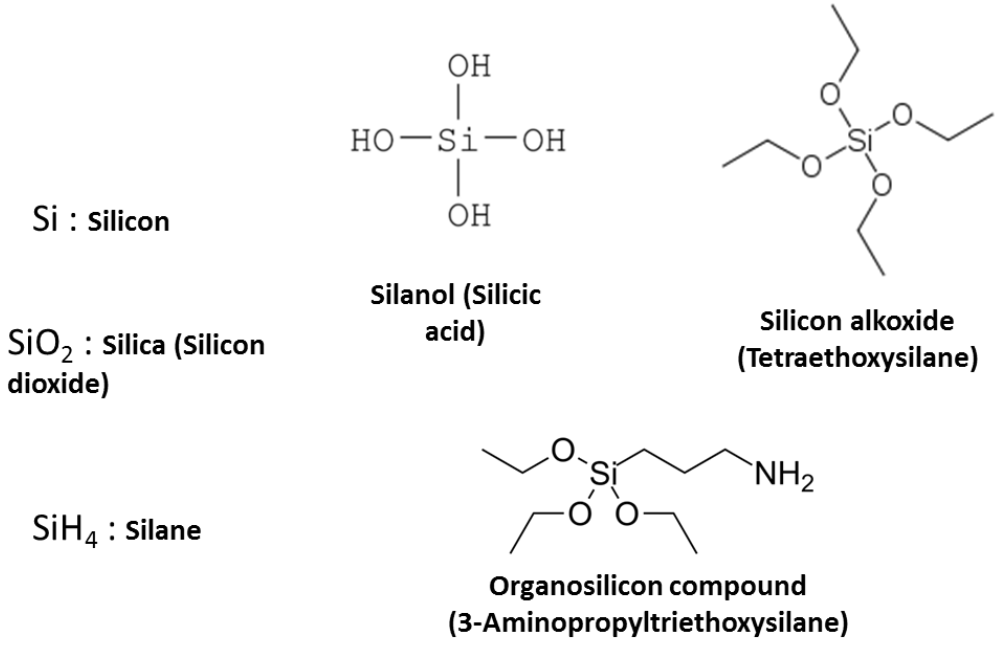

Figure 1.7: Examples of silicon containing compounds

1.2.2 *Silica nanoparticles*

As mentioned previously, silica is found in nature in its crystalline form (as quartz sand), however amorphous silica is industrially manufactured, in forms such as silica gels, precipitated silica, fumed silica and colloidal silica. Silica gel is most commonly found in paper packets and used as a desiccant to absorb moisture and so avoid degradation of some goods. Precipitated silica products are used as thickening agents and anti-corrosion pigments to improve performance and sustainability of coating, paints, inks, etc. Fumed silica, like silica gel, acts as a desiccant and is also used as a thickening and anti-caking agent in powders. It is also found in products like toothpaste, acting as a light abrasive. Colloidal silica is the stable dispersion of solid silica particles and so is in liquid form, as opposed to powder. All of these forms of silica particles consist of an amorphous network of silicon and oxygen and are non-crystalline (they do not have long range order). They can all be produced from silica ore using various synthetic routes, thus ultimately producing particles with varying sizes, shapes, uniformity, sphericity and stability. Colloidal silica nanoparticles which are used in this research can be prepared from silica ore via ion exchange of sodium silicate, or direct oxidation of silicon, or by milling and peptization of silica gel or fumed silica, or more commonly via a Sol-gel process, which involves the hydrolysis and condensation of silanes. It is with the Sol-gel synthesis that nanoparticles of a controlled and uniform shape and size are obtained, as reaction parameters such as the solvent, catalyst, concentrations, temperature and reaction time are controlled [60,67,68]. The process will be described in further detail in the following section.

Table 1.2: Starting materials and preparation methods for colloidal silica [67]

Starting material	**Preparation method**
Sodium silicate	Ion exchange
Silicon	Direct oxidation
Silica gel/fumed silica	Milling and peptization
Silanes	Sol-gel (hydrolysis and condensation)

1.2.2.A Dense Silica Nanoparticles (DSNs)

The Sol-gel process originates from the so-called Stöber process. In 1968, Stöber et al. established a method of synthesis of silica particles with controlled growth and a uniform size (between 0.5 - 2 µm), with narrow particle size distributions [69]. These monodispersed silica colloids were prepared by hydrolysis of alkyl silicates and subsequent condensation of silicic acid in alcohol, with ammonia as a catalyst. Many studies have since been performed in this area in order to have a greater understanding of the processes occurring during the reaction, which can thus lead to a more efficient and controlled synthesis of silica nanoparticles. The Sol-gel process involves two distinct steps: (i) hydrolysis and (ii) condensation.

$$SiOR_4 + H_2O \xrightarrow{Hydrolysis} Si(OR)_3OH + ROH$$

$$Si(OR)_3OH + Si(OR)_3OH \xrightarrow{Condensation} (OR)_3Si - O - Si(OR)_3 + H_2O$$

During hydrolysis, a hydroxyl ion becomes attached to the silicon atom of the alkoxysilane species. Two of these products react together to generate a siloxane [Si – O – Si] bond, liberating water or alcohol in the process. This condensation step is catalysed by the presence of a base and as the reaction continues, a large network of silicon-containing molecules is generated by the process of polymerization, thus forming a silica nanoparticle with a dense amorphous core of silica, as shown in Figure 1.8.

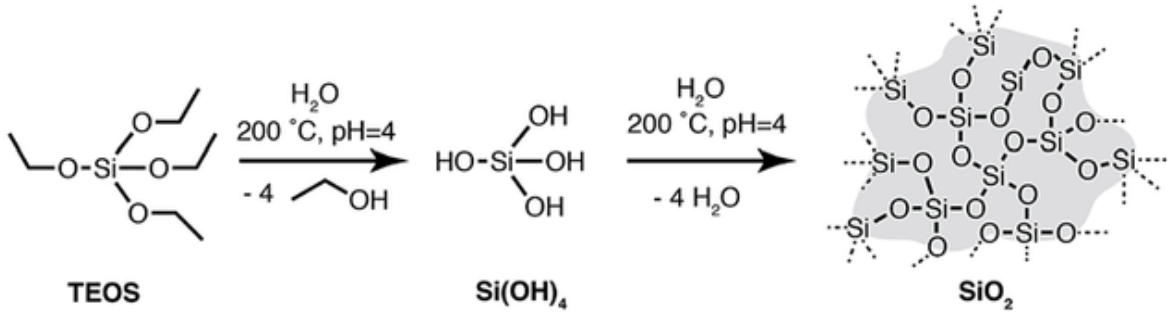

Figure 1.8: Sol-gel synthesis of silica particle with dense silica core [70]

The size of the resulting particle depends on the type of silicon alkoxide and alcohol used during the reaction [61,71]. Typically the particle size increases with increasing chain length of the alcohol and also the hydrocarbon chain length of the alkyl silicates [72]. Furthermore, research on varying the temperature by Tan et al. showed a decrease in temperature resulted in monodisperse particles with a size of ~2 μm [73]. The effect of the catalyst concentration was studied by Ibrahim et al. who demonstrated that particle size increases with ammonium concentration [62].

Monodispersed silica nanoparticles synthesized with a specific particle size and narrow distribution by the Sol-gel process have various applications in research. Sacks and Tseng investigated the sintering behaviour of these colloids, which produced highly ordered compacts [74]. Unger et al. used them as a packing material for capillary chromatography [75]. They have also been investigated as a material from which to fabricate photonic crystals of 3D periodic structure [76,77]. As mentioned in Section 1.2, due to the low toxicity and biocompatibility of silica nanoparticles, they are used in medical, biological and chemical industries [78,79]. Functionalisation of the surfaces of the nanoparticles has allowed their range of applications to spread and dye-doped silica nanoparticles have been designed for potential uses in the biomedical field and also coating applications [80,81]. Self-assembly of the colloids have generated patterns which have potential applications in optical, magnetic and electronic devices as photonic band gap materials. Furthermore self-assembly at the liquid-liquid interface has gained popularity and stabilised 2 or 3D silica sphere structures have been self-assembled at the LLI to fabricate 2 or 3D ordered structures [82].

1.2.2.B Mesoporous Silica Nanoparticles (MSNs)

A desire for the use of nanoparticles as catalysts and sorption media required nanoparticles with high surface area [83]. This resulted in the formation of silica nanoparticle with pores, thus giving them attractive features such as large surface areas, tunable pore sizes and volumes and stable structures with well-defined surface properties [84]. The pores of these mesoporous nanoparticles range in size from ~2 – 50 nm, as described in Figure 1.9.

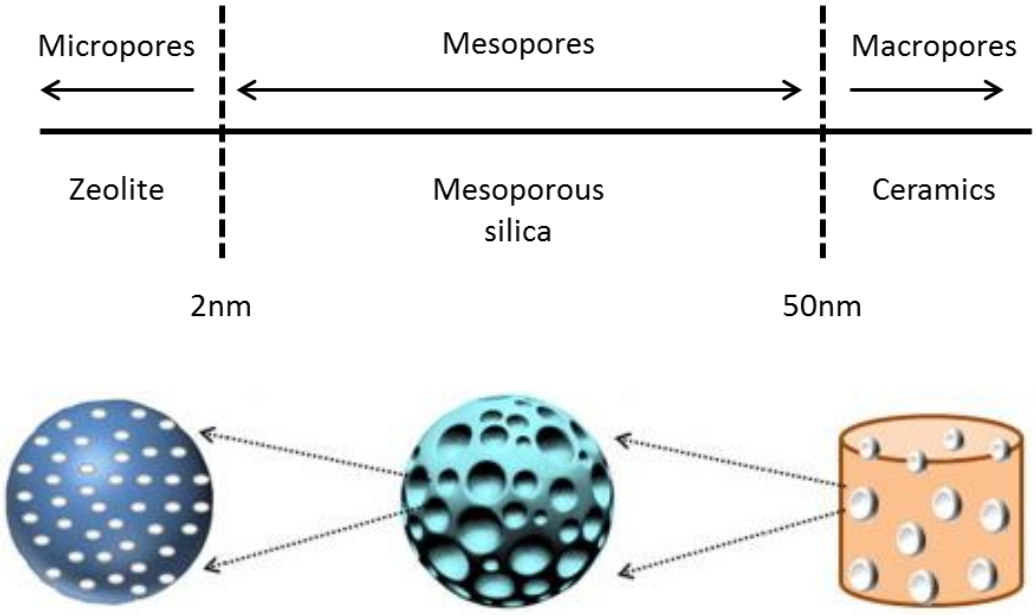

Figure 1.9: Distinguishing between micro-, meso- and macro- pores according to size, with examples. Image adapted from Owens et al. [85]

The first mesoporous silica was discovered in 1992 by Kresge and co-workers [86]. They proposed a liquid-crystal 'templating' route to generate mesopores in the silica. Highly ordered materials with ~3 nm sized pores were obtained from silicate gels and quaternary ammonium surfactants of differing chain lengths. The alignment of pores was either hexagonal (MCM-41) or cubic (MCM-48) [87]. The nomenclature MCM represents Mobil Composition of Matter, as these mesoporous silica nanoparticles were first developed in the labs of the Mobil Corporation [88]. However, it wasn't until 2003 that Lin and co-workers were able to control the morphology and generate nanosized mesoporous particles that could be stabilised as colloidal solutions. They synthesized functionalized mesoporous silica nanospheres with an average size of 200 nm and pore diameter of 2.3 nm [84]. Since then many different procedures have been developed to synthesise mesoporous silica nanoparticles, in the shape of spheres or rods, with mostly cylindrical shaped pores which vary in the level of order of molecular organisation [89–92]. The inorganic silica framework can have a well ordered hexagonal, disordered or cubic pore structure, which is determined by the synthesis conditions applied [88].

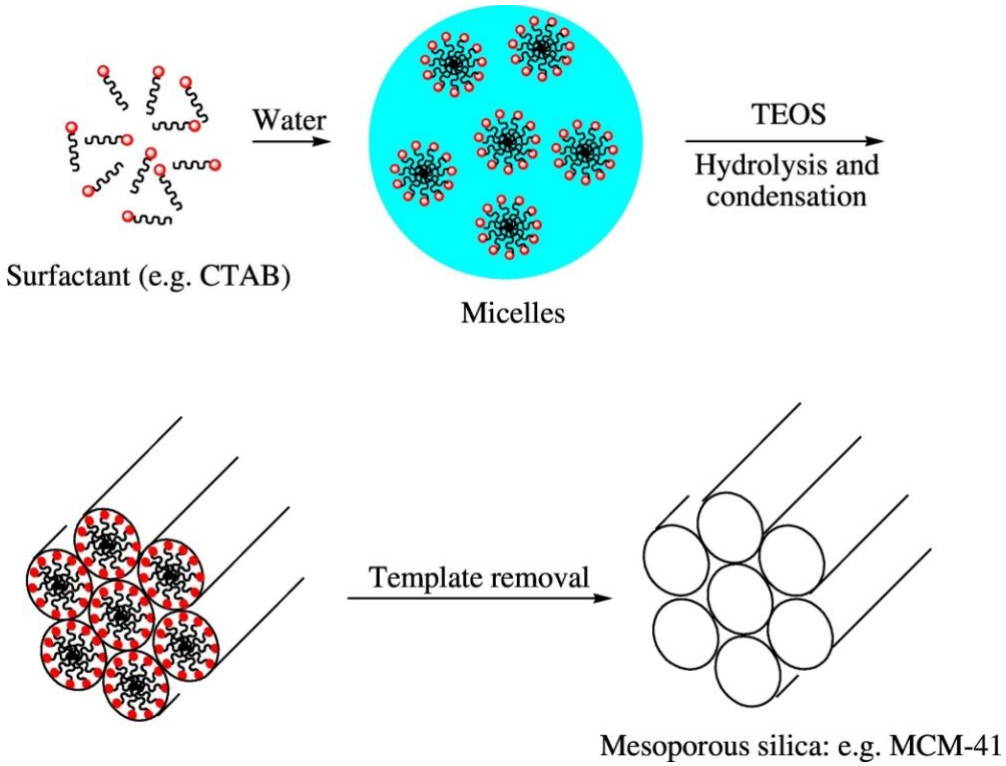

Figure 1.10: Schematic of MSN synthesis using a surfactant templated sol-gel approach [93]

The general synthesis route for uniform mesoporous silica nanoparticles is based on a surfactant templated sol-gel approach as shown in Figure 1.10. Thus, hydrolysis and condensation of the alkoxysilane occurs in an aqueous alkaline solution, similar to the procedure for dense silica nanoparticles, but in the presence of an ammonium surfactant. It is the presence of the surfactant that creates the porosity in the material. The first step is to dissolve the surfactant in water, add the base and alkoxysilane and heat the mixture to allow the polymerization of the silica [88]. During this process, the surfactant forms micelles with a hydrophobic interior and hydrophilic surface. The silica network grows around these micelles, resulting in particles with surfactant and solvent filled channels [94]. Compared with the procedure for dense silica nanoparticles, an extra step is required here to remove the surfactant template and so expose the pores.

Methods of extraction include calcination and solvent extraction, ozone treatment, reflux or sonication and centrifugation with an acidic mixture (ion exchange), depending on the nature of the mesoporous material [95,96]. The resulting nanoparticles are generally dispersed in a liquid medium, however template removal greatly effects their dispersity and so they tend for form large aggregates which greatly reduces their benefits [95].

As with the dense nanoparticles, synthesis conditions, for example pH, temperature, surfactant and co-solvent, can be manipulated to control the size and shape of the nanoparticles that are produced. The pH of the precursor solution is influential during the hydrolysis step of the synthesis. Hydrolysis can take place in acidic or basic solutions but is very slow at neutral pH. Furthermore, silica is only negatively charged at pH values above its isoelectric point of pH 2. The silica needs to be negatively charged in order to have an electrostatic interaction with the positively charged surfactant and assemble to form the silica-surfactant nuclei. The greater the pH the larger the amount of mesoporous silica nanoparticles generated, thus Ding & Su determined pH 2.6 to be optimal in their synthesis [97]. Möller et al. showed that if the common base sodium hydroxide (NaOH) is replaced by triethanolamine (TEA), then the reaction can be run at a lower pH with the condensation step being influenced by the complexation effect of TEA and thus generating discrete mesoporous nanoparticles with narrow particle size distribution [83]. The groups of Vansant and Ogawa varied the surfactant concentration, which allows control over the diameter and volume of pores, and thus of the surface area of the product material [98]. Increasing the amount of surfactant leads to increases in total pore volume and hence particle surface area, but with individual pore diameters remaining unchanged [99]. Vansants group also determined that varying the amount of ammonia used relative to surfactant concentration allowed tuning of the pore diameter; additional ammonia leads to pores with greater diameters, but with a corresponding decrease in total pore volume and particle surface area. Furthermore, they investigated the effect of the time allowed for the reaction to proceed on particle porosity, with greater reaction times leading to increases in total pore volume and particle surface area. Longer reaction times also lead to increases in overall silica particle size and decreases in the uniformity of the size distribution [98].

MSNs have two different surfaces – an interior channel surface as well as the exterior particle surface. Modification of these surfaces has allowed the range of applications of mesoporous nanoparticles to widen. There are two main strategies for modifying the surface of the nanoparticles: postsynthesis functionalization (grafting) [100,101] and in situ functionalization (co-condensation) [102–104]. Grafting selectively functionalises the exterior surface of a post synthesized nanoparticle. It is based on a condensation reaction between an organoalkoxysilane and free and geminal silanol groups (which have two hydroxyl groups attached to one silicon atom) on the silica surface and openings of the pores [105,106]. Following this, cross linking or click chemistry based reactions can easily bind the target analytes (proteins, DNA) with the grafted functional groups (-NH_2, -COOH, -SH) [88,107]. Organosilica materials (a siliceous material with silicon – carbon bonds) can be used which allow the synthesis of hybrid materials, incorporating carbon groups into the inorganic silica matrix. On the other hand, co-condensation is a direct synthesis method which generates monodisperse, multi-functionalised MSN, with better bonding between the organoalkoxysilane and the pore walls, thus giving a more homogenous distribution of organic groups throughout the pore structure. The co-condensing agent (organoalkoxysilane) is added to the aqueous surfactant and alkoxysilane solution during condensation to control the shape of the resulting mesoporous silica nanoparticles, as outlined in Figure 1.11. The characteristics of the co-condensating agent, for example concentration, molecular size and hydrophobicity/hydrophilicity, determine the ability of the co-condenser to influence the stabilization of the micelles during MSN formation. This ultimately controls functionality, shape and size of the MSN produced [92,104,108].

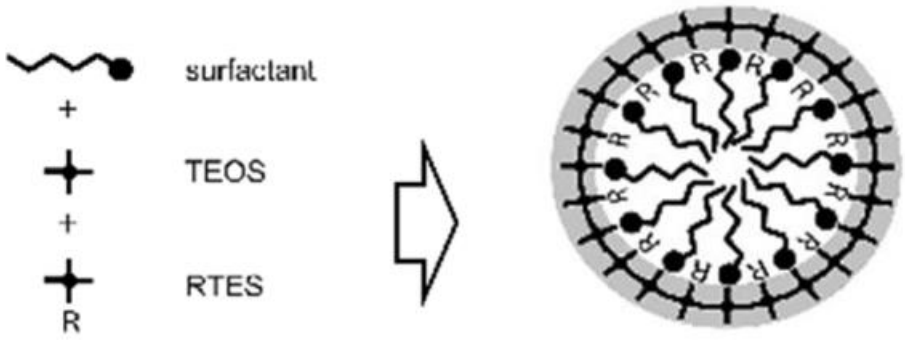

Figure 1.11: Schematic of alkoxysilanes (TEOS) with organoalkoxysilanes (RTES) and micelle forming surfactant, in a co-condensation reaction, adapted from reference [108]

Various techniques are used to characterize dense and mesoporous silica nanoparticles [89–91,104,108]. Scanning electron microscopy (SEM) and transmission electron microscopy (TEM) are used to determine sample morphology and microstructure, allowing the measurement of particle diameter and distance between pores (for MSN) within a particle. Dynamic light scattering (DLS) also allows particle morphology and size to be recorded. X-ray powder diffractometry (XRD) shows the long range order of materials, i.e. their structure and crystallinity. Gas adsorption volumetry of MSNs characterizes the porous materials using two different equations. The Brunauer-Emmett-Teller (BET) method calculates the specific surface area of porous materials, while the Barrett, Joyner and Halenda (BJH) method derives pore size distribution [109]. With regards functionalized silica nanoparticles, additional techniques are used to characterize the presence, connectivity and surface coverage of the functional groups on the silica. Infrared (IR), Ultraviolet-visible (UV/Vis) and Raman spectroscopy are used to confirm the presence of the functional groups and template. Nuclear magnetic resonance (NMR) spectroscopy studies the incorporation of the organic groups, specifically the connectivity of the functional organic groups, to the silica framework. Thermogravimetric analysis measures the weight change in a sample relating to desorption of template, thus quantifying the amount of template that was incorporated. It can also be used to measure the surface coverage of functional groups.

The combination of excellent physical and chemical properties, large surface area and ability of the surface to be functionalized gives mesoporous silica nanoparticles a huge range of applications, in fields such as catalysis [110], pollutant adsorption [111], chemical sensors [112] and electroanalysis [113]. Furthermore, they have been used in biochemistry as carriers for the controlled release delivery of drugs, biocides and proteins [84,114]. There is a growing interest for the use of silica based porous materials at the LLI due to their favourable adsorption kinetics and selectivity [96,115]. Silica nanoparticles themselves do not have any sensing signal but serve as an aid to enhance the selectivity and preconcentration of ionic species at the interface and thus their transfer across the ITIES. This ability to detect ionic species is of major benefit in both environmental monitoring and clinical diagnosis. The sensing of synthetic organic molecules, such as drug molecules and pollutants, is of significant interest. Functionalized silica nanoparticles can be used as a base on which a target molecule (e.g. drug molecule) can be imprinted and used to improve selectivity of detection in systems such as the liquid-liquid interface.

1.3 ***Molecular imprinting***

The field of molecular imprinting has gained a lot of attention in recent years as a result of its attractive properties of selectivity, stability and low cost. Molecular imprinting is defined as the arrangement of a cross-linked silica or polymer matrix around an imprint molecule, interacting via covalent or non-covalent interactions with chosen functional groups on the silica or polymer. Upon removal of the imprint molecule, a cavity with a specific size and shape is exposed, with the functional groups on the surface which give it a molecular memory, thus allowing it to selectively rebind to the target imprint molecule [116,117].

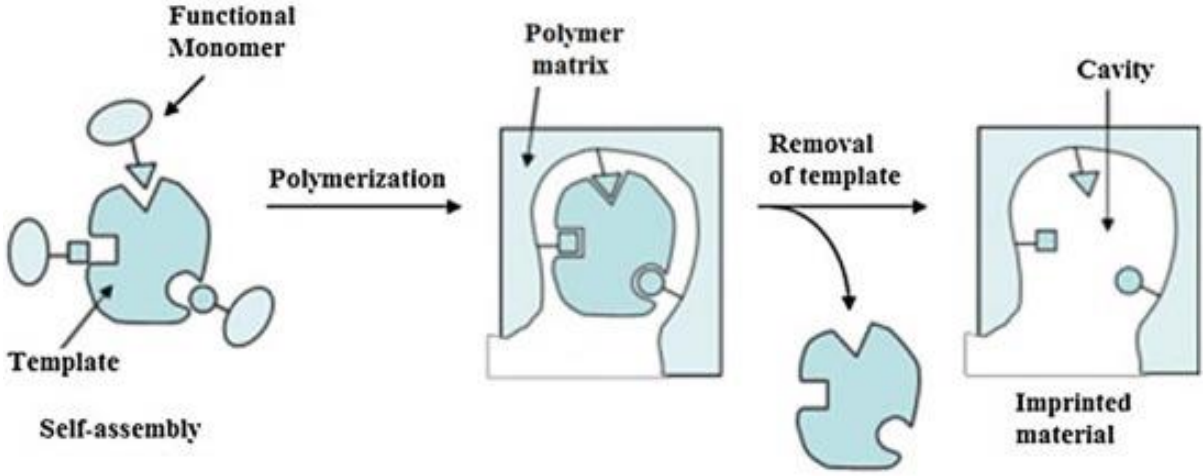

Figure 1.12: Schematic of the principle of Molecular Imprinting [118]

Molecular recognition is the underlying principle for biological processes such as that between antibodies and their target antigens, enzymes with their substrates and hormone receptors with their hormones [117]. This 'lock and key' concept allows specialized structures to recognize and bind with their target molecules with a high affinity and selectivity. As a result these biomacromolecules have numerous applications in medicine and biotechnology. ELISA (enzyme linked immunosorbent assays) use a specific biological recognition mechanism to detect and quantify targets. Antibodies have been used to treat infections, diseases and more recently cancer. Unfortunately though, these natural mechanisms have their disadvantages. Lack of stability, degradation, low abundance and problems with integration in industry have meant that researchers have been looking for alternatives [117]. Consequently, artificial structures have been synthesized from silica and polymers, that are tailor made with high selectivity.

1.3.1 *History of Molecular Imprinting*

The concept of molecular imprinting evolved after investigations by the botanist Tswett in 1906, for its usefulness in purifying and analysing single compounds from crude mixtures. Tswett carried out research into plant pigments and invented adsorption chromatography. Research during much of the 1900's was focused on developing raw materials and techniques for use in chromatography [119–121]. The use of silica as a material in chromatography was first noted by Polyakov in the early 1930's. He investigated the effect of organic additives (benzene, toluene and xylene) on the structure of silica pores, further observing that after the synthesis, the quantity of additive re-adsorbing depended on the structure of the additive present during silica drying [122]. The explanation for this preferential uptake can be explained by the additive generating a templating effect and thus the concept of molecular imprinting was born. Further research by Polyakov gave more detail of this selective molecular recognition phenomenon [123,124].

The link between the biological antibody-antigen relationship and the chemical silica-additive interaction was made by Linus Pauling and Frank Dickey in 1949, based on results of experiments carried out by Dickey. At that time, Pauling's research was focused on the origin of the selectivity of antibodies. Dickey synthesized what he called 'specific adsorbents' by mixing alkyl orange dyes with sodium silicate and glacial acetic acid. The polymerization of the silica around the dye molecules and their subsequent extraction, generated a cavity (imprint), which was able to preferentially rebind the template dye over the other dyes [125]. Dickey suggested two related processes that could explain what was occurring during the experiments and published them in a later paper [126]. The term 'imprint' was coined by Haldeman and Emmett, after they reinvestigated Dickey's research and used the term to describe the micropores that were created in the adsorbent by the dye molecule used [121,127]. Unfortunately much debate ensued about the true mechanism occurring and limitations in stability and reproducibility of imprinted silica materials caused research in imprinting to shift away from silica and towards organic polymers [116,128]. After many years of research into the mechanisms occurring during imprinting with polymer imprinted materials, limitations were also observed and so, more recently, the use of silica has regained appeal. Thus a brief introduction on polymer imprinted materials will be discussed in section 1.3.3, including their limitations which are resulting in the drive of research back towards silica imprinted materials, discussed in section 1.3.4.

The first results of molecular imprinting in synthetic organic polymers were reported independently by Wulff and Klotz in 1972 [129,130]. Their imprinting involved covalent interactions between the polymer matrix and the template (imprint) molecule. However in 1993, a non-covalent approach was pioneered by Mosbach, who recognized the potential of molecularly imprinted polymers as synthetic antibody mimics [131]. Furthermore, Whitcombe et al. introduced a semi-covalent molecular imprinting strategy which helped overcome the drawbacks that were associated with covalent and non-covalent molecular imprinting, i.e. slow binding kinetics and low imprinting fidelity, respectively [132,133]. This significantly broadened the scope of molecular imprinting. The wide range of organic polymer precursors as well as compatible functional monomers available, coupled with the high stability and lower cost of molecularly imprinted polymers resulted in greater popularity of the use of polymers over silica. Consequently, they have been studied extensively and several types /methods have been categorized.

1.3.2 *Interactions in Molecular Imprinting*

Molecular imprinting is achieved by the interaction between an imprint molecule with its corresponding functional monomer. The type of interaction differentiates the types of molecular imprinting. The five main types are covalent, non-covalent, electrostatic/ionic, semi-covalent and metal centre coordination, each of which are shown in Figure 1.13 [116]. Covalent imprinting generally uses reversible condensation reactions with boronate esters, ketals/acetals and Schiff's base. While this method gives highly specific imprints, it is limited by slow binding and dissociation. Conversely, non-covalent imprinting involves ionic interactions, hydrogen bonding, van der Waals forces and $\pi - \pi$ interactions, thus resulting in rapid binding and removal and a more simplistic method. However, its dominant limiting factor is diffusion and it is also very sensitive to slight disruptions of the interactions within the complex and so not very robust. Finally, semi-covalent imprinting offers a compromise whereby the template is bound covalently to the functional monomer during the synthesis, but rebinding after uses non-covalent interactions. It uses small sacrificial spacer fragments, for example carbon dioxide, to facilitate the transition from covalent to non-covalent interactions. Semi-covalent imprinting combines the positive aspects of the two methods i.e. durability and high specificity, as well as rapid target uptake [116,134].

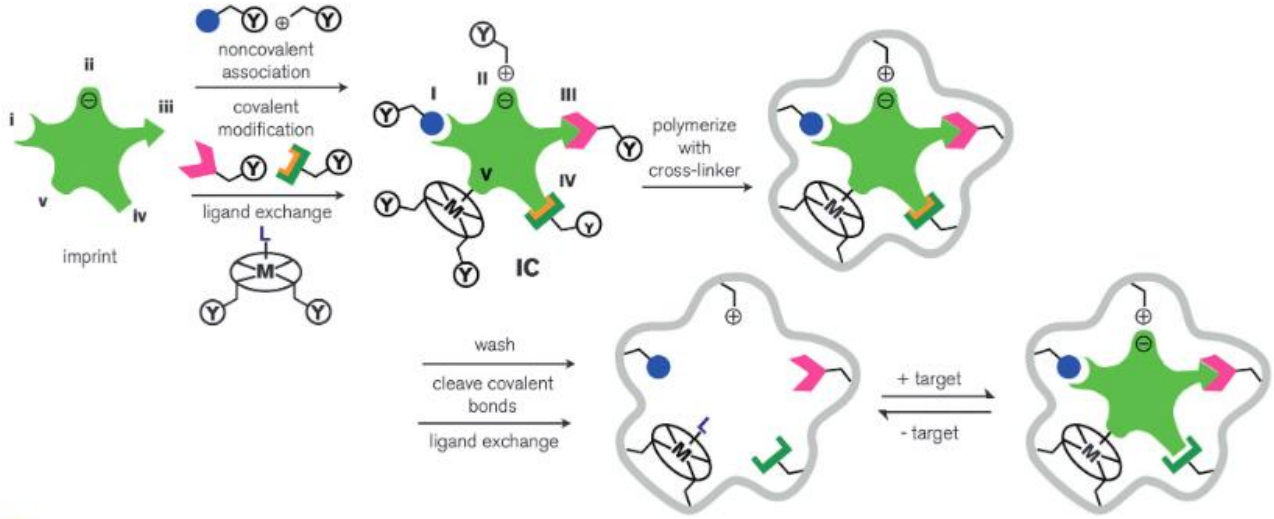

Figure 1.13: Schematic showing the five main types of molecular imprinting (i) noncovalent, (ii) electrostatic/ionic, (iii) covalent, (iv) semicovalent and (v) metal centre coordination [116]

The efficiency of the molecular recognition process is not only dependent on the template-ligand binding affinity but also on reaction parameters such as initial ligand concentration and the stiffness of the matrix. The quality of a molecularly imprinted particle (MIP) can be measured two ways. The first is its efficiency at binding to a target analyte vs a non-imprinted particle (NIP). Secondly, its ability to distinguish between analytes that are very similar, i. e. have the same size but different spatial pattern.

1.3.3 *Molecularly Imprinted Polymers*

Firstly, we will take a brief look at molecularly imprinted polymers. Their general synthesis requires a template, functional monomer, cross-linker, polymerization initiator and solvent. It involves the imprint molecule (template) combining with its corresponding functional monomer, either non-covalently, covalently or via a ligand to metal interaction. This forms an imprint-functional monomer complex. Within this, the functional groups on the monomer bind via hydrogen bonding or van der Waals interactions, electrostatic or ionic interactions, covalent bonding or ligand-metal coordination. A separate functional group on the monomer interacts with a cross-linker, polymerizing the complex and securing the interactions within. Extraction of the imprint via washing, cleavage of chemical bonds or ligand exchange, results in an imprint cavity with surface functional groups, which thus allows the uptake of the target molecule via the specified interactions [116,134]. Molecularly imprinted polymers can take the form of porous microspheres, nanospheres, nanowires, thin films, nanostructured films,

nanocomposites and quasi-soluble nanogels. Depending on their size, their number of binding sites can vary between thousands and millions [117].

Molecular imprinting is an interdisciplinary field, combining synthetic chemistry with polymer chemistry and physics, as well as analytical science and computational design [133]. Consequently the range of applications for molecularly imprinted polymers spans many disciplines. Initially the focus was on the use of molecularly imprinted particles as specific separation materials in chromatography, however once knowledge of their ability to recognize specific molecular targets grew, their popularity in the fields of affinity separation, chemical sensors and assays, catalysis and biomedical applications also increased [117,134,135].

However, challenges still remain such as incomplete template removal, slow mass transfer and limitation to organic solvents. Thus, a shift to using other materials has emerged in recent years and silica is now regaining its importance as an imprinting matrix [117].

1.3.4 *Molecularly Imprinted Silica*

Moving back to the more relevant topic of molecularly imprinted silicas, these are synthesized via a Sol-gel approach, similar to that discussed in Section 1.2.2.A, to make silica nanoparticles. This process requires a template (imprint molecule), solvent, functional monomer, cross-linker and catalyst. The chosen imprint molecule will dictate the choice of functional monomer to be used, with the cross-linker defining the properties of the matrix. As with the synthesis of imprinted polymers, the interaction between the imprint molecule and the monomer can be covalent or non-covalent, as shown in Figure 1.14. Organosilica materials can be used which allow the synthesis of hybrid materials, incorporating carbon groups into the inorganic silica matrix [116]. (Organo)alkoxysilanes are used as molecular precursors, reacting together to produce siloxanes during a hydrolysis reaction, which interact with the template molecule. This forms a colloidal solution (sol) which then polycondenses with the cross-linking alkoxysilane in the next step to form an integrated network (gel) of amorphous highly cross-linked silica material with the template inside. The solvent and by-products of the hydrolysis reaction serve as porogens in the material.

Typically, the pores in the bulk Sol-gel silica synthesized using this method, are a mixture of micropores (<2 nm) and mesopores (2 - 50 nm), with broad pore size and shape distribution [116,134,136]. Extraction of the template is achieved by washing of the product with several solvents, creating the imprint cavity with a specific size and shape (as shown in Figure 1.14 A) and with functional groups for specific molecule recognition on its interior surface (for example the NH_2 groups in the cavity after chemical cleavage which can rebind the template molecule, shown in Figure 1.14 B).

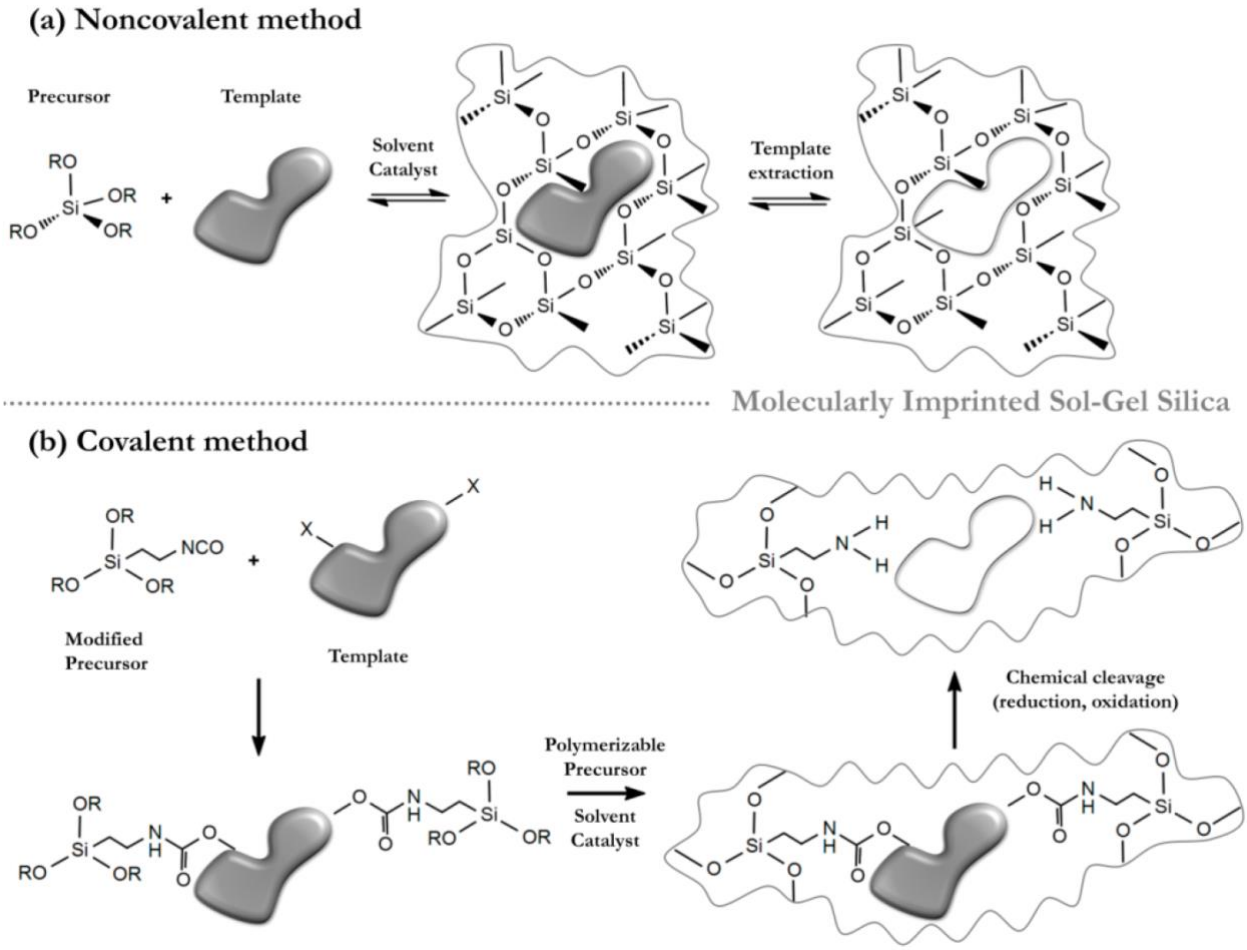

Figure 1.14: Schematic of MI silica synthesis using sol-gel process, with (a) noncovalent and (b) covalent interactions between the silica precursor and template [137]

The synthesis can take place under base catalysis (> pH 2) or acid catalysis (< pH 2) conditions, with the crossover at pH 2 indicating the isoelectric point of silica, at which reaction rates are slow as a result of the silica being neutral. Experiments are generally done between temperatures of 0 - 100 °C. The rate of hydrolysis is dependent on pH, water content and the nature of the alkyl group (represented by 'R' in the silica precursor in Figure 1.14), as

in general the larger this group, the slower the rate of hydrolysis. Furthermore, the rate of condensation can also be hindered by steric effects from large alkyl groups. The porosity of the Sol-gel silica product can be disordered with indirect diffusion pathways, thus control over the porosity and shape of the particles, by regulating the quantity of water, solvent and additives present in solution, needs to be exerted during the synthesis process [116]. However, on the whole, the Sol-gel method for silica synthesis has several distinct advantages that make it stand out as an excellent method for generating imprinting material. It is extremely versatile and allows controllable pore size of the product during synthesis, it takes place at room temperature without thermal or chemical decomposition and uses eco-friendly solvents (for example water and ethanol, as opposed to harsh solvents such as chloroform, acetonitrile and toluene used during the molecularly imprinted polymer synthesis) [134,138]. Furthermore, the imprinted product generated has a robust, rigid structure which gives it the advantage of having a high degree of shape, size and functional recognition selectivity, as opposed to the more flexible polymers. They are stable and compatible with aqueous and biological systems, and their low cost and ease of production has resulted in their use across many fields, both in analysis and sample preparation [116,138].

In order to overcome the limitations of poor diffusion and accessibility in the imprinted molecules synthesized as a bulk monolith using the Sol-gel process above, as well as issues with heterogenous distribution of binding sites, research has been directed towards the synthesis of templated mesoporous materials, which give controlled porosity in the form of uniform channels and thus better adsorption/desorption kinetics. Studies have shown that diffusion is effected by porosity and thus the best solution to improve diffusion is to increase porosity in the molecularly imprinted materials [116]. A silica matrix with a close packed network of nanometer sized channels, reduces the diffusion distance, as the channels will be open at the outer surface of the individual particles, allowing for easier flow of the molecules through the material, to the imprint sites [139]. Mesoporous silica materials have a high pore volume with nanosized pore wall thickness, thus giving greater accessibility to the target molecule and fast kinetic binding [140]. Thus the benefits of these imprinted mesoporous silica particles have allowed the field of molecular imprinting in mesoporous silica, which although still a relatively new concept, to advance in recent years, with research and knowledge of this topic expanding and continuing to do so, thus a positive future lies ahead for this interesting topic.

2. MATERIALS AND METHODS:

This section provides information on all experimental, technical and instrumental details used during the course of the research. It begins with a full list of the chemicals used, followed by the electrochemical setup used during liquid-liquid electrochemistry experiments and then a summary of other instrumentation used in this work. Finally some protocols for fabrication, methodology and synthesis are given.

2.1 ***Chemicals***

Information on the:

- Name
- Purity
- Abbreviation
- CAS number
- Molar mass
- Source
- Function
- Molecule

are given for each chemical used during this work in Table 2.1.

The chemicals are subdivided under the following headings:

- Aqueous and organic electrolytes
- Silica synthesis materials
- Solvents
- Interfacial active species
- Other compounds

The procedure to make the solutions in *italics* in the table will be outlined in section 2.4.

Table 2.1: List of chemicals used during research

Name	***Purity***	***Abbreviation***	***CAS registry number***	***Molar mass g mol^{-1}***	***Source***	***Function***	***Molecule***
Aqueous and organic electrolytes							
Bis (triphenylphosphoranyldiene) ammonium chloride	97%	$BTPPA^+Cl^-$	21050-13-5	574.03	Aldrich	For organic electrolyte preparation	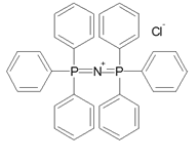
Potassium tetrakis (4-chlorophenylborate)	≥98%	K^+TPBCl^-	14680-77-4	496.11	Fluka	For organic electrolyte preparation	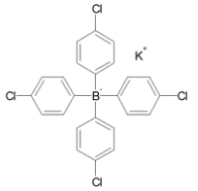
Bis (triphenylphosphoranyldiene) ammonium tetrakis (4-chlorophenylborate)	-	*$BTPPA^+$ $TPBCl^-$*	-	*995.59*	*Synthesised in this research*	*Organic phase electrolyte*	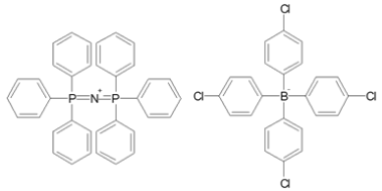
Lithium chloride	≥99%	LiCl	7447-41-8	42.39	Aldrich	Aqueous phase electrolyte	Li^+ Cl^-

Name	*Purity*	*Abbreviation*	*CAS registry number*	*Molar mass g mol^{-1}*	*Source*	*Function*	*Molecule*
Silica synthesis materials							
Ludox® HS-40 12nm colloidal silica	40 wt. % suspension in H_2O	DSNs	7631-86-9	60.08	Aldrich	SiO_2	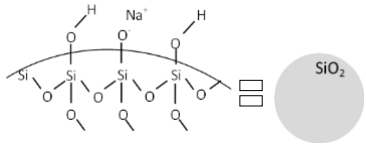
Tetraethylorthosilicate (tetraethoxysilane)	98%	TEOS	78-10-4	208.33	Alfa - Aesar	Synthesise MSNs, NINs and DINs	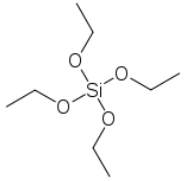
Hexadecyltrimethylammonium chloride (cetyltrimethylammonium chloride)	98%	CTACl	112-02-07	320.00	Aldrich	Synthesise MSNs	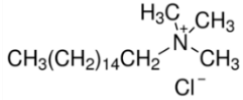
Triethylamine	97%	TEA	121-44-8	101.19	Carlo - Erba	Synthesise MSNs	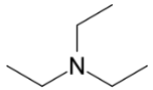

Name	*Purity*	*Abbreviation*	*CAS registry number*	*Molar mass g mol^{-1}*	*Source*	*Function*	*Molecule*
Silica synthesis materials							
Mesoporous silica nanoparticles	*10% w/w suspension in ethanol*	*MSNs*	-	-	*Synthesised in this research*	-	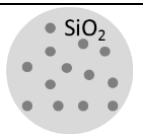
(3-aminopropyl) triethoxysilane	99%	APTES	919-30-2	221.37	Aldrich	Synthesise NINs and DINs	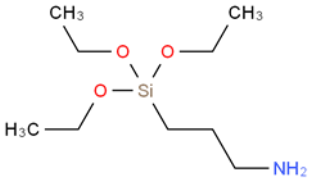
Non-imprinted nanoparticles	-	*NINs*	-	-	*Synthesised in this research*	-	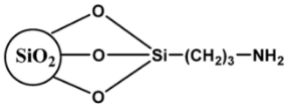
Diclofenac-imprinted nanoparticles	-	*DINs*	-	-	*Synthesised in this research*	-	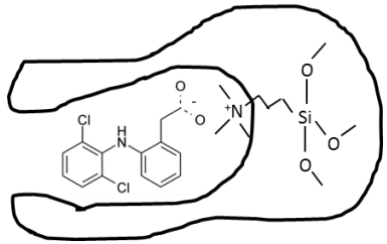

Name	*Purity*	*Abbreviation*	*CAS registry number*	*Molar mass g mol^{-1}*	*Source*	*Function*	*Molecule*
Solvents							
1,2 - Dichloroethane	≥99%	DCE	107-06-2	98.96	Sigma - Aldrich	Organic phase solvent	
5 - Nonanone	98%	-	502-56-7	142.24	Alfa - Aesar	Organic phase solvent	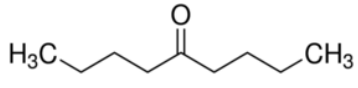
Water	from miliQ system	H_2O	7732-18-5	18.02	-	Aqueous phase solvent	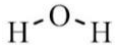
Ethanol	ethanol absolute	EtOH	64-17-5	46.07	Sigma - Aldrich	Extraction of MSNs	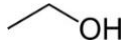
Hydrochloric acid	≥37%	HCl	7647-01-0	36.46	Sigma - Aldrich	Extraction of MSNs	H^+Cl^-

Name	*Purity*	*Abbreviation*	*CAS registry number*	*Molar mass g mol^{-1}*	*Source*	*Function*	*Molecule*
Interfacial active species							
Tetraethylammonium chloride	≥99%	TEA^+Cl^-	56-34-8	165.70	Fluka	Interfacial active species	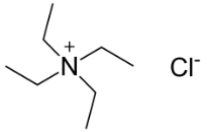
Methylene blue	>82%	MB^+	122965-43-9	319.85	Fluka	Cationic dye	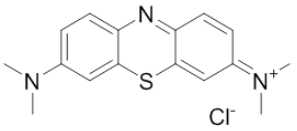
Eosin B	>85%	EB^-	548-24-3	624.06	Sigma - Aldrich	Anionic dye	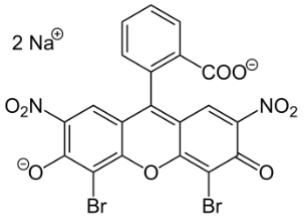
Diclofenac sodium	>98%	Diclo Na	15307-79-6	318.14	Alfa - Aesar	Anionic drug	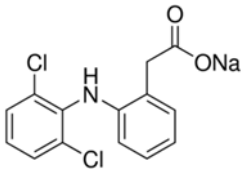

Name	*Purity*	*Abbreviation*	*CAS registry number*	*Molar mass g mol^{-1}*	*Source*	*Function*	*Molecule*
Interfacial active species							
Diclofenac free acid	>98%	Diclo FA	15307-86-5	296.15	Carbosynth	Anionic drug	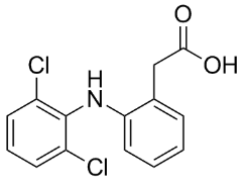
Aceclofenac	99%	Aceclo	89796-99-6	354.18	Alfa - Aesar	Anionic drug	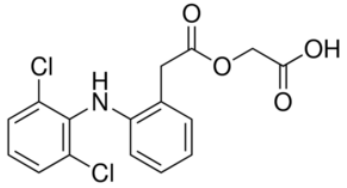
4-phenylazo benzoic acid	98%	PABA	1562-93-2	226.23	Aldrich	Anionic drug	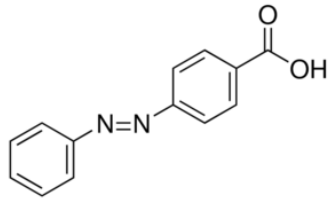

Name	*Purity*	*Abbreviation*	*CAS registry number*	*Molar mass g mol^{-1}*	*Source*	*Function*	*Molecule*
Other compounds							
Iron (III) chloride hexahydrate	99-102%	$FeCl_3.6H_2O$	10025-77-1	270.30	Fluka	Ag/AgCl electrode preparation	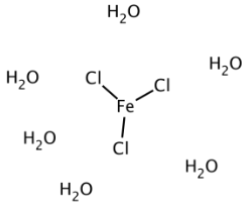
Potassium bromide	99%	KBr	7758023	119.00	Sigma - Aldrich	Used to make IR pellets	K^+Br^-
Acetonitrile	>99,95%	ACN	75-05-8	41.04	Biosolve	HPLC mobile phase	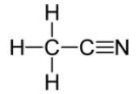
Tris(hydroxymethyl)amino methane	99%	Tris	77-86-1	121.14	Sigma	Buffer	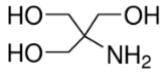
Boric acid	>99,8%	-	10043-35-3	61.83	Aldrich	Buffer	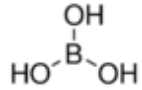
Dimethyl sulfoxide	≥99%	DMSO	67-68-5	78.13	Fluka	CE	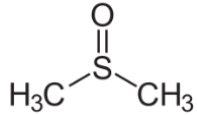

2.2 ***Electrochemical setup***

The custom-made electrochemical cell used to study ion transfer at the ITIES in the presence and absence of silica nanoparticles, was made from glass tubes with inner diameters 12 mm and an interfacial surface area ($A_{interface}$) equal to 1.13 cm^2. The counter electrodes used were made of platinum (Pt) mesh and reference electrodes were silver/silver chloride (Ag/AgCl) wires. The protocol for preparation of the Pt counter electrodes will be discussed in Section 2.4.2. The Ag/AgCl electrodes were prepared by oxidation of silver wire in a saturated $FeCl_3$ solution. There were two sets of reference and counter electrodes present, one for the aqueous phase and the second for the organic phase. The solutions used in each phase during electrochemical experiments are outlined in the scheme below. The organic reference phase (represented by the number 3 in the figure below) consists of 10mM $BTPPA^+Cl^-$ in 10mM LiCl. A more detailed explanation of the electrochemical setup is described in Appendix 1.

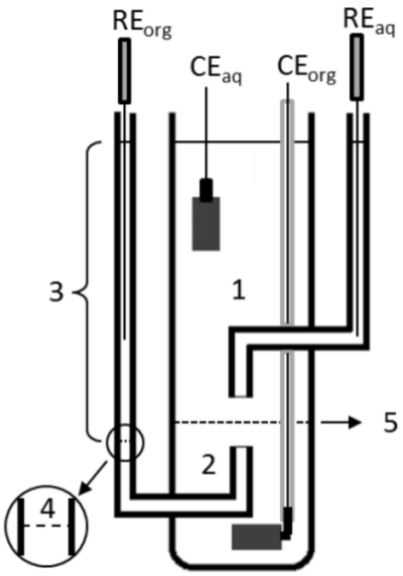

Figure 2.1: Four-electrode electrochemical cell with macroscopic liquid-liquid interface. RE_{org} and RE_{aq} represent the organic and aqueous reference electrodes, CE_{org} and CE_{aq} corresponding to the organic and aqueous counter electrodes respectively. 1 – Aqueous phase; 2 – Organic phase; 3 – Organic reference phase; 4 – Liquid-liquid interface between the organic and organic reference phases; 5 – ITIES

Different electrochemical cell compositions were used during experiments and are as follows:

Electrochemical cell 1:

$$Ag_{(s)} \,|\, AgCl_{(s)} \,|\, \begin{matrix} 10\ mM\ LiCl_{(aq)} \\ x\ mM\ interfacial\ active\ ion_{(aq)} \\ y\ g\ L^{-1}\ silica\ nanoparticles \end{matrix} \,\Big|\, \begin{matrix} 10mM\ BTPPA^{+}TPBCl^{-}_{(org)} \\ in\ 1{,}2-DCE \end{matrix} \,\Big|\, \begin{matrix} saturated\ BTPPA^{+}Cl^{-} \\ 10\ mM\ LiCl \end{matrix} \,|\, AgCl_{(s)} \,|Ag_{(s)}$$

Electrochemical cell 2:

$$Ag_{(s)} \,|\, AgCl_{(s)} \,|\, \begin{matrix} 100\ mM\ LiCl_{(aq)} \\ y\ g\ L^{-1}\ silica\ nanoparticles \end{matrix} \,\Big|\, \begin{matrix} 10mM\ BTPPA^{+}TPBCl^{-}_{(org)} \\ in\ 1{,}2-DCE \end{matrix} \,\Big|\, \begin{matrix} saturated\ BTPPA^{+}Cl^{-} \\ 10\ mM\ LiCl\ in\ H_2O \end{matrix} \,|\, AgCl_{(s)} \,|Ag_{(s)}$$

Electrochemical cell 3:

$$Ag_{(s)} \,|\, AgCl_{(s)} \,|\, \begin{matrix} 10\ mM\ HCl_{(aq)} \\ y\ g\ L^{-1}\ silica\ nanoparticles \end{matrix} \,\Big|\, \begin{matrix} 10mM\ BTPPA^{+}TPBCl^{-}_{(org)} \\ in\ 1{,}2-DCE \end{matrix} \,\Big|\, \begin{matrix} saturated\ BTPPA^{+}Cl^{-} \\ 10\ mM\ LiCl\ in\ H_2O \end{matrix} \,|\, AgCl_{(s)} \,|Ag_{(s)}$$

Electrochemical cell 4:

$$Ag_{(s)} \,|\, AgCl_{(s)} \,|\, \begin{matrix} saturated\ BTPPA^{+}Cl^{-} \\ 10\ mM\ LiCl \end{matrix} \,\Big|\, \begin{matrix} 10mM\ BTPPA^{+}TPBCl^{-}_{(org)}\ in \\ 40{:}60\ DCE{:}5-nonanone\ (v/v) \end{matrix} \,\Big|\, \begin{matrix} 10\ mM\ LiCl_{(aq)} \\ y\ g\ L^{-1}\ silica\ nanoparticles \end{matrix} \,|\, AgCl_{(s)} \,|Ag_{(s)}$$

2.3 ***Instrumentation***

Electrochemical measurements:

Two electrochemical techniques were used during these experiments – Alternating Current (AC) Voltammetry and Cyclic Voltammetry (CV).

Cyclic voltammetry experiments were run with an Autolab 302N potentiostat using Nova 1.10.1.9 software by Metrohm Autolab B.V. Scans were run at a sweep rate of 5 mV s^{-1}.

Cyclic voltammograms were plotted using the Galvani scale, in order to make all results uniform. The formal transfer potential of TEA^+, $\Delta_o^w\phi^{0'}_{TEA^+}$ = 0.049 V, was calculated from the following equation (where ΔG is the Gibbs energy of TEA^+ in 1,2-DCE [141], z is the charge on the ion and F is the Faraday constant) and then used to calibrate the potential window.

$$\Delta G = zF\Delta_o^w\phi^{0'}_{TEA^+}$$

TEA^+ was added to the aqueous phase of the electrochemical cell at the end of a series of experiments for potential calibration purposes.

For CV experiments, the transfers of Li^+ and Cl^- from the aqueous phase to the organic phase establish the positive and negative limits of the potential window, respectively. In the presence of SiO_2, the potential was calibrated using the limits of the potential window as previous studies have shown that the transfer of both Li^+ and Cl^- is not hindered by the presence of electrogenerated silica [142].

AC voltammetry experiments were run using GPES software with an Autolab PGSTAT-12. Parameters for the AC experiments were as follows - modulation time: 0.33 s, interval time: 0.73 s, frequency (*f*): 6 Hz, step potential: 5 mV, amplitude (*A*): 5 mV RMS. The potential region was scanned at phase angles of 0° and 90°. The phase shift (ϕ) was determined from the currents obtained at both phase angles, using the following equation [44,143]:

$$\phi = \tan^{-1}\frac{i_{90}}{i_0}$$

The total impedance (*Z*) was calculated as follows:

$$Z = \frac{A}{\sqrt{i_{90}^2 + i_0^2}}$$

It comprised of real (Z_{Re}) and imaginary (Z_{Im}) parts:

$$Z_{Re} = Z\cos\phi$$

$$Z_{Im} = Z\sin\phi$$

The real part was connected to the resistance of the solution and the imaginary part of the impedance expressed the interfacial capacitance (*C*), which could then be calculated:

$$C = \frac{1}{\omega Z_{Im}}$$

where $\omega = 2\pi f$.

UV-Vis spectroscopy:

UV/Vis experiments were carried out using an Agilent Technologies Cary 60 UV/Vis spectrometer, with plastic cuvettes used for experiments with Methylene blue and Eosin and quartz cuvettes for experiments with Diclofenac, Aceclofenac and PABA.

Ultrafiltration (UF) setup:

A 25 mm diameter stirred ultrafiltration cell (Amicon Model 8010) was used with Millipore Ultrafiltration membranes in regenerated cellulose (PLGC, 10 kD) [144]. The filtration took place under pressure using nitrogen gas, while stirring at 300 rpm.

Zeta-potential measurements:

Zeta-potential measurements were recorded using a Zetasizer NanoZS by Malvern Instruments, with DTS 1061 folded capillary cells.

Gas adsorption volumetry:

A Belsorp-max volumetric gas adsorption instrument from MicrotracBEL was used to obtain adsorption isotherms for the mesoporous silica nanoparticles (MSNs), from which specific surface area was calculated using the BET (Brunauer, Emmett, Teller) equation.

Stop flow (SF) experiments:

Stop flow experiments were carried out using equipment from Bio-Logic. The set up consists of two syringes powered by motors, which push a pre-selected quantity of liquid from both syringes into a cell simultaneously, combining them at high speed. The incident radiation from the arc lamp was set at 650 nm, the light travels through the cell and intensity of transmitted light recorded using a photomultiplier detector [145–147].

Elemental analysis

This analysis was carried out using Thermo Finnigan Flash 1112 CHN analyser with Eager 300 software. The weight percent of carbon, hydrogen and nitrogen was measured for both NINs and DINs, by burning the solid samples in excess oxygen at 940 °C in the presence of tungstic anhydride (WO_3) for 15 s. This generated their oxides which flowed to a gas chromatograph (Chromosorb) column by helium and detected by a thermal conductivity detector, generating a chromatograph whose curves are analysed by the software, generating percentages.

Syringe filter:

This apparatus was attached to a syringe and used type GVWP 0.22 µm filter paper, to successfully remove NINs and DINs from solutions.

Fourier transform Infra-red spectroscopy (FT-IR):

IR spectra were recorded in transmission mode using a Thermo Scientific Nicolet 8700 FT-IR apparatus, with more detailed spectrums achieved using KBr pellets with the same apparatus.

Inductively coupled plasma atomic emission spectroscopy (ICP-AES)

The Si concentration in solutions of 0.01 – 0.4 mM Diclofenac with 0.1 g L^{-1} NINs and DINs, which had been syringe filtered before analysis, were measured using a Horiba Jobin Yvon - ULTIMA 2. 0.4% Hydrofluoric acid was used and two wavelengths chosen for detection – 212.412 and 251.611 nm.

High Performance Liquid Chromatography (HPLC):

Chromatograms were recorded using a Shimadzu HPLC with UV/Vis detector. Two different types of columns were used during these experiments. The first was a commercially available Chromolith® RP-18e by Merck. The mobile phase consisted of 0.65 ACN: 0.45 H_2O (flow rate) and the stock solution of Diclofenac Na was 10 mM in 10 mM LiCl. The solutions of Diclofenac with DINs were filtered by a syringe filter, before injecting into the HPLC. The second type were empty LC columns with dimensions 30 x 2.1 mm x ¼'' OD which were obtained from Restek. One was filled with NINs, the other with DINs, prepared in the lab. The mobile phase used consisted of UP H_2O with 10% ACN and 5 mM NaCl, with a flow rate of 0.1 mL min^{-1}. Chromatograms were recorded at 275 nm for all except PABA, which was recorded at 325 nm.

Capillary Electrophoresis (CE):

A Beckman Coulter PA 800 plus instrument was used containing a capillary with a total length (L) of 60 cm and effective length (l) of 50 cm. The separation voltage used during these experiments (ΔV) was always 20 kV. Electropherograms were obtained using a diode array detector @ 200 nm. Before each injection the capillary was rinsed with the following sequence: 1M NaOH, then H_2O, then background electrolyte (BGE), all for 2 mins each at 20 psi. The first injection was always 0.005% v/v Dimethylsulfoxide (DMSO) in the BGE, a 5 sec injection followed by a 5 sec injection of the sample in the BGE.

*2.4 **Protocols***

2.4.1 *Preparation of $BTPPA^+$ $TPBCl^-$*

Bis(triphenylphosphoranyldiene)ammonium tetrakis(4-chlorophenylborate) was used as the organic electrolyte salt and prepared according to the following reaction:

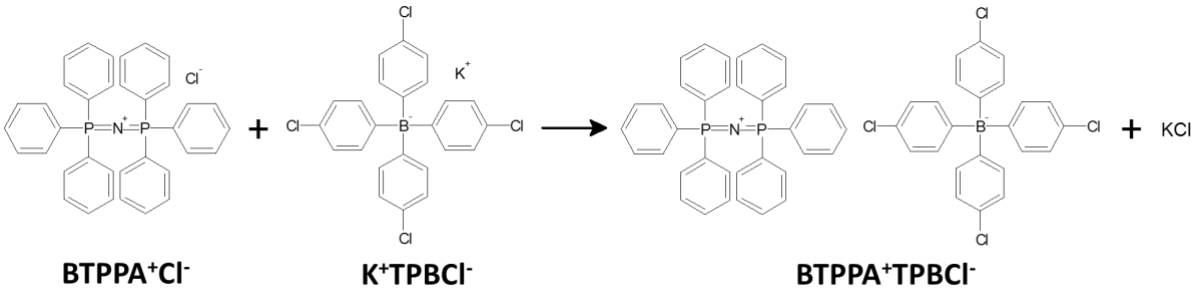

1. 1.25 g of $BTPPA^+Cl^-$ and 1 g of K^+TPBCl^- were dissolved in 10 ml and 20 ml of a 2:1 MeOH:H_2O solution respectively. The $BTPPA^+Cl^-$ solution was added to the K^+TPBCl^- dropwise while stirring, forming a white precipitate. The beaker was then covered in parafilm and left in the fridge for 48 hours, continuously stirring.

2. After this time, the solution was filtered under vacuum for approximately 30 minutes to remove the solvent. The resulting product was transferred to a dry beaker, covered with aluminium foil and stored in a desiccator overnight.

3. Following this, the reaction product was rinsed with acetone to dissolve the $BTPPA^+TPBCl^-$ and the solution was filtered under gravity using filter paper. The beaker was covered with parafilm that had holes in it to allow the acetone to evaporate and then stored in the fridge, until crystals had formed.

4. The rectangular crystals were rinsed with a 1:1 Acetone:H_2O mixture, filtered under vacuum and placed in a desiccator overnight.

5. The resulting crystals of $BTPPA^+TPBCl^-$ were stored in the fridge, with the sample vial covered in aluminium foil to prevent degradation from light exposure.

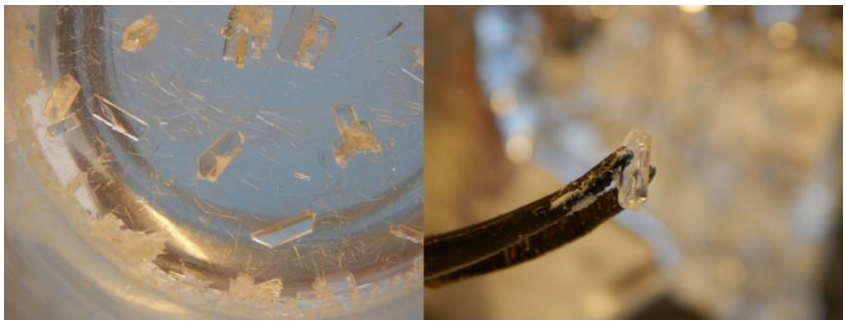

Figure 2.2: $BTPPA^{+}TPBCl^{-}$ crystals after acetone evaporation

2.4.2 *Preparation of counter electrode*

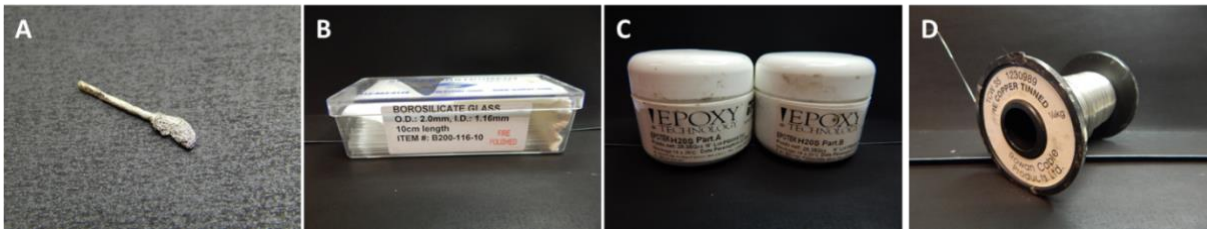

Figure 2.3: Components used for the counter electrode assembly

A – platinum mesh fixed to platinum wire; B – borosilicate capillaries; C – dual-component conductive epoxy; D – copper-tinned contact wire.

1. A small amount of platinum mesh was welded around a platinum wire of ~1 cm in length.

2. The wire was then placed inside a borosilicate capillary. Using a Bunsen burner, the glass around the platinum wire was gently melted to seal the platinum mesh and wire to the capillary.

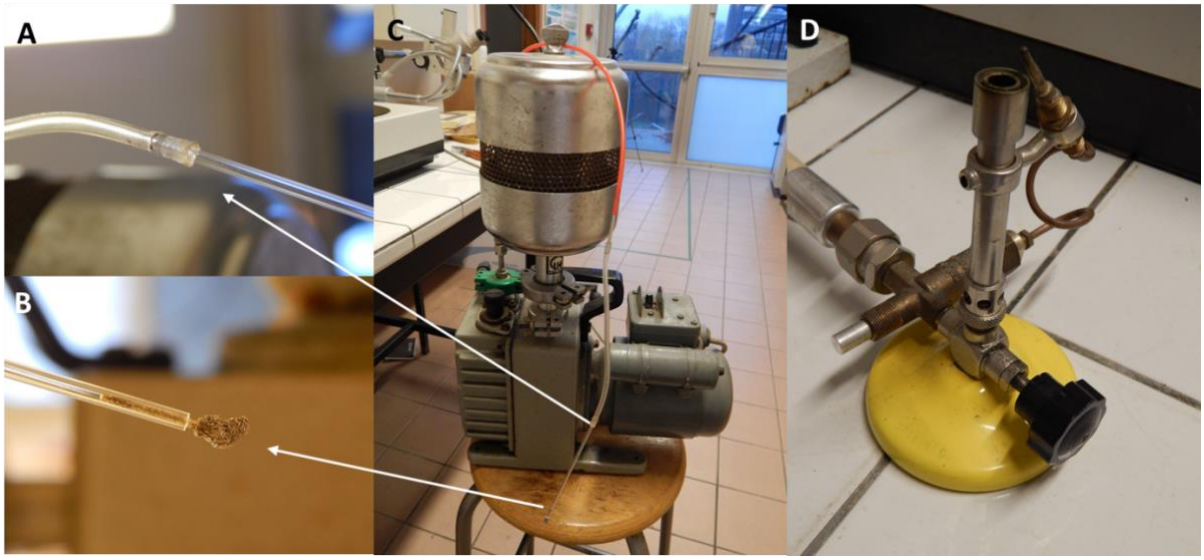

Figure 2.4: Melting the platinum wire inside the glass capillary was performed with the pump (C) using the Bunsen burner (D). One side of capillary was attached to the pump hose (A) whereas the platinum mesh and wire occupied second side (B).

3. Using a syringe with a long needle, conductive resin was inserted inside the capillary, just above the wire. Next, ~15 cm of copper-tinned wire was placed inside the glass capillary until it came into contact with the conductive resin, then left in the oven at 130 °C for a few hours to set. The length of the copper-tinned wired needs to be longer than that of the capillary as a few cm needs to extend out for electrical contact.

Figure 2.5: Successive steps of electrode preparation

A – Platinum mesh and wire inserted into the capillary; B – glass melted around the platinum wire; C – conductive resin placed above the wire.

4. Once the resin was cured, a microneedle was used to fill the interior of the capillary with silicon sealant and it was placed the oven overnight to set.

5. Finally, rubber tubing was added to the top of the capillary to secure the contact wire.

Figure 2.6: Platinum mesh based counter electrode

2.5 ***Dense (DSNs) and Mesoporous (MSNs) silica nanoparticles***

2.5.1 *Product specification for DSNs*

As mentioned in Section 2.1, the DSNs used in this research were commercially available LUDOX® HS-40, obtained from Aldrich. These colloidal silica nanoparticles are roughly spherical, non-porous and are dispersed in alkaline aqueous solution, containing ~40% silica. They have a dense silica core with silanol (Si-OH) groups on the surface. The alkaline solution is used to stabilise the particles, preventing aggregating and gelling. The nanoparticles are negatively charged and have sodium counter ions to balance the charge [148,149]. Table 2.2 gives a summary of the product specification [150].

Table 2.2: DSN characteristics

Silicon dioxide (SiO_2)	39-41 % m/m	**Density (ρ)**	1.3 g cm^{-3}
pH (25°C)	9.2 – 9.9	**Melting point**	1710 °C, 3110 F
Specific surface area (SSA)	198 – 258 m^2 g^{-1}	**Boiling point**	2230 °C, 4046 F

LUDOX® HS-40 nanoparticles are monodisperse, having a narrow particle size distribution with an average particle size ($\emptyset_{mean}$) 12 nm [149]. The following equation was used to calculate the standard deviation [65], which was found to be 10.6 < ∅ < 13.7 nm:

$$SSA\ (m^2.g^{-1}) = \frac{6000}{\rho\ (g.cm^{-3}).\emptyset\ (nm)}$$

2.5.2 *Synthesis of MSNs*

MSNs with mean diameter of 50 - 60 nm and pore diameter ~3nm were synthesised using a procedure by Hamdi et al., which was based on a modified Stöber method [69,83,96].

Chemical:	TEOS	CTACl	H_2O	EtOH	TEA
Molar ratio:	1	0.31	137	7.4	1.31

Synthesis:

The precursor used was TEOS (tetraethoxysilane), and surfactant was CTACl (cetyltrimethylammonium chloride). TEA (triethylamine) was used as a catalyst.

1. The first step involved dissolving the surfactant CTACl in a mixture of water, ethanol and TEA under stirring at 60 °C. After adding TEA, the pH of the solution was 9.4.

2. Next, TEOS was added dropwise to the solution, the vigorous stirring at elevated temperature was maintained for one hour before allowing the solution to cool to room temperature. The pH of the white suspension obtained after this was 8.2.

Extraction:

Extraction of the surfactant from the pores was achieved using an acidic solution. This extraction solution consisted of a mixture of 10% HCl in ethanol.

3. 50 mL of the extraction solution was added to the suspension of nanoparticles obtained after synthesis.

4. The nanoparticles-extraction solution mixture was sonicated for 20 minutes and then centrifuged at 10,000 rpm for 10 minutes.

5. The solid deposited in the bottom of the container was recovered and dispersed in 50 mL of the extraction solution again. The extraction steps (sonication and centrifugation) are repeated identically to the first extraction.

6. Finally the solid fraction was washed thoroughly with water and stored in 10% w/w ethanol.

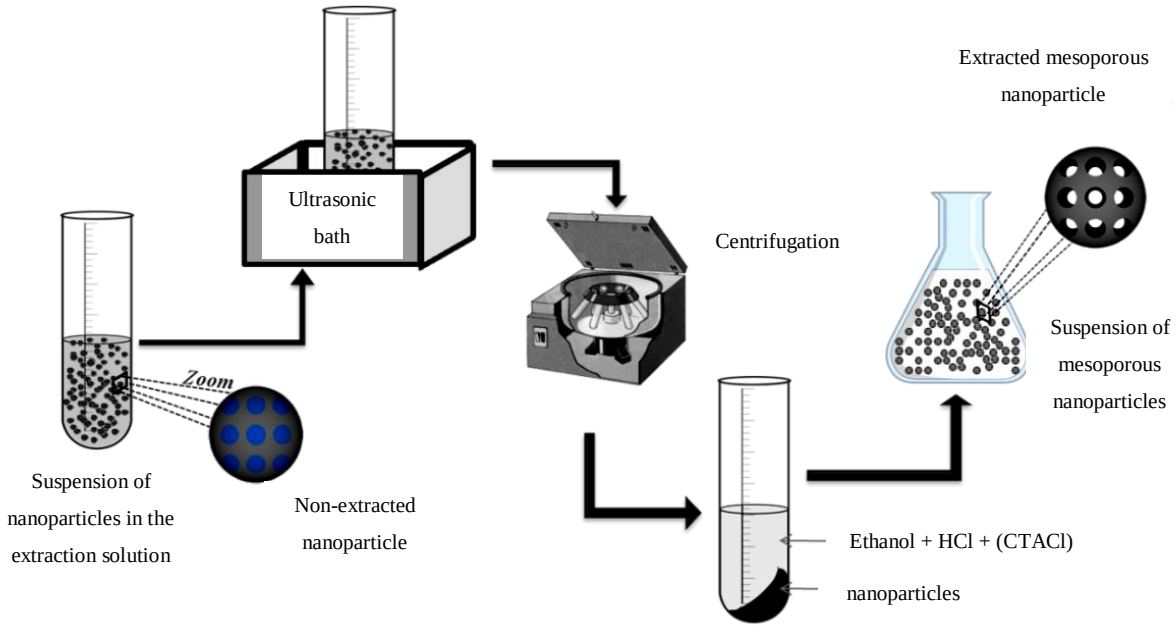

Fig. 2.7 Schematic of MSN extraction procedure

2.5.3 *Characterisation of DSNs and MSNs*

2.5.3.1 Zeta potential measurements for DSNs and MSNs

Zeta potential values were obtained for both DSNs and MSNs in solutions of increasing pH, from ~3.5 to 9. The solutions consisted of 0.5 g L^{-1} DSNs/MSNs in 10 mM LiCl, using HCl to vary the pH. The results obtained using the Zetasizer NanoZS were plotted in Figure 2.8. As can be seen, the black line representing DSNs confirms they are always negatively charged (the zeta potential values are negative for all pH values). In solution these negatively charged silica particles are surrounded by stationary positive charges and the zeta potential is the difference between the charge of this layer and that of the bulk solution [60]. The red line for MSNs shows their isoelectric point (where they go from being positively charged to negatively charged in solution) is at approximately pH 4.5 and because of the differences in the ionisation states between DSNs and MSNs, the size of the nanoparticles and thus the number of particles in the system at a given mass content is not the same.

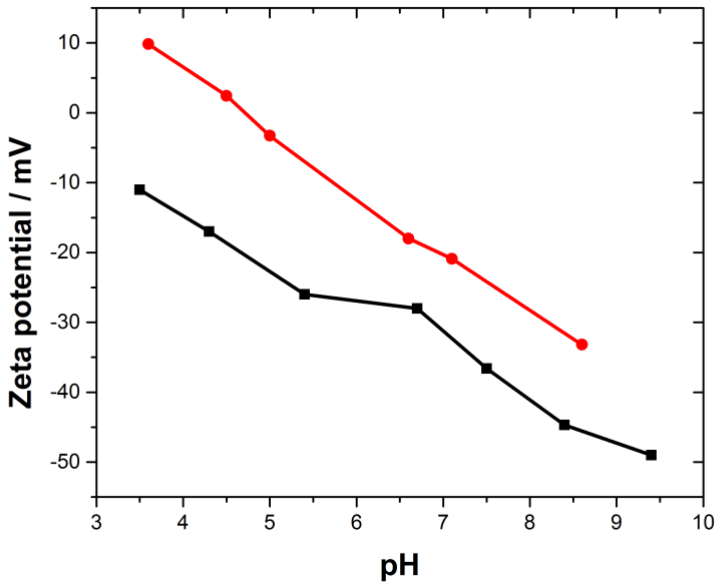

Figure 2.8: Zeta potential results for 0.5 g L^{-1} dense silica nanoparticles (black line) and mesoporous silica nanoparticles (red line) in 10mM LiCl with increasing pH.

2.5.3.2 Gas adsorption volumetry measurements for MSNs

Gas adsorption volumetry was carried out in order to obtain adsorption isotherms for the mesoporous silica nanoparticles, from which BET analysis could be applied. BET analysis allows the evaluation of the silica porosity, after the extraction of the surfactant used during synthesis. In order to obtain an adsorption isotherm and BET plot for the mesoporous silica nanoparticles, they were pre-treated by the technician, which involved drying in the oven at 50 °C for 1600 minutes and a vacuum of 3.877 10^{-6} Pa generated, weighed and then analysed using the Belsorp-max instrument. This gave values of p (equilibrium pressure in kPa), p_0 (saturation pressure in kPa) and V_a (adsorption amount in mL (STP) g^{-1}). From this an adsorption isotherm was plotted which shows the relationship between pressure and adsorption amount at a constant temperature (nitrogen at 77 K), as shown in Figure 2.9 A. Consequently the BET plot, as shown in Figure 2.9 B, allowed specific surface area (SSA) to be calculated using the BET equation:

$$\frac{p}{V_a(p_0 - p)} = \frac{1}{CV_m} + \frac{C-1}{CV_m}.\frac{p}{p_0}$$

$$SSA = \frac{V_m}{22414}.6.02x10^{23}.\sigma.10^{-18}$$

with monolayer adsorption amount (V_m) and BET constant (C) obtained from its slope and intercept, obtained between 0.1 and 0.4 p/p_0, respectively. The cross-section area of a single gas molecule of nitrogen (σ) equals 0.166 nm^2 at 77K [151,152].

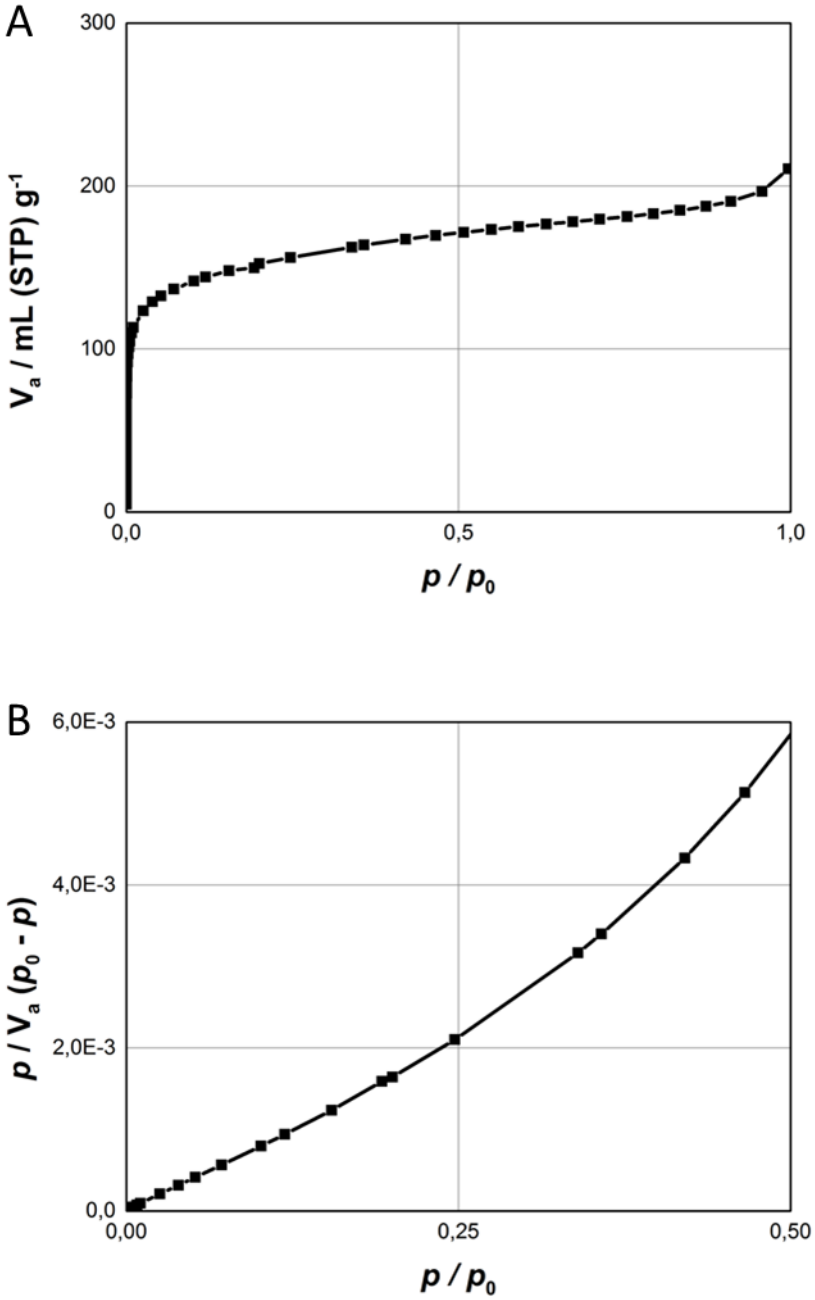

Figure 2.9: A) Adsorption isotherm for mesoporous silica nanoparticles and B) BET figure for mesoporous silica nanoparticles

The specific surface area of the mesoporous silica nanoparticles was found to be 560 m^2 g^{-1}. This figure is relevant for calculations performed in Chapter 4 Section 4.1. Gas adsorption volumetry measurements were not necessary for the dense silica nanoparticles as they have no pores. Their SSA was calculated from their geometrical dimensions and was found to equal 250 m^2 g^{-1}, which is in agreement with the experimental value given in Chapter 2, Table 2.2.

Table 2.3: Results obtained from BET analysis of mesoporous silica nanoparticles

V_m	C	**Mean pore diameter**	***SSA***	**Total pore volume**
128.84 cm^3 (STP) g^{-1}	643.64	2.29 nm	560 m^2 g^{-1}	0.322 cm^3 g^{-1}

2.5.4 *Protocol for pre-concentration of Methylene Blue with DSNs*

In order to carry out pre-concentration experiments with dense silica nanoparticles, large volumes of small concentrations of Methylene Blue (MB^+) and DSNs were prepared in 10 mM LiCl, mixed and centrifuged. The liquid was removed and 3 mL of fresh 10 mM LiCl added to the DSN-MB^+ precipitate, which was then used as the aqueous phase in the electrochemical cell.

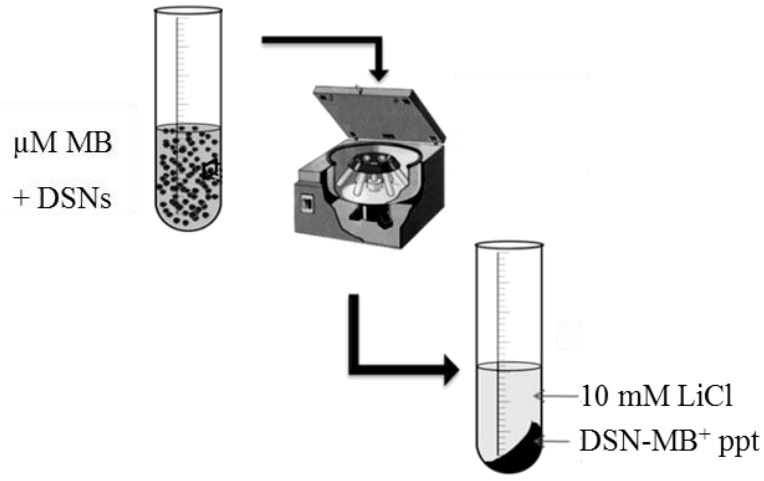

Figure 2.10: Schematic showing first step for pre-concentration of MB with DSNs

2.5.5 *Protocol for pre-concentration of Methylene Blue with MSNs*

Pre-concentration with MSNs involved mixing µM quantities of MB^+ with MSNs continuously (undiluted) for 5 minutes, then adding it to the aqueous phase in the cell and allowing it to settle for 1 hour before running the cyclic voltammograms.

2.6 ***Non-imprinted (NINs) and Diclofenac-imprinted (DINs) silica nanoparticles***

2.6.1 *Synthesis of NINs*

The surface functionalised dense nanoparticles synthesised here were obtained from a procedure previously used by Labrosse et al. during his PhD research [61,71].

Chemical:	TEOS	APTES	H_2O	EtOH
Molar ratio:	0.86	0.086	5.8	11.71

The reaction took place at room temperature.

1. First TEOS and APTES (aminopropyltriethoxysilane) were combined in one beaker, and H_2O and EtOH mixed in a separate beaker.

2. The solution of H_2O and EtOH was then added to the beaker of TEOS and APTES.

3. The mixture was shaken for 5 mins and then sonicated for 5 minutes.

4. Finally the resulting cloudy solution was left to cool and dry for 4 days, forming ~1g of a white/cream powder which was stored in 10% w/w 10 mM LiCl.

2.6.2 *Synthesis of DINs*

The procedure for making diclofenac-imprinted silica nanoparticles was the same as that for the non-imprinted particles (outlined above), except diclofenac was incorporated into the reaction mixture and an extraction step occurs at the end.

Chemical:	TEOS	APTES	Diclofenac	H_2O	EtOH
Molar ratio:	0.86	0.086	0.086	5.8	11.71

Synthesis:

The reaction took place at room temperature and generated 1:1 APTES:Diclofenac DINs.

1. First TEOS and APTES were combined in one beaker, and H_2O and EtOH mixed in a separate beaker.

2. Diclofenac was mixed in with the TEOS and APTES solution, quickly followed by H_2O and EtOH.

3. The mixture was shaken for 5 mins and then sonicated for 5 minutes.

4. Finally the resulting cloudy solution was left to cool and dry for 4 days, forming a white/cream powder.

Extraction:

The extraction process involved two steps, first washing in H_2O, secondly extraction with an acidic solution.

5. The powder was washed with DI H_2O by sonicating for 15 mins and then centrifuging for 15 mins.

6. The solid phase was resuspended and extraction performed by adding a solution of HCl in EtOH to it and then sonicating for 15 mins, followed by centrifuging for 15 mins.

7. After emptying the liquid, the solid precipitate was allowed to dry for 4 days, resulting in ~0.8g of a white/cream powder which was stored in 10% w/w 10 mM LiCl.

2.6.3 *Characterisation of NINs and DINs*

2.6.3.1 Elemental analysis of NINs and DINs

Firstly, the newly synthesized nanoparticles were characterised by elemental analysis and the weight percentage of carbon, hydrogen and nitrogen obtained for each sample presented in Table 2.4 below.

Table 2.4: Table showing elemental analysis results for NINs and DINs

	C	H	N
Non-imprinted silica nanoparticles (**NINs**)	5,67	2,28	3,16
Diclofenac-imprinted silica nanoparticles (**DINs**)			
Non-extracted	13,21	2,70	3,11
H_2O washed	5,57	2,35	3,22
HCl in EtOH extracted	3,95	2,18	2,86

The elemental results show the weight percentages of C, H and N in non-imprinted silica are 5.67, 2.28 and 3.16 respectively. However the C value for newly synthesised diclofenac-imprinted silica (that has not been washed or extracted) is much larger than that for the non-imprinted silica and the H value is also slightly larger. This could be explained by the presence of diclofenac in the silica. The amount of N remains much the same. After washing the DINs with water, the C and H values return to a value similar to that of NINs. However after extracting the Diclofenac from the imprinted cavities using HCl in EtOH, the values of C, H and N decrease for all.

2.6.3.2 Zeta potential measurements for NINs and DINs

The zeta potential values for the non-imprinted nanoparticles (NINs) agree well with previous results obtained for both the dense and mesoporous silica nanoparticles, as discussed in Section 2.5.3.1. However the results for the Diclofenac imprinted silica nanoparticles (DINs) show that at almost all pH values the silica nanoparticles are positively charged. A similar curve with an isoelectric point near pH 7.5 was shown by NanoComposix for amine-terminated silica [153], which would compare well with DINs as APTES was used during the synthesis to give the silica amine functionality. Furthermore Zhao et al. obtained an almost identical graph for their amino-functionalised mesoporous carbon [154]. They describe how the isoelectric point of the carbon after it is grafted with the amino group increases to a higher pH value due to the deprotonation of the $-NH_3^+$ in acidic and neutral conditions. However APTES was also used in the synthesis of NINs but its curve below has an isoelectric point near pH 5.

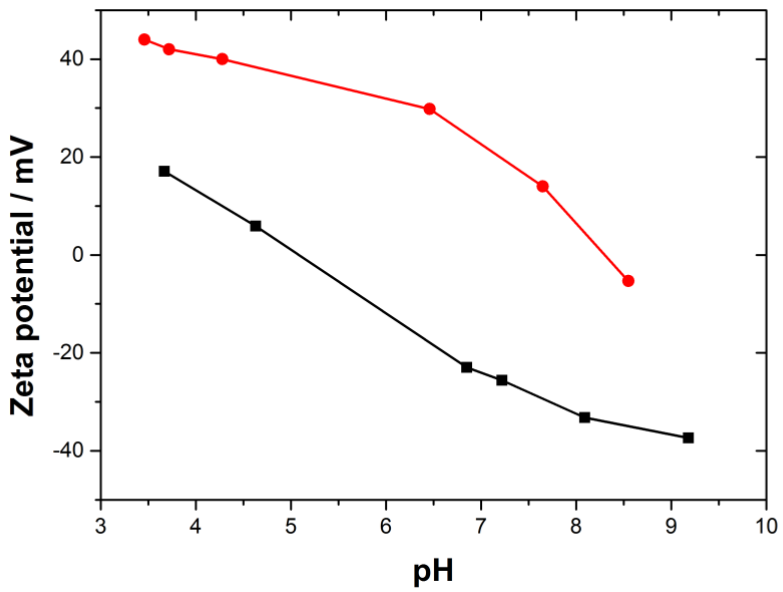

Figure 2.11: Zeta potential results for 0.05 g L^{-1} NINs (black line) and DINs (red line) in solution of 1 mM Tris with increasing pH

3. SILICA NANOPARTICLE ADSORPTION AT THE LIQUID-LIQUID INTERFACE (LLI) AND INTERACTION WITH IONS

The adsorption of nano-objects at a liquid-liquid interface is governed by their dimensions, the organic-aqueous interfacial tension and the wettability of the material [35,155–158]. The ITIES allows the application of an external electric field that can drive the adsorption of nanoparticles (Au or TiO_2) to the interface [43–45]. Despite the abundant literature on silica nanoparticles, their assembly at the ITIES has not been investigated yet. Silica sphere structures have been self-assembled at non-polarised liquid-liquid interfaces to fabricate 2 or 3D ordered structures with potential applications in optical, magnetic and electronic devices as photonic band gap materials [82]. But here in this research, silica nanoparticles assemble and are studied at the polarised liquid-liquid interface, i.e. the ITIES.

Dense and mesoporous silica nanoparticles are used throughout Chapter 3 and 4. The product specifications of DSNs and synthesis of MSNs were previously outlined in Chapter 2, Section 2.5.1 and 2.5.2. Their characterisation results (zeta potential measurements and gas adsorption volumetry for MSNs) were presented in Section 2.5.3.

In this chapter, electrochemical experiments followed the adsorption of both dense and mesoporous silica nanoparticles onto the ITIES and monitored the impact of the DSNs on the transfer behaviour of a cation across the LLI. The effect of ionic strength and pH on the nanoparticle adsorption and ion transfer at the ITIES was studied in the view of obtaining a greater understanding of the processes occurring with silica nanoparticles at the polarised LLI.

3.1 ***Adsorption of dense and mesoporous silica nanoparticles at the LLI***

Previous studies on the behaviour of nanoparticles at the liquid-liquid interface have shown that their adsorption is the result of the presence of a promoter or a modifier that weakens the electrostatic repulsion between the nanoparticles in suspension and allows the assembly of nanoparticles at the interface [159]. An alternative to this chemically induced assembly is the application of an interfacial potential difference that causes the assembly [43]. The adsorption of silica nanoparticles was investigated here by both cyclic and AC voltammetries at the ITIES.

3.1.1 *DSNs adsorption at the LLI*

Firstly, taking a look at the results with dense silica nanoparticles (DSNs), after the addition of 0.5 g L^{-1} of these silica nanoparticles to the aqueous phase, the dashed red line confirms there was no significant change to the CV (Figure 3.1), suggesting that no ion transfer was taking place in the potential window due the presence of the silica nanoparticles. DSNs did not transfer across the interface and remained on the aqueous side of the interface throughout the potential window.

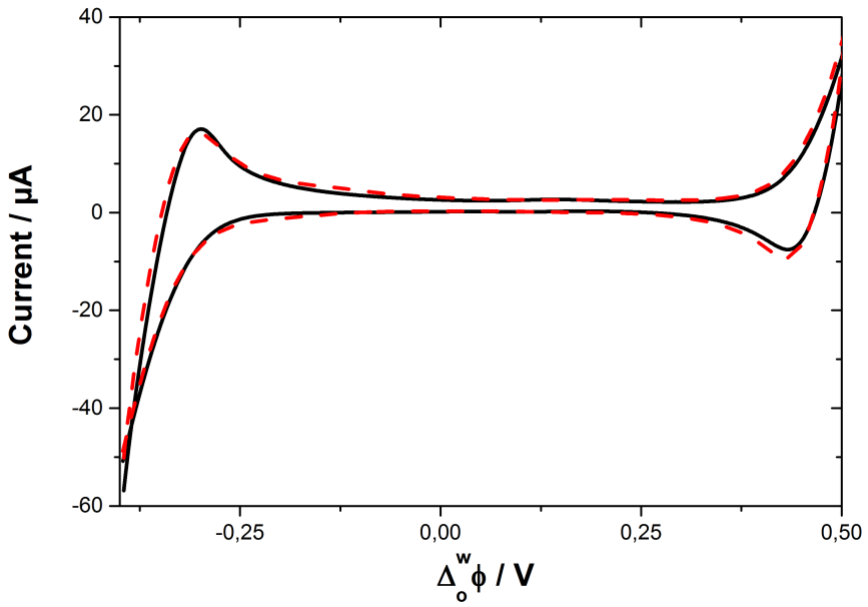

Figure 3.1: Cyclic voltammetry in the absence (black solid line) and in the presence (red dashed line) of 0.5 g L^{-1} of dense silica nanoparticles in the aqueous phase. Electrochemical cell 1, ν = 5 mV s^{-1}

AC voltammetry is more sensitive to interfacial phenomena than cyclic voltammetry and was then further used for the characterisation of the interface modified with silica nanoparticles. Even with quantities of DSNs as low as 0.05 g L^{-1}, significant changes were visible on the AC voltammograms in Figure 3.2, recorded in the potential region where no background salt ion transfer was observed in cyclic voltammetry. The differential capacitance was calculated from the AC voltammograms (see Chapter 2, Section 2.3). The potential of zero charge (PZC) was taken as the potential of minimum of capacitance. In the absence of silica nanoparticles, it was measured at -0.06 V. Upon addition of DSNs to the aqueous phase, the capacitance value at -0.145 V increased from 14 (0 g L^{-1}) to 19 µF cm^{-2} (0.1 g L^{-1}) indicating that the quantity of charge located at the interface grew in the presence of silica nanoparticles. This behaviour can be attributed to the adsorption of negatively charged silica nanoparticles accumulating at the ITIES.

This result is in agreement with that previously obtained for the interfacial assembly of TiO_2 nanoparticles [44] or Au nanoparticles [43] upon polarization at the liquid-liquid interface. Positively charged TiO_2 particles (at pH 3.5) caused the capacitive current to increase at positive Galvani potentials, whereas at pH 11, TiO_2 nanoparticles are negatively charged due to ionisation of the oxide surface and so the interfacial excess of the particles is increased at negative potentials.

The potential value for the minimum capacitance shifted to higher potential values with the increase of silica nanoparticles amount in suspension (from -0.062 V in the absence of silica nanoparticles to -0.013 V for 0.1 g L^{-1}). This observation agrees with previous studies on the behaviour of haemoglobin at the liquid-liquid interface where positively charged haemoglobin caused a shift to lower potential values [143].

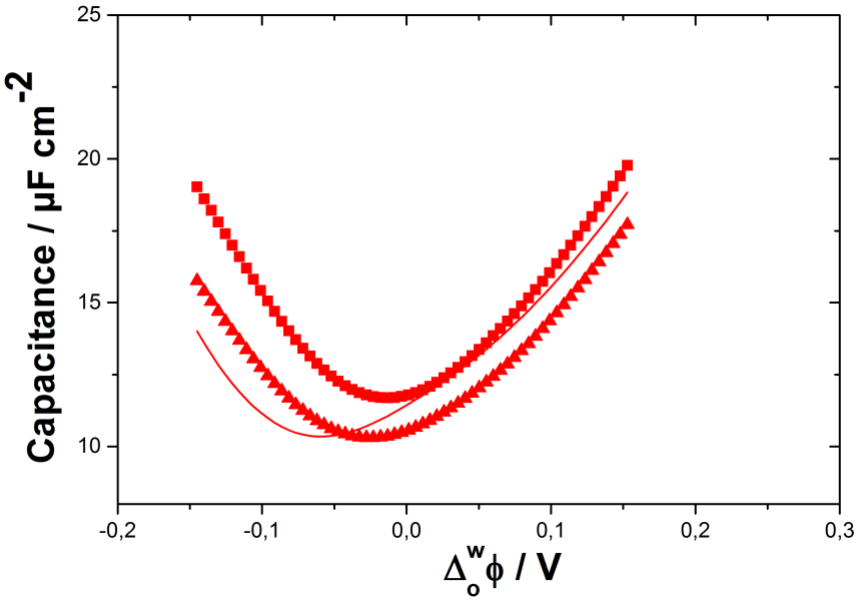

Figure 3.2: Potential dependence of the interfacial capacitance for the blank cell (red solid line) and for (▲) 0.05 and (■) 0.1 g L^{-1} of dense silica nanoparticles. Electrochemical cell 1.

3.1.2 *Effect of ionic strength and pH on DSNs adsorption to LLI*

At a higher ionic strength, *I*, of the aqueous phase (*I* = 100 mM), the potential for the lowest capacitance value was slightly shifted from + 0.020 to + 0.035 V when the concentration of DSNs increased from 0 to 0.1 g L^{-1}, as shown by the green lines in Figure 3.3. The capacitance variation was very limited due to the charge screening of higher electrolyte concentration. When the pH was decreased to 2 (10 mM HCl), no significant potential shift or increase in capacitance values was observed in the blue lines in Figure 3.3. At this pH, DSNs are expected to be nearly neutral [160] explaining why changes in the PZC or in the capacitance were not observed.

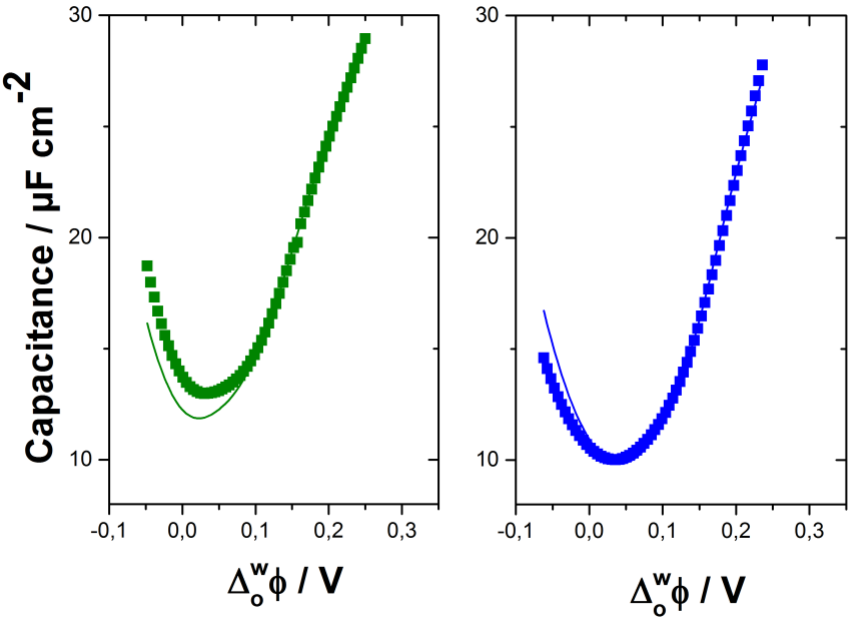

Figure 3.3: Potential dependence of the interfacial capacitance for the blank cell (solid line) and for (■) 0.1 g L^{-1} of dense silica nanoparticles with 100 mM LiCl (Green - Electrochemical cell 2) or 10 mM HCl (Blue - Electrochemical cell 3) as an aqueous electrolyte solution.

In the previous experiments, the electrochemical cell was prepared with an organic phase denser than water (the organic solvent was 1,2-Dichloroethane, d = 1.25 g mL^{-1}). To prove that silica nanoparticles assembled at the liquid-liquid interface, and did not just sediment because of gravity, an organic phase less dense than water was used. Recent studies have shown that a mixture of 40:60 1,2-Dichloroethane:5-Nonanone is lighter than water and it can be used for electrochemistry at the ITIES [161]. Figure 3.4 shows the AC voltammogram obtained at such an electrochemical cell in the absence and in the presence of 0.5 g L^{-1} DSNs in the aqueous phase. The PZC charge shifted to higher potential values and the capacitance increased at -0.195 V from 26 to 32 µF cm^{-2} in the presence of silica nanoparticles. This observation confirmed that silica nanoparticles adsorbed at the ITIES.

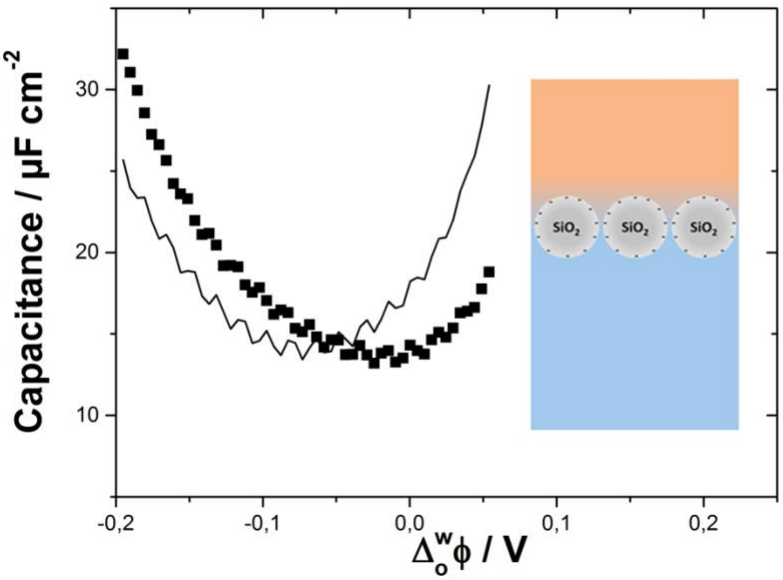

Figure 3.4: Potential dependence of the interfacial capacitance for the blank cell (solid line) and for 0.5 g L^{-1} of dense silica nanoparticles (■) with a less dense organic phase. Electrochemical cell 4.

3.1.3 *MSNs adsorption at the LLI*

Next, looking at results with mesoporous silica nanoparticles (MSNs), clear comparisons can be made with the results obtained above with DSNs. Even on addition of large quantities of MSNs to the aqueous phase, the red and blue lines showed there was no significant change to the CV in Figure 3.5, thus proving that no ion transfer was taking place in the potential window due the presence of the silica nanoparticles. Furthermore, MSNs did not transfer across the interface and remained on the aqueous side of the interface throughout the potential window. The decrease in the size of the potential window on addition of the larger quantity of MSNs could be due to the release of H^+ from the pores, as the nanoparticles had been extracted twice in HCl. This phenomenon is described in Section 3.2.3, which discusses the effect of pH of the solution.

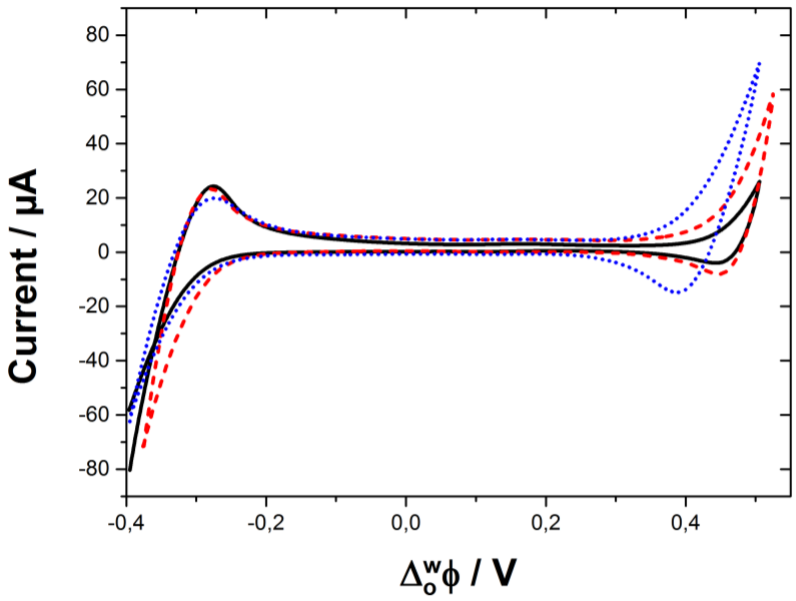

Figure 3.5: Cyclic voltammetry in the absence (black solid line) and in the presence of 1.3 g L^{-1} (dashed red line) and 5.2 g L^{-1} (dotted blue line) of mesoporous silica nanoparticles in the aqueous phase. Electrochemical cell 1, $\nu = 5$ mV s^{-1}

The increasing capacitance with increasing concentration of MSNs, from 25 to 32.5 µF cm^{-2} at -0.195 V, confirms that the silica nanoparticles have adsorbed at the LLI, calculated from the black to green lines on Figure 3.6.

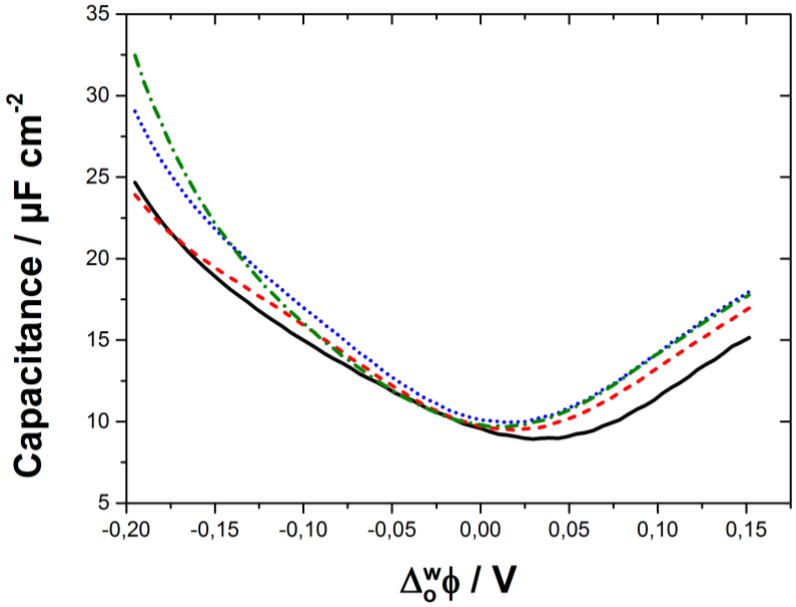

Figure 3.6: Potential dependence of the interfacial capacitance for 0 (black solid line), 1 (dashed red line), 3.0 (dotted blue line) and 5.0 (dash and dot green line) g L^{-1} of mesoporous silica nanoparticles. Electrochemical cell 1

Although the PZC values obtained with both DSNs and MSNs are very comparable, represented by the black and red lines in Figure 3.7 respectively, one cannot consider the adsorption is the same. The less prominent shift of the potential of zero charge with increasing concentrations of MSNs demonstrates that these silica nanoparticles are not as negatively charged as the DSNs. This was confirmed by zeta potential measurements that were recorded for both types of silica nanoparticles in solutions of increasing pH, as discussed in Section 2.5.3.1. Furthermore the zeta potential measurements also confirmed that because of the difference in ionisation states between DSNs and MSNs, the number of particles in the system at a given mass content is not the same. This could explain the noise in the curve for DSNs because, even though the mass quantity of silica used is the same, the number of DSNs is much greater and so results in noise at the LLI, whereas MSNs do not. When lower concentrations of DSNs are used, like that in Figure 3.2, then no noise is recorded for the scan with DSNs.

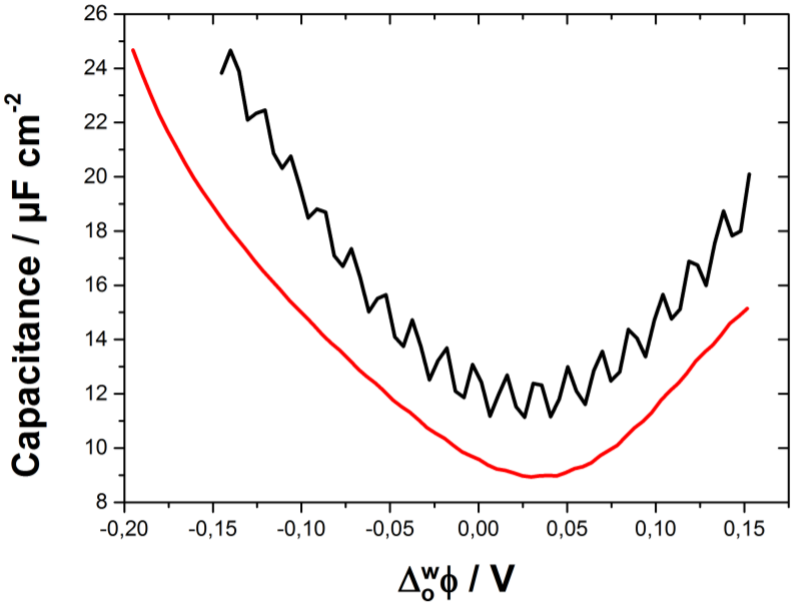

Figure 3.7: Potential dependence of the interfacial capacitance for 0.5 g L^{-1} DSNs (black line) and MSNs (red line) Electrochemical cell 1

However, to conclude, electrochemical results obtained prove that both dense and mesoporous silica nanoparticles adsorb to the liquid-liquid interface. Next, experiments with the dense silica nanoparticles and a cation were carried out, as a model to monitor the effect of silica on the transfer of the cation across the liquid-liquid interface. Furthermore, properties such as the pH and ionic strength of the solution were varied to help achieve a better understanding of the interactions between the cation and silica.

3.2 ***Interaction of DSNs with TEA^+ at the LLI and effect of solution parameters***

Monitoring the current generated in a cyclic voltammogram when analyte ions transfer from the aqueous to the organic phase, and back, allows the quantitative and qualitative detection of these charged species. By examining changes in the shape and peak heights in voltammograms obtained when the experimental conditions are varied, the interactions of the analytes within the system become apparent. Hence, after proving silica nanoparticles adsorb to the liquid-liquid interface in the previous section, the effect of dense silica nanoparticles on a small interfacial active cation, tetraethylammonium chloride ($TEA^+ Cl^-$), is studied here, as well as the effect of changing solution parameters (pH and ionic strength) on these dense silica nanoparticles.

3.2.1 *TEA^+ transfer across the LLI in the presence and absence of DSNs*

The transfer of TEA^+ from an aqueous to organic phase results in a peak being generated at ~0.09 V, demonstrated by the black line in Figure 3.8. When DSNs are added to the liquid-liquid interface, the peak current for TEA^+ decreases slightly as can be seen by the red line. Thus the quantity transferred is lower in the presence of silica nanoparticles than in their absence. As only a slight shift in the transfer peak potential value was observed (from ~0.09 V without DSNs, to ~0.11 V in the presence of DSNs) the decrease of transfer current could possibly be due to an interaction between the cationic TEA^+ and the negatively charged silica, with another reason being linked to the possible change of the interfacial surface area when silica nanoparticles are present [162,163]. The presence of DSNs at the interface, slightly reduces the surface area of the LLI, resulting in the transfer of TEA^+ being negatively affected (hence the small shift to higher potential) and thus less is transferred (explaining the reduced peak height).

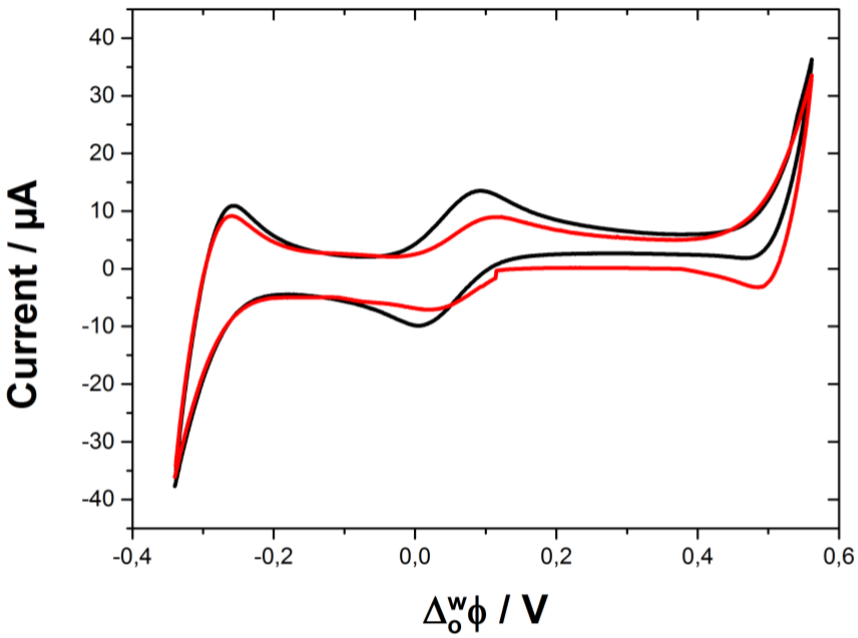

Figure 3.8: Cyclic voltammetry of 300 µM of TEA^+ in the absence (black line) and in the presence (red line) of 1 g L^{-1} of dense silica nanoparticles in the aqueous phase. Electrochemical cell 1, $\nu = 5$ mV s^{-1}

3.2.2 *Effect of ionic strength of solution and DSNs concentration*

The trend becomes more complicated in solutions with increasing ionic strength. At a constant [TEA^+] and increasing concentration of dense silica nanoparticles, in solutions of varying ionic strength, the calibration curve obtained from the peak heights of TEA^+ transfer recorded in cyclic voltammograms, allows three main points to be deduced (Figure 3.9). To note, the peak height values were measured by taking the peak height obtained (in µA) and subtracting the level baseline of its curve (in µA) at lower potentials, at ~0.1 V.

The first is that at low ionic strengths (5-25 mM LiCl) a decreasing peak height is observed with increasing concentrations of DSNs. Secondly, for medium ionic strengths (50-75 mM LiCl) the peak height remains unchanged as the the DSNs concentration increases. Finally, at the largest ionic strength (100 mM) an increase in the TEA^+ transfer peak height is obtained with increasing DSNs concentration. It leads to the conclusion that when the concentration of DSNs are high and the ionic strength is low, more ionic interactions occur between the cationic TEA^+ and anionic DSNs resulting in less TEA^+ available for transfer across the liquid-liquid interface and so a lower peak height is obtained. Conversely, when the concentrations of both DSNs and LiCl are high, these interact allowing more TEA^+ to transfer

across the interface unimpeded, thereby giving rise to a higher peak current value. This shows that TEA^+ and Li^+ compete for interaction with DSNs.

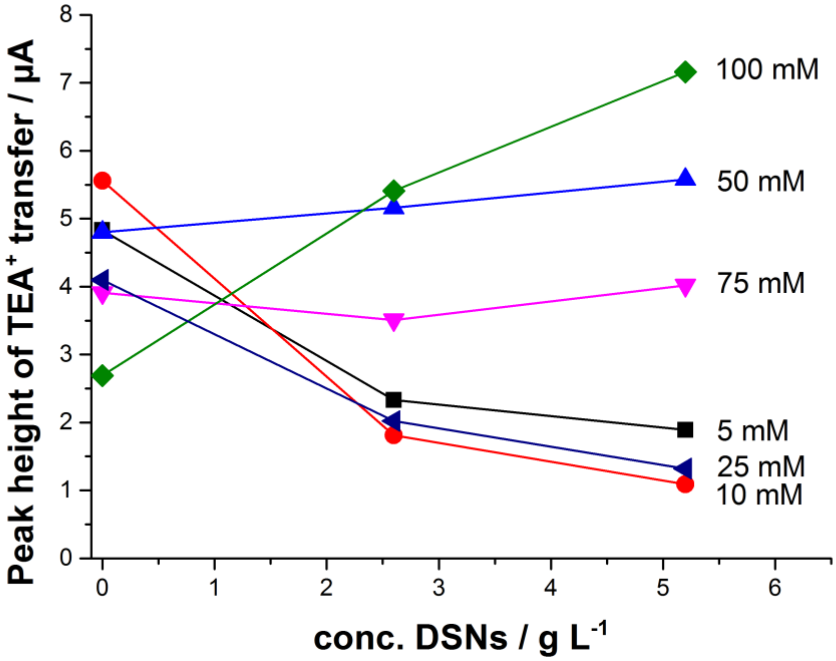

Figure 3.9: Transfer peak current (µA) of 0.1 mM TEA^+ ion transfer vs concentration of DSNs (g L^{-1}) with increasing ionic strength, [LiCl] 5 mM (black line), 10 mM (red line), 25 mM (navy line), 50 mM (blue line), 75 mM (pink line) and 100 mM (green line). Obtained from cyclic voltammograms using Electrochemical cell 1, ν = 5 mV s^{-1}, but with varying [LiCl]

Focusing on the cyclic voltammograms obtained when 2.6 g L^{-1} DSNs were present, it is clear to see that increasing the ionic strength decreases the potential window from the right side, from ~0.6 V to 0.4V, as shown in Figure 3.10. Furthermore the transfer peak potential of the cation shifts to lower potentials, from ~0.14 V (black line) to ~0.035 V (pink line), with increasing ionic strength of the aqueous solution (from 5 mM to 100 mM respectively). An increase in capacitance between -0.2 and 0 V is also visible and these can all be explained by the change in the resistance of the solution, as a result of the increasing abundance of Li^+ and Cl^- ions as the ionic strength is increased.

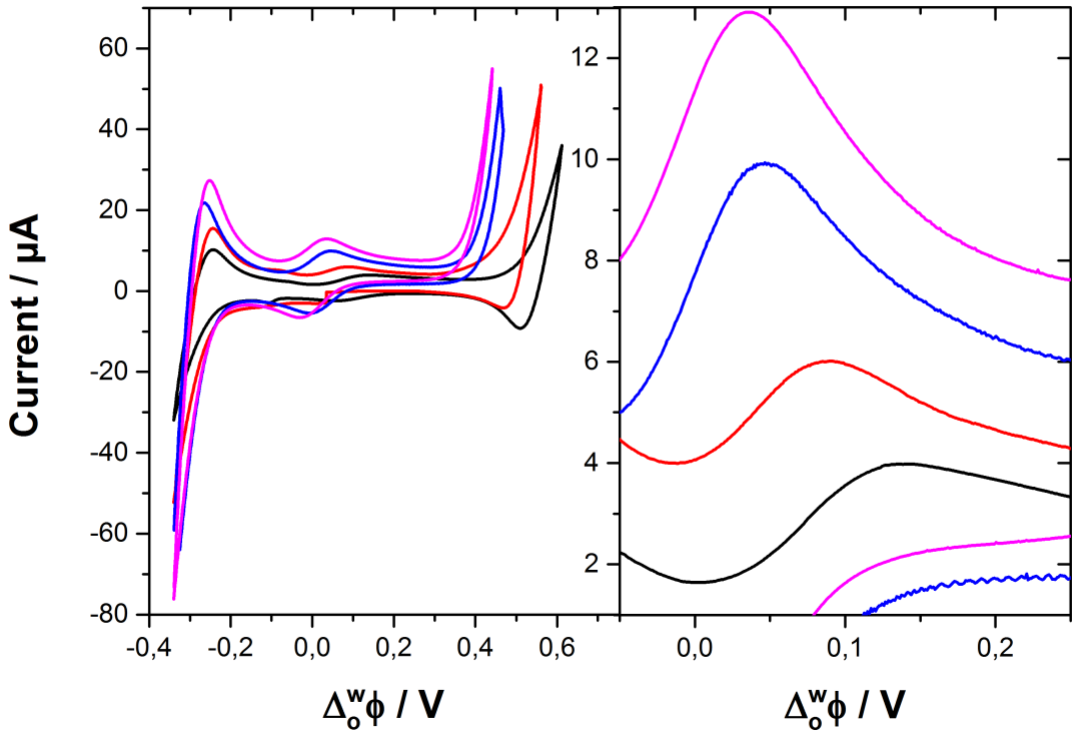

Figure 3.10: Cyclic voltammogram of 0.1 mM TEA^+ and 2.6 g L^{-1} DSNs with increasing ionic strength of solution, [LiCl] 5 mM (black line), 25 mM (red line), 50 mM (blue line), 100 mM (pink line). Figure on right shows zoomed in forward transfer potential peaks. Electrochemical cell 1, ν = 5 mV s^{-1}, but with varying [LiCl]

Further analysis of the transfer peak height of TEA^+ reveals that in the absence of DSNs, the value decreases with increasing ionic strength, as can be seen by the black line in Figure 3.11. However, in the presence of DSNs, the TEA^+ transfer peak current increases as the ionic strength increases, depicted by the red line. This could be attributed to a charge screening effect, i.e. TEA^+ and Li^+ competing for interaction with the anionic DSNs.

The interaction between TEA^+ and DSNs is weaker and so at high ionic strengths (100 mM LiCl), interactions between DSNs and Li^+ are abundant, allowing TEA^+ to transfer across the interface unimpeded. This gives rise to higher peak current values. The opposite can be said at low ionic strengths (10 mM LiCl). Here there are more DSNs and TEA^+ interactions, resulting in less TEA^+ available and so a lower peak height is obtained.

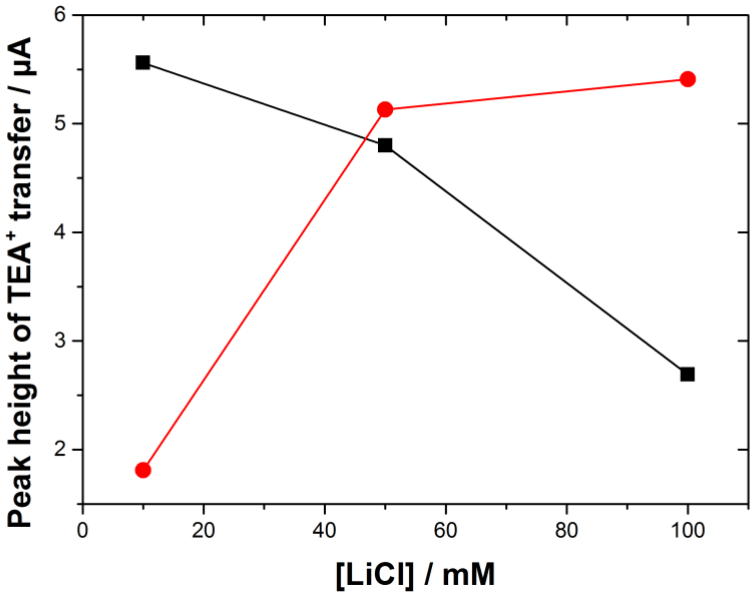

Figure 3.11: TEA^+ transfer peak height vs ionic strength with 2.6 g L^{-1} DSNs (red line) and without DSNS (black line).

To sum, increasing ionic strength of the aqueous solution has the effect of creating competition between TEA^+ and Li^+ for interaction with DSNs and thus negatively impacts the interaction between the DSNs and TEA^+, resulting in more TEA^+ transferring across the LLI.

3.2.3 *Effect of pH of solution*

The pH of the aqueous solution was varied to investigate its effect on the DSN-TEA^+ interaction. As in the previous section, the peak heights of TEA^+ were calculated from the cyclic voltammograms obtained for each experimental condition and results combined and plotted together in Figure 3.12. The initial pH of the aqueous solution in 10 mM LiCl was 6.5. Increasing concentrations of hydrochloric acid were added to reduce this from 5.2 to 3.1 to 2.4, from pink to blue to red to black lines in Figure 3.12 respectively. The addition of DSNs resulted in the pH increasing to ~8.8 for three out of the four solutions analysed. The pH of the system with just HCl (black line) stayed constant at ~2.45 regardless of the quantity of DSNs added. Similarly the transfer peak height of TEA^+ also stayed constant for this system, regardless of the presence or absence of DSNs. As it was unaffected by the presence of DSNs, one could conclude that the adsorption of nanoparticles at the interface does not have a significant impact on the available interfacial surface area and thus on the transfer of TEA^+.

The results obtained from the system with just HCl can be explained by the fact that at such a low pH, the negative charge of DSNs is greatly reduced (the silica becomes practically neutral as discussed in Section 2.5.3.1) and so it does not interact with the TEA^+, allowing unimpeded transfer of the cation across the liquid-liquid interface. Furthermore, another plausible explanation could be that at pH 2 the concentration of H^+ is high and so this competes with TEA^+ for interaction with anionic DSNs. As a result, most of the TEA^+ in solution can transfer across the liquid-liquid interface unimpeded. This is a similar situation to that discussed in the previous section, when a large Li^+ concentration competed with the TEA^+ for interaction with the DSNs. However, when DSNs are added to the three other solutions, the increase in pH permits electrostatic interactions between them and TEA^+ to occur, resulting in less cation available to transfer across the LLI and thus a reduced transfer peak height.

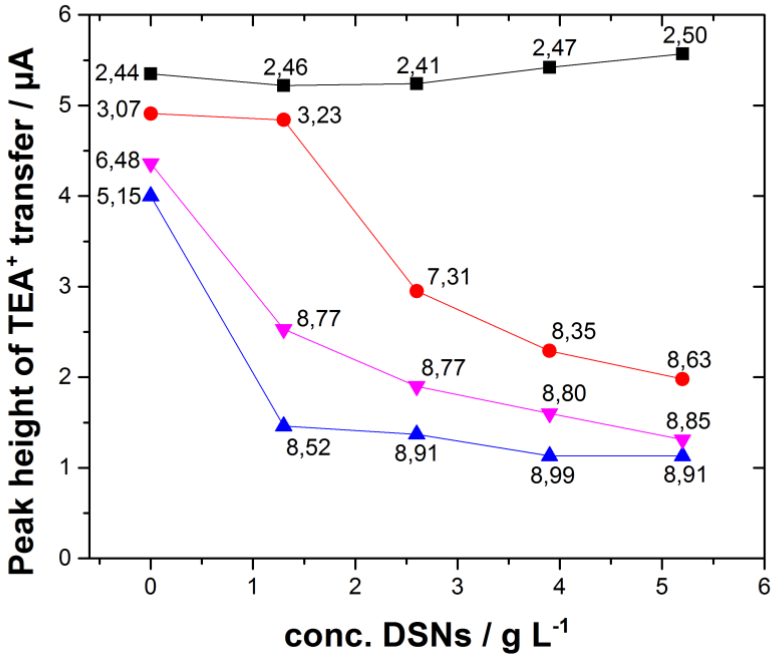

Figure 3.12: Transfer peak current of 0.1mM TEA^+ vs concentration of DSNs (g L^{-1}) with varying pH. Aqueous solution consisting of just 10 mM LiCl represented by the pink line, comprising of 0.4 mM HCl shown by the blue line, 1mM HCl by the red line and just 10mM HCl alone by the black line. Figures on each data point represent the pH of the solution, recorded for each experimental condition.

Focusing on the transfer peak height of TEA^+ as a function of pH, as shown in Figure 3.13, a trend in the decreasing peak height is visible. It reiterates the point made previously that at low pH a large quantity of TEA^+ transfers across the interface, possibly due to the high concentration of H^+ ions in solution successfully competing with TEA^+ for interaction with DSNs or also the fact that the DSNs are less negatively charged and so do not interact as efficiently with the cations in solution. The quantity gradually declines as the pH of the aqueous solution increases. The variation of pH is more rapid when large quantities of DSNs are present at the LLI, especially between pH 7 and 9, and in this range the more strongly anionic DSNs interact with the cationic TEA^+ in solution, leaving less free to transfer across the LLI.

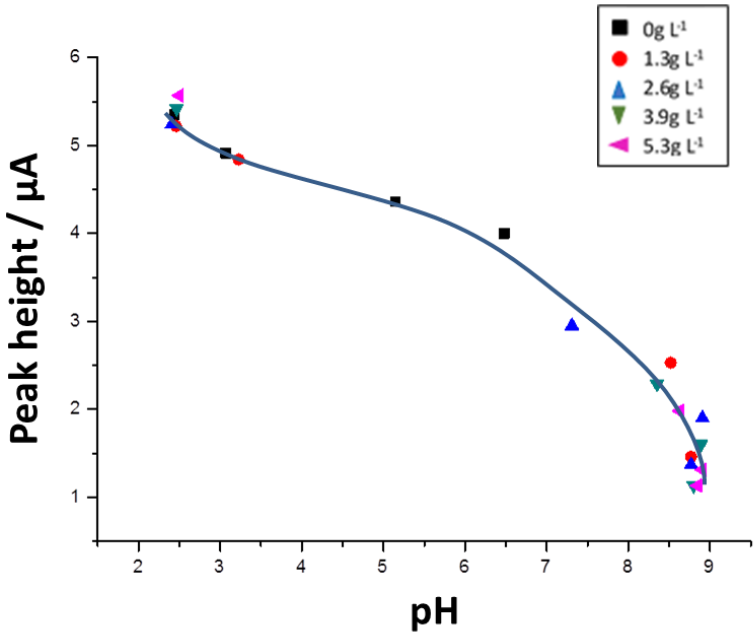

Figure 3.13: Transfer peak height Vs pH for 0.1mM TEA^+ with increasing concentration of silica nanoparticles

In Figure 3.14, the cyclic voltammograms from which the peak heights were obtained are shown for the situation with 2.6 g L^{-1} DSNs in solutions of varying pH. From it, the decrease in peak height with increasing pH (from black to red to blue to pink) is clearly evident. The peak positions do not vary greatly, only a slight shift to higher potentials is observed with the increase in the pH. This could be due to the fact that with the solution of 10 mM HCl (black line), the potential window of the system is shorter by ~0.1 V.

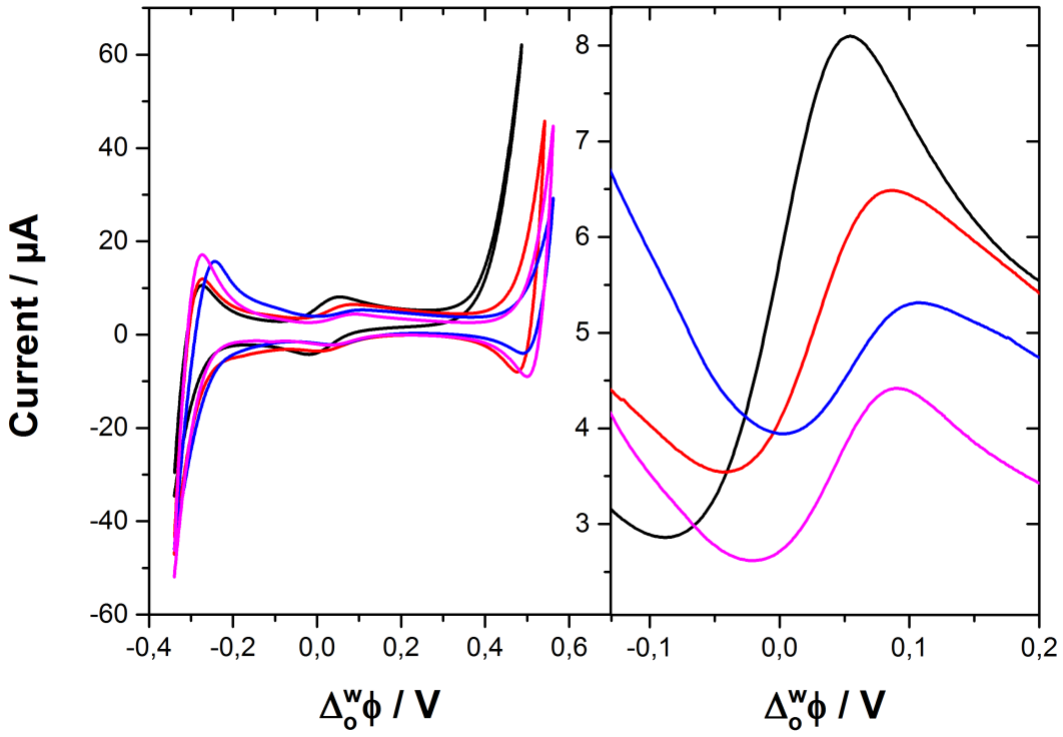

Figure 3.14: Cyclic voltammogram of 0.1mM TEA^+ and 2.6 g L^{-1} DSNs with pH 2.41 (black line), 7.31 (red line), 8.77 blue line and 8.9 (pink line). Electrochemical cell 1, ν = 5 mV s^{-1}

3.3 ***Conclusion***

This chapter provided information on the adsorption of silica nanoparticles and their interactions with a cation at the LLI.

Electrochemical results obtained prove that both dense and mesoporous silica nanoparticles adsorb to the liquid-liquid interface. AC voltammetry experiments showed that, upon addition of silica nanoparticles to the aqueous phase, the capacitance value increased, indicating that the quantity of charge located at the interface grew in the presence of silica nanoparticles. Furthermore the shift in the PZC to higher potentials was attributed to the adsorption of negatively charged silica nanoparticles accumulating at the ITIES.

The presence of DSNs at the LLI caused a decrease in the transfer peak height of the cation and a slight shift to higher transfer potential. The transfer peak height of TEA^+ in the absence of DSNs only slightly decreased with increasing ionic strength. However, in the presence of DSNs, the TEA^+ transfer peak current increased as the ionic strength increased. This could be attributed to a charge screening effect, i.e. TEA^+ and Li^+ competing for interaction with the anionic DSNs. The interaction between TEA^+ and DSNs is weaker and so at high ionic strengths (100 mM LiCl), interactions between DSNs and Li^+ were abundant, allowing TEA^+ to transfer across the interface unimpeded. This gave rise to higher peak current values. The opposite can be said at low ionic strengths (10 mM LiCl). Here there are more DSNs and TEA^+ interactions, resulting in less TEA^+ available and so a lower peak height is obtained.

With regards the pH of the aqueous solution, the quantity of the cation transferred gradually declines as the pH of the aqueous solution increases. The reasoning was that at low pH a large quantity of TEA^+ transfers across the interface, possibly due to the high concentration of H^+ ions in solution successfully competing with TEA^+ for interaction with DSNs or also the fact that the DSNs are less negatively charged and so do not interact as efficiently with the cations in solution.

Further detail on the kinetics and thermodynamics of the interactions between negatively charged silica nanoparticles with cations, and anions, are studied in the next section.

4. INTERACTION OF DENSE AND MESOPOROUS SILICA NANOPARTICLES WITH CATIONS AND ANIONS

The interaction between the negatively charged dense and mesoporous silica nanoparticles, which adsorb at the ITIES, and two contrasting dye species (cationic Methylene Blue and anionic Eosin B) were experimentally observed.

Methylene blue (MB^+) is a cationic phenothiazine. These biologically important heterocyclic compounds have many applications as insecticides, anthelmintics, dyes, pigments and oxidation-reduction indicators. Furthermore, in medicine they are used as sedatives, antidepressants and antihistamines. Most recently, MB^+ has been investigated for its photochemotherapeutic effects against carcinomas [164–166].

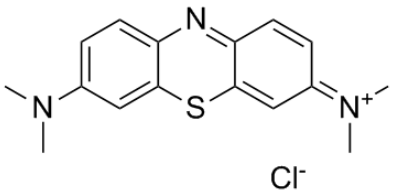

Methylene blue

Eosin B (EB^-) is a red, anionic dye commonly used in microscopy as a counterstain to visualize proteins, for example collagen, and other biological samples [167,168].

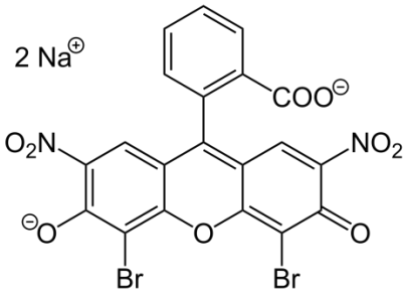

Eosin B

The interactions were studied, firstly in a monophasic aqueous system, in order to determine the interaction of MB^+ with the silica nanoparticles, using UV/Vis spectrometry and stopped-flow analysis. Secondly, the changes in the thermodynamics of the MB^+ transfer across the liquid-liquid interface in the presence of silica nanoparticles was studied by cyclic voltammetric experiments. In all experiments, EB^- was used as comparison analyte to show the interaction of silica nanoparticles to cations was specific.

4.1 ***Investigation of MB^+ adsorption onto silica nanoparticles in aqueous solutions***

The extent of the adsorption was studied at equilibrium by UV/Vis spectroscopy and the ultrafiltration technique (UF, described in Chapter 2, Section 2.3 and used for dense silica nanoparticles only). With the UF technique, the amount of dye found in the permeate is assumed to be the same as that in the bulk water surrounding the particles. When using the UV/Vis technique the amount of adsorbed dye is deduced from the optical density variation. Owing to experimental uncertainty due to light diffusion by particles, this method is only usable when this adsorption is not too strong. To compare the adsorption on the two types of silica nanoparticles instead of considering the number of gram per litre we expressed the number of m^2 available for adsorption (taking into account a specific surface area 250 $m^2\ g^{-1}$ for DSNs as calculated on geometrical considerations and 560 $m^2\ g^{-1}$ for MSNs as determined by gas adsorption volumetry (Chapter 2 Section 2.5.3.2).

The kinetics of the adsorption of MB^+ to both silica nanoparticles, in aqueous solution, was investigated using the Stopped-flow technique, which is discussed in detail in Section 4.1.2.

4.1.1 *Calculation of K_{ads} for MB^+ to DSNs and MSNs using UV/Vis spectroscopy*

Firstly, in order to understand the interactions of the analytes with dense silica nanoparticles, MB^+ was dissolved in the aqueous phase at 50 µM and a UV/Vis absorption spectrum was recorded before and after a DSNs suspension was added to reach a concentration of 0.5 $g\ L^{-1}$, shown in Figure 4.1. In the absence of DSNs (solid blue line), two bands were observed in the UV/Vis spectrum of MB^+, as can be seen in Figure 4.1. The main band at λ = 664 nm is attributed to the n-π* transition whereas the shoulder at λ = 614 nm is attributed to the vibronic transition [164,169,170]. In the presence of DSNs (dashed blue line), the UV/Vis spectrum looks quite different with the largest band at λ = 590 nm and a smaller at λ = 664 nm, suggesting that MB^+ and DSNs interact with one another.

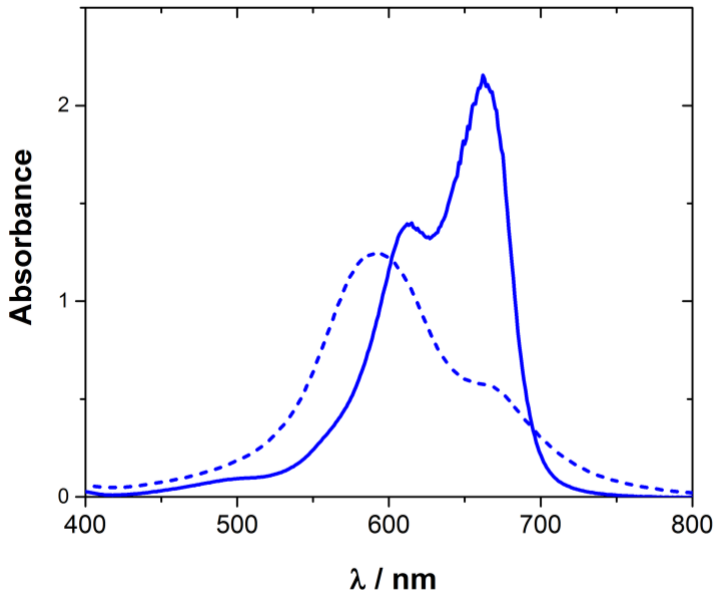

Figure 4.1: UV/Vis absorption spectrum of 50 µM MB^+ free in solution (solid blue line) and adsorbed on 0.5 g L^{-1} of DSNs (dashed blue line). Both solutions contained 10 mM LiCl.

To compare, there was no difference between the EB^- spectra in the absence (solid black line) or in the presence (dashed red line) of DSNs, clearly visible in Figure 4.2. This confirms that no interaction exists between both negatively charged species and so no further action was taken with EB^- in this section.

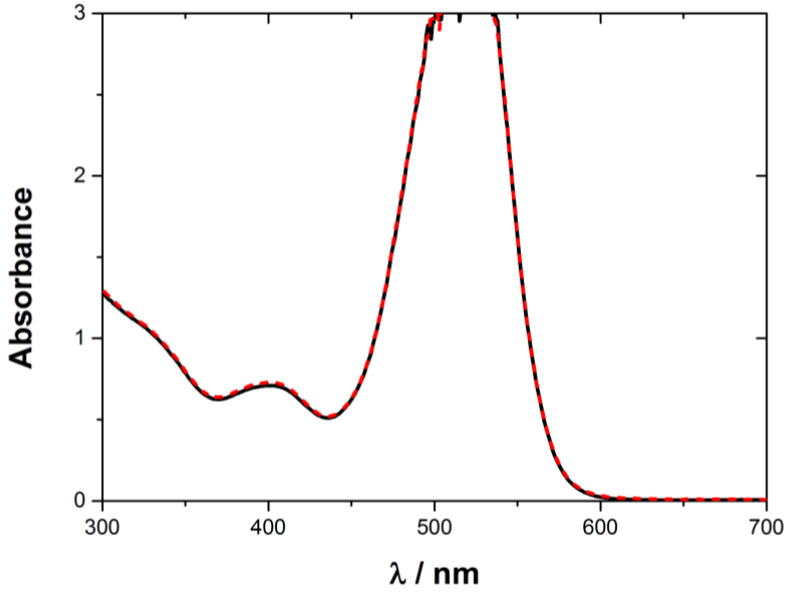

Figure 4.2: UV/Vis absorption spectroscopy of 0.1 mM EB^- without (solid black line) and with 0.867 g L^{-1} of DSNs (dashed red line). Both solutions contained 10 mM LiCl. (Unfortunately the absorbance was too large and so the top of the peak is void, however this does not affect the main point that it conveys)

Thus moving back to MB^+, the aim was to determine the total number of adsorption sites, S_T, available for MB^+ adsorption on DSNs and the association constant, K_{ads}^{aq}, of adsorption of MB^+ onto DSNs. The adsorption of free MB^+ in solution onto silica free sites, S_F, can be described by the following equilibrium.

$$MB_{free}^{+} + S_F \leftrightarrow MB_{ads}^{+} \quad (1)$$

$$K_{ads}^{aq} = \frac{[MB^+]_{ads}}{[MB^+]_{free}[S_F]} \quad (2)$$

The total number of sites is equal to the sum of the occupied sites, S_O, and of the free sites, S_F. Similarly, the total number of MB^+ is equal to the sum of adsorbed MB^+ and of MB^+ free in solution. Since we worked at constant volume, equations 3 and 4 are valid.

$$[S_T] = [S_O] + [S_F] \quad (3)$$

$$[MB^+]_T = [MB^+]_{ads} + [MB^+]_{free} \quad (4)$$

The number of occupied sites is assumed to be equal to the number of MB^+ molecules adsorbed, thus equation (2) becomes:

$$K_{ads}^{aq} = \frac{[MB^+]_{ads}}{([MB^+]_T - [MB^+]_{ads})([S_T] - [MB^+]_{ads})} \quad (5)$$

Experimentally, the adsorption of MB^+ onto DSNs was investigated by UV/Vis spectroscopy. The initial amount of MB^+ in 10 mM LiCl solution was kept constant, $[MB^+]_T$ = 50 µM, throughout the series of experiments and the DSNs concentration varied from 0.040 to 0.867 g L^{-1}. DSNs and MB^+ were mixed together and the solution was then filtered through a membrane using the ultrafiltration technique. The filtrate was collected and analysed by UV/Vis absorption spectroscopy, which allowed the amount of MB^+ present in the filtrate, $[MB^+]_{free}$, to be determined from the optical density variation at 650 nm. $[MB^+]_{ads}$ were then deduced from equation (4) and the results were plotted as the function of silica concentration and fitted with a Langmuir isotherm to determine (a) the SiO_2 surface area per MB^+ (i.e. equivalent to the total site concentration) and (b) the adsorption constant (K_{ads}^{aq}). These two parameters were left as adjustable parameters [171]. The best fit was obtained for K_{ads}^{aq} = 1.66 10^5 and a = 1.0 nm^2 / MB^+. This represents approximately 900 adsorption sites per nanoparticle.

Such a value of K_{ads}^{aq} indicated a high affinity of MB^+ for the silica nanoparticle surface and hence suggesting that all the adsorption sites were occupied as the silica concentration increased. K_{ads}^{aq} can be related to the free Gibbs energy of adsorption:

$$\Delta G^0_{SiO_2-MB^+} = -RT \ln K_{ads}^{aq} \quad (6)$$

Where T is the temperature (T = 293 K) and R is the universal gas constant (R = 8.314 J mol^{-1} K^{-1}). The value of -29.3 kJ mol^{-1} for the Gibbs free energy of adsorption testified of the spontaneous nature of the adsorption of MB^+ onto DSNs. These results are in agreement with the existing literature, where spontaneous adsorption of MB^+ on mesoporous silica formed as a thin film on an electrode was reported [165] with similar free Gibbs energy of adsorption. Based on the fitting of Figure 4.3, the surface area per MB^+ was calculated at 1 nm^2, which is lower than the results of the adsorption of one MB^+ molecule for every 3 nm^2 of silica reported in the literature for a different type of silica and other experimental conditions [43].

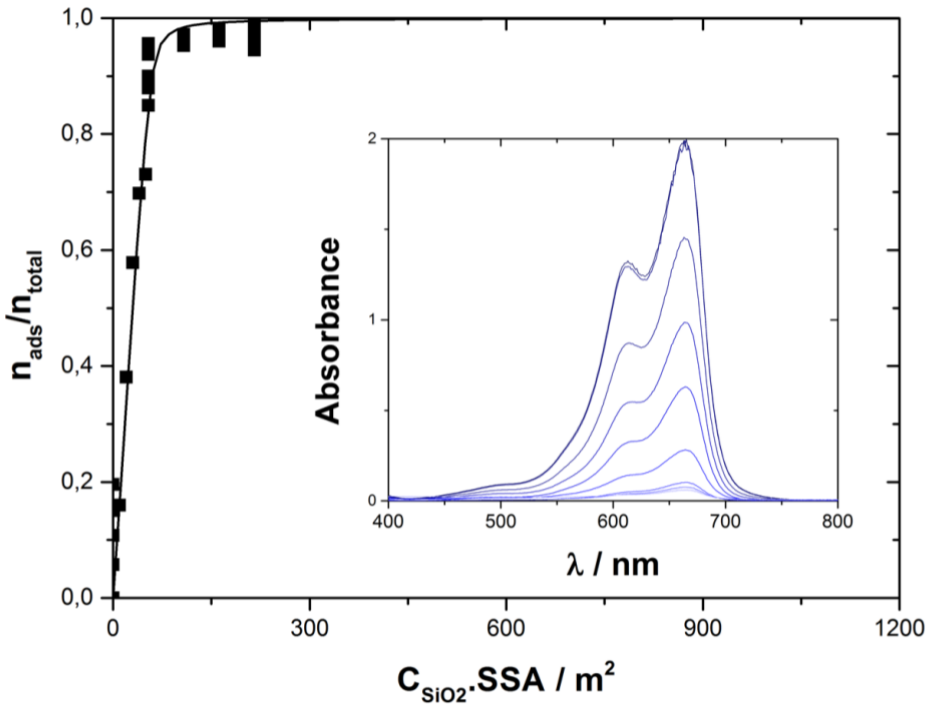

Figure 4.3: Number of adsorbed MB^+ (n_{ads})/total number of MB^+ (n_{total}) plotted as a function of the mass concentration of DSNs (C_{SiO2}) x Specific surface area of DSNs (SSA). Experimental data represented by the black squares were fitted using a Langmuir isotherm (black line). Inset shows the UV/Vis absorption spectra of free MB^+ in the filtrate after mixing with DSNs (concentrations between 0.040 and 0.867 g L^{-1}) and filtration.

With regards the MSNs, the same experimental procedure was followed, whereby the initial amount of MB^+ in 10 mM LiCl solution was kept constant at $[MB^+]_T$ = 50 µM throughout the series of experiments and the MSNs concentration was varied from 0.1 to 2 g L^{-1}. The shape of the MB^+ UV/Vis spectrum is unchanged when MSNs are added to the solution, unlike the situation with DSNs above. Once again the $[MB^+]_{free}$ was deduced from the optical density variation at 650 nm. The $[MB^+]_{ads}$ were then deduced from equation (4) and the results were plotted as the function of silica concentration and fitted with a Langmuir isotherm to determine (a) the SiO_2 surface area per MB^+ (i.e. equivalent to the total site concentration) and (b) the adsorption constant (K_{ads}^{aq}). As mentioned previously, these two parameters were left as adjustable parameters [171]. The best fit was obtained for K_{ads}^{aq} = 3.68 10^3 and a = 1.0 nm^2 / MB^+. Consequently a value of -20 kJ mol^{-1} was obtained for the Gibbs free energy of adsorption, $\Delta G^0_{SiO_2-MB^+}$.

To compare the adsorption of MB^+ between DSNs and MSNs, the values obtained for each are plotted in Table 4.1 and graphically represented in Figure 4.4.

Table 4.1:

	Adsorption constant / K_{ads}	SiO_2 surface area per MB^+ / a	Gibbs free energy of adsorption / $\Delta G^0_{SiO_2-MB^+}$
DSNs	1.66 10^5	1.0 nm^2 / MB^+	-29.3 kJ mol^{-1}
MSNs	3.68 10^3	1.0 nm^2 / MB^+	-20 kJ mol^{-1}

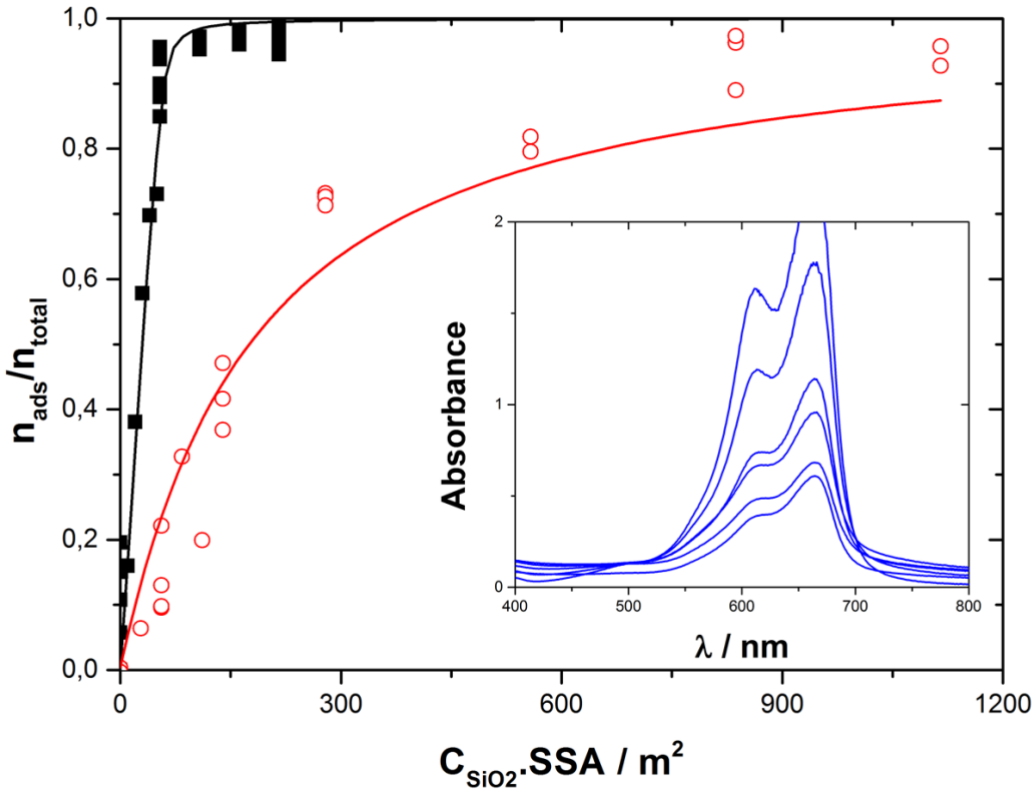

Figure 4.4: Number of adsorbed MB^+ (n_{ads})/total number of MB^+ (n_{total}) plotted as a function of the mass conc. of silica (C_{SiO2}).specific surface area of silica (SSA). Experimental data for DSNs (black squares) and MSNs (red circles) were both fit using a Langmuir isotherm (black line and red line for DSNs and MSNs respectively). Inset shows the UV/Vis absorption spectra of MB after mixing with MSNs (concentrations between 0.1 and 2 g L^{-1}).

It is clear to see from both the larger K_{ads} value and the almost straight ascending line for DSNs in Figure 4.4, that the adsorption of Methylene blue to DSNs is much stronger than that with MSNs. Furthermore the ΔG_{ads} value obtained for MSNs is slightly less compared with that of DSNs, further demonstrating that the adsorption of MB^+ to DSNs is stronger than that to MSNs. The variation in results obtained between DSNs and MSNs could potentially be explained by the difference of ionisation states between MSNs and DSNs in the conditions of this study, as outlined in Chapter 2, Figure 2.8.

4.1.2 *Study of kinetics of MB^+ adsorption and desorption to DSNs and MSNs via Stopped-flow technique*

Kinetics data was obtained using the stopped-flow technique. The adsorption interactions with both DSNs and MSNs were studied using this technique in order to be able to compare and contrast and obtain a greater understanding of the processes occurring. This technique involved monitoring the optical density (OD) variation of MB^+ during its adsorption. UV/Vis spectrums were obtained at equilibrium, as seen in Figure 4.5, using solutions of 50 µM analyte and 0.5 g L^{-1} silica nanoparticles in 50 mM Tris at pH 9, in order to determine the expected OD values at a specific wavelength. Tris was chosen to try prevent clumping of the silica nanoparticles in solution, as at pH 9 they should be more strongly negatively charged and so repel each other. A wavelength of 650 nm was chosen as, at this value, the absorbance values of MB^+ on its own (black line), MB^+ with DSNs (red line) and MB^+ with MSNs (blue line) all differ and so can be distinguished. The stopped-flow experiments used 0.1 mM MB^+ with 0.05 – 5 g L^{-1} silica nanoparticles. The procedure involved placing the solution of MB^+ into a syringe, while the silica nanoparticles solution is placed in another separate syringe, from which 400 µL from each are injected into a small cell simultaneously, which has a light of 650 nm passing through it.

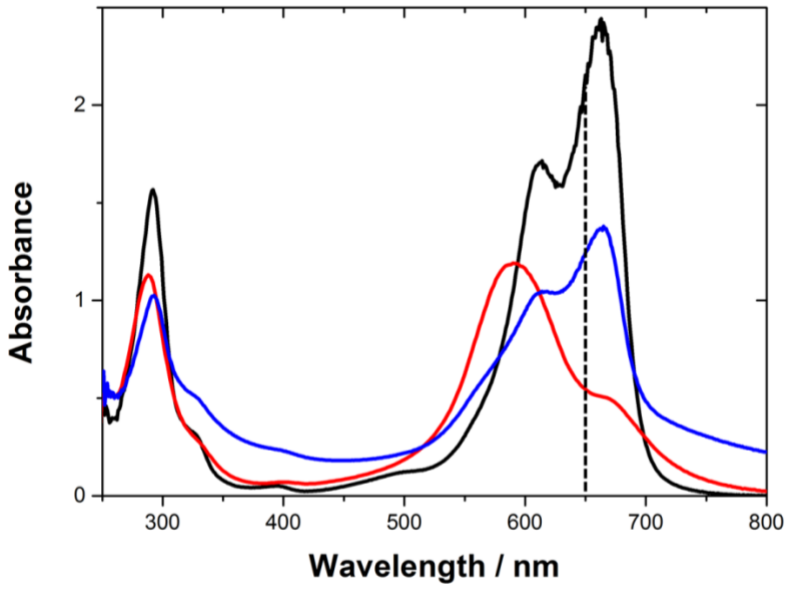

Figure 4.5: UV/Vis spectrums of 50 µM MB^+ alone (black line), with 0.5 g L^{-1} DSNs (red line) and MSNs (blue line) in 50 mM Tris, showing wavelength value chosen (dashed black line) for stopped-flow experiments

From the UV/Vis spectrums in Figure 4.5, the following information can be obtained: at 650 nm the maximum OD value for MB^+ is ~2.2, in the presence of MSNs it is reduced to ~1 and with DSNs ~0.6. Thus when performing the stopped-flow experiments the initial OD should be at 2.2 and then decrease as the silica nanoparticles are mixed with the MB^+. Thus in Figure 4.6, the OD at time = 0 should be 2.2 for all the measurements. This is close to the experimental observation for MSNs whereas all the results with DSNs are flat lines at OD = 0.75. Therefore the first result to be concluded is that with DSNs the adsorption process is finished within the mixing time of the stopped flow (known to be < 3 ms) whereas it has almost not begun with MSNs. The different ionization states of the two types of silica nanoparticles, as previously described in Chapter 2, Figure 2.8, which showed that DSNs are more strongly negatively charged than MSNs across the whole pH range, can explain why the adsorption is faster with DSNs than with MSNs but not that the ion pair formation, known to be generally a diffusion limited process, takes place in the 1 to 2 tens of second range. Diffusion into the pore of MSNs is thus presumably the explanation of this result.

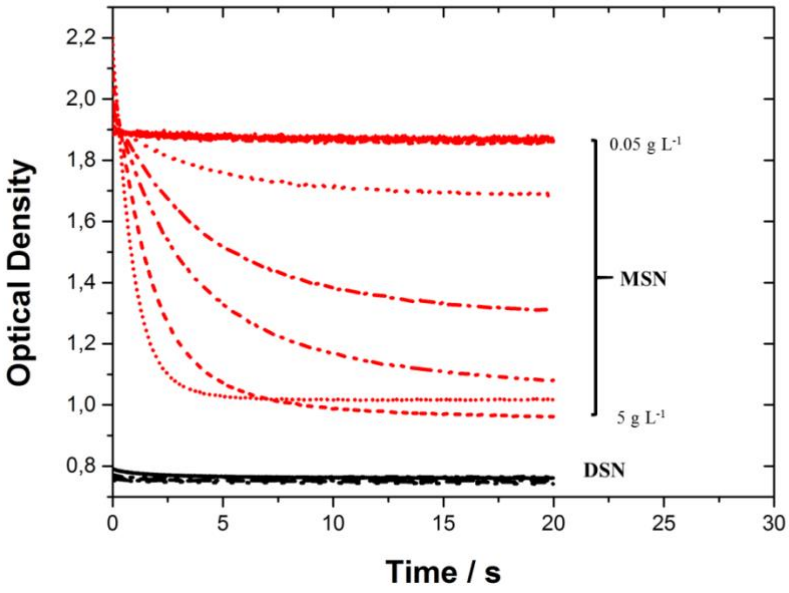

Figure 4.6: Stopped-flow results for 50 µM MB^+ with increasing concentrations (0.05 – 5 g L^{-1}) of DSNs (black lines) and MSNs (red lines), λ = 650 nm

As no further information could be obtained for the adsorption of MB^+ to DSNs, besides the fact that it occurs extremely quickly, the focus was placed on studying the kinetics of the adsorption of MB^+ to MSNs. The observed rate constants (k_{obs}) for adsorption of MB^+ to MSNs were calculated from Figure 4.6 using the following equation:

$$OD\ (t) = A_0 exp^{(-k_{obs}t)} + C_0$$

These values were plotted based on exponential fit of MSN adsorption data, shown in Figure 4.7. It is surprising that the data can be fitted to an exponential fit given that it is diffusion into pores and thus not a very straight forward process. The experimental curves of adsorption of MB^+ onto MSNs were found to be perfectly fitted with a monoexponential function. Obtaining a monoexponential variation of the optical density when studying a diffusion process in a complex medium sounds unusual but it was initially reported by Lagergren and has often been reported as a pseudo first order kinetic [172]. It was recently demonstrated that this approach, although physically inconsistent, gives good fits to describe the solute diffusion from the liquid to the solid interface [173].

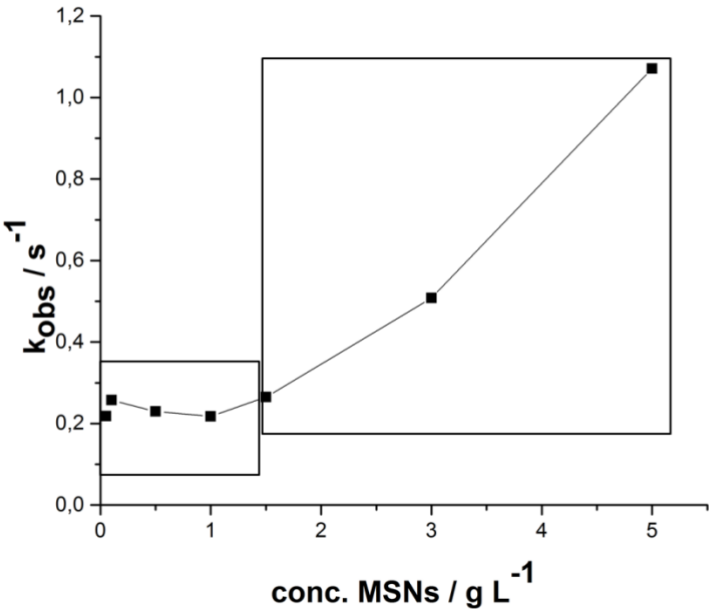

Figure 4.7: Observed rate constant (k_{obs}) as a function of the amount of dispersed MSNs in suspension. The smaller, first box shows the flat line which describes the constant rate of adsorption into the pores. The larger, second box shows the increased rate observed with increasing concentration, related to surface adsorption of MB^+ to the MSNs. $\lambda = 650$ nm

The explanation of a non-linear k_{obs} variation with the amount of MSNs dispersed given in Figure 4.7 is not straight forward. One can imagine that increasing the ratio MSNs/MB^+ allows an increase in the number of easily accessible sites to the MB^+ and thus a faster adsorption. This was also the explanation obtained in the literature when such a variation was observed for dye adsorption on clays studied by stopped-flow [174]. Owing to the complex phenomenon studied here it is difficult to draw a solid conclusion, but, a potential explanation of the graph suggests that there are two processes occurring. The first, shown by the flat line between 0 and 1.5 g L^{-1}, suggests a constant rate of adsorption into pores. The second, which is an increase in k_{obs} with increasing concentration of MSNs from 1.5 to 5 g L^{-1}, relates to surface adsorption, i.e. the more MSNs, the more surface area available and so a faster adsorption rate. Thus, leading to the conclusion that the overall rate is dependent on the combination of these two phenomena.

Some attempts to characterize the kinetics of desorption of MB^+, by adding 0.1 M salt or 0.1 M HCl to the suspension containing equilibrated MB^+ and silica nanoparticles, were performed and the results for those with HCl shown in Figure 4.8.

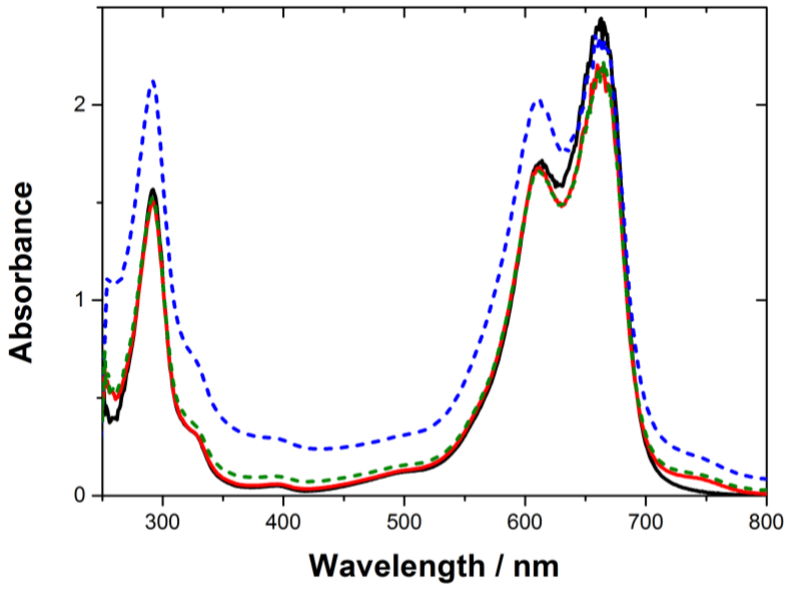

Figure 4.8: UV/Vis spectrum for 50 µM Methylene Blue alone (solid black line), MB^+ with 0.1 M HCl (solid red line), MB^+, HCl and 0.5 g L^{-1} DSNs (dashed blue line) and MSNs (dashed green line) in 50mM Tris

In these conditions the adsorption was shown to be reversible and rapid, i.e. within the mixing time of the stopped-flow, as can be seen in Figure 4.9.

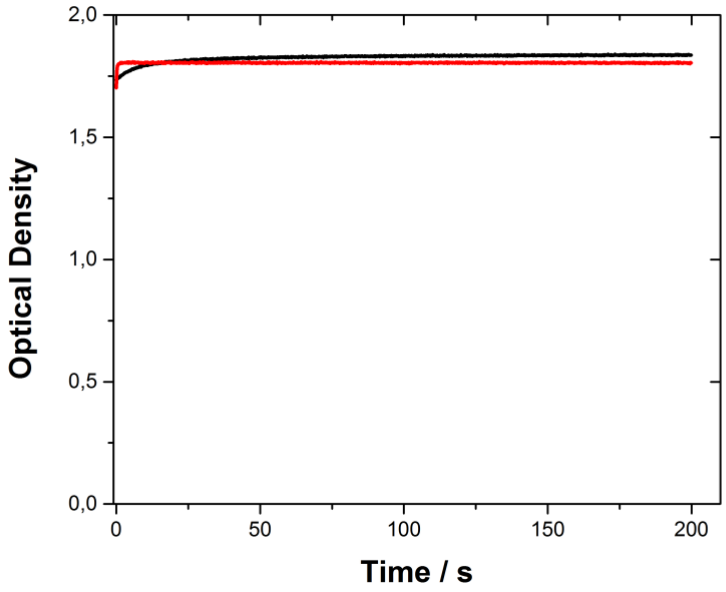

Figure 4.9: Stopped-flow diagram for 50μM MB with 0.5 g L^{-1} DSNs and 0.1 M HCl (black line) and for 50 μM MB with 0.5 g L^{-1} MSNs and 0.1 M HCl (red line), λ = 650nm

However, although the result is the desorption of MB^+, the reaction is more likely an ion exchange than a true desorption. This 'observed' desorption process might be in fact the result of protonation of silanolate groups and thus limited by H^+ diffusion (which is very concentrated in these experiments due to the presence of HCl) and not by the desorption itself. Thus no clear kinetic information is obtained regarding the desorption process.

4.2 ***Electrochemical experiments with MB^+ and silica nanoparticles at the LLI***

Following on from determining the kinetics of the adsorption interaction in monophasic aqueous solutions, the interactions between silica nanoparticles and analytes at the biphasic liquid-liquid interface were monitored electrochemically, using cyclic voltammetry to study their impact on ion transfer at the ITIES.

4.2.1 *Thermodynamic studies of MB^+ adsorption to DSNs and MSNs at the LLI*

In the absence of silica nanoparticles, the standard transfer potential of MB^+ was measured at $\Delta_o^w\phi_{MB^+}^{0'}$ = -0.223 V (Figure 4.10), which was only 0.034 V larger than the open circuit potential of electrochemical cell 1 ($\Delta_o^w\phi_{ocp}$ = -0.257 V). The concentration ratio of MB^+ in both phases at open circuit potential can be calculated using the Nernst equation:

$$\frac{[MB^+]_{org}}{[MB^+]_{aq}} = e^{(\Delta_o^w\phi_{ocp} - \Delta_o^w\phi_{MB^+}^{0'})\frac{zF}{RT}} \quad (7)$$

$\Delta_o^w\phi_{MB^+}^{0'}$ is the formal transfer potential of MB^+, z is the MB^+ charge and F is the Faraday constant. At open circuit potential, the ratio $\frac{[MB^+]_{org}}{[MB^+]_{aq}}$ was 0.26 in the absence of silica nanoparticles at the interface, confirming some spontaneous MB^+ transfer from the aqueous to the organic phase. The spontaneous transfer was observed experimentally at open circuit potential with a blue coloration of the organic solution. However, in the presence of dense silica nanoparticles, the transfer potential of MB^+, $\Delta_o^w\phi_{MB^+}^{1/2}$, shifts to a potential of -0.131 V, confirming the strong affinity between DSNs and MB^+. $\Delta_o^w\phi_{MB^+}^{1/2}$ is calculated as the half-wave potential of MB^+ transfer in the presence of silica nanoparticles adsorbed at the ITIES. At open circuit potential and in the presence of DSNs, the ratio $\frac{[MB^+]_{org}}{[MB^+]_{aq}}$, calculated with Eq (7), was 0.007. Less than 1 % of MB^+ transfers spontaneously across the interface modified with DSNs. The shift of transfer potential allows the estimation of the Gibbs free energy of ion association between the MB^+ and the DSNs adsorbed at the ITIES [175–177].

$$\Delta G_{DSNs-MB^+}^{0,interface} = zF\left(\Delta_o^w\phi_{MB^+}^{0'} - \Delta_o^w\phi_{MB^+}^{1/2}\right) \quad (8)$$

$\Delta G^{0,interface}_{DSNs-MB^+}$ was -8.9 kJ mol^{-1}, which is lower than the Gibbs free energy of adsorption, $\Delta G^{0}_{DSNs-MB^+}$ value of -29.3 kJ mol^{-1}, previously determined in the aqueous phase by UV/Vis spectroscopy in section 4.1.1. The difference between the two energies can be explained by the amphiphilic nature of MB^+ [178], i.e. the presence of the organic phase at the interface for the electrochemical experiments has the effect of lowering the adsorption of MB^+ to the silica, whereas for the UV/Vis experiments the organic phase is absent.

In the presence of MSNs, a shift in the transfer peak potential of MB^+ occurs from -0.22 V to -0.18 V. From this the $\Delta G^{0,interface}_{MSNs-MB^+}$ was calculated to be -3.3 kJ mol^{-1} (using Equation 8), which is lower than the Gibbs free energy of adsorption, $\Delta G^{0}_{MSNs-MB^+}$ value of -20 kJ mol^{-1} for the adsorption interaction in a monophasic system, obtained in section 4.1.1. Both figures are less than those obtained with DSNs. The change in the shape of the cyclic voltammogram (Figure 4.10) is different to that observed with DSNs, further signifying that the interaction between MB^+ and DSNs is different to that between MB^+ and MSNs.

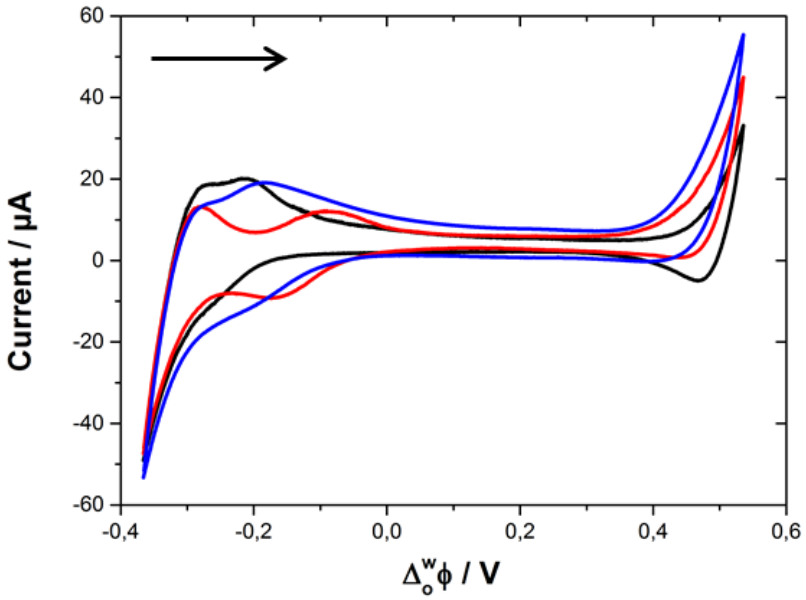

Figure 4.10: Cyclic voltammetry of 600 µM MB^+ in the absence of (black line) and presence of 0.867 g L^{-1} DSNs (red line) and MSNs (blue line). Electrochemical cell 1, ν = 5 mV s^{-1}. Arrow indicates the initial scan direction.

The influence of the presence of DSNs and MSNs on anionic EB^- was also investigated (Figure 4.11). There was little effect on the transfer potential of EB^- when either DSNs or MSNs were added. Thermodynamic values determined from the cyclic voltammograms for MB^+ and EB^- are summarised in Table 4.2.

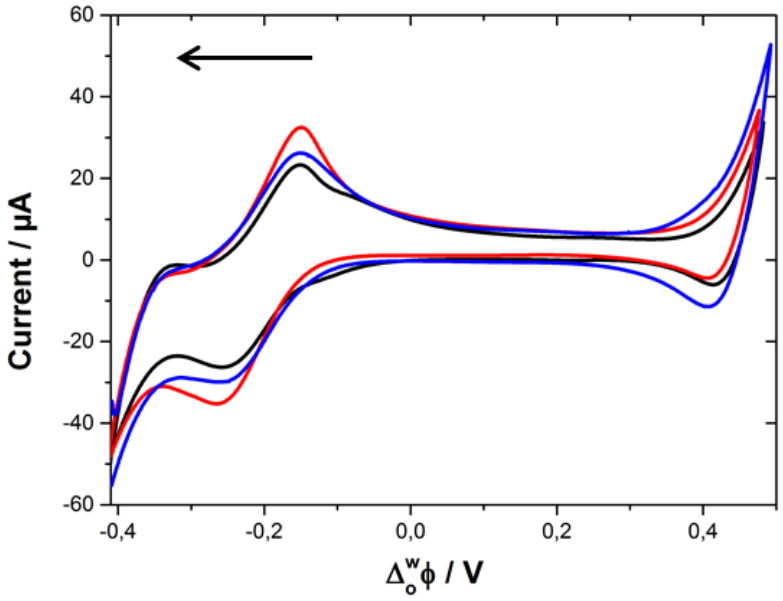

Figure 4.11: Cyclic voltammetry of 300 µM EB^- in the absence of (black line) and presence of 0.867 g L^{-1} DSNs (red line) and MSNs (blue line). Electrochemical cell 1, ν = 5 mV s^{-1}. Arrow indicates the initial scan direction.

Table 4.2: Thermodynamics parameters with DSNs and MSNs determined experimentally

Ion	$\Delta_o^w\phi_{ion}^{0'}$ **/ V**	ΔG_{ion}^0 **/ kJ mol^{-1}**	$\Delta_o^w\phi_{ion}^{1/2}$ **(DSNs) / V**	$\Delta G_{DSNs-ion}^{0,interface}$ **/ kJ mol^{-1}**	$\Delta_o^w\phi_{ion}^{1/2}$ **(MSNs) / V**	$\Delta G_{MSNs-ion}^{0,interface}$ **/ kJ mol^{-1}**
MB^+	-0.223	-20.9	-0.131	-8.9	-0.189	-3.3
EB^-	-0.204	+19.7	-0.193	-1.1	-0.2045	-0.05

Two phenomena can explain the higher level of energy needed to be reached in order for MB^+ to transfer across the LLI: steric hindrance at the interface caused by the adsorption of silica nanoparticles or thermodynamic stabilisation of MB^+ by adsorption onto the nanoparticles.

Peak heights of MB^+ transfer obtained from cyclic voltammograms with increasing concentrations of DSNs and MSNs were plotted in Figure 4.12. The decrease in the peak height of MB^+ transfer on addition of DSNs remains almost constant even in solutions of increasing quantities of DSNs and can be explained by both steric hindrance at the interface caused by the adsorption of silica nanoparticles or thermodynamic stabilisation of MB^+ by adsorption onto the nanoparticles, whereas with MSNs the peak height is increasing with the silica amount.

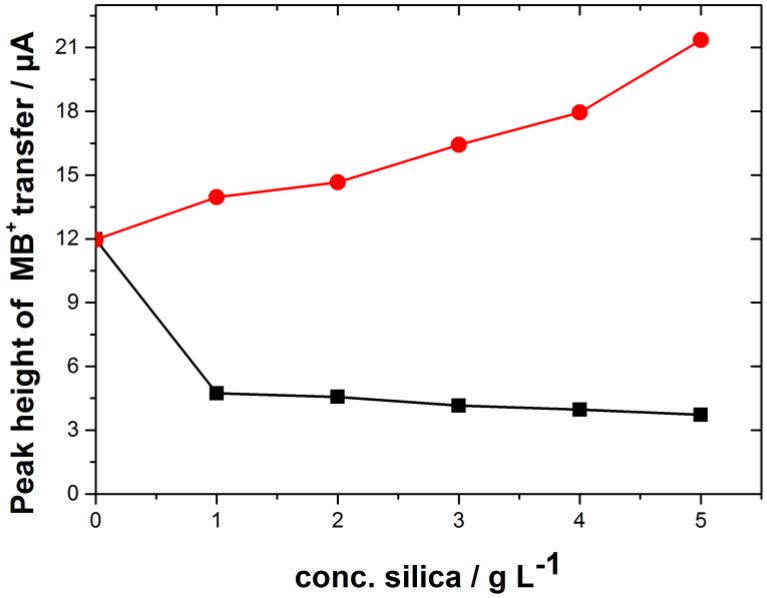

Figure 4.12: Peak height of electrochemical transfer of 300 µM MB^+ in the presence of 0 -5 g L^{-1} of DSNs (black line) and MSNs (red line). Electrochemical cell 1, ν = 5 mV s^{-1}

Peak heights obtained from cyclic voltammograms with the reverse situation, i.e. where the $[MB^+]$ is increasing and the silica concentration is constant, were plotted in Figure 4.13. It is clear to see that there is an increasing transfer of MB^+ across the interface in the presence of MSNs, however with DSNs the quantity transferred remains relatively constant even with increasing $[MB^+]$. As previously discussed in Chapter 3, Section 3.2 with DSNs and TEA^+, the presence of DSNs at the LLI did not significantly affect the transfer of TEA^+ and so the explanation resting on the steric hindrance is questionable, definitely showing that the effects of the nanoparticles are related to MB^+ adsorption.

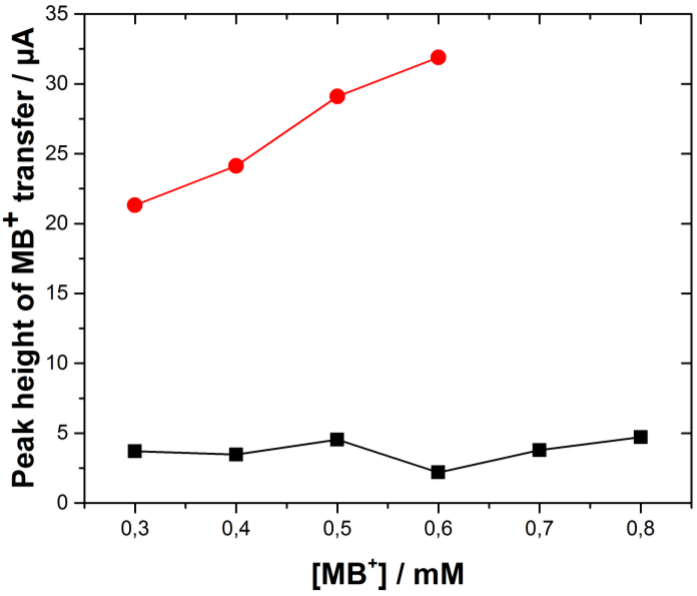

Figure 4.13: Peak height of 300 - 800 µM MB with 5 g L^{-1} DSNs (black line) and MSNs (red line). Electrochemical cell 1, ν = 5 mV s^{-1}

As can be seen in Figure 4.14, the peak position of MB^+ alone is at -0.22 V, it then increases to reach a maximum of -0.127 V for DSNs and -0.143 V for MSNs. The peak potential plateaus at -0.143 V for both at high silica concentrations.

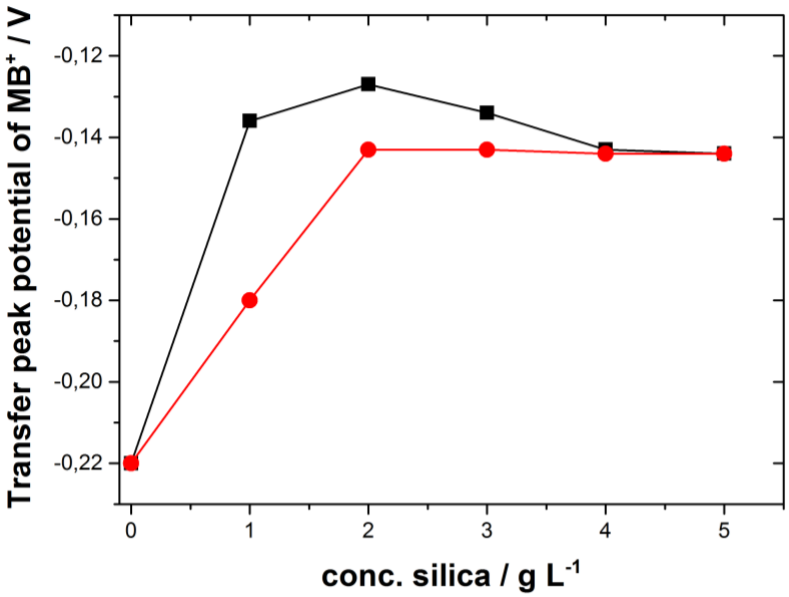

Figure 4.14: Peak position of electrochemical transfer of 300 µM MB^+ in presence of 0 - 5 g L^{-1} DSNs (black line) and MSNs (red line). Electrochemical cell 1, ν = 5 mV s^{-1}

Next cyclic voltammetry experiments with increasing scan rate were carried out, in the presence and absence of DSNs, and the results of the peak height of MB^+ transfer for each plotted in Figure 4.15. The Randles-Sevcik equation was used to relate the peak current, i_p, to the scan rate, v, thus allowing the diffusion coefficient to be determined once the plot produced a linear line.

$$i_p = (2.69\ x\ 10^5)\ n^{3/2}\ A\ c\ D^{1/2}\ v^{1/2}$$

From the linear plots obtained with increasing $\sqrt{Scan\ rate}$, the decrease of the slope of the line as a function of the $\sqrt{Scan\ rate}$ indicates a decrease of the apparent diffusion coefficient of the MB^+ in the water, thus diffusion in the water was the limiting step of the transfer. Taking into account that the transfer of the non-adsorbing EB^- is not modified by the adsorption of silica nanoparticles on the interface and that nanoparticles are not transferring through the interface, the variation of the rate of transfer of MB^+ induced by the nanoparticles may only be explained by the variation of either the local concentration of free MB^+ close to the interface or the diffusion length mean average.

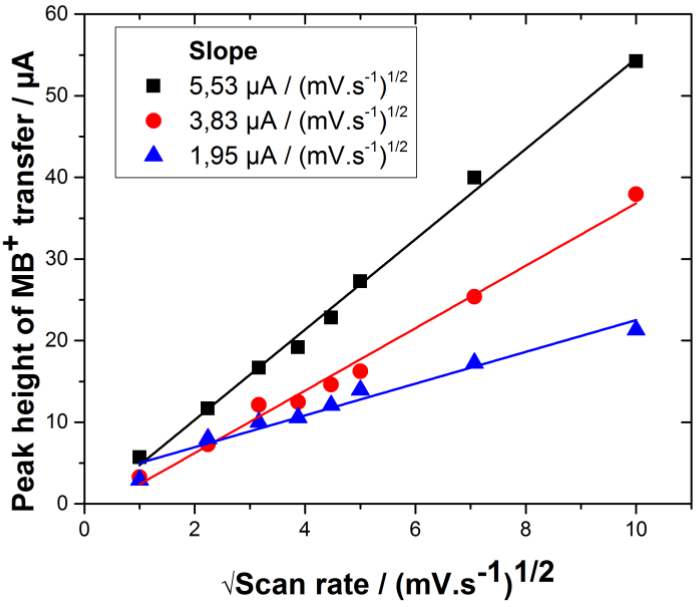

Figure 4.15: Calibration curve of Peak height Vs $\sqrt{Scan\ rate}$ for 600 µM MB^+ (black squares), with 0.5 g L^{-1} DSNs (red circles) and 5.2 g L^{-1} DSNs (blue triangles). Electrochemical cell 1, ν = 100 - 1 mV s^{-1}. Inset: values of the slope obtained from linear fitting of each line (solid black, red and blue lines)

To sum up this data set one can imagine the interfacial mechanism of MB^+ transfer in the presence of silica nanoparticles as outlined in Figure 4.16. The transferring MB^+ can arrive from the water phase as if there were no silica nanoparticles present. The direct transfer cannot be ruled out either. MB^+ have shown a strong affinity constant, K_{ads}^{aq}, for the silica nanoparticles. When silica nanoparticles are adsorbed on the interface, MB^+ transfer remained possible, provided that a sufficient excess of energy is provided: $\Delta G_{SiO_2-MB^+}^{0,interface}$. The decreasing apparent diffusion coefficient of MB^+ in presence of DSNs may either be attributed to a non-diffusion of the adsorbed MB^+ or to a slow motion of the particles sorbing the MB^+. Nevertheless, this type of transfer requires an adsorbed MB^+ to be exactly located on the zone of the silica nanoparticle surface touching the interface. Taking into account the Brownian motions, this seems kinetically unfavourable and if it exists, is presumably representing a small proportion of the transferred amount of MB^+.

Understanding the experimental fact that the peak height decreases with DSNs and increases with MSNs is not straightforward. By considering the nanoparticles rich interfacial zone as a kind of membrane through which the MB^+ has to be transported, similar to the analogy of the transport phenomena by carriers through organic membranes, may help in understanding the process [179]. The optimum transport rate is obtained with a not too low or too high stability of the carrier-solute adduct. With too low a stability not enough solute arrives at the membrane, with too high a stability there is a lot of solute, but it is not released at the interfacial zone. The affinity of MB^+ for DSNs would be thus too high to allow rapid desorption and transport whereas, despite the adsorption of MB^+ onto MSNs being less intense, the easier desorption would result in an increase of the transfer current.

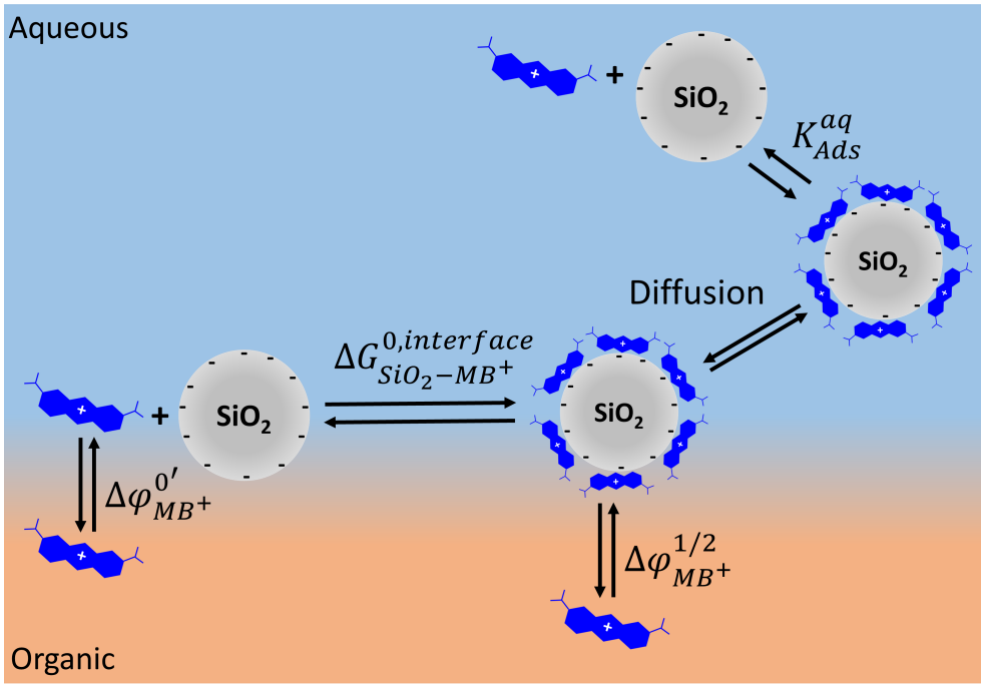

Figure 4.16: Schematic of the interfacial mechanism for the transfer of MB^+ in the presence of silica nanoparticles, $\Delta G_{MSNs-MB^+}^{0,interface} < \Delta G_{DSNs-MB^+}^{0,interface}$

This view is reinforced by experiments performed in view of increasing the sensitivity of the electrochemical detection of MB^+, by harnessing the affinity between MB^+ and silica nanoparticles and the adsorption of silica nanoparticles at the ITIES to accumulate MB^+ ions at the ITIES and increase locally the MB^+ concentration. This is described in detail in the next section.

4.2.2 *Improving detection sensitivity via pre-concentration with silica nanoparticles*

To demonstrate the accumulation of MB^+ at ITIES modified with dense silica nanoparticles, a solution of 25 μM MB^+ was mixed with 0.05 g L^{-1} of silica nanoparticles. Although in the previous section the adverse effect DSNs have on MB^+ transfer was discussed, with the following procedure artificial conditions were created which allowed an increase of the local concentration of MB^+ at the LLI. The resulting effect was a greater enhancement of the peak height, allowing the detection of MB^+ at very low concentrations for which nothing could be seen without nanoparticles. The procedure involved centrifuging the DSNs-MB^+ suspension to concentrate it and subsequent removal of the supernatant. The nanoparticles were then re-suspended in a 10 mM LiCl solution, which was used to prepare an electrochemical cell.

Figure 4.17 shows the cyclic voltammograms obtained with such an electrochemical cell. MB^+ transfer can be seen at ~-0.1 V (dashed line), whereas no transfer was observed for a 25 µM MB^+ solution in the absence of silica nanoparticles (solid line). Such an experiment demonstrated that MB^+ ions were accumulated at the ITIES with the help of the dense silica nanoparticles.

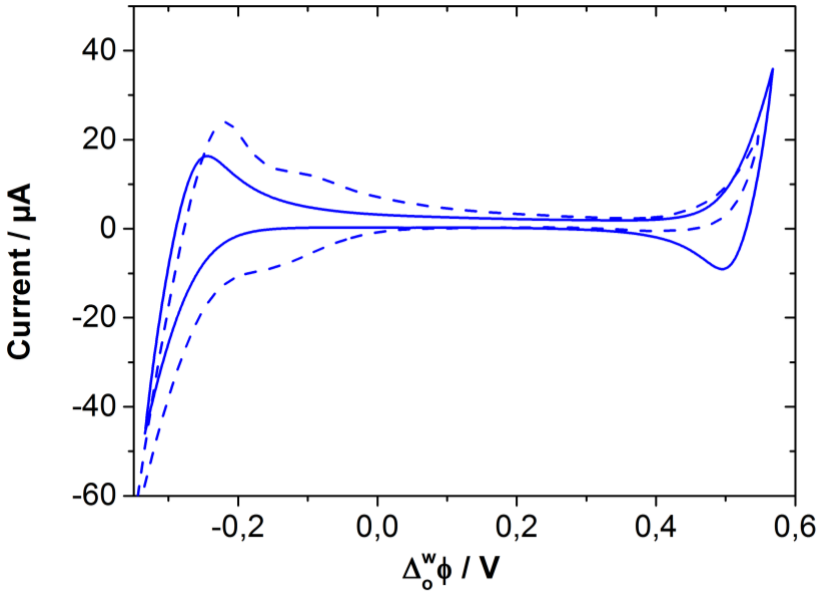

Figure 4.17: Cyclic voltammetry of 25 µM of MB^+ in the absence of DSNs (solid line) and in the presence of DSNs and MB^+ after centrifugation and re-suspension with 3 mL of 10 mM LiCl (dashed line). Initial concentrations were 25 µM MB^+ and 0.05 g L^{-1} of DSNs. Electrochemical cell 1, ν = 5 mV s^{-1}.

The favourable case of MSNs is much more straightforward at improving the sensitivity of the MB^+ detection. First, a MB^+ concentration under the detection limit without nanoparticles was obtained. A value of 50 µM was chosen, as at this concentration no transfer peak is obtained for MB^+ in the CV, as can be seen when the blank and 50 µM MB^+ cyclic voltammograms are compared (black and red lines respectively). Next 2 g L^{-1} MSNs were added and it can be clearly seen in Figure 4.18, a MB^+ concentration not measurable without MSN is detected with a peak at -0.15 V (blue line).

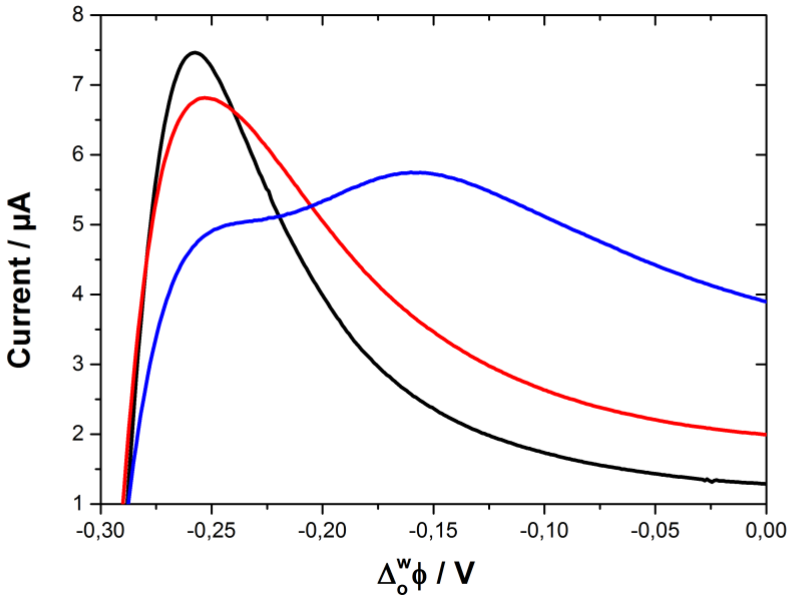

Figure 4.18: Cyclic voltammogram of 50 µM Methylene Blue (red line) and with 2 g L^{-1} MSNs (blue line). The blank solution is shown as the black line. Electrochemical cell 1, ν = 5 mV s^{-1}

Although these results are not significant for MB^+, as concentrations of the dye less than 50 µM can be detected using other methods such as spectrophotometry, this result is important for compounds that are not spectrophotometrically active. The interaction of compounds with silica nanoparticles and the adsorption of the nanoparticles to the LLI, combine to create a pre-concentration effect, thereby allowing the detection of low quantities of the compound.

4.2.3 *Ion – pairing and selective extraction using DSNs at the LLI*

Further experiments with MB^+ and EB^-, in the absence and presence of dense silica nanoparticles at the LLI, resulted in the discovery of an ion-pairing interaction between the two analytes. Ion pairing is defined as the formation of a chemically distinct species as a result of the electrostatic interaction of oppositely charged ions in electrolyte solutions [180]. In order to be deemed an ion pair, valid experimental evidence of their existence must be obtained and the oppositely charged ions in solution should stay together at a separation smaller than a specified cutoff distance. Electrochemical techniques, solubility measurements and spectroscopic measurements have been used to investigate ion pairs. The liquid-liquid interface allows the study of ion selectivity between solvents with different dielectric solvents but also the interactions between ions in either phase. The transfer of ions, as ion pairs, from one phase to another is important in phase transfer catalysis and ion separations [180].

Venkateshwaran et al. describes how knowledge of ion interactions at interfaces, is necessary to understand self-assembly at aqueous interfaces and uses molecular simulations to achieve this aim [181]. Ishimatsu et al. examined the specific interaction of N-tetradecylisoquinolinium $(C_{14}Iq^+)_{org}$ with Cl^-_{aq} and Br^-_{aq} at the interface between an aqueous solution and room temperature ionic liquid (RTIL) using voltammetry of ion transfer and electrocapillarity [182]. They demonstrated an interfacial ion pairing between the hydrophilic anions and the cation of the RTIL at the liquid-liquid interface, and also in the bulk RTIL phase. Schweighofer and Benjamin studied the thermodynamics and dynamics of ion-pair dissociation of NaCl at the water/1,2-Dichloroethane interface [183]. Using calculations and modelling they attempted to understand ion pairs at the interface between a polar and non-polar liquid. Given the natural tendency of Na^+ and Cl^- to transfer to the aqueous phase, he concluded that the ion pair was more stable at the interface compared with the bulk aqueous solution.

This section studies the influence of dense silica nanoparticles on the ion pair between MB^+ and EB^-, and its effect on the transfer of the ions at the liquid-liquid interface, with a final step demonstrating the potential of selective extraction, when DSNs are present in the system.

Firstly individual cyclic voltammograms of cationic MB^+ and anionic EB^- in the absence of silica nanoparticles were obtained, shown by the red and blue lines in Figure 4.19. The CV resulting from a mixture of these two ions reveals some disturbance occurring between -0.1 and 0.1 V. This can be explained by the formation of an ion pair between the cation and anion, which destabilises the interface, thus resulting in the multiple peaks in the CV. The sharp peaks in the voltammogram are due to the breaking of the ion-pair to allow the transfer of MB^+ from the aqueous to organic phase during the forward scan, and the transfer of EB^- from aqueous to organic during the reverse scan. This interaction can also be seen by UV/Vis spectroscopy in Figure 4.20. The spectrums for EB^- and MB^+ alone show their characteristic peaks at 520 and 664 nm respectively. When mixed the peak for EB^- remains unchanged, however the absorbance of the peak for MB^+ decreases significantly and its position shifts to ~680 nm, thereby indicating an interaction between these two ions. Unfortunately, with each UV/Vis spectrum obtained in this section the absorbance was too large and so the top of the peak is void, however this does not affect the main point that it conveys. The larger than recommended concentrations were necessary to be able to see all the peaks and have all the results comparable.

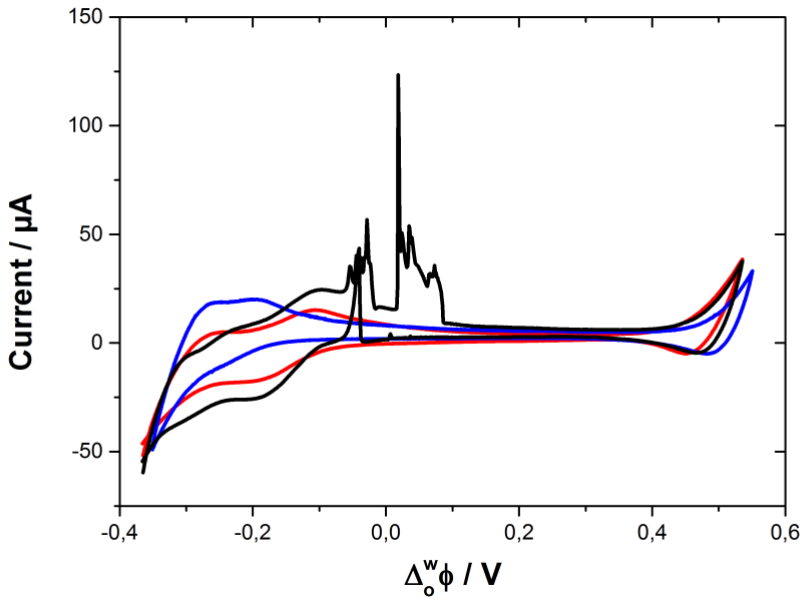

Figure 4.19: Cyclic voltammograms showing the individual electrochemical responses of 300 µM EB^- (red line) and MB^+ (blue line), and the ion pairing effect between them when mixed (black line), in the absence of DSNs. Electrochemical cell 1; $\nu = 5$ mV s^{-1}

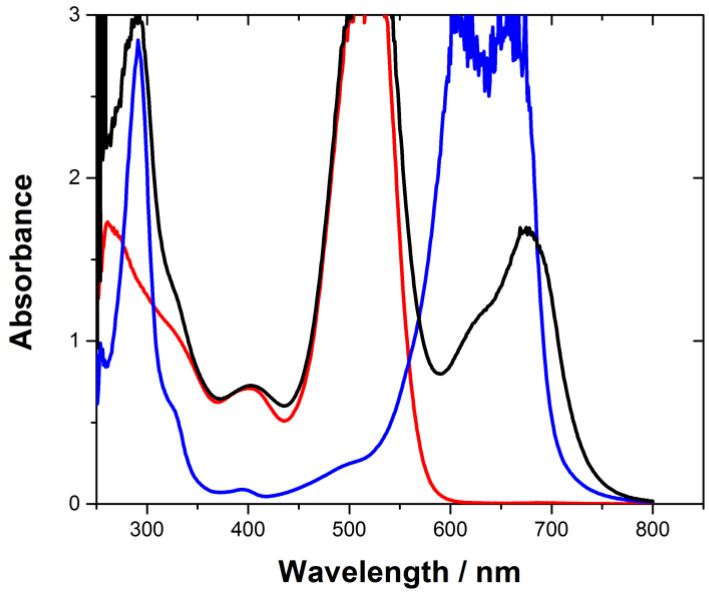

Figure 4.20: Corresponding UV/Vis spectrum of EB^- (red line), MB^+ (blue line) and them mixed (black line) with no DSNs

Next we repeat the same experiment but with 0.867 g L^{-1} DSNs in the solutions. As can be seen in Figure 4.21, both MB^+ and EB^- transfer at the same potential, -0.1 V, in the presence of DSNs when in separate solutions. When DSNs are added to a mixture of the two ions, the interaction between the ions changes compared to that obtained in Figure 4.19. As proven earlier in this chapter from kinetics and thermodynamics experiments (Section 4.1 and 4.2.1), DSNs accumulate MB^+ but do not interact with EB^-. Thus when MB^+ is adsorbed to DSNs in solution, it no longer interacts with EB^- to form ion pairs and so the interface is no longer destabilized, thus little or no disturbances are observed in the CV. The affinity of MB^+ for adsorption to DSNs appears to be much greater than the ion-pairing interaction of MB^+ to EB^-. The change in interactions between EB^-, MB^+ and DSNs in solution can also be seen in the UV/Vis spectrum, Figure 4.22. The presence of DSNs has no effect on Eosin B and it stays at 520 nm. The shape of the peak for MB^+ changes in the presence of DSNs, as was previously discussed in Figure 4.1 and 4.5. The larger band occurs at 590 nm and the smaller peak at 664 nm. The shape of the continuous black line, which represents the Eosin and Methylene blue interaction, changes in the presence of DSNs to reflect this also. This is to be expected as the presence of DSNs breaks the MB^+-EB^- ion pair, thus the occurrence of Methylene blue – Eosin B interactions decreases as the frequency of DSNs – Methylene blue interactions increases.

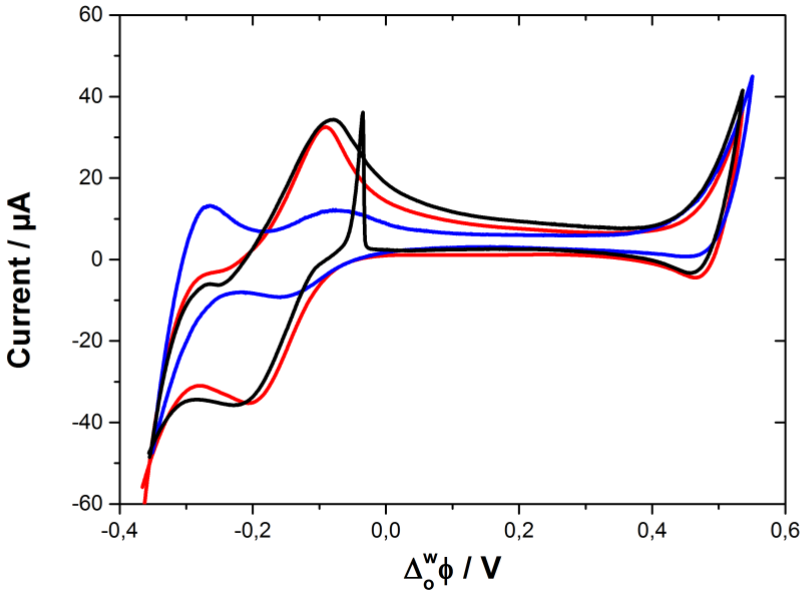

Figure 4.21: Cyclic voltammogram showing the individual responses of 300 µM EB^- (red line) and MB^+ (blue line), and the ion pairing effect between them when mixed (black line), in the presence of 0.867 g L^{-1} DSNs. Electrochemical cell 1; ν = 5 mV s^{-1}

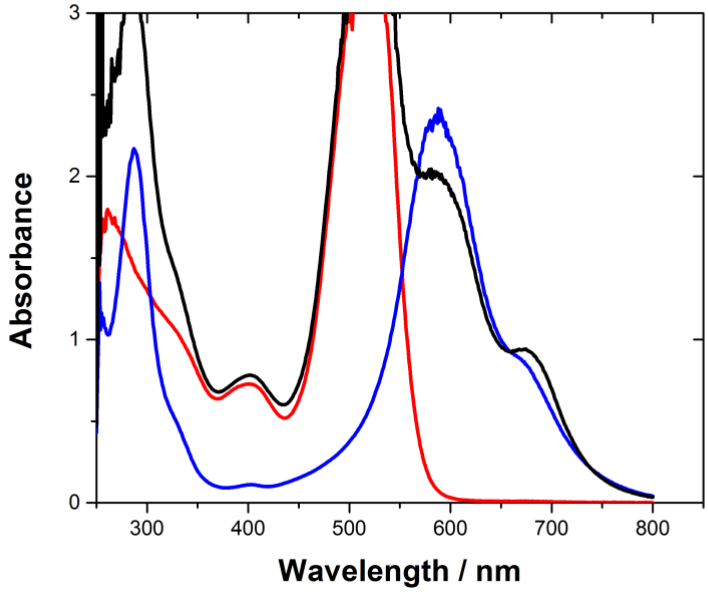

Figure 4.22: The corresponding UV/Vis spectrum of EB^- (red line), MB^+ (blue line) and them mixed (black line) with 0.867 g L^{-1} DSNs

When the Eosin B, Methylene blue and DSNs mixture is ultrafiltrated, the filtrate is predominantly composed of Eosin B, with only a very small amount of Methylene blue, as shown by the red line in Figure 4.24. The red colour of the filtrate obtained further confirms that the Eosin B does not interact with DSNs and passes through the membrane to be detected by UV/Vis. Methylene blue adsorbs on the DSNs which are too large to pass through the membrane and so remains on it after UF. When this is added to 10 mM LiCl it forms a blue solution and generates an electrochemical signal at its usual position of -0.1 V on the CV Figure 4.23 (red line), and characteristic peak at ~600 nm on the UV/Vis spectrum Figure 4.24 (blue line).

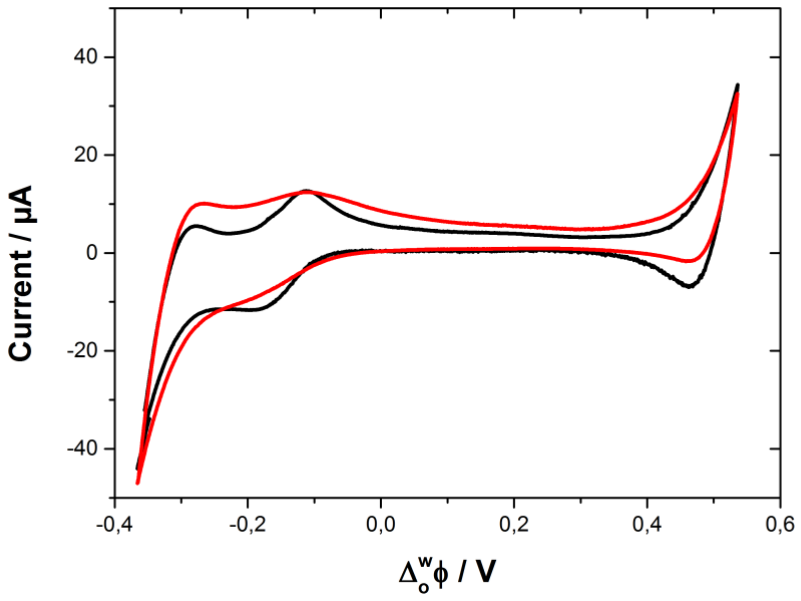

Figure 4.23: Cyclic voltammograms of 100 µM mixture of EB^- and MB^+ in 0.867 g L^{-1} DSNs, with no ultrafiltration step (black line) and after ultrafiltration and re-suspension with 3 mL of 10 mM LiCl (red line). Electrochemical cell 1; ν = 5 mV s^{-1}

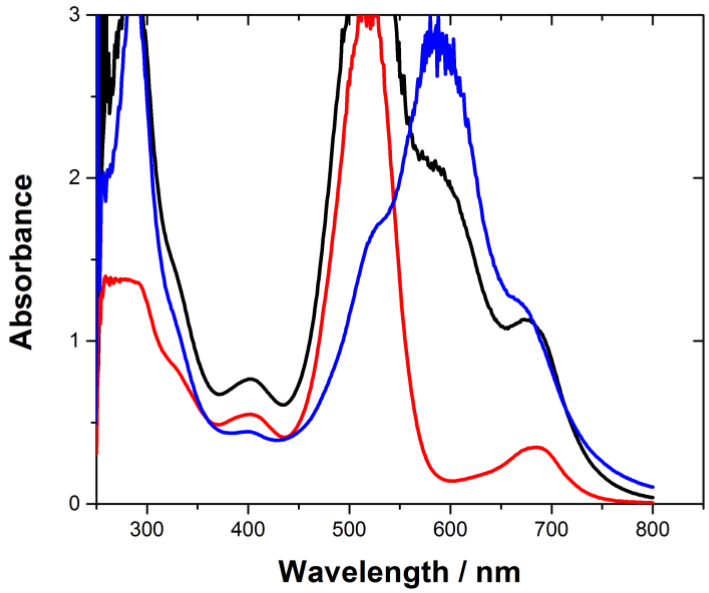

Figure 4.24: Corresponding UV/Vis spectrum of the mixture before ultrafiltration (black line) and the separated components after ultrafiltration – filtrate (red line), retentate (blue line)

These experiments prove the point that a selectivity of charge occurs when silica nanoparticles are present at the liquid-liquid interface. Filtration of a mixture of MB^+, EB^- and dense silica nanoparticles confirm that silica nanoparticles accumulate MB^+ but do not interact with EB^-. Hence a mix of two species can be separated according to their interaction with silica nanoparticles.

4.3 ***Conclusion***

In this chapter, MB^+, a cation, and EB^-, an anion, were considered as model molecule spectroscopic probes, thereby allowing both electrochemical and spectroscopic results be obtained. The first section of experiments were in monophasic aqueous solutions, with the electrochemical experiments taking place at the LLI.

Firstly, UV/Vis spectroscopy experiments followed the interaction of the ions with the silica nanoparticles. It was clearly apparent that the anionic EB^- had no interaction with the silica nanoparticles and so the focus was placed on the interactions between silica and the cation. The UV/Vis spectrums for MB^+ alone and MB^+ with DSNs had different shapes and from this the quantity of adsorbed MB^+ could be deduced and the adsorption constant calculated and found to equal $1.66\ 10^5$. The value obtained experimentally for MB^+ adsorption to MSNs was calculated as $3.68\ 10^3$. Thus the much larger value obtained with DSNs proves the adsorption of MB^+ to DSNs is much stronger than that with MSNs. Furthermore, the ΔG_{ads} value obtained for MSNs (-20 kJ mol^{-1}) is slightly less compared with that of DSNs (-29.3 kJ mol^{-1}), further demonstrating that the adsorption of MB^+ to DSNs is stronger than that to MSNs. The SiO_2 surface area per MB^+ was calculated as 1.0 nm^2/MB^+ for both DSNs and MSNs.

Stopped-flow experiments showed that with DSNs the adsorption process was finished within the mixing time of the stopped flow (known to be < 3 ms) whereas it had almost not begun with MSNs. The observed rate constants (k_{obs}) for adsorption of MB^+ to MSNs were calculated and the values plotted based on exponential fit of MSN adsorption data. The experimental curves of adsorption of MB^+ onto MSNs were found to be perfectly fitted with a monoexponential function. From this it was clear to see that there were two processes occurring. The first, shown by the flat line between 0 and 1.5 g L^{-1}, suggests a constant rate of adsorption into pores. The second, which is an increase in k_{obs} with increasing concentration of MSNs from 1.5 to 5 g L^{-1}, relates to surface adsorption, i.e. the more MSNs, the more surface area available and thus faster adsorption rate. Thus leading to the conclusion that the overall rate is dependent on the combination of these two phenomenon. The adsorption of MB^+ to DSNs and MSNs was found to be reversible and rapid however it could not be confirmed as a true desorption, potentially more of an ion exchange due to the large quanity of H^+ ions in the low pH solution.

Electrochemical experiments allowed information on the thermodynamics of the adsorption of MB^+ to DSNs and MSNs to be calculated. A difference of 5.6 kJ mol^{-1} between the Gibbs free energy of ion association for MB^+ adsorption on DSNs and MSNs suggests the interactions between them are not the same. Furthermore, the differing shape of the cyclic voltammograms for MB^+ in the presence of DSNs and MSNs confirms this. The affinity of MB^+ for DSNs is much greater than that for MSNs, resulting in a more difficult desorption and thus less transferring across the LLI. The large energy needed for MB^+ to cross the LLI could be explained by steric hindrance at the interface cause by the presence of the silica nanoparticles or due to thermodynamic stabilisation of MB^+ by adsorption to the silica. However no significant variation in the peak position was observed and the cyclic voltammograms of EB^- were unaffected by the presence of silica nanoparticles, thus thermodynamic stabilisation was the most plausible reason.

By harnessing the affinity of MB^+ to silica nanoparticles and the adsorption of these at the LLI, it was possible to accumulate MB^+ ions at the interface, thereby increasing the sensitivity of electrochemical detection of MB^+. Thus with DSNs and MSNs, artificial conditions were created which allowed an increase of the local concentration of MB^+ at the LLI, resulting in a greater enhancement of the transfer peak height of MB^+. Low concentrations that could not be detected without silica nanoparticles can now be detected in their presence.

The study of the ion pair formation between MB^+ and EB^- in the presence and absence of DSNs at the LLI, allowed the development of a selective extraction procedure. The presence of DSNs and their strong affinity for MB^+ adsorption, favoured their interaction over the MB^+ - EB^- ion pair, and following filtration of the solution, it was clear to see a selectivity of charge occurred. The anionic EB^- passed through the filter, however the DSNs were too large and thus MB^+ that had adsorbed to them were retained on the membrane. Thus the cation and anion that was originally mixed in the solution were separated.

This improvement in selectivity is furthered in the next chapter as results with molecularly imprinted silica nanoparticles are presented and real pollutants (drug molecules) analysed.

5. MOLECULARLY IMPRINTED DENSE SILICA NANOPARTICLES

As described in the introduction (Chapter 1 Section 1.3), molecular imprinting involves the arrangement of a cross linked silica matrix around a chosen imprint molecule, which is held in place by interactions with specified functional groups on the silica. Removal of the imprint molecule gives rise to a cavity with its specific size and shape, along with the functional groups giving it a molecular memory, allowing rebinding of the target molecule.

Non-imprinted dense silica nanoparticles (NINs) were synthesised, as outlined in the materials and methods section (Chapter 2 Section 2.6.1), as a basis from which the imprinted silica nanoparticles could be synthesised (Section 2.6.2). Their characterisation was reported in Section 2.6.3. The NINs consisted of tetraethoxysilane (TEOS) as the cross-linker, with aminopropyltriethoxysilane (APTES) as the functional monomer. These NINs acted like a control during the experiments. The only difference between NINs and the imprinted particles was the presence of the template, i.e. the NINs also contained N^+ functionality from the APTES and so a true blank was obtained, from which imprinted nanoparticles results could be compared. The template chosen to be imprinted into the silica nanoparticles was Diclofenac.

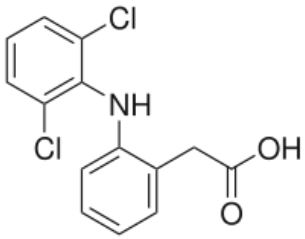

Diclofenac free acid

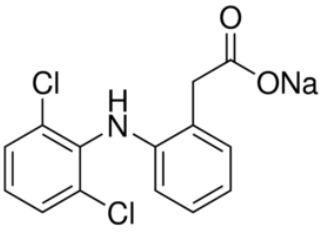

Diclofenac sodium salt

	Molecular weight	Cation/Anion	pka	Log P
Sodium salt	318.129 g mol^{-1}	anion	4	4.26
Free acid	296.147 g mol^{-1}	anion	4.15	4.51

Diclofenac is available as a free acid or more commonly as the sodium salt. It is an aminophenyl acetic acid and categorised as a nonsteroidal anti-inflammatory drug (NSAID) used to treat mild to moderate pain, fever and inflammation [184]. Prostaglandins are chemicals produced by the body that cause pain, fever and inflammation. NSAIDs work by blocking the enzyme that makes prostaglandins (cyclooxygenases) thereby reducing the production of prostaglandin, which in turn reduces pain, fever and inflammation. Its brand

names are Voltaren, Cataflam,Voltaren-XR, Cambia, Zipsor, Zorvolex. It is classified by ChEBI (Chemical Entities of Biological Interest) as an environmental contaminant and has been added to the watch list of emerging aquatic pollutants in the 2000 Water Framework Directive. This Directive dictates the monitoring of river, lake and coastal waters and controls emissions into them across the EU [185]. As Diclofenac is one of the most used drugs, it was one of the first to be detected in the aquatic environment and so has been well investigated. Studies found a concentration of 560 and 365 ng/L Diclofenac in the influents and effluents of sewage water of Greece [186]. Research on the toxicity of Diclofenac in embryos of zebrafish (Danio rerio) found that for concentrations above 1.5 mg/L, specific effects on hatching, yolk sac and tail deformation were observed [186]. Furthermore, the veterinary use of Diclofenac in cattle attributed to renal failure and visceral gout in vulture species in Asia, which has implications for human health indirectly, via ecological, socio-economic and cultural impacts [187]. Thus it is of high importance to be able to detect this drug in the environment and deal with it accordingly. Diclofenac imprinted silica nanoparticles (DINs) with greater sensitivity and selectivity could have the ability to do this. In order to prove the specificity of the imprinted silica, experimental results obtained with Diclofenac were compared with two of its analogues – Aceclofenac and 4-phenylazo benzoic acid (PABA).

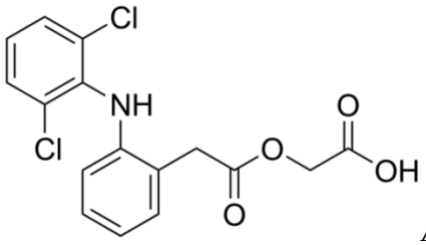

Aceclofenac

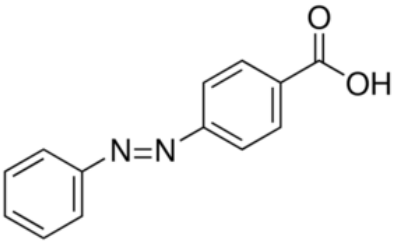

PABA

	Molecular weight	Cation/Anion	pKa	Log P
Aceclofenac	354.18 g mol^{-1}	anion	3.44	2.17
PABA	226.23 g mol^{-1}	anion	2.45	3.87

This chapter presents the results obtained from experiments with diclofenac imprinted dense silica nanoparticles and the comparison of results between Diclofenac, Aceclofenac, PABA and a mixture of all three.

5.1 ***Spectroscopic evidence for formation of Diclofenac-imprinted cavities***

5.1.1 *Infrared spectroscopic analysis of DINs*

As was discussed in the synthesis of DINs (Chapter 2, Section 2.6.2), after the procedure to make the nanoparticles, they were first washed in H_2O and then extracted with HCl in EtOH. Samples of the powder were taken and dried and used in the following experiments. Spectrums for Diclofenac-imprinted nanoparticles were obtained using FT-IR. Unfortunately using this technique, no clear result could be concluded, except for the presence of a large band between 2750 - 3750 cm^{-1} in the spectrum for extracted DINs, representing O-H stretch of ethanol which was used during the extraction process [188].

However, on using the KBr-IR technique, much clearer spectrums were obtained (Figure 5.1 A). The pellets were prepared with 0.5 % silica nanoparticles mixed with KBr. The IR spectrum of Diclofenac has peaks of interest between 500 + 1750 cm^{-1}. Unfortunately the large silica bands block these peaks between 500 + 1250 cm^{-1}, with the largest band between 1000 and 1130 cm^{-1} due to Si-O-Si and the smaller peak between 810 and 950 cm^{-1} representing the Si-OH group [189]. The large band due to ethanol blocks the spectrum at the higher wavenumbers, between 2750 + 3750 cm^{-1}. However in Figure 5.1 B, zooming in on wavenumbers 1425 – 1650 cm^{-1} allows comparisons to be drawn between Diclofenac Na and DINs. The significant peaks of diclofenac at ~1510 and 1575 cm^{-1} (black line), which represent the aromatic and carboxylate groups, as well as the bands at 1450 and 1470 cm^{-1} corresponding to the C-N stretching, can also be seen in the spectrum of DINs before extraction (blue line) [184].These non-extracted DINs still contain the Diclofenac used during their synthesis and so they show the peaks of Diclofenac in their IR spectrum. However once the Diclofenac is removed from the nanoparticles during washing and extraction, these peaks disappear and the spectrum becomes comparable to that of non-imprinted dense silica nanoparticles, thus proving that extraction removes Diclofenac from the imprint cavities in the DINs.

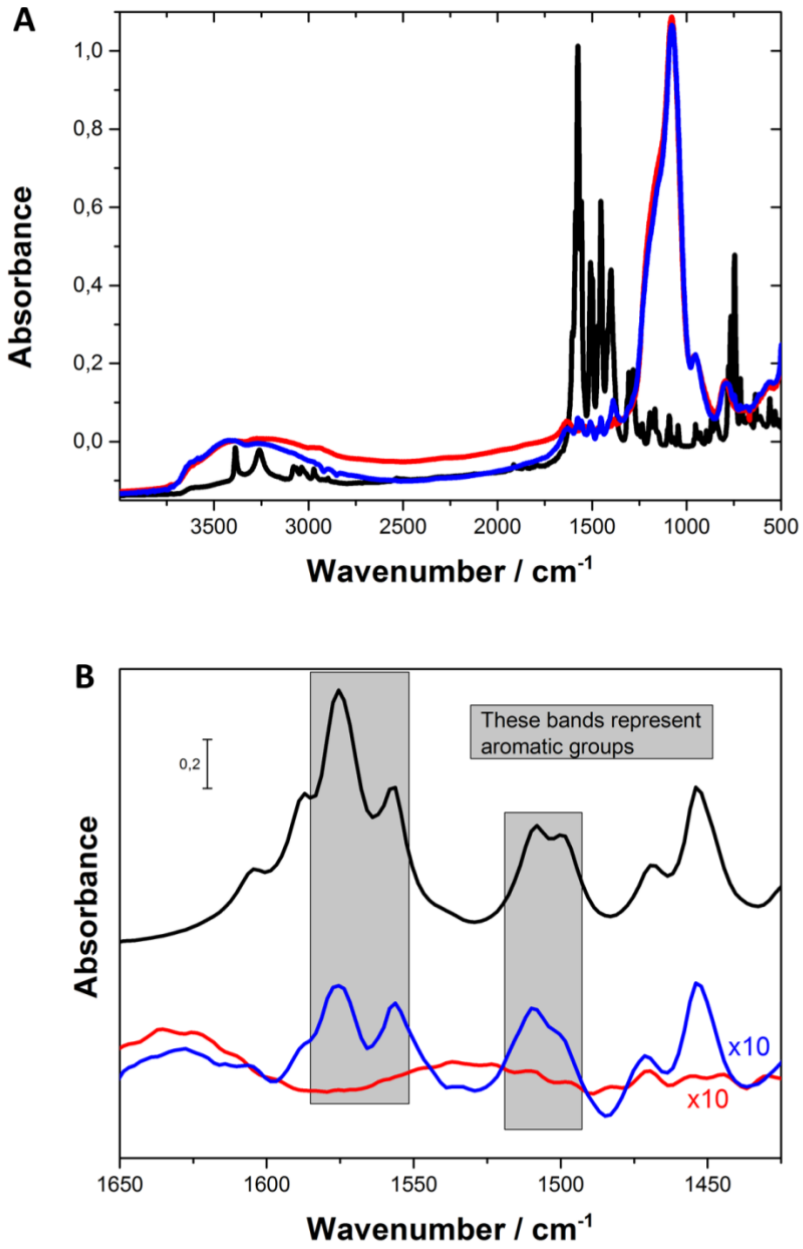

Figure 5.1: (A) IR spectrum of non-imprinted dense silica nanoparticles (red line), Diclofenac alone (black line) and DINs non extracted (blue line), all achieved using KBr discs (B) Figure 5.3 A zoomed in between 1425 + 1650 cm^{-1} and rescaled

5.1.2 *UV/Vis spectroscopy of Diclofenac with DINs*

Figure 5.2 shows spectrums recorded with 10 mm quartz cuvettes for 0.1 g L^{-1} NINs (dashed red line) and DINs (dashed blue line) alone, 0.2 mM Diclofenac (black line) alone and with 0.1 g L^{-1} of NINs (solid red line) and extracted DINs (solid blue line). The solutions were not filtered before analysis, which explains the slightly higher baseline for the spectrums that contained nanoparticles. The blank solutions with just NINs and DINs alone show no peaks. It is clear to see that there is no difference in the curves between Diclofenac alone and Diclofenac with NINs, thus confirming no interaction between them. However, the peak height for Diclofenac with extracted DINs is much lower, indicating the Diclofenac adsorbed into the cavities of the imprinted nanoparticles and when this happened the Diclofenac is no longer visible in the UV/Vis spectrum. This only happens for Diclofenac adsorbed into the imprint cavities, as Diclofenacs analogues, Aceclofenac and PABA, are still visible in UV/Vis spectra after mixing with DINs (Figures 5.5 and 5.6).

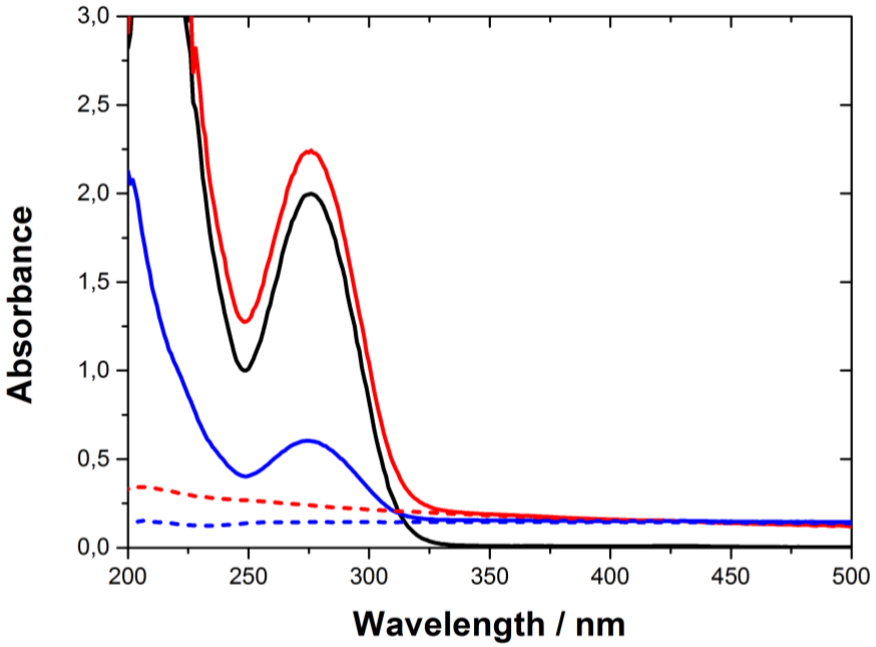

Figure 5.2: UV/Vis spectrum of 0.1 g L^{-1} NINs (dashed red line) and DINs (dashed blue line) alone, 0.2 mM Diclofenac alone (black line) and with 0.1 g L^{-1} NINs (solid red line), extracted DINs (solid blue line)

5.2 ***Spectroscopic investigation of NINs and DINs interactions with Diclofenac and its analogues in aqueous solution***

This section describes results obtained from UV/Vis spectroscopy experiments using quartz cuvettes. Diclofenac, Aceclofenac and PABA can all be recorded on the spectrums and so this technique allows the affinity of the three drugs for the imprinted silica to be compared and contrasted. Firstly the affinity constant, K_a, was calculated for Diclofenac with both the non-imprinted and diclofenac-imprinted silica nanoparticles. Next UV/Vis spectrums were recorded for Aceclofenac and PABA with and without DINs. Finally an adsorption isotherm comparing all three drugs affinity for DINs was plotted, allowing a conclusion to be drawn.

5.2.1 *Calculation of K_a for Diclofenac Na to NINs and DINs using UV/Vis spectroscopy*

Here we determine the affinity constant, K_a, of Diclofenac Na for DINs and NINs. The solutions of Diclofenac alone, with NINs and with DINs were made in 10 mM LiCl, then filtered using a syringe filter before UV/Vis experiments. 1 mm quartz cuvettes were used here in order to have a shorter path length and thus measure larger concentrations. The absorbance spectrum for Diclofenac gives a peak at 276 nm and the height of the absorbance bands were measured at this wavelength value. The results of one set of concentrations (2 mM Diclofenac) are shown in Figure 5.3 inset. The peak heights were measured for all concentrations and a calibration curve for Diclofenac alone (black squares) and Diclofenac free in solution after it that had been mixed with NINs (red circles) and DINs (blue triangles) and filtered, are presented in Figure 5.3. It can be seen that the peak heights for free Diclofenac after interaction with DINs (blue) are significantly lower than those of Diclofenac alone (black) and Diclofenac with NINs (red). This implies an interaction occurred between Diclofenac and the DINs, as a quantity of Diclofenac was adsorbed to the DINs and so less Diclofenac was free in solution after filtering, to be detected by UV/Vis spectroscopy. Conversely, much less Diclofenac adsorbed to NINs and so the quantity left free in solution after filtering is similar to that of Diclofenac alone.

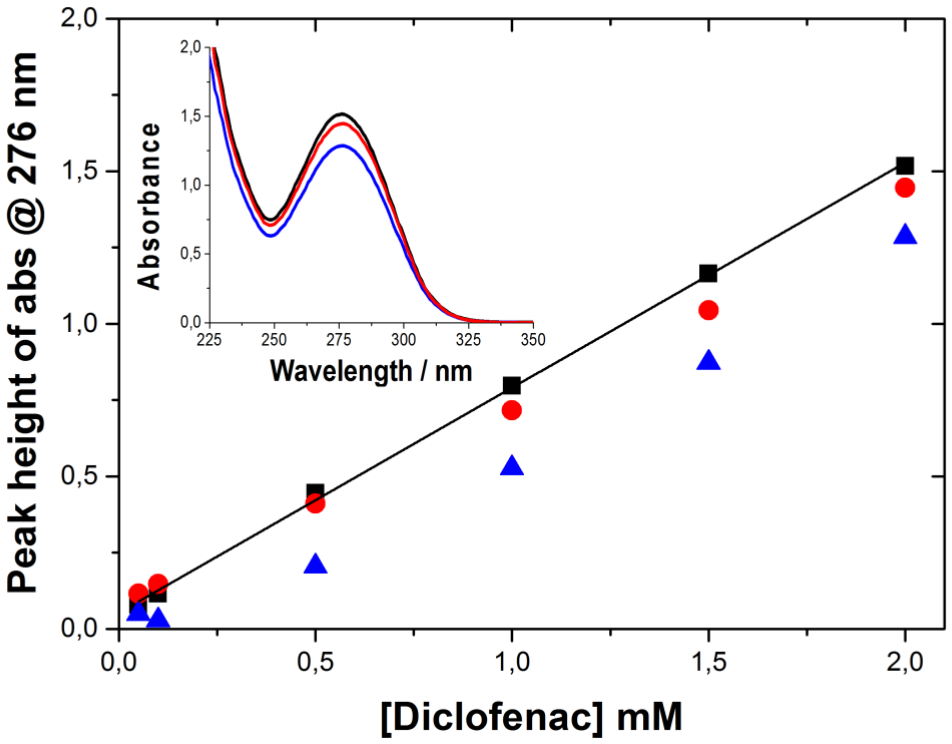

Figure 5.3: Calibration curve of 0.05 - 2 mM Diclofenac (black squares), after mixing and filtering with 0.1 g L^{-1} NINs (red circles) and DINs (blue triangles). The black line represents the linear fitting of the Diclofenac data. Inset showing UV/Vis spectrum of results with 2 mM Diclofenac from which the calibration curve was deduced

By subtracting the peak heights of Diclofenac with the silica nanoparticles from Diclofenac alone, then dividing by the slope of Diclofenac alone, the quantity of Diclofenac adsorbed to the silica nanoparticles in mM was deduced. Converting from mM to mol g^{-1} (given the total volume of the aqueous solution was 3 x 10^{-3} L and the quantity of silica nanoparticles used was 0.1 g L^{-1}) gave Figure 5.4. It clearly shows the quantity of Diclofenac adsorbed to DINs is much larger than that to NINs. The reasoning for this is the presence of the imprint cavities for Diclofenac in DINs, which have the specific size, shape and functional groups to interact with Diclofenac in solution.

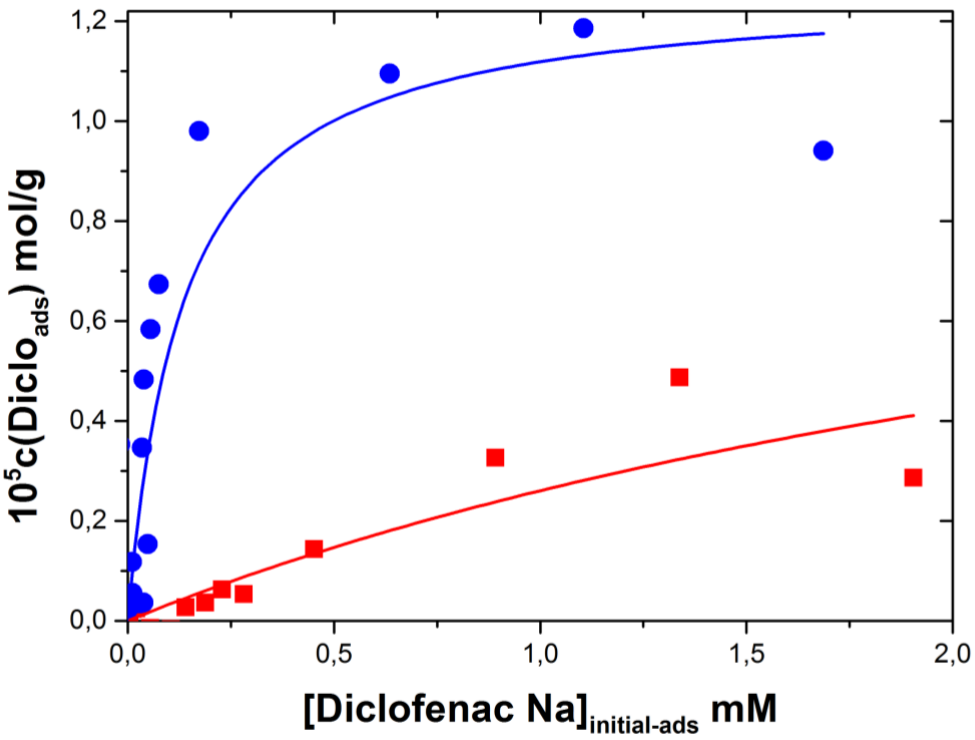

Figure 5.4: Plot of quantity of Diclofenac adsorbed to silica nanoparticles in mol g^{-1} Vs $[Diclofenac]_{free}$ in mM, for NINs (red squares) and DINs (blue circles). The red and blue lines represent the fitting of the curves for NINs and DINs respectively

From the fitting of the two curves in Figure 5.4, the affinity constant (K_a) and total no. of sites (s) were obtained from the slope and intercept respectively. It can be seen that there are slightly more adsorption sites for Diclofenac on DINs compared with NINs, explained by the presence of the imprint cavities in DINs. What is more striking is the affinity of Diclofenac for DINs is much larger than that for NINs, due to the presence of these cavities.

Table 5.1:

	Affinity constant / K_a	**Total no. of sites / s**
NINs	296 10^5	1.14 10^{-5} mol g^{-1}
DINs	7473 10^5	1.27 10^{-5} mol g^{-1}

5.2.2 *Investigation of interactions between DINs and Diclofenac analogues in solution*

For this section, the stock solutions of Aceclofenac and PABA were in 50 mM Tris at pH 8, but added to 10 mM LiCl with DINs and NINs before experiments and then filtered using the syringe filter (as described in Section 5.3.1) before recording a spectrum. From the UV/Vis spectrum and calibration curve it is clear to see that there is little to no adsorption of Aceclofenac in the DINs (Figure 5.5). The peak height for Aceclofenac after being mixed with DINs and filtered is approximately the same as that of Aceclofenac on its own.

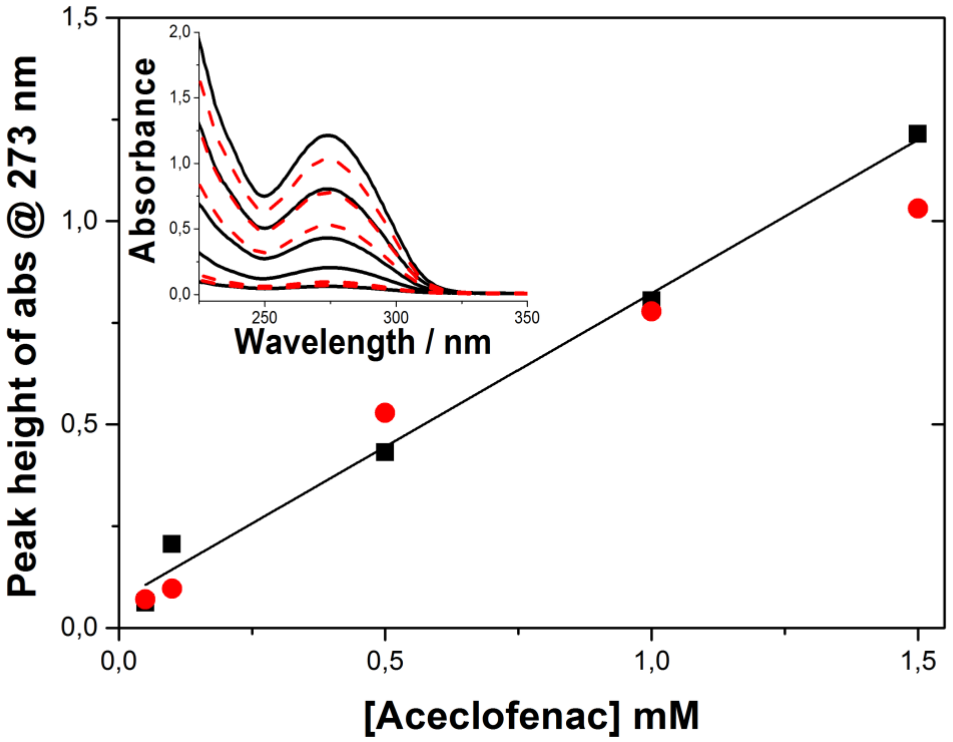

Figure 5.5: Calibration curve of peak heights in Absorbance for Aceclofenac (black squares) and with DINs (red circles), with black line representing linear fitting of Aceclofenac data. Inset: UV/Vis spectrum of 0.05 - 1.5 mM Aceclofenac (continuous black line) and with 0.1 g L^{-1} DINs (dashed red line) from which peak heights were obtained

Likewise for experiments with PABA, it is clearly apparent that there is no adsorption of PABA in the DINs. The peak height for PABA after being mixed with DINs and filtered is approximately the same as that of PABA on its own (Figure 5.6).

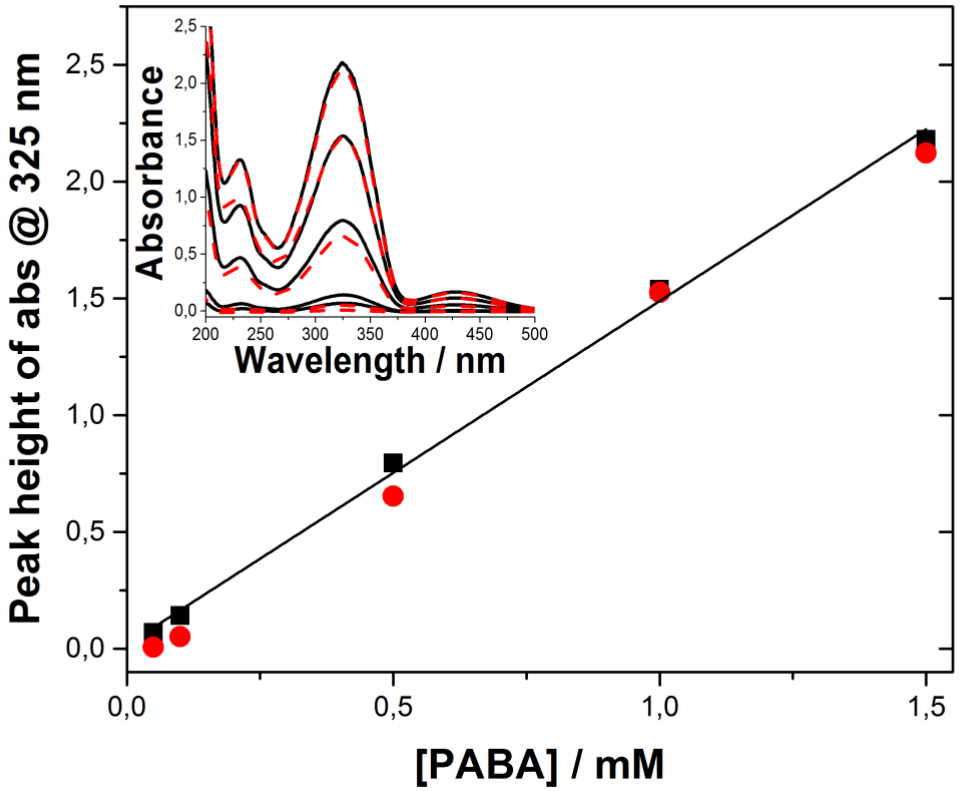

Figure 5.6: Calibration curve of peak heights in Absorbance for PABA (black squares) and with DINs (red circles), with black line representing linear fitting of PABA data. Inset: UV/Vis spectrum of 0.05 - 1.5 mM PABA (continuous black line) and with 0.1 g L^{-1} DINs (dashed red line) from which peak heights were obtained

Thus, based on Figure 5.7, where the results of the adsorption of all three drugs on DINs (Figure 5.3, 5.5 and 5.6) are plotted, one could conclude that the DINs are selective to Diclofenac. DINs absorb Diclofenac the most and only small amounts of Aceclofenac and PABA. However it is important to note that the parameters were not the same for each experiment. The Diclofenac results were obtained from solutions in 10 mM LiCl @ pH 6.8. Whereas the Aceclofenac and PABA stock solutions were in 50 mM Tris @ pH 8, with only µL volumes of this added to the 10 mM LiCl solutions for the UV/Vis experiments. The negative absorbance value that would have been obtained for 0.5 mM Aceclofenac due to the absorbance reading of Aceclofenac with DINs being larger than that of Aceclofenac alone (Figure 5.5) is omitted below and can be explained by experimental error.

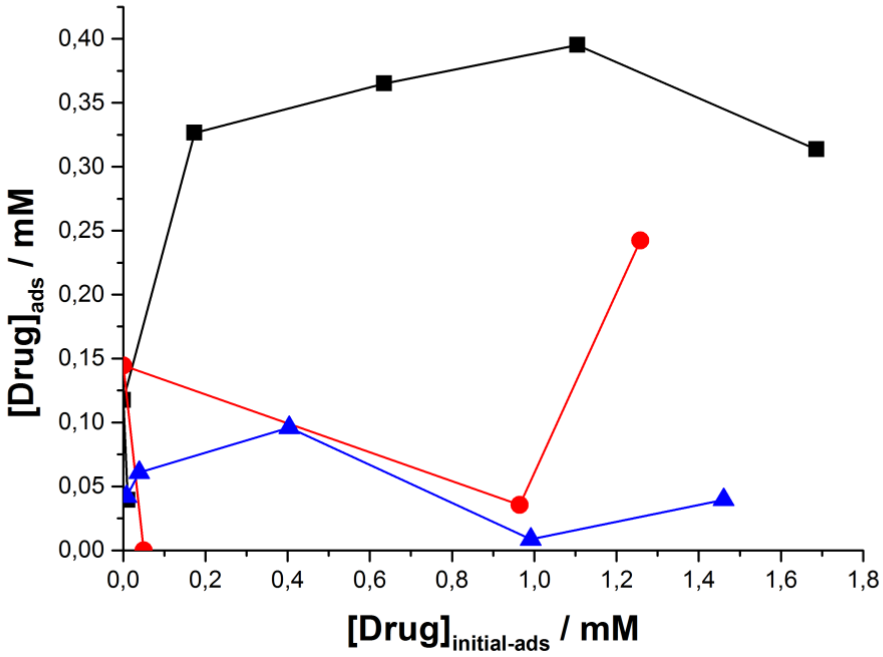

Figure 5.7: Comparison of adsorption of Diclofenac (black line), Aceclofenac (red line) and PABA (blue line) on 0.1 g L^{-1} DINs, from results obtained in Figures 5.3, 5.5 + 5.6, using procedure described on page 112

5.3 ***Chromatographic analysis of interactions between Diclofenac and DINs in solution***

The principle of high performance liquid chromatography (HPLC) is to separate and distinguish chemicals based on their interactions with the mobile phase (liquid) and stationary phase (solid), as they pass through the chromatography column. Some chemicals have a stronger affinity for the stationary phase than others and so take longer to pass through the column, resulting in their elution peak on the chromatogram appearing after a longer time than a chemical which has less interaction and thus elutes faster [190].

In this section, a commercially available column was used to measure the quantity of Diclofenac in the injection solution. The elution of Diclofenac Na alone, and Diclofenac Na that had been previously mixed with DINs and filtered using a syringe filter before injecting into the HPLC, was monitored through a Chromolith® RP-18e by Merck column [191,192]. This monolithic column was produced from a continuous piece of porous silica with macro and mesopores in the micro and nanometer range. Consequently, the high permeability and porosity of the silica skeleton, combined with columns internal diameter and short length of just 3 mm and 100 mm respectively, results in a low back pressure and thus allowing higher flow rate. The area of the elution peaks were calculated, retention times recorded and the results compared and also contrasted with UV/Vis results obtained in Section 5.2.

HPLC chromatograms were obtained for Diclofenac Na with and without DINs, which can be seen in Figure 5.9 and 5.8, respectively. The experimental details are described in Chapter 2, Section 2.3. As can be seen the peak position is not constant for all concentrations. Peak tailing is observed in both situations. In the absence of DINs it is prominent at high concentrations. In chromatograms where DINs were included in the solutions and then filtered before HPLC, peak fronting is visible in all. Fronting peaks can be due to the sample capacity of the analytical column being exceeded. Normally in HPLC the maximum concentration of sample injected is 1 mM, however in order to be able to compare HPLC results with results from UV/Vis experiments obtained in the previous section, larger concentrations and intensity values were recorded which may affect the accuracy of the experimental results.

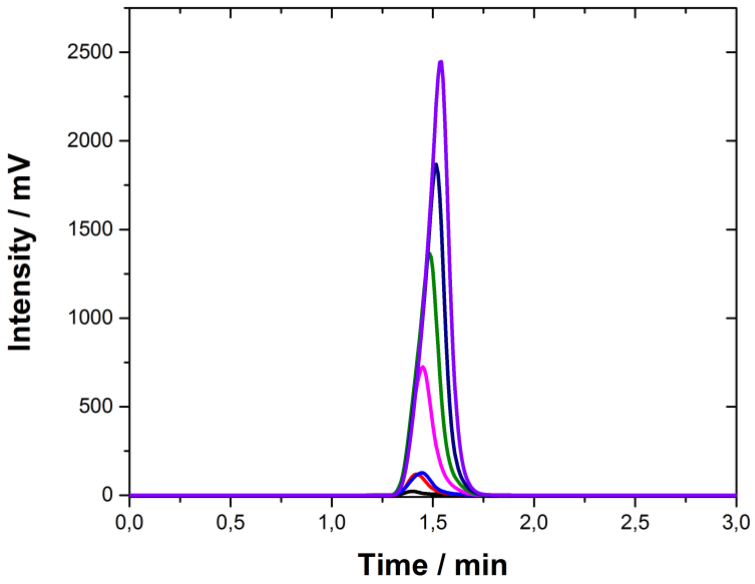

Figure 5.8: HPLC chromatogram of increasing concentrations of Diclofenac, from 0.01 – 2.0 mM, with a mobile phase composition of 0.65 ACN: 0.45 H_2O

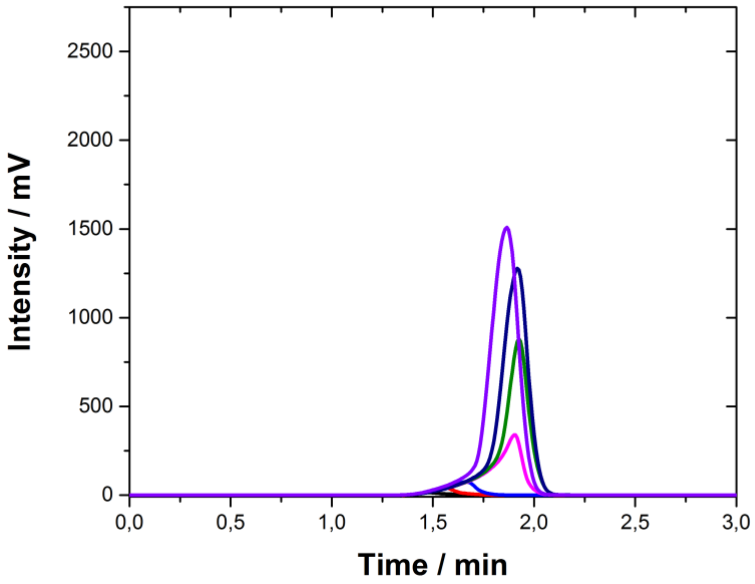

Figure 5.9: HPLC chromatogram of increasing concentrations of Diclofenac, from 0.01 – 2.0 mM, that had been mixed with 0.1 g L^{-1} DINs and filtered before injecting into the HPLC, with a mobile phase composition of 0.65 ACN: 0.45 H_2O

It can be seen by comparing the two graphs that the retention time of Diclofenac increases in the chromatograms obtained when Diclofenac was first mixed with DINs and filtered before injection, by ~0.4 minutes for each peak. This peak shift could be explained by the HPLC column not functioning properly. There were no DINs entering the HPLC as ICP spectroscopy analysis was carried out on the solutions after filtering and no silica was detected in the filtrate. Thus this cannot be to blame for the shift in retention time. A decrease in the peak area of Diclofenac which had been mixed with DINs and filtered before injecting into the HPLC was expected, as the Diclofenac which had interacted with the imprint cavities in DINs would be retained with the DINs on the filter paper, resulting in less free Diclofenac being injected into the HPLC. The peak area values for each concentration of Diclofenac before and after it had been mixed with DINs and then filtered, were obtained from Figure 5.8 + 5.9 respectively and then plotted in Figure 5.10. It shows that a quantity of Diclofenac was adsorbed on the DINs as the peak area values for free Diclofenac after it had been mixed with DINs and then filtered (red circles) are lower than those of Diclofenac alone (black squares). When this quantity of adsorbed Diclofenac was plotted in an adsorption isotherm (red line, Figure 5.11), the trend is quite difficult to interpret. An initial increase between 0.1 and 0.8 mM starts to plateau between 0.8 and 1.3 mM before increasing again until 1.6 mM.

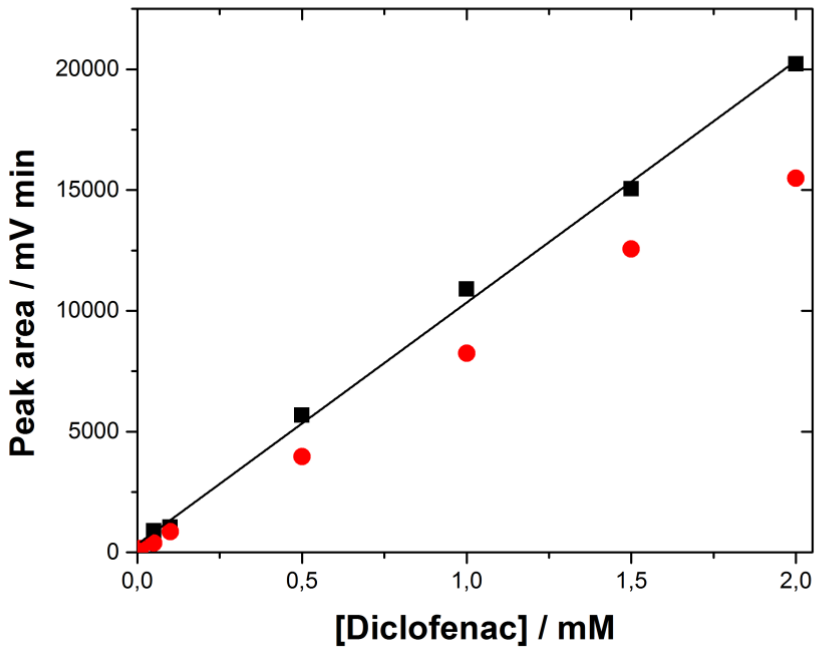

Figure 5.10: Calibration curve of 0.01 - 2 mM Diclofenac (black squares), with 0.1 g L^{-1} DINs (red circles). The black line represents the linear fitting of the Diclofenac data with no DINs.

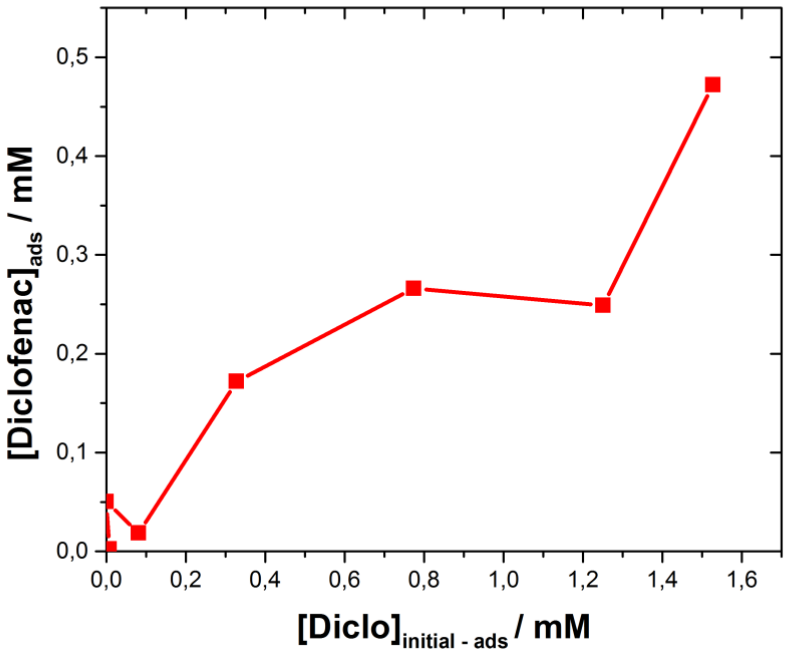

Figure 5.11: Adsorption isotherm showing quantity of Diclofenac adsorbed to DINs, based on the results from Figure 5.11

5.3.1 *Comparison of results for Diclofenac Na adsorption to DINs obtained with UV/Vis spectroscopy and HPLC*

Figure 5.12 combines the adsorption isotherms for Diclofenac from UV/Vis (Figure 5.7 black line) and HPLC (Figure 5.11) experiments on one graph. Both of these experiments used a stock solution of Diclofenac Na in 10 mM LiCl and the solutions of Diclofenac and DINs were filtered using a syringe filter before analysis. Firstly it can be seen that UV/Vis results give larger $[\text{Diclofenac Na}]_{ads}$ values than HPLC. This could be explained by the fact that ACN was used, along with H_2O, in the mobile phase of the HPLC, which may have affected the pKa of the solution and thus the solvation of Diclofenac. There may have been less anionic Diclofenac in solution and so less interacting electrostatically with the imprint cavity, resulting in less being adsorbed. The trend of initial increase followed by plateau between 0.1 + 1.2 mM $[\text{Diclofenac Na}]_{initial\text{-}ads}$ is common between both and so HPLC results confirm the tendency of the UV/Vis results. Thus, Diclofenac interacts with the imprint cavities in DINs.

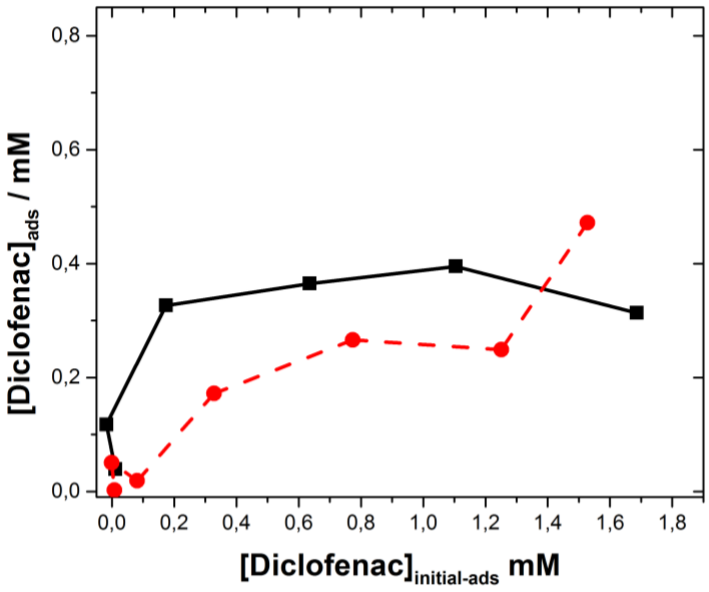

Figure 5.12: Adsorption isotherm for 0.01 – 2 mM Diclofenac with 0.1 g L^{-1} DINs, results from UV/Vis (continuous black line) and HPLC (dashed red line)

5.4 ***Investigation of the selectivity of DINs in solutions of Diclofenac and Diclofenac's analogues***

In order to further investigate the specificity of the DINs, HPLC and Capillary electrophoresis techniques were used. However to accurately compare interactions between DINs, Diclofenac and Diclofenac's analogues, a common solvent should have been used, but as described in Appendix 2, problems with solubility of the drugs meant that differing solvents were used.

5.4.1 *HPLC experiments with Diclofenac and its analogues, using columns loaded with NINs and DINs*

For HPLC experiments, empty columns were filled with NINs and DINs, as opposed to the commercially available column used in the previous section. Diclofenac free acid as opposed to Diclofenac Na was used and the solutions of all the drugs were in EtOH. The aim was to record the retention time and measure the peak area of each drug on its chromatograph, before and after mixing with DINs. The difference would allow the quantity of drug adsorbed to the DINs to be obtained. The peak area should be lower for Diclofenac FA using the column with DINs, as the Diclofenac should interact with the imprint cavities of the DINs. For all other combinations there should be no interactions and so the peak area and retention times for the drugs should be unchanged.

Table 5.2: Retention times and peak areas calculated from HPLC chromatograms

		Retention time / mins	Peak area / mV min
Diclofenac free acid	NINs	3.485	6,932,883
	DINs	3.715	7,072,067
Aceclofenac	NINs	3.465	1,733,410
	DINs	3.91	1,714,416
PABA	NINs	3.435	7,257,334
	DINs	3.47	10,557,807
Mixture	NINs	3.455	9,154,903.5
	DINs	3.53	10,085,770.5

However, as can be seen in the above table, the retention time for each solution only slightly increases when using the column filled with DINs as opposed to that with NINs, and the peak area remains relatively constant for all except PABA, which could be explained by an interaction of the drug molecules with DINs and not with NINs. However, variations in the column packing between NINs and DINs mean these results are not entirely accurate. A more detailed synopsis of the results obtained using HPLC with the NINs and DINs filled columns is described in Appendix 3.

5.4.2 *Capillary electrophoresis experiments with NINs and DINs as pseudo-stationary phases*

The aim of CE was to compare the interaction of Diclofenac and its analogues with DINs. NINs and DINs were used as pseudo-stationary phases and added to the BGE solution which was run through the capillary. It was assumed the speed of NINs and DINs through the capillary would be much slower than Diclofenac, due to their charge and size, and thus adsorbed Diclofenac would have a different elution time to that of free Diclofenac. The migration times of the drugs passing through the capillary were recorded and it was expected that they would remain largely unchanged in the presence of NINs and DINs, except for Diclofenac with DINs, as the interaction of Diclofenac with the imprint cavities in DINs should decrease the quantity of free Diclofenac eluting and another peak for Diclofenac which was adsorbed to DINs would elute at a different time.

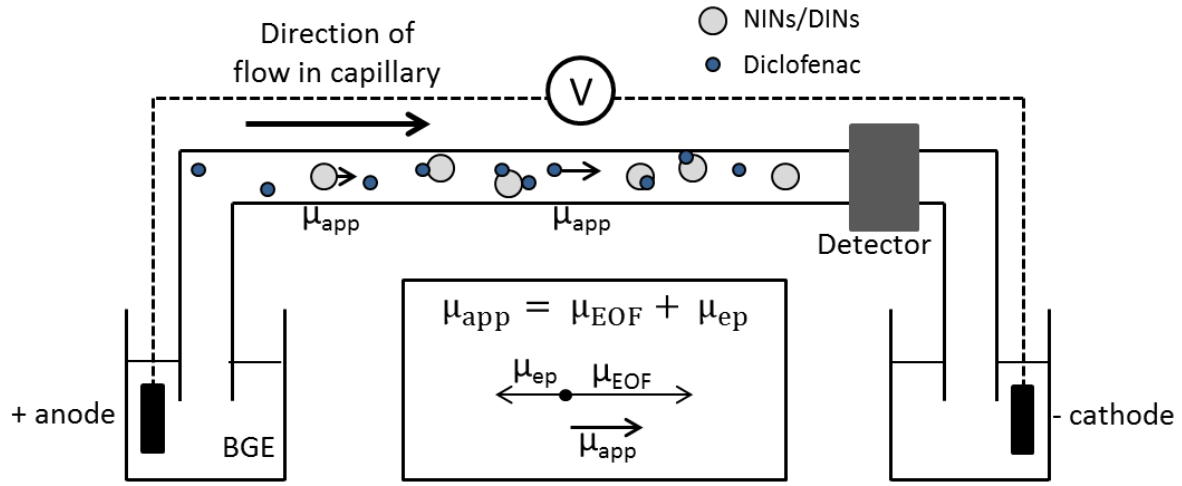

Figure 5.13: Schematic of Capillary electrophoresis set up

As with the HPLC results in Section 5.4.1, the more detailed description of the investigation of DINs specificity using CE is outlined in Appendix 3, but the following chromatogram and table sums up the results obtained during CE experiments. Figure 5.14 shows the peak for DMSO at 3.05 minutes and Diclofenac FA at 4.1 minutes in the absence of silica nanoparticles (black line). The peak for Diclofenac very slightly shifts when DINs are in the capillary but the table shows the electrophoretic mobility (μ_{ep}) of Diclofenac does not vary significantly when NINs and DINs are present in the BGE.

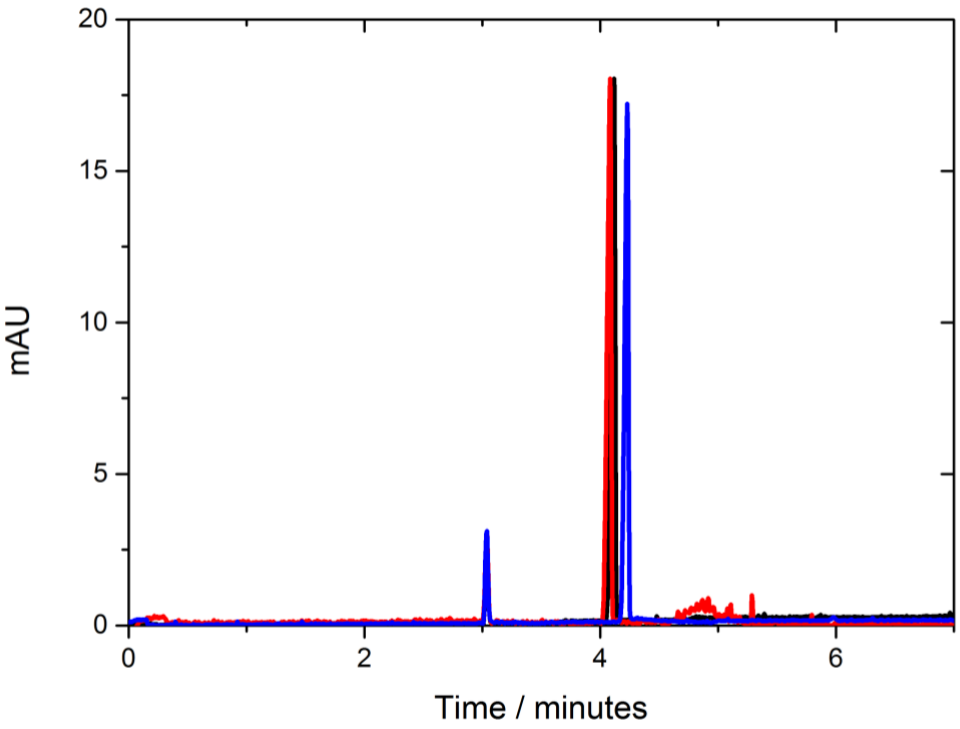

Figure 5.14: Electropherogram of 0.1 mM Diclofenac FA (black line), with 0.5 g L^{-1} NINs (red line) and 0.5 g L^{-1} DINs (blue line), all in 10 mM Borate buffer with 0.005% DMSO @ pH 9. ΔV = 20 kV, inj. 5 s

The μ_{ep} of Diclofenac is calculated from the apparent mobility (μ_{app}) of Diclofenac minus the electroosmostic mobility (μ_{EOF}) of DMSO (also referred to as $\mu_{app\ (DMSO)}$).

$$\mu_{ep} = \mu_{app} - \mu_{app\ (DMSO)}$$

The apparent mobility depends on the migration time (t_m) of the drug molecules, amongst other experimental parameters (separation voltage ΔV, total length of capillary L, and effective length l) and is calculated using the following equation:

$$\mu_{app} = \frac{L.l}{\Delta V.t_m}$$

This is discussed in greater detail in Appendix 3.

Table 5.3: Calculation of μ_{EOF}, μ_{app} and μ_{ep} values based on Figure 5.14 (units: $m^2\ V^{-1}\ s^{-1}$)

	μ_{EOF} x 10^{-8}	μ_{app} x 10^{-8}	μ_{ep} x 10^{-8}
Diclo	8.2	6.0	-2.2
Diclo + NINs	8.2	6.1	-2.1
Diclo + DINs	8.2	5.9	-2.3

5.5 ***Electrochemical study of interactions between NINs/DINs and Diclofenac in solution at the LLI***

The same procedure for electrochemistry experiments at the ITIES, as outlined in Chapter 2, Section 2.2 with the silica nanoparticles and analytes, was repeated here but with the molecularly imprinted silica and drug molecules. The cyclic voltammograms obtained for experiments with increasing quantities of Diclofenac Na in the presence of non-imprinted nanoparticles and Diclofenac-imprinted nanoparticles at the LLI are shown in Figure 5.15 and 5.16 respectively. A clear comparison can be made between these two cyclic voltammograms and the following conclusion drawn. In the presence of non-imprinted silica, Diclofenac crosses the liquid-liquid interface unaffected by their presence. This is demonstrated by the peak obtained at -0.1 V in Figure 5.15, whose height (in µA) increases with increasing concentration of Diclofenac. However in Figure 5.16, Diclofenac-imprinted silica, which has been washed and extracted, is present. This silica contains the 'Diclofenac-imprinted cavities'. It can be seen from the graph that even at high Diclofenac concentrations, no free Diclofenac in solution crosses the liquid-liquid interface, i.e. the peak at -0.1 V is absent. No peak implies no ion transfer. The Diclofenac in solution has been adsorbed into the imprint cavities and is no longer free to cross the liquid-liquid interface. Thus the Diclofenac imprinted cavities on the imprinted silica can re-adsorb diclofenac in solution.

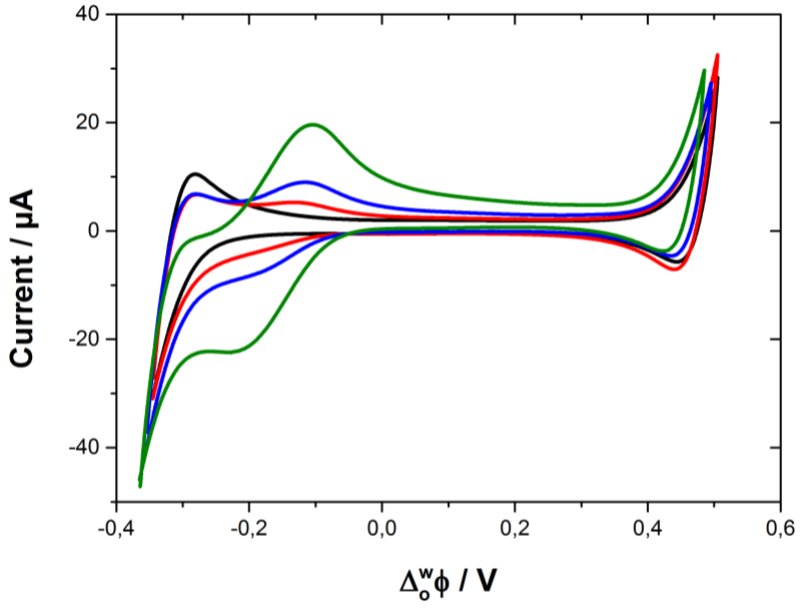

Figure 5.15: Cyclic voltammogram of 0.5 g L^{-1} NINs with 0 mM (black line), 0.1 mM (red line), 0.2 mM (blue line) and 0.5 mM (green line) Diclofenac at the liquid-liquid interface. Electrochemical cell 1, ν = 5 mVs^{-1}

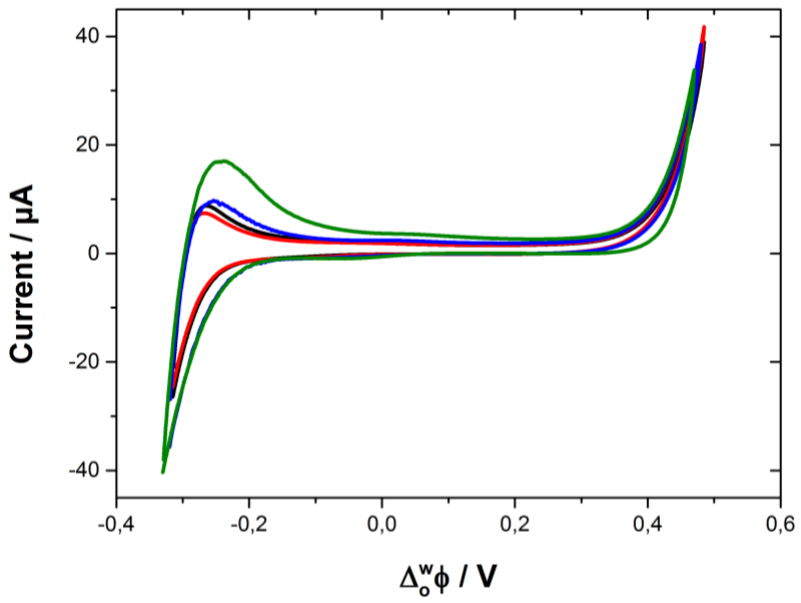

Figure 5.16: Cyclic voltammogram of 0.5 g L^{-1} DINs with 0 mM (black line), 0.1 mM (red line), 0.2 mM (blue line) and 0.5 mM (green line) Diclofenac at the liquid-liquid interface. Electrochemical cell 1, ν = 5 mVs^{-1}

Although this technique gave very clear results demonstrating the adsorption of Diclofenac into the imprint cavities, unfortunately it was not suitable for experiments with Diclofenac's analogues. Aceclofenac and PABA are very poorly soluble in aqueous solutions (refer to Appendix 2), thus electrochemistry at the LLI could not be used to compare the selectivity of the imprinted silica with the three drugs.

5.6 ***Conclusion***

IR and UV/Vis spectroscopy both proved the existence of Diclofenac-imprinted cavities in the DINs after synthesis. IR spectrums showed peaks for Diclofenac in the non-extracted DINs, which disappear after extraction. These peaks were not seen in UV/Vis spectrums, however Diclofenac free in solution was visible at 275 nm. When Diclofenac was mixed with DINs, its peak height decreased, indicating that Diclofenac was adsorbed into the imprint cavities. UV/Vis spectrums showed that when Diclofenac is adsorbed into the imprint cavities in DINs, it is no longer visible by UV/Vis spectroscopy. The results allowed the calculation of the affinity constant for Diclofenac to NINs (296 10^5) and DINs (7473 10^5), with the much larger value for DINs clearly indicating that the presence of the imprint cavities in DINs results in a greater attraction of Diclofenac than in just NINs. Furthermore the interaction of Diclofenac's analogues with DINs was analysed using UV/Vis spectroscopy and results compared to that with Diclofenac and from the graph it was clear to see Aceclofenac and PABA have little or no interaction with DINs, compared to the large adsorbance recorded with Diclofenac.

The adsorbance of Diclofenac to DINs was also recorded using HPLC with a commercially available column and a significant value, comparable to that obtained with UV/Vis spectroscopy was recorded. Thus, HPLC confirmed the tendency of the UV/Vis results.

Unfortunately, the columns that were filled with NINs and DINs did not provide clear results when Diclofenac and its analogues were eluted through it. Consequently, capillary electrophoresis was used to try characterise the interaction between Diclofenac and DINs. The capillary electrophoresis technique allowed electrophoretic mobility values to be calculated for Diclofenac in the presence and absence of NINs and DINs but no clear difference was recorded. However, CE has the ability to potentially be used to determine the selectivity of DINs, if the parameters can be optimised to work with silica nanoparticles. This has been studied before and will be discussed in Chapter 7 Future perspectives.

Electrochemical results at the LLI, showed the disappearance of the peak for Diclofenac in the presence of silica nanoparticles at ~0.1 V, confirmed the DINs readsorbed Diclofenac in aqueous solution and thus prevented Diclofenac from crossing the LLI. Consequently, this evidence proved that the DINs contained imprinted cavities that can interact with Diclofenac in solution.

6. GENERAL CONCLUSIONS

This research has studied silica nanoparticles at the liquid-liquid interface and investigated their effect on ion transfer across the interface.

Electrochemical results proved the adsorbance of dense and mesoporous silica nanoparticles to the LLI, confirmed by the increased capacitance values and shift of the potential of zero charge to higher values obtained on addition of the silica to the system.

The presence of DSNs at the interface resulted in less transfer of the cation, TEA^+, across the LLI, due to an interaction between the negatively charged silica and the cation. Increasing the ionic strength of the aqueous solution increases the quantity of silica transferred, as the larger amount of Li^+ in solution successfully competed with TEA^+ for interaction with DSNs. As a result, less TEA^+ interacts with the DSNs and thus more is free to transfer across the LLI. Similarly at low pH the same effect is observed but is explained by the abundance of H^+ ions interacting with DSNs, leaving TEA^+ free to cross the interface. Another explanation was obtained from the zeta potential experiments, which shows silica is less strongly negatively charged at low pH and so does not strongly interact with the cation.

The interaction of DSNs and MSNs with the model cation Methylene blue was studied by UV/Vis spectroscopy and absorption constants calculated for both. The value obtained for MB^+ adsorption to DSNs was calculated as $1.66\ 10^5$, much larger than that for MSNs, which equaled $3.68\ 10^3$. From these the ΔG_{ads} values for each could be determined and found to be -20 and -29.3 kJ mol^{-1} respectively. Both demonstrate that the adsorption of MB^+ to DSNs is stronger than that to MSNs. Kinetics experiments with stopped-flow also showed that the adsorption of MB^+ to DSNs occurred extremely quickly, within 3 ms, whereas it had almost not begun with MSNs. The observed rate constants (k_{obs}) for adsorption of MB^+ to MSNs were calculated and the values plotted. The shape of the graph suggested two processed were occurring – first a constant rate of adsorption into the pores, secondly an increasing rate with increasing concentration of MSNs which related to surface adsorption.

The thermodynamics of the adsorption of MB^+ to DSNs and MSNs were studied electrochemically. Thermodynamic stabilisation of MB^+ following adsorption to the silica nanoparticles resulted in more energy being needed for MB^+ to cross the LLI. A difference of 5.6 kJ mol^{-1} between the Gibbs free energy of ion association for MB^+ adsorption on DSNs and MSNs suggested the interactions between them were not the same. Taking into consideration the stronger affinity of MB^+ for DSNs than MSNs, more energy was needed to desorb MB^+ from DSNs to allow it to cross the LLI.

By combining the affinity of MB^+ to silica nanoparticles and the adsorption of these at the LLI, it was possible to accumulate MB^+ ions at the interface, thereby increasing the sensitivity of electrochemical detection of MB^+. The development of a selective extraction procedure was achieved by harnessing the strong affinity of DSNs for cation adsorption, considering that anions have no affinity for silica nanoparticles. This interaction was favoured over the ion pairing interactions between a cation and anion in solution and thus, following filtration of the mixture with DSNs, the cation was successfully separated from the anion in solution.

Diclofenac-imprinted silica nanoparticles were synthesized with the aim of further improving selectivity at the LLI. The presence of imprint cavities was confirmed by IR and UV/Vis spectroscopy. The affinity of Diclofenac for DINs was measured by UV/Vis spectroscopy ($7473\ 10^5$) and compared to that of the NINs ($296\ 10^5$). The much larger value for DINs clearly indicates that the presence of the imprint cavities in DINs results in a greater attraction of Diclofenac than in just NINs. Furthermore the interaction of Diclofenac's analogues with DINs was also analysed using UV/Vis spectroscopy and results compared to that with Diclofenac and from the graph it was clear to see Aceclofenac and PABA have little or no interaction with DINs, compared to the large adsorbance recorded with Diclofenac. Attempts were made to study the selectivity of the DINs using HPLC and CE, however further research needs to be undertaken to properly identify the optimum experimental parameters. Electrochemical results showed Diclofenac could be readsorbed into the imprint cavities after extraction, further confirming the existence of Diclofenac-imprinted cavities in DINs.

To sum, silica nanoparticles were successfully studied at the LLI and their influence on ion transfer investigated. Imprinted silica nanoparticles were synthesised and their affinity for the imprint molecule obtained.

7. FUTURE PERSPECTIVES

One of the main future perspectives for this research would be to develop a technique that allows the selectivity of the imprinted nanoparticles to be studied in detail. Furthermore, improving the sensitivity and selectivity of the molecular imprinting technique, with a focus on synthesizing mesoporous imprinted silica nanoparticles. Finally, gaining a greater knowledge of the processes occurring at the liquid-liquid interface during ion transfer in the presence of silica, by using spectroscopic techniques.

As previously touched on at the end of Chapter 5, Capillary electrophoresis has the potential to be used to examine the selectivity of DINs in a mixture of Diclofenac and its analogues, if the optimum parameters are achieved. The technique clearly distinguished the individual components of the mixture and showed small groupings of peaks representing the silica nanoparticles. Several groups have published papers with CE experiments involving silica nanoparticles.

Adelantado et al. used capillary zone electrophoresis coupled to an evaporative light scattering detector, to identify and separate silica nanoparticles based on their size [58]. They used an uncoated fused silica capillary, with internal diameter 50 µm and length 100 cm. Their mobile phase consisted of 3 mM ammonium acetate buffer with 1% methanol at pH 6.9, separation voltage used was 27 kV and injection time 10 s. Silica nanoparticles of 20, 50 and 100 nm were in a 100 g L^{-1} aqueous salt solution at 2 ng nL^{-1} for each size. The electropherogram obtained shows three distinct peaks representing each size of nanoparticle.

Similarly Vanifatova et al. showed that the electrophoretic mobility of silica nanospheres was effected by the pH and concentration of the mobile phase [193]. They found that at a phosphate buffer concentration of 2.5 mM, the silica nanoparticle electrophoretic mobilities increase with pH. At pH greater than 9 and buffer concentration between 2.5 – 5 mM, only small differences in particle electrophoretic mobilities are observed. A decrease in electrophoretic mobility is observed in acidic buffer solutions of increasing concentration, whereas an increase is observed in alkaline buffer solutions.

Wang et al. investigated the impact of silica nanoparticles on the resolution and selectivity of the separation of seven quinolones [194]. Their buffer solution was 12 mM disodium tetraborate-phosphate at pH 9.08, separation voltage 10 kV and injection time 7 s. The amount of silica nanoparticles they added to the buffer solution ranged from 3.6 – 5.7 µg mL^{-1}.

They did not detect any peak for the silica nanoparticles on their electropherograms, only the seven peaks representing the quinolones. They concluded that too low of a concentration did not greatly improve the separation but a higher concentration decreased the electroosmotic flow, resulting in good resolution. They also found that varying the separation voltage had little impact on the electrophoretic behaviour of the silica nanoparticles but pH changes altered the surface properties of the silica, thus effecting their interaction with the quinolones and improving separation.

Thus in my case I would need to use larger concentrations of silica nanoparticles during the CE experiments, and also the synthesis would need to generate nanoparticles with a specific monodisperse size that do not aggregate, to avoid the cluster of small peaks. Varying the pH and ionic concentration of the buffer to find the optimum parameters is also necessary.

Keeping with the topic of molecularly imprinted silica, another future perspective would be to synthesise mesoporous molecularly imprinted silica nanoparticles. A brief introduction to this was given in Chapter 1, Section 1.3.4. Combining mesoporosity and molecular imprinting in the same silica nanoparticles gives the advantage of high pore volume with nanosized pore wall thickness, which reduces the diffusion distance allowing better accessibility to the target molecule and faster kinetic binding [139,140]. Adapting my DINs synthesis procedure to include a surfactant which will incorporate the porosity into the silica nanoparticles is a challenge. If I were to use CTACl, which was used in the synthesis of MSNs, it has the potential to react with APTES (which was used to give the surface functionality in the imprinted silica so the imprint molecule will be attracted to it), without first combining with TEOS to create the mesoporosity in the nanoparticle.

Furthermore modifying the molecularly imprinted mesoporous silica nanoparticles to incorporate the imprint molecule in, and not on, the walls of the mesoporous particle is quite challenging, as the organosilane compounds used during synthesis are generally too large to be incorporated into the pore walls, preferring to occupy the surface sites of the particles instead [116,139]. However Chang and Ozin's groups have had success and their methods are outlined in the following paragraphs.

Chang's group reported their synthesis of diethylstilbestrol (DES) imprinted MCM-41 type mesoporous silica particles in 2010 [140]. They first synthesized a triethoxysilane-template complex and then mixed this with a structure directing surfactant and an alkoxysilane cross-linker. X-ray diffraction (XRD) proved that most of the template molecules were embedded in the silica matrix, between the pores.

In 2011, Ozin's group incorporated bisphenol A (BPA), as the imprint molecule, into SBA-15 type mesoporous silica [139]. This type of silica possesses larger pore diameters, thicker walls and better hydrothermal stability compared with MCM-41 type silica. They also synthesised an alkoxysilane-template complex, and combined it with an alkoxysilane cross-linker and Pluronic P123 surfactant. By examining the pore volume, diameter and wall thickness by gas adorption and small-angle X-ray scattering, they also concluded that their imprint cavities were more than likely embedded in the pore walls. The advantage of wall imprinting, as opposed to surface imprinting, is that the imprinted particles have a high degree of size and shape selectivity, similar to that of the bulk imprinted silica mentioned previously, but also have rapid kinetic binding profiles as a result of the templated mesopores. Thus the benefits of these imprinted mesoporous silica particles have allowed them to find many applications, along with those mentioned earlier. The field of molecular imprinting in mesoporous silica, although still a relatively new concept, has advanced in recent years, with research and knowledge of this topic expanding and continuing to do so, thus a positive future lies ahead for this interesting topic.

Finally, a third future perspective for this research involves moving back to the liquid-liquid interface, in order to further investigate the processes occurring with the silica nanoparticles when they adsorb and desorb ions in solution. This could be studied using a technique such as raman spectroscopy [195,196]. This non-destructive, light scattering technique involves a photon of light interacting with a sample and producing scattered radiation with different wavelengths. The incident radiation can be reflected, adsorbed or scattered upon interaction with the sample. The change in the wavelength of the scattered photon provides chemical identification, as well as structural information. Furthermore, there are additional properties that can be derived from raman spectrums. The peak intensity provides information on the quantity of a specified compound. A peak shift denotes stress and strain states. The degree of crystallinity can be determined from the peak width, with crystal symmetry and orientation information obtained from the polarization state. In general no sample prep is required and measurements can be taken in situ, in vitro and in vivo. Raman analysis can be performed on

gaseous, liquid, powder and solid samples, however, pure metals are raman-inactive. Water is a weak raman scatterer and so does not greatly interfere with the technique.

However raman scattering itself is also weak, generating only few raman scattered photons, and so in order to improve the sensitivity, new processes such as active substrates and surface enhanced raman spectroscopy (SERS) have been developed. SERS increases the raman intensity thereby allowing single molecule detection [196,197]. The principle of this technique is that raman scattering can be enhanced when noble metal nanoparticles are in close proximity to the measurement position. The raman excitation laser generates surface plasmons on the surface of the metal which interact with the analyte and enhance the raman emission. Enhancement occurs with molecules adsorbed on metal surfaces that have nanoscale roughness. Examples of metals that have been used to generate structures that molecules can adsorb on include silver, gold, aluminum, copper, palladium and platinum.

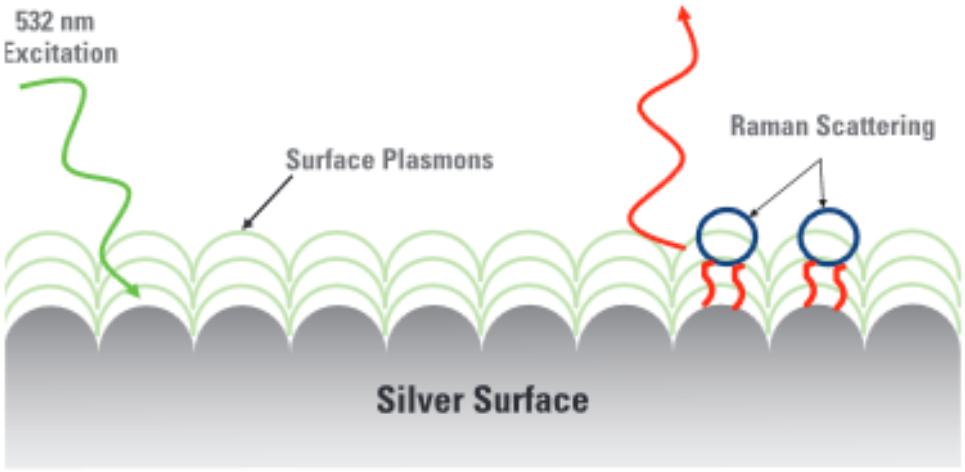

Figure 7.4: Principle of SERS

SERS has allowed the range of applications of raman spectroscopy to extend to part per million level detection of a contaminant in water. Furthermore it can be used in the field of forensics to analyse trace evidence from a crime scene, in food safety to examine bacteria on food and in medical diagnostics to investigate blood glucose samples. Moving beyond mechanisms for detection, SERS has also been developed for use in conjunction with electrochemistry, as SERS substrates and electrochemical electrodes are usually metal surfaces, thus allowing the combination of these techniques to study electrochemically active molecules spectroscopically.

Another recent development in this field has been the invention of Shell-Isolated Nanoparticles (NPs)-Enhanced Raman Spectroscopy (SHINERS) by Tian and his group in Xiamen University. SHINERS overcome the limiting aspect of SERS, which is, that only a few metals with nanostructured surfaces provide a large SERS effect. In SHINERS, a thin silica shell coats plasmonic Au nanoparticles which prevent them from interacting with analytical targets or the chemical environment, but do not affect the enhanced electromagnetic field generated at the core surface [198,199].

Poltorak et al. have used raman spectroscopy at the polarised liquid-liquid interface to study interfacial processes.[200] They coupled electrochemistry at the LLI with in-situ confocal raman spectroscopy to follow the electrochemically assisted generation of mesoporous silica deposits. This technique would not only be useful in studying the adsorption of ions into the cavities of imprinted silica at the LLI, but if this method was used in my setup when the mesoporous silica nanoparticles have assembled at the LLI and they interact with ions in solution, to be able to follow the adsorption and desorption at that level would provide a much greater understanding of the processes occurring and the reasoning behind the changes in the thermodynamics, which were studied in Chapters 3 + 4.

To conclude, a lot of research has still to be done to get a greater understanding in the area of molecularly imprinted silica and liquid-liquid electrochemistry. There is no shortage in the vast amount of different avenues that can be studied.

BIBLIOGRAPHY:

[1] P. Vanýsek, L.B. Ramírez, Interface between two immiscible liquid electrolytes: A review, J. Chil. Chem. Soc. 53 (2008) 1455–1463. doi:10.4067/S0717-97072008000200002.

[2] Z. Samec, J. Langmaier, T. Kakiuchi, Charge-transfer processes at the interface between hydrophobic ionic liquid and water, Pure Appl. Chem. 81 (2009) 1473–1488. doi:10.1351/PAC-CON-08-08-36.

[3] Z. Samec, Electrochemistry at the interface between two immiscible electrolyte solutions (IUPAC Technical Report), Pure Appl. Chem. 76 (2004) 2147–2180. doi:10.1351/pac200476122147.

[4] Z. Samec, Dynamic electrochemistry at the interface between two immiscible electrolytes, Electrochim. Acta. 84 (2012) 21–28. doi:10.1016/j.electacta.2012.03.118.

[5] W. Nernst, Ueber die Potentialdifferenz verdünnter Lösungen, Ann. Der Phys. Und Chemie. 281 (1892) 360–369. doi:10.1002/andp.18922810212.

[6] E.J.W. Verwey, K.F. Niessen, XL. The electrical double layer at the interface of two liquids, London, Edinburgh, Dublin Philos. Mag. J. Sci. 28 (1939) 435–446. doi:10.1080/14786443908521199.

[7] M. Gouy, Sur la constitution de la charge électrique à la surface d'un électrolyte, J. Phys. Théorique Appliquée. 9 (1910) 457–468. doi:10.1051/jphystap:019100090045700.

[8] D.L. Chapman, A contribution to the theory of electrocapillarity, Philos. Mag. Ser. 6. 25 (1913) 475–481. doi:10.1080/14786440408634187.

[9] C. Gavach, P. Seta, B. D'epenoux, The double layer and ion adsorption at the interface between two non miscible solutions, J. Electroanal. Chem. Interfacial Electrochem. 83 (1977) 225–235. doi:10.1016/S0022-0728(77)80168-X.

[10] H.H. Girault, D.J. Schiffrin, Thermodynamic surface excess of water and ionic solvation at the interface between immiscible liquids, J. Electroanal. Chem. Interfacial Electrochem. 150 (1983) 43–49. doi:10.1016/S0022-0728(83)80188-0.

[11] H.H.J. Girault, D.J. Schiffrin, Thermodynamics of a polarised interface between two immiscible electrolyte solutions, J. Electroanal. Chem. Interfacial Electrochem. 170 (1984) 127–141. doi:10.1016/0022-0728(84)80041-8.

[12] H. Deng, Oxygen Reduction at Soft Interfaces, PhD Thesis, Ecole Polytechnique Fédérale de Lausanne, 2014.

[13] L. Poltorak, Electrochemical modification of the liquid-liquid interface with mesoporous silica, PhD Thesis, Université de Lorraine, 2015.

[14] W. Nernst, E.H. Riesenfeld, Ueber elektrolytische Erscheinungen an der Grenzfläche zweier Lösungsmittel, Ann. Phys. 313 (1902) 600–608. doi:10.1002/andp.19023130707.

[15] G. Herzog, Recent developments in electrochemistry at the interface between two immiscible electrolyte solutions for ion sensing, Analyst. 140 (2015) 3888–3896. doi:10.1039/C5AN00601E.

[16] G. Herzog, V. Beni, Stripping voltammetry at micro-interface arrays: a review., Anal. Chim. Acta. 769 (2013) 10–21. doi:10.1016/j.aca.2012.12.031.

[17] F. Reymond, D. Fermín, H.J. Lee, H.H. Girault, Electrochemistry at liquid/liquid interfaces: methodology and potential applications, Electrochim. Acta. 45 (2000) 2647–2662. doi:10.1016/S0013-4686(00)00343-1.

[18] L. Poltorak, E.J.R. Sudhölter, L.C.P.M. de Smet, Effect of charge of quaternary ammonium cations on lipophilicity and electroanalytical parameters: Task for ion transfer voltammetry, J. Electroanal. Chem. 796 (2017) 66–74. doi:10.1016/J.JELECHEM.2017.04.051.

[19] S. Amemiya, Voltammetric Ion Selectivity of Thin Ionophore-Based Polymeric Membranes: Kinetic Effect of Ion Hydrophilicity., Anal. Chem. 88 (2016) 8893–901. doi:10.1021/acs.analchem.6b02551.

[20] F. Reymond, P.-A. Carrupt, H.H. Girault, Facilitated ion transfer reactions across oil|water interfaces. Part I. Algebraic development and calculation of cyclic voltammetry experiments for successive complex formation, J. Electroanal. Chem. 449 (1998) 49–65. doi:10.1016/S0022-0728(97)00430-0.

[21] P.J. Greenawalt, M.B. Garada, S. Amemiya, Voltammetric Characterization of Ion–Ionophore Complexation Using Thin Polymeric Membranes: Asymmetric Thin-Layer Responses, Anal. Chem. 87 (2015) 8564–8572. doi:10.1021/acs.analchem.5b02355.

[22] J. Koryta, Electrochemical polarization phenomena at the interface of two immiscible electrolyte solutions, Electrochim. Acta. 24 (1979) 293–300. doi:10.1016/0013-4686(79)85048-3.

[23] Y. Shao, M.D. Osborne, H.H. Girault, Assisted ion transfer at micro-ITIES supported at the tip of micropipettes, J. Electroanal. Chem. Interfacial Electrochem. 318 (1991) 101–109. doi:10.1016/0022-0728(91)85297-3.

[24] D. Homolka, H. Wendt, Transfer of Multicomplexed Ions Across the Interface Between two Immiscible Electrolyte Solutions I; Fe(II, III), Ni(II) and Zn(II) Ions Complexed by Bidentate Nitrogen Bases, Berichte Der Bunsengesellschaft Für Phys. Chemie. 89 (1985) 1075–1082. doi:10.1002/bbpc.19850891012.

[25] G. Lagger, L. Tomaszewski, M.D. Osborne, B.J. Seddon, H.H. Girault, Electrochemical extraction of heavy metal ions assisted by cyclic thioether ligands, J. Electroanal. Chem. 451 (1998) 29–37. doi:10.1016/S0022-0728(97)00389-6.

[26] Z. Ding, B.M. Quinn, A.J. Bard, Kinetics of Heterogeneous Electron Transfer at Liquid/Liquid Interfaces As Studied by SECM, J. Phys. Chem. B. 105 (2001) 6367–6374. doi:10.1021/jp0100598.

[27] A.J. Bard, C.G. Zoski, Electroanalytical chemistry: A series of Advances Volume 23, CRC Press, Boca Raton, FL, 2010.

[28] S. Liu, Q. Li, Y. Shao, Electrochemistry at micro- and nanoscopic liquid/liquid interfaces, Chem. Soc. Rev. 40 (2011) 2236–2253. doi:10.1039/c0cs00168f.

[29] Y. Liu, J. Strutwolf, D.W.M. Arrigan, Ion-Transfer Voltammetric Behavior of Propranolol at Nanoscale Liquid–Liquid Interface Arrays, Anal. Chem. 87 (2015) 4487–4494. doi:10.1021/acs.analchem.5b00461.

[30] R. Matsui, T. Sakaki, T. Osakai, Amperometric Determination of Creatinine with a Dialysis Membrane-Covered Nitrobenzene/Water Interface for Urine Analysis, Electroanalysis. 24 (2012) 2325–2331. doi:10.1002/elan.201200497.

[31] L. Poltorak, A. Gamero-Quijano, G. Herzog, A. Walcarius, Decorating soft electrified interfaces: From molecular assemblies to nano-objects, Appl. Mater. Today. 9 (2017) 533–550. doi:10.1016/j.apmt.2017.10.001.

[32] E. Smirnov, M.D. Scanlon, D. Momotenko, H. Vrubel, M.A. Méndez, P.-F. Brevet, H.H. Girault, Gold Metal Liquid-Like Droplets, ACS Nano. 8 (2014) 9471–9481. doi:10.1021/nn503644v.

[33] W.H. Binder, Supramolecular assembly of nanoparticles at liquid-liquid interfaces, Angew. Chem. Int. Ed. Engl. 44 (2005) 5172–5175. doi:10.1002/anie.200501220.

[34] J.B. Edel, A.A. Kornyshev, M. Urbakh, Self-Assembly of Nanoparticle Arrays for Use as Mirrors, Sensors, and Antennas, ACS Nano. 7 (2013) 9526–9532. doi:10.1021/nn405712r.

[35] S.G. Booth, R.A.W. Dryfe, Assembly of Nanoscale Objects at the Liquid/Liquid Interface, J. Phys. Chem. C. 119 (2015) 23295–23309. doi:10.1021/acs.jpcc.5b07733.

[36] S. Biswas, L.T. Drzal, A Novel Approach to Create a Highly Ordered Monolayer Film of Graphene Nanosheets at the Liquid-Liquid Interface, Nano Lett. 9 (2009) 167–172. doi:10.1021/nl802724f.

[37] M.M. Gudarzi, F. Sharif, Self assembly of graphene oxide at the liquid–liquid interface: A new route to the fabrication of graphene based composites, Soft Matter. 7 (2011) 3432–3440. doi:10.1039/c0sm01311k.

[38] X. Bian, M.D. Scanlon, S. Wang, L. Liao, Y. Tang, B. Liu, H.H. Girault, Floating conductive catalytic nano-rafts at soft interfaces for hydrogen evolution, Chem. Sci. 4 (2013) 3432–3441. doi:10.1039/c3sc51290h.

[39] P. Asuri, S.S. Karajanagi, J.S. Dordick, R.S. Kane, Directed Assembly of Carbon Nanotubes at Liquid−Liquid Interfaces: Nanoscale Conveyors for Interfacial Biocatalysis, J. Am. Chem. Soc. 128 (2006) 1046–1047. doi:10.1021/JA0573965.

[40] P.S. Toth, Q.M. Ramasse, M. Velický, R.A.W. Dryfe, Functionalization of graphene at the organic/water interface, Chem. Sci. 6 (2015) 1316–1323. doi:10.1039/C4SC03504F.

[41] P.S. Toth, A.N.J. Rodgers, A.K. Rabiu, R.A.W. Dryfe, Electrochemical activity and

metal deposition using few-layer graphene and carbon nanotubes assembled at the liquid–liquid interface, Electrochem. Commun. 50 (2015) 6–10. doi:10.1016/j.elecom.2014.10.010.

[42] P.-P. Fang, S. Chen, H. Deng, M.D. Scanlon, F. Gumy, H.J. Lee, D. Momotenko, V. Amstutz, F. Cortés-Salazar, C.M. Pereira, Z. Yang, H.H. Girault, Conductive Gold Nanoparticle Mirrors at Liquid/Liquid Interfaces, ACS Nano. 7 (2013) 9241–9248. doi:10.1021/nn403879g.

[43] B. Su, J.-P. Abid, D.J. Fermín, H.H. Girault, H. Hoffmannová, P. Krtil, Z. Samec, Reversible Voltage-Induced Assembly of Au Nanoparticles at Liquid|Liquid Interfaces, J. Am. Chem. Soc. 126 (2004) 915–919. doi:10.1021/ja0386187.

[44] H. Jensen, D.J. Fermín, J.E. Moser, H.H. Girault, Organization and Reactivity of Nanoparticles at Molecular Interfaces. Part I. Photoelectrochemical Responses Involving TiO 2 Nanoparticles Assembled at Polarizable Water|1,2-Dichloroethane Junctions, J. Phys. Chem. B. 106 (2002) 10908–10914. doi:10.1021/jp0261253.

[45] D.J. Fermín, H. Jensen, J.E. Moser, H.H. Girault, Organisation and Reactivity of Nanoparticles at Molecular Interfaces. Part II. Dye Sensitisation of TiO2 Nanoparticles Assembled at the Water|1,2-Dichloroethane Interface, ChemPhysChem. 4 (2003) 85–89. doi:10.1002/cphc.200390013.

[46] L. Zhang, Y. Kitazumi, T. Kakiuchi, Potential-Dependent Adsorption and Transfer of Poly(diallyldialkylammonium) Ions at the Nitrobenzene|Water Interface, Langmuir. 27 (2011) 13037–13042. doi:10.1021/la2028077.

[47] Y. Kitazumi, T. Kakiuchi, Potential-Dependent Adsorption of Decylsulfate and Decylammonium Prior to the Onset of Electrochemical Instability at the 1,2-Dichloroethane|Water Interface, Langmuir. 25 (2009) 8062–8068. doi:10.1021/la9005696.

[48] Z. Samec, A. Trojánek, P. Krtil, Dynamics of phospholipid monolayers on polarised liquid–liquid interfaces, Faraday Discuss. 129 (2005) 301–313. doi:10.1039/B405377J.

[49] I. Uyanik, Y. Cengeloglu, Voltammetric and visual evidence of adsorption reactions at the liquid–liquid interfaces supported on a metallic electrode, Electrochim. Acta. 62 (2012) 290–295. doi:10.1016/j.electacta.2011.12.037.

[50] A.K. Patri, I.J. Majoros, J.R. Baker, Dendritic polymer macromolecular carriers for drug delivery, Curr. Opin. Chem. Biol. 6 (2002) 466–471. doi:10.1016/S1367-5931(02)00347-2.

[51] G.P. Perez, R.M. Crooks, Selectively Permeable Dendrimers as Molecular Gates, Electrochem. Soc. Interface. 10 (2001) 34–38.

[52] R.C. Hedden, B.J. Bauer, A. Paul Smith, F. Gröhn, E. Amis, Templating of inorganic nanoparticles by PAMAM/PEG dendrimer–star polymers, Polymer. 43 (2002) 5473–5481. doi:10.1016/S0032-3861(02)00428-7.

[53] A. Berduque, M.D. Scanlon, C.J. Collins, D.W.M. Arrigan, Electrochemistry of Non-Redox-Active Poly(propylenimine) and Poly(amidoamine) Dendrimers at Liquid−Liquid Interfaces, Langmuir. 23 (2007) 7356–7364. doi:10.1021/la063294w.

[54] M. Calderon, L.M.A. Monzón, M. Martinelli, A. V. Juarez, M.C. Strumia, L.M. Yudi, Electrochemical Study of a Dendritic Family at the Water/1,2-Dichloroethane Interface, Langmuir. 24 (2008) 6343–6350. doi:10.1021/la704052b.

[55] M.D. Scanlon, J. Strutwolf, D.W.M. Arrigan, Voltammetric behaviour of biological macromolecules at arrays of aqueous|organogel micro-interfaces, Phys. Chem. Chem. Phys. 12 (2010) 10040–10047. doi:10.1039/c003323e.

[56] G. Herzog, V. Kam, D.W.M. Arrigan, Electrochemical behaviour of haemoglobin at the liquid/liquid interface, Electrochim. Acta. 53 (2008) 7204–7209. doi:10.1016/j.electacta.2008.04.072.

[57] U. Pyell, Characterization of nanoparticles by capillary electromigration separation techniques, Electrophoresis. 31 (2010) 814–831. doi:10.1002/elps.200900555.

[58] C. Adelantado, N. Rodríguez-Fariñas, R.C. Rodríguez Martín-Doimeadios, M. Zougagh, Á. Ríos, Analysis of silica nanoparticles by capillary electrophoresis coupled to an evaporative light scattering detector, Anal. Chim. Acta. 923 (2016) 82–88. doi:10.1016/j.aca.2016.03.055.

[59] T. Sun, Y.S. Zhang, B. Pang, D.C. Hyun, M. Yang, Y. Xia, Engineered Nanoparticles for Drug Delivery in Cancer Therapy, Angew. Chemie Int. Ed. 53 (2014) 12320–12364. doi:10.1002/anie.201403036.

[60] H.E. Bergna, W.O. Roberts, Colloidal Silica: Fundamentals and Applications, Volume 131, CRC Press, Boca Raton, FL, 2005.

[61] P.E. Lafargue, J.J. Gaumet, J.F. Muller, A. Labrosse, Laser Ablation of Silica: Study of Induced Clusters by Fourier Transform Ion Cyclotron Resonance Mass Spectrometry, J. Mass Spectrom. 31 (1996) 623–632. doi:10.1002/(SICI)1096-9888(199606)31:6<623::AID-JMS333>3.0.CO;2-J.

[62] I.A.M. Ibrahim, A.A.F. Zikry, M.A. Sharaf, Preparation of spherical silica nanoparticles: Stober silica, J. Am. Sci. (2010) 985–989. doi:10.7537/marsjas061110.133.

[63] C.S.G. Phillips, R.J.P. Williams, Inorganic chemistry, 2nd ed., Oxford Clarendon Press, New York, 1965.

[64] T.L. Simpson, B.E. Volcani, Silicon and Siliceous Structures in Biological Systems, Springer, New York, 1981. doi:10.1007/978-1-4612-5944-2.

[65] R.K. Iler, The chemistry of silica : solubility, polymerization, colloid and surface properties, and biochemistry, John Wiley and Sons, Chichester, 1979.

[66] Silicon - Element information, properties and uses | Periodic Table, (n.d.). http://www.rsc.org/periodic-table/element/14/silicon (accessed March 5, 2018).

[67] H.M. Lim, J. Lee, J.-H. Jeong, S.-G. Oh, S.-H. Lee, Comparative Study of Various Preparation Methods of Colloidal Silica, Engineering. 02 (2010) 998–1005. doi:10.4236/eng.2010.212126.

[68] M. Meier, J. Ungerer, M. Klinge, H. Nirschl, Synthesis of nanometric silica particles via a modified Stöber synthesis route, Colloids Surfaces A Physicochem. Eng. Asp. 538 (2018) 559–564. doi:10.1016/j.colsurfa.2017.11.047.

[69] W. Stöber, A. Fink, E. Bohn, Controlled growth of monodisperse silica spheres in the micron size range, J. Colloid Interface Sci. 26 (1968) 62–69. doi:10.1016/0021-9797(68)90272-5.

[70] L. Leimhofer, B. Baumgartner, M. Puchberger, T. Prochaska, T. Konegger, M.M. Unterlass, Green one-pot synthesis and processing of polyimide–silica hybrid materials, J. Mater. Chem. A. 5 (2017) 16326–16335. doi:10.1039/C7TA02498C.

[71] A. Labrosse, A. Burneau, Characterization of porosity of ammonia catalysed alkoxysilane silica, J. Non. Cryst. Solids. 221 (1997) 107–124. doi:10.1016/S0022-3093(97)00414-6.

[72] R. Lindberg, J. Sjöblom, G. Sundholm, Preparation of silica particles utilizing the sol-gel and the emulsion-gel processes, Colloids Surfaces A Physicochem. Eng. Asp. 99 (1995) 79–88. doi:10.1016/0927-7757(95)03117-V.

[73] C.G. Tan, B.D. Bowen, N. Epstein, Production of monodisperse colloidal silica spheres: Effect of temperature, J. Colloid Interface Sci. 118 (1987) 290–293. doi:10.1016/0021-9797(87)90458-9.

[74] M.D. Sacks, T.-Y. Tseng, Preparation of SiO2 Glass from Model Powder Compacts: I, Formation and Characterization of Powders, Suspensions, and Green Compacts, J. Am. Ceram. Soc. 67 (1984) 526–532. doi:10.1111/j.1151-2916.1984.tb19164.x.

[75] K.. Unger, D. Kumar, M. Grün, G. Büchel, S. Lüdtke, T. Adam, K. Schumacher, S. Renker, Synthesis of spherical porous silicas in the micron and submicron size range: challenges and opportunities for miniaturized high-resolution chromatographic and electrokinetic separations, J. Chromatogr. A. 892 (2000) 47–55. doi:10.1016/S0021-9673(00)00177-1.

[76] V.N. Astratov, Y.A. Vlasov, O.Z. Karimov, A.A. Kaplyanskii, Y.G. Musikhin, N.A. Bert, V.N. Bogomolov, A.V. Prokofiev, Photonic band gaps in 3D ordered fcc silica matrices, Phys. Lett. A. 222 (1996) 349–353. doi:10.1016/0375-9601(96)00669-X.

[77] H. Míguez, C. López, F. Meseguer, A. Blanco, L. Vázquez, R. Mayoral, M. Ocaña, V. Fornés, A. Mifsud, Photonic crystal properties of packed submicrometric SiO2 spheres, Appl. Phys. Lett. 71 (1997) 1148–1150. doi:10.1063/1.119849.

[78] D. Knopp, D. Tang, R. Niessner, Review: Bioanalytical applications of biomolecule-functionalized nanometer-sized doped silica particles, Anal. Chim. Acta. 647 (2009) 14–30. doi:10.1016/j.aca.2009.05.037.

[79] M. Montalti, G. Battistelli, A. Cantelli, D. Genovese, Photo-tunable multicolour fluorescence imaging based on self-assembled fluorogenic nanoparticles, Chem. Commun. 50 (2014) 5326–5329. doi:10.1039/c3cc48464e.

[80] M.J. Ruedas-Rama, J.D. Walters, A. Orte, E.A.H. Hall, Fluorescent nanoparticles for intracellular sensing: A review, Anal. Chim. Acta. 751 (2012) 1–23. doi:10.1016/j.aca.2012.09.025.

[81] H.N. Tran, T.H. Lien Nghiem, T.T. Duong Vu, M.T. Pham, T. Van Nguyen, T.T. Tran, V.H. Chu, K.T. Tong, T.T. Tran, T.T. Xuan Le, J.-C. Brochon, T.Q. Nguyen, M.N. Hoang, C.N. Duong, T.T. Nguyen, A.T. Hoang, P.H. Nguyen, Dye-doped silica-based nanoparticles for bioapplications, Adv. Nat. Sci. Nanosci. Nanotechnol. 4 (2013) 043001. doi:10.1088/2043-6262/4/4/043001.

[82] J.X. He, M.Y. Cui, Y.Y. Zheng, W.H. Tang, B.Y. Chen, K. Tsukamoto, C.R. Li, Self-assembly of modified silica nanospheres at the liquid/liquid interface, Mater. Lett. 64 (2010) 463–465. doi:10.1016/j.matlet.2009.11.048.

[83] K. Möller, J. Kobler, T. Bein, Colloidal Suspensions of Nanometer-Sized Mesoporous Silica, Adv. Funct. Mater. 17 (2007) 605–612. doi:10.1002/adfm.200600578.

[84] C.-Y. Lai, B.G. Trewyn, D.M. Jeftinija, K. Jeftinija, S. Xu, S. Jeftinija, V.S.-Y. Lin, A Mesoporous Silica Nanosphere-Based Carrier System with Chemically Removable CdS Nanoparticle Caps for Stimuli-Responsive Controlled Release of Neurotransmitters and Drug Molecules, J. Am. Chem. Soc. 125 (2003) 4451–4459. doi:10.1021/JA028650L.

[85] G.J. Owens, R.K. Singh, F. Foroutan, M. Alqaysi, C.-M. Han, C. Mahapatra, H.-W. Kim, J.C. Knowles, Sol–gel based materials for biomedical applications, Prog. Mater. Sci. 77 (2016) 1–79. doi:10.1016/J.PMATSCI.2015.12.001.

[86] C.T. Kresge, M.E. Leonowicz, W.J. Roth, J.C. Vartuli, J.S. Beck, Ordered mesoporous molecular sieves synthesized by a liquid-crystal template mechanism, Nature. 359 (1992) 710–712. doi:10.1038/359710a0.

[87] K. Möller, T. Bein, Talented Mesoporous Silica Nanoparticles, Chem. Mater. 29 (2017) 371–388. doi:10.1021/acs.chemmater.6b03629.

[88] Q. Ma, Y. Li, X. Su, Silica-nanobead-based sensors for analytical and bioanalytical applications, TrAC Trends Anal. Chem. 74 (2015) 130–145. doi:10.1016/j.trac.2015.06.006.

[89] Q. Cai, Z.-S. Luo, W.-Q. Pang, Y.-W. Fan, X.-H. Chen, F.-Z. Cui, Dilute Solution Routes to Various Controllable Morphologies of MCM-41 Silica with a Basic Medium, Chem. Mater. 13 (2001) 258–263. doi:10.1021/cm990661z.

[90] C.E. Fowler, D. Khushalani, B. Lebeau, S. Mann, Nanoscale Materials with Mesostructured Interiors, Adv. Mater. 13 (2001) 649–652. doi:10.1002/1521-4095(200105)13:9<649::AID-ADMA649>3.0.CO;2-G.

[91] R.I. Nooney, D. Thirunavukkarasu, Y. Chen, R. Josephs, A.E. Ostafin, Synthesis of Nanoscale Mesoporous Silica Spheres with Controlled Particles Size, Chem. Mater. 14 (2002) 4721–4728. doi:10.1021/cm0204371.

[92] A. Caras, L. Kut, Glucan Particle Delivery of Mesoporous Silica-drug Nanoparticles, BSc Project report, Worcester Polytechnic Institute, 2011. https://web.wpi.edu/Pubs/E-project/Available/E-project-042711-125810/unrestricted/MQP_aclk.pdf.

[93] A. Maleki, H. Kettiger, A. Schoubben, J.M. Rosenholm, V. Ambrogi, M. Hamidi, Mesoporous silica materials: From physico-chemical properties to enhanced dissolution of poorly water-soluble drugs, J. Control. Release. 262 (2017) 329–347. doi:10.1016/j.jconrel.2017.07.047.

[94] H. Herd, H. Ghandehari, Synthetic and Toxicological Characteristics of Silica Nanomaterials for Imaging and Drug Delivery Applications, 1st ed., CRC Press, Boca Raton, FL, 2011.

[95] C. Urata, Y. Aoyama, A. Tonegawa, Y. Yamauchi, K. Kuroda, Dialysis process for the removal of surfactants to form colloidal mesoporous silica nanoparticles, Chem. Commun. 63 (2009) 5094–5096. doi:10.1039/b908625k.

[96] K. Hamdi, M. Hébrant, P. Martin, B. Galland, M. Etienne, Mesoporous silica nanoparticle film as sorbent for in situ and real-time monitoring of volatile BTX (benzene, toluene and xylenes), Sensors Actuators B Chem. 223 (2016) 904–913. doi:10.1016/j.snb.2015.09.062.

[97] L. Ding, B. Su, An electrochemistry assisted approach for fast, low-cost and gram-scale synthesis of mesoporous silica nanoparticles, RSC Adv. 5 (2015) 65922–65926. doi:10.1039/C5RA13482J.

[98] S. Liu, L. Lu, Z. Yang, P. Cool, E.F. Vansant, Further investigations on the modified Stöber method for spherical MCM-41, Mater. Chem. Phys. 97 (2006) 203–206. doi:10.1016/j.matchemphys.2005.09.003.

[99] K. KAMBARA, N. SHIMURA, M. OGAWA, Larger Scale Syntheses of Surfactant-Templated Nanoporous Silica Spherical Particles by the Stöber Method, J. Ceram. Soc. Japan. 115 (2007) 315–318. doi:10.2109/jcersj.115.315.

[100] A. Cauvel, G. Renard, D. Brunel, Monoglyceride Synthesis by Heterogeneous Catalysis Using MCM-41 Type Silicas Functionalized with Amino Groups, J. Org. Chem. 62 (1997) 749–751. doi:10.1021/JO9614001.

[101] X.S. Zhao, G.Q. Lu, Modification of MCM-41 by Surface Silylation with Trimethylchlorosilane and Adsorption Study, J. Phys. Chem. B. 102 (1998) 1556–1561. doi:10.1021/jp972788m.

[102] S.L. Burkett, S.D. Sims, S. Mann, Synthesis of hybrid inorganic–organic mesoporous silica by co-condensation of siloxane and organosiloxane precursors, Chem. Commun. (1996) 1367–1368. doi:10.1039/CC9960001367.

[103] M.C. Burleigh, M.A. Markowitz, M.S. Spector, B.P. Gaber, Direct Synthesis of Periodic Mesoporous Organosilicas: Functional Incorporation by Co-condensation with Organosilanes, J. Phys. Chem. B. 105 (2001) 9935–9942. doi:10.1021/JP011814K.

[104] S. Huh, J.W. Wiench, J.-C. Yoo, M. Pruski, V.S.-Y. Lin, Organic Functionalization and Morphology Control of Mesoporous Silicas via a Co-Condensation Synthesis Method, Chem. Mater. 15 (2003) 4247–4256. doi:10.1021/cm0210041.

[105] E.F. Vansant, P. Van Der Voort, K.C. Vrancken, The surface chemistry of silica, in: Charact. Hemical Modif. Silica Surf., Elsevier, 1995: pp. 3–556. doi:10.1016/S0167-2991(06)81511-9.

[106] R.M.A. Roque-Malherbe, Adsorption and Diffusion in Nanoporous Materials., Second, CRC Press, Boca Raton, FL, 2018.

[107] B.G. Trewyn, I.I. Slowing, S. Giri, H.-T. Chen, V.S.-Y. Lin, Synthesis and Functionalization of a Mesoporous Silica Nanoparticle Based on the Sol–Gel Process and Applications in Controlled Release, Acc. Chem. Res. 40 (2007) 846–853.

doi:10.1021/ar600032u.

[108] J. Kobler, K. Möller, T. Bein, Colloidal suspensions of functionalized mesoporous silica nanoparticles., ACS Nano. 2 (2008) 791–9. doi:10.1021/nn700008s.

[109] K. Sing, The use of nitrogen adsorption for the characterisation of porous materials, Colloids Surfaces A Physicochem. Eng. Asp. 187–188 (2001) 3–9. doi:10.1016/S0927-7757(01)00612-4.

[110] L. Shang, T. Bian, B. Zhang, D. Zhang, L.-Z. Wu, C.-H. Tung, Y. Yin, T. Zhang, Graphene-Supported Ultrafine Metal Nanoparticles Encapsulated by Mesoporous Silica: Robust Catalysts for Oxidation and Reduction Reactions, Angew. Chemie Int. Ed. 53 (2014) 250–254. doi:10.1002/anie.201306863.

[111] L.T. Gibson, Mesosilica materials and organic pollutant adsorption: part A removal from air, Chem. Soc. Rev. 43 (2014) 5163–5172. doi:10.1039/C3CS60096C.

[112] Z. Qi, I. Honma, H. Zhou, Ordered-mesoporous-silica-thin-film-based chemical gas sensors with integrated optical polarimetric interferometry, Appl. Phys. Lett. 88 (2006) 053503. doi:10.1063/1.2171490.

[113] A. Walcarius, Mesoporous materials and electrochemistry, Chem. Soc. Rev. 42 (2013) 4098–4140. doi:10.1039/c2cs35322a.

[114] J. Lu, M. Liong, J.I. Zink, F. Tamanoi, Mesoporous Silica Nanoparticles as a Delivery System for Hydrophobic Anticancer Drugs, Small. 3 (2007) 1341–1346. doi:10.1002/smll.200700005.

[115] S. Dai, M.C. Burleigh, Y.H. Ju, H.J. Gao, J.S. Lin, S.J. Pennycook, C.E. Barnes, Z.L. Xue, Hierarchically Imprinted Sorbents for the Separation of Metal Ions, J. Am. Chem. Soc. 122 (2000) 992–993. doi:10.1021/ja993168x.

[116] J.E. Lofgreen, G.A. Ozin, Controlling morphology and porosity to improve performance of molecularly imprinted sol-gel silica, Chem. Soc. Rev. 43 (2014) 911–933. doi:10.1039/c3cs60276a.

[117] K. Haupt, ed., Molecular Imprinting, Springer Berlin Heidelberg, Berlin, Heidelberg, 2012. doi:10.1007/978-3-642-28421-2.

[118] A. Sarafraz-Yazdi, N. Razavi, Application of molecularly-imprinted polymers in solid-phase microextraction techniques, TrAC Trends Anal. Chem. 73 (2015) 81–90. doi:10.1016/J.TRAC.2015.05.004.

[119] M. Tswett, Physikalisch-chemische Studien uber das Chlorophyll. Die Adsorptionen, Ber. Dtsch. Bot. Ges. 24 (1906) 316–323.

[120] M. Tswett, Adsorptions analyse und chromatographische Methode. Anwendung auf die Chemie des Chlorophylls, Ber. Dtsch. Bot. Ges. 24 (1906) 384–393.

[121] B. Sellergren, Molecularly imprinted polymers : man-made mimics of antibodies and their applications in analytical chemistry, 1st ed., Elsevier Science B.V., Amsterdam, 2001.

[122] M.V. Polyakov, Adsorption properties and structure of silica gel, Zhurnal Fizieskoj Khimii/Akademiya SSSR. 2 (1931) 799–805.

[123] M.V. Polyakov, P. Stadnik, M. Paryckij, I. Malkin, F. Duchina, On the structure of silica, Zhurnal Fizieskoj Khimii/Akademiya SSSR. 4 (1933) 454–456.

[124] M.V. Polyakov, L. Kuleshina, I. Neimark, On the dependence of silica gel adsorption properties on the character of its porosity, Zhurnal Fizieskoj Khimii/Akademiya SSSR. 10 (1937) 100–112.

[125] F.H. Dickey, The Preparation of Specific Adsorbents., Proc. Natl. Acad. Sci. U. S. A. 35 (1949) 227–229. doi:10.1073/pnas.35.5.227.

[126] F.H. Dickey, Specific Adsorption, J. Phys. Chem. 59 (1955) 695–707. doi:10.1021/j150530a006.

[127] R.G. Haldeman, P.H. Emmett, Specific Adsorption of Alkyl Orange Dyes on Silica Gel., J. Phys. Chem. 59 (1955) 1039–1043. doi:10.1021/j150532a012.

[128] A. Martin-Esteban, T. Casimiro, Molecular Imprinting: A New Journal, A New Home for Imprinters, Mol. Imprinting. 1 (2012) 1–2. doi:10.2478/molim-2012-0001.

[129] G. Wulff, A. Sarhan, Über die Anwendung von enzymanalog gebauten Polymeren zur Racemattrennung, Angew. Chemie. 84 (1972) 364–364. doi:10.1002/ange.19720840838.

[130] T. Takagishi, I.M. Klotz, Macromolecule-small molecule interactions; introduction of additional binding sites in polyethyleneimine by disulfide cross-linkages, Biopolymers. 11 (1972) 483–491. doi:10.1002/bip.1972.360110213.

[131] G. Vlatakis, L.I. Andersson, R. Müller, K. Mosbach, Drug assay using antibody mimics made by molecular imprinting, Nature. 361 (1993) 645–647. doi:10.1038/361645a0.

[132] M.J. Whitcombe, M.E. Rodriguez, P. Villar, E.N. Vulfson, A New Method for the Introduction of Recognition Site Functionality into Polymers Prepared by Molecular Imprinting: Synthesis and Characterization of Polymeric Receptors for Cholesterol, J. Am. Chem. Soc. 117 (1995) 7105–7111. doi:10.1021/ja00132a010.

[133] L. Ye, New Frontiers in Molecular Imprinting: From Micro- to Nanofabrication, in: L. Ye (Ed.), Mol. Imprinting Princ. Appl. Micro- Nanostructured Polym., Pan Stanford Publishing, 2013: pp. 1–24. doi:10.4032/9789814364874.

[134] L. Chen, X. Wang, W. Lu, X. Wu, J. Li, Molecular imprinting: perspectives and applications, Chem. Soc. Rev. 45 (2016) 2137–2211. doi:10.1039/C6CS00061D.

[135] K. Mosbach, O. Ramström, The Emerging Technique of Molecular Imprinting and Its Future Impact on Biotechnology, Nat. Biotechnol. 14 (1996) 163–170. doi:10.1038/nbt0296-163.

[136] A. Katz, M.E. Davis, Molecular imprinting of bulk, microporous silica, Nature. 403 (2000) 286–289. doi:10.1038/35002032.

[137] K. Donato, L. Matějka, R. Mauler, R. Donato, Recent Applications of Ionic Liquids in the Sol-Gel Process for Polymer–Silica Nanocomposites with Ionic Interfaces, Colloids and Interfaces. 1 (2017). doi:10.3390/colloids1010005.

[138] V. Samanidou, M. Kehagia, A. Kabir, K.G. Furton, Matrix molecularly imprinted mesoporous sol–gel sorbent for efficient solid-phase extraction of chloramphenicol from milk, Anal. Chim. Acta. 914 (2016) 62–74. doi:10.1016/J.ACA.2016.02.003.

[139] J.E. Lofgreen, I.L. Moudrakovski, G.A. Ozin, Molecularly imprinted mesoporous organosilica, ACS Nano. 5 (2011) 2277–2287. doi:10.1021/nn1035697.

[140] B.M. Jung, M.S. Kim, W.J. Kim, J.Y. Chang, Molecularly imprinted mesoporous silica

particles showing a rapid kinetic binding, Chem. Commun. 46 (2010) 3699–3701. doi:10.1039/c003173a.

[141] M.H. Abraham, A.F. Danil de Namor, Solubility of electrolytes in 1,2-dichloroethane and 1,1-dichloroethane, and derived free energies of transfer, J. Chem. Soc. Faraday Trans. 1. 72 (1976) 955–962.

[142] L. Poltorak, K. Morakchi, G. Herzog, A. Walcarius, Electrochemical characterization of liquid-liquid micro-interfaces modified with mesoporous silica, Electrochim. Acta. 179 (2015) 9–15. doi:10.1016/j.electacta.2015.01.129.

[143] G. Herzog, W. Moujahid, J. Strutwolf, D.W.M. Arrigan, Interactions of proteins with small ionised molecules: electrochemical adsorption and facilitated ion transfer voltammetry of haemoglobin at the liquid/liquid interface., Analyst. 134 (2009) 1608–1613. doi:10.1039/b905441n.

[144] M.F. Ebersold, A.L. Zydney, Separation of Protein Charge Variants by Ultrafiltration, Biotechnol. Prog. 20 (2004) 543–549. doi:10.1021/bp034264b.

[145] M. Hohammad, M. Razaq, Stopped-flow voltammetry, J. Electroanal. Chem. Interfacial Electrochem. 98 (1979) 335–338. doi:10.1016/S0022-0728(79)80272-7.

[146] I. Grillo, E.I. Kats, A.R. Muratov, Formation and Growth of Anionic Vesicles Followed by Small-Angle Neutron Scattering, Langmuir. 19 (2003) 4573–4581. doi:10.1021/la0208732.

[147] R. Favilla, F. Del Signore, E. Dainese, M. Beltramini, B. Salvato, Dissociation kinetics of hemocyanin from Octopus vulgaris, Biochim. Biophys. Acta - Protein Struct. Mol. Enzymol. 1385 (1998) 115–125. doi:10.1016/S0167-4838(98)00037-5.

[148] W. R. Grace & Co.-Conn, Technical information: LUDOX colloidal silica, Grace Mater. Technol. (2012). https://grace.com/general-industrial/en-us/Documents/ludox_br_E_2012_f120504_web.pdf (accessed November 16, 2015).

[149] W. R. Grace & Co.-Conn., Technical information: LUDOX® Colloidal Silica in Coatings, Grace Davison Eng. Mater. (2007). https://grace.com/coatings-and-inks/en-us/Documents/LUDOX Coatings TI.pdf (accessed November 16, 2015).

[150] Sigma-Aldrich Co. LLC, LUDOX® HS-40 colloidal silica 40 wt. % suspension in

H2O, Sigma-Aldrich Co. LLC. (2015). http://www.sigmaaldrich.com/catalog/product/aldrich/420816?lang=fr&region=FR (accessed November 16, 2015).

[151] I.M.K. Ismail, Cross-sectional areas of adsorbed nitrogen, argon, krypton, and oxygen on carbons and fumed silicas at liquid nitrogen temperature, Langmuir. 8 (1992) 360–365. doi:10.1021/la00038a006.

[152] L.E. Cascarini de Torre, J.L. Llanos, E.J. Bottani, Nitrogen cross-sectional area on standard graphite, Collect. Czechoslov. Chem. Commun. 53 (1988) 251–257. doi:10.1135/cccc19880251.

[153] Nanocomposix.eu, Silica Physical Properties, (2015). http://nanocomposix.eu/pages/silica-physical-properties (accessed November 10, 2015).

[154] W. Teng, Z. Wu, J. Fan, W. Zhang, D. Zhao, Amino-functionalized ordered mesoporous carbon for the separation of toxic microcystin-LR, J. Mater. Chem. A. 3 (2015) 19168–19176. doi:10.1039/C5TA05320J.

[155] H. Duan, D. Wang, D.G. Kurth, H. Möhwald, Directing self-assembly of nanoparticles at water/oil interfaces, Angew. Chemie - Int. Ed. 43 (2004) 5639–5642. doi:10.1002/anie.200460920.

[156] W.H. Binder, Supramolecular assembly of nanoparticles at liquid-liquid interfaces, Angewan. Chem. Int. Ed. 44 (2005) 5172–5175. doi:10.1002/anie.200501220.

[157] A. Böker, J. He, T. Emrick, T.P. Russell, Self-assembly of nanoparticles at interfaces, Soft Matter. 3 (2007) 1231–1248. doi:10.1039/b706609k.

[158] L. Hu, M. Chen, X. Fang, L. Wu, Oil–water interfacial self-assembly: a novel strategy for nanofilm and nanodevice fabrication, Chem. Soc. Rev. 41 (2012) 1350–1362. doi:10.1039/C1CS15189D.

[159] Y. Xu, M.P. Konrad, W.W.Y. Lee, Z. Ye, S.E.J. Bell, A Method for Promoting Assembly of Metallic and Nonmetallic Nanoparticles into Interfacial Monolayer Films, Nano Lett. 16 (2016) 5255–5260. doi:10.1021/acs.nanolett.6b02418.

[160] M. Kosmulski, Positive Electrokinetic Charge of Silica in the Presence of Chlorides, J.

Colloid Interface Sci. 208 (1998) 543–545. doi:10.1006/JCIS.1998.5859.

[161] P.S. Toth, R.A.W. Dryfe, Novel organic solvents for electrochemistry at the liquid/liquid interface, Analyst. 140 (2015) 1947–1954. doi:10.1039/C4AN02250E.

[162] A.K. Rabiu, P.S. Toth, A.N.J. Rodgers, R.A.W. Dryfe, Electrochemical Investigation of Adsorption of Single-Wall Carbon Nanotubes at a Liquid/Liquid Interface, ChemistryOpen. 6 (2017) 57–63. doi:10.1002/open.201600136.

[163] E. Smirnov, P. Peljo, M.D. Scanlon, H.H. Girault, Interfacial Redox Catalysis on Gold Nanofilms at Soft Interfaces, ACS Nano. 9 (2015) 6565–6575. doi:10.1021/acsnano.5b02547.

[164] C. Párkányi, C. Boniface, J.. Aaron, M. Maafi, A quantitative study of the effect of solvent on the electronic absorption and fluorescence spectra of substituted phenothiazines: evaluation of their ground and excited singlet-state dipole moments, Spectrochim. Acta Part A Mol. Spectrosc. 49 (1993) 1715–1725. doi:10.1016/0584-8539(93)80239-7.

[165] Y. He, L. Ding, B. Su, Vertically ordered silica mesochannels as preconcentration materials for the electrochemical detection of methylene blue, Sci. China Chem. 58 (2015) 1593–1599. doi:10.1007/s11426-015-5365-2.

[166] J.J. Aaron, M.D. Gaye Seye, S. Trajkovska, N. Motohashi, Bioactive Phenothiazines and Benzo[a]phenothiazines: Spectroscopic Studies, and Biological and Biomedical Properties and Applications, in: N. Motohashi (Ed.), Bioact. Heterocycles VII, Springer, Berlin, Heidelberg, 2008: pp. 153–231. doi:10.1007/7081_2008_125.

[167] Merck, Eosin B (bluish) (C.I.45400) CAS 548-24-3 | 115934, (2017). https://www.merckmillipore.com/IE/en/product/Eosin-B-bluish-C.I.45400,MDA_CHEM-115934 (accessed October 25, 2017).

[168] A.A. Waheed, P.D. Gupta, Estimation of Protein Using Eosin B Dye, Anal. Biochem. 233 (1996) 249–252. doi:10.1006/abio.1996.0037.

[169] D. Heger, J. Jirkovský, P. Klán, Aggregation of methylene blue in frozen aqueous solutions studied by absorption spectroscopy, J. Phys. Chem. A. 109 (2005) 6702–6709. doi:10.1021/jp050439j.

[170] X. Yu, L. Huang, Y. Wei, J. Zhang, Z. Zhao, W. Dai, B. Yao, Controllable preparation, characterization and performance of Cu2O thin film and photocatalytic degradation of methylene blue using response surface methodology, Mater. Res. Bull. 65 (2015) 410–417. doi:10.1016/j.materresbull.2015.01.009.

[171] V. Russo, D. Masiello, M. Trifuoggi, M. Di Serio, R. Tesser, Design of an adsorption column for methylene blue abatement over silica: From batch to continuous modeling, Chem. Eng. J. 302 (2016) 287–295. doi:10.1016/j.cej.2016.05.020.

[172] S. Lagergren, About the Theory of So-Called Adsorption of Soluble Substances, K. Sven. Vetenskapsakademiens Handl. 24 (1898) 1–39.

[173] A.E. Rodrigues, C.M. Silva, What's wrong with Lagergreen pseudo first order model for adsorption kinetics?, Chem. Eng. J. 306 (2016) 1138–1142. doi:10.1016/j.cej.2016.08.055.

[174] A.S. Elsherbiny, Adsorption kinetics and mechanism of acid dye onto montmorillonite from aqueous solutions: Stopped-flow measurements, Appl. Clay Sci. 83–84 (2013) 56–62. doi:10.1016/j.clay.2013.07.014.

[175] H. Nagatani, T. Sakamoto, T. Torikai, T. Sagara, Encapsulation of Anilinonaphthalenesulfonates in Carboxylate-Terminated PAMAM Dendrimer at the Polarized Water|1,2-Dichloroethane Interface, Langmuir. 26 (2010) 17686–17694. doi:10.1021/la1032477.

[176] H. Sakae, H. Nagatani, K. Morita, H. Imura, Spectroelectrochemical characterization of dendrimer-porphyrin associates at polarized liquid|liquid interfaces., Langmuir. 30 (2014) 937–945. doi:10.1021/la404079m.

[177] T. Osakai, T. Yoshimura, D. Kaneko, H. Nagatani, S.H. Son, Y. Yamagishi, K. Yamada, Potential-modulated fluorescence spectroscopy of zwitterionic and dicationic membrane-potential-sensitive dyes at the 1,2-dichloroethane/water interface, Anal. Bioanal. Chem. 404 (2012) 785–792. doi:10.1007/s00216-012-6199-9.

[178] J.S. da Silva, H.C. Junqueira, T.L. Ferreira, Effect of pH and dye concentration on the n-octanol/water distribution ratio of phenothiazine dyes: a microelectrode voltammetry study, Electrochim. Acta. 144 (2014) 154–160. doi:10.1016/j.electacta.2014.08.094.

[179] J.P. Behr, M. Kirch, J.M. Lehn, Carrier-mediated transport through bulk liquid membranes: dependence of transport rates and selectivity on carrier properties in a diffusion-limited process, J. Am. Chem. Soc. 107 (1985) 241–246. doi:10.1021/ja00287a043.

[180] M. Yizhak, G. Hefter, Ion Pairing, Chem. Rev. 106 (2006) 4585–4621. doi:10.1021/CR040087X.

[181] V. Venkateshwaran, S. Vembanur, S. Garde, Water-mediated ion-ion interactions are enhanced at the water vapor-liquid interface., Proc. Natl. Acad. Sci. U. S. A. 111 (2014) 8729–8734. doi:10.1073/pnas.1403294111.

[182] R. Ishimatsu, N. Nishi, T. Kakiuchi, Interfacial Ion Pairing at the Interface between Water and a Room-Temperature Ionic Liquid, N -Tetradecylisoquinolinium Bis(pentafluoroethylsulfonyl)imide, Langmuir. 23 (2007) 7608–7611. doi:10.1021/la700884q.

[183] K. Schweighofer, I. Benjamin, Ion pairing and dissociation at liquid/liquid interfaces: Molecular dynamics and continuum models, J. Chem. Phys. 112 (2000) 1474–1482. doi:10.1063/1.480713.

[184] T. Iliescu, M. Baia, W. Kiefer, FT-Raman, surface-enhanced Raman spectroscopy and theoretical investigations of diclofenac sodium, Chem. Phys. 298 (2004) 167–174. doi:10.1016/J.CHEMPHYS.2003.11.018.

[185] Regulatory, Pharmaceuticals added to EU's pollutant "watch list," PM Live. (2013). http://www.pmlive.com/pharma_news/pharmaceuticals_added_to_eus_pollutant_watch_list_487813 (accessed June 15, 2015).

[186] L. Araujo, M.E. Troconis, M.B. Espina, A. Prieto, Persistence of Ibuprofen , Ketoprofen , Diclofenac and Clofibric Acid in Natural Waters, J. Environ. Hum. 1 (2014) 32–38.

[187] A.B.A. Boxall, New and Emerging Water Pollutants arising from Agriculture, Organ. Econ. Co-Operation Dev. (2012). http://www.oecd.org/tad/sustainable-agriculture/49848768.pdf (accessed June 15, 2015).

[188] Infrared Spectroscopy Absorption Table, Chem. Libr. (2014).

https://chem.libretexts.org/Reference/Reference_Tables/Spectroscopic_Parameters/Infrared_Spectroscopy_Absorption_Table (accessed June 18, 2018).

[189] P.J. Launer, B. Arkles, Infrared analysis of organosilicon compounds: Spectra-structure correlations, in: B. Arkles, G.L. Larson (Eds.), Silicon Compounds: Silanes and Silicones, Third edition, Gelest, Inc., Morrisville, PA, 2013.

[190] C.F. Poole, The Essence of Chromatography, First, Elsevier Science B.V., Amsterdam, 2002. doi:10.1016/B978-044450198-1/50013-6.

[191] Merck | Chromolith® RP-18e Endcapped HPLC Columns, (2018). https://www.merckmillipore.com/IE/en/analytics-and-sample-preparation/chromolith-RP-18-endcapped/fast-separation-at-lower-flow-rates/3lyb.qB.mDoAAAFC4DBJ3_uV,nav (accessed June 5, 2018).

[192] Merck | Chromolith® RP-18e L1 USP HPLC Columns, (2018). https://www.merckmillipore.com/IE/en/products/analytics-sample-prep/chromatography-for-analysis/analytical-hplc/columns-for-usp-specifications/l1-octadecylsilane-chemically-linked-to-porous-silica-or-ceramic-micro-particles/chromolith-rp-18-endcapped/lyeb (accessed June 5, 2018).

[193] N.G. Vanifatova, B.Y. Spivakov, J. Mattusch, R. Wennrich, Size separation of silica nanospheres by means of capillary zone electrophoresis, Talanta. 59 (2003) 345–353. doi:10.1016/S0039-9140(02)00523-4.

[194] Y. Wang, W.R.G. Baeyens, C. Huang, G. Fei, L. He, J. Ouyang, Enhanced separation of seven quinolones by capillary electrophoresis with silica nanoparticles as additive, Talanta. 77 (2009) 1667–1674. doi:10.1016/J.TALANTA.2008.10.002.

[195] HORIBA - Raman Spectroscopy, (2018). http://www.horiba.com/scientific/products/raman-spectroscopy/raman-academy/raman-tutorial/raman-scattering/ (accessed June 5, 2018).

[196] WITec || Raman spectroscopy, (2018). https://www.witec.de/resources-and-education/knowledge-base/ (accessed June 5, 2018).

[197] B. Sharma, R.R. Frontiera, A.-I. Henry, E. Ringe, R.P. Van Duyne, SERS: Materials, applications, and the future, Mater. Today. 15 (2012) 16–25. https://cpb-us-

e1.wpmucdn.com/sites.northwestern.edu/dist/f/44/files/2012/08/SERS-Materials-applications-and-the-future.pdf.

[198] X.-D. Tian, B.-J. Liu, J.-F. Li, Z.-L. Yang, B. Ren, Z.-Q. Tian, SHINERS and plasmonic properties of Au Core SiO2 shell nanoparticles with optimal core size and shell thickness, J. Raman Spectrosc. 44 (2013) 994–998. doi:10.1002/jrs.4317.

[199] H. Zhang, C. Wang, H.-L. Sun, G. Fu, S. Chen, Y.-J. Zhang, B.-H. Chen, J.R. Anema, Z.-L. Yang, J.-F. Li, Z.-Q. Tian, In situ dynamic tracking of heterogeneous nanocatalytic processes by shell-isolated nanoparticle-enhanced Raman spectroscopy, Nat. Commun. 8 (2017). doi:10.1038/ncomms15447.

[200] L. Poltorak, M. Dossot, G. Herzog, A. Walcarius, Interfacial processes studied by coupling electrochemistry at the polarised liquid–liquid interface with in situ confocal Raman spectroscopy, Phys. Chem. Chem. Phys. 16 (2014) 2147–2180. doi:10.1039/C4CP03254C.

[201] Prince Technologies :: Introduction to Capillary Electrophoresis, (2018). http://www.princetechnologies.eu/products/ce-systems/ce-technologies/ce-introduction/ (accessed June 5, 2018).

APPENDIX 1: Electrochemical cell setup

The four different electrochemical cell compositions, briefly described in Chapter 2, Section 2.2 and used during experiments in Chapter 3 + 4, are shown in greater detail here to aid in the understanding of the setup used during electrochemical experiments.

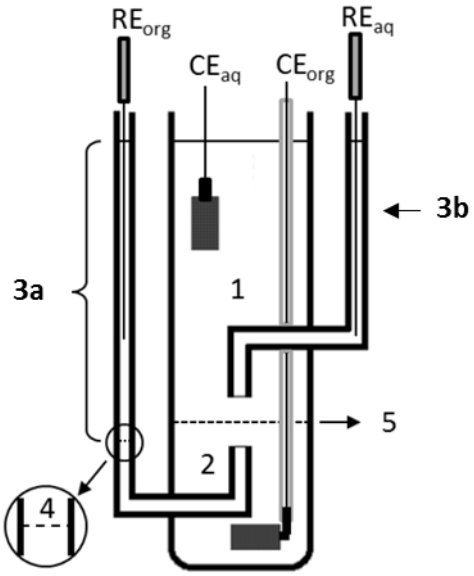

Figure A1.1: Four electrode electrochemical cell with macroscopic liquid-liquid interface. RE_{org} and RE_{aq} represent the organic and aqueous reference electrodes, CE_{org} and CE_{aq} corresponding to the organic and aqueous counter electrodes respectively.

1 – Aqueous phase

2 – Organic phase

3a+b – Organic reference phase

4 – Liquid-liquid interface between the organic and organic reference phases

5 – ITIES

Electrochemical cell 1:

$Ag_{(s)}$ | $AgCl_{(s)}$ | 10 mM $LiCl_{(aq)}$ + *x* mM interfacial active $ion_{(aq)}$ + *y* g L^{-1} silica nanoparticles || 10 mM $BTPPA^{+}TPBCl^{-}_{(org)}$ in 1,2-DCE | Saturated $BTPPA^{+}Cl^{-}$ in 10 mM LiCl in H_2O | $AgCl_{(s)}$ | $Ag_{(s)}$;

1 – 10 mM LiCl + *x* mM interfacial active ion + *y* g L^{-1} silica nanoparticles

2 – 10 mM BTPPA $TPBCl^{-}$ in 1,2-DCE

3a – Saturated $BTPPA^{+}Cl^{-}$ in 10 mM LiCl in H_2O

Electrochemical cell 2:

$Ag_{(s)}$ | $AgCl_{(s)}$ | 100 mM $LiCl_{(aq)}$ + *y* g L^{-1} silica nanoparticles || 10 mM $BTPPA^{+}TPBCl^{-}_{(org)}$ in 1,2-DCE | Saturated $BTPPA^{+}Cl^{-}$ in 10 mM LiCl in H_2O | $AgCl_{(s)}$ | $Ag_{(s)}$;

1 – 100 mM LiCl + *y* g L^{-1} silica nanoparticles

2 – 10 mM BTPPA $TPBCl^{-}$ in 1,2-DCE

3a – Saturated $BTPPA^{+}Cl^{-}$ in 10 mM LiCl in H_2O

Electrochemical cell 3:

$Ag_{(s)}$ | $AgCl_{(s)}$ | 10 mM $HCl_{(aq)}$ + *y* g L^{-1} silica nanoparticles || 10 mM $BTPPA^{+}TPBCl^{-}_{(org)}$ in 1,2-DCE | Saturated $BTPPA^{+}Cl^{-}$ in 10 mM LiCl in H_2O | $AgCl_{(s)}$ | $Ag_{(s)}$;

1 – 10 mM HCl + *y* g L^{-1} silica nanoparticles

2 – 10 mM BTPPA $TPBCl^{-}$ in 1,2-DCE

3a – Saturated $BTPPA^{+}Cl^{-}$ in 10 mM LiCl in H_2O

Electrochemical cell 4:

$Ag_{(s)}$ | $AgCl_{(s)}$ | Saturated $BTPPA^{+}Cl^{-}$ in 10 mM LiCl in H_2O | 10mM $BTPPA^{+}TPBCl^{-}_{(org)}$ in 40:60 1,2-DCE:5-nonanone (v/v) || 10mM $LiCl_{(aq)}$ + *y* g L^{-1} silica nanoparticles | $AgCl_{(s)}$ | $Ag_{(s)}$.

1 – 10mM $BTPPA^{+}TPBCl^{-}_{(org)}$ in 40:60 1,2-DCE:5-nonanone (v/v)

2 – 10 mM LiCl + *y* g L^{-1} silica nanoparticles

3b – Saturated $BTPPA^{+}Cl^{-}$ in 10 mM LiCl in H_2O

APPENDIX 2: Solubility issues with Diclofenac and its analogues

For the experiments in Chapter 5, in order to be able to accurately compare the selectivity of the imprinted silica nanoparticles, a solution combining Diclofenac and its analogues was desired. However, here many problems were encountered. Although Diclofenac was soluble in aqueous solutions, its analogues – Aceclofenac and PABA were not.

Initial experiments with electrochemistry (Section 5.5) and UV/Vis spectroscopy (Section 5.2) only used Diclofenac Na, and so the stock solution of this was always 10 mM in 10 mM LiCl @ pH 6.9. However not even 1 mM Aceclofenac or PABA would dissolve in LiCl, regardless of varying the pH from 6.5 to 10. The Aceclofenac solution was cloudy and PABA was more of a yellow/orange colour than the strong orange expected.

Next 50 mM Tris at pH 9 was used to make 1 mM solutions, PABA dissolved but Aceclofenac formed dust-like strands. Nevertheless, their calibration curves from UV/Vis experiments were not linear as the solution was too dilute. With the pH decreased to 8 and 10 mM solutions made, both solutions dissolved after stirring overnight, however Diclofenac Na was cloudy/creamy. Further reduction of the pH to 6.6 resulted in a cloudy solution of Aceclofenac and Diclofenac Na went cloudy/creamy again with foaming. It was the solutions of Aceclofenac and PABA at pH 8 that dissolved very well which were used during the UV/Vis experiments in Section 5.2.

Following this a compromise was investigated, using a solution of 50:50 10 mM LiCl:10mM Tris @ pH 6.7. Still the 10 mM solution of Aceclofenac was creamy/cloudy with the drug powder visible in the liquid and PABA was a slightly orange colour but with undissolved drug also visible. Similar results were obtained with 1 mM solutions of each.

Next the attention turned to ACN and 1 mM solutions of Aceclofenac and PABA both dissolved perfectly, but Diclofenac Na was cloudy and so the decision was made to try Diclofenac FA. 10mM solutions of each were made but the UV/Vis spectrums obtained did not have good baselines and there were interference bands, as when the small quantity of stock solution of the drug was added to the larger volume of LiCl for UV/Vis analysis, the solution turned cloudy. After the solutions were left stirring overnight the 10 mM Diclofenac FA turned cloudy and formed a film on top, Aceclofenac became a cloudy/powdery suspension and PABA turned bright orange with a shimmery powdery solution. This was possibly due to the evaporation of some ACN, thereby forming more concentrated solutions.

A 5:1 ACN:MeOH mixture was next chosen to make the 10 mM drug solutions and they all dissolved very well. However UV/Vis spectroscopy experiments showed no adsorption of Diclofenac to the DINs, even though adsorption should occur and was the affinity was previously proven using Diclofenac in LiCl. Two possible reasons to explain the result might be that the pKa of Diclofenac changes in a solution of ACN:MeOH, compared to that in LiCl. This could result in the charge being less strongly negative or even neutralized, thus it wouldn't interact with the imprint cavity and so would not be adsorbed. Secondly the solvation of Diclofenac in solution could be too strong that it effects its ability to interact with the imprinted silica nanoparticles. A comparison of Diclofenac Na in LiCl and ACN:MeOH was carried out using UV/Vis spectroscopy and it was seen the wavelength of the Diclofenac peak shifted to slightly higher values when the stock solution of ACN:MeOH was used, however the peak shape remained the same.

Finally 10 mM solutions of Diclofenac FA, Aceclofenac and PABA were made in EtOH and they all dissolved. These were used during experiments in Section 5.4. The results obtained showed no adsorption of Diclofenac to DINs and so the issue of solvation was questioned again, however very small volumes of EtOH were used during chromatography and capillary electrophoresis experiments, and much larger quantities of mobile phases should have well diluted the samples. Thus it was concluded that the main reason for these negative results was due to insufficient knowledge of the optimal parameters in which to conduct these techniques.

APPENDIX 3: Attempts to investigate the selectivity of DINs

As previously mentioned in Chapter 5, Section 5.4, experiments with HPLC and Capillary electrophoresis did not give conclusive results on the specificity of DINs. A summary of the findings was given in that chapter but here a more detailed description of the trials and results is presented.

HPLC experiments with Diclofenac and its analogues, using columns loaded with NINs and DINs

To recap, the principle of high performance liquid chromatography (HPLC) is to separate and distinguish chemicals based on their interactions with the mobile phase (liquid) and stationary phase (solid), as they pass through the chromatography column. Some chemicals have a stronger affinity for the stationary phase than others and so take longer to pass through the column, resulting in their elution peak on the chromatogram appearing after a longer time than a chemical which has less interaction and thus elutes faster [190]. Thus the aim in this case, was to measure the retention time and peak area of each drug obtained after eluting through the columns with NINs and DINs. The difference would allow the quantity of drug adsorbed to the DINs to be obtained. The peak area should be lower for Diclofenac FA using the column with DINs, as the Diclofenac should interact with the imprint cavities of the DINs. For all other combinations there should be no interactions and so the peak area and retention times for the drugs should be unchanged.

These HPLC experiments were carried out with the empty columns obtained from Restek, which were loaded with the NINs in one column and DINs in a separate column. The columns were filled with the dry silica, then screwed shut and the mobile phase pumped through them for a period of time in order to allow the column to equilibrate. The experimental conditions for these experiments are outlined in Chapter 2, Section 2.3. Chromatograms were recorded at 275 nm for all except PABA, which was recorded at 325 nm, as this wavelength was the optimum for PABA based on its UV/Vis spectrum, seen in Figure 5.6 inset. In order to be able to compare the results between Diclofenac, Aceclofenac and PABA, a common solvent in which they all dissolved was used and thus the 10 mM stock solutions of each drug were in EtOH. However the 0.05 mM solutions injected were prepared in the mobile phase. Thus to have a well dissolved and clear solution, Diclofenac free acid as opposed to Diclofenac sodium salt was used here.

Firstly chromatograms were recorded for all three drugs in the absence of a column, as can be seen in Figure A3.1. The mobile phase consisted of 1 mM NaCl in UP H_2O @ pH 5.8 and a flow rate of 0.3 mL min^{-1} was used.

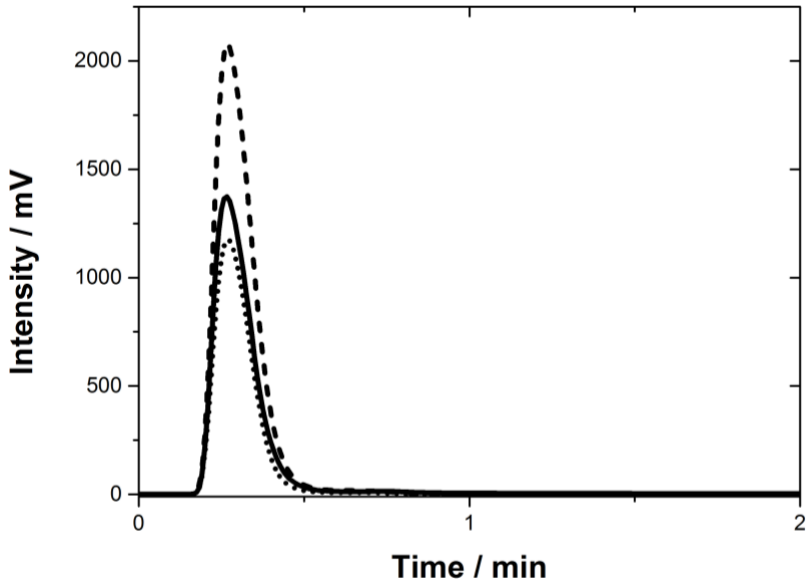

Figure A3.1: Chromatograms of 0.5 mM Diclofenac FA (continuous line), Aceclofenac (dotted line) and PABA (dashed line) in the absence of a column. Mobile phase 1 mM NaCl in UP H_2O, flow rate of 0.3 mL min^{-1}, Diclofenac and Aceclofenac recorded at 275 nm, PABA recorded at 325 nm

Figure A3.2 shows the chromatograms of (A) Diclofenac FA, its analogues (B) Aceclofenac and (C) PABA and then (D) a mixture of all three after were injected into the HPLC with both columns, separately, in order to be able to compare and contrast the chromatograms obtained.

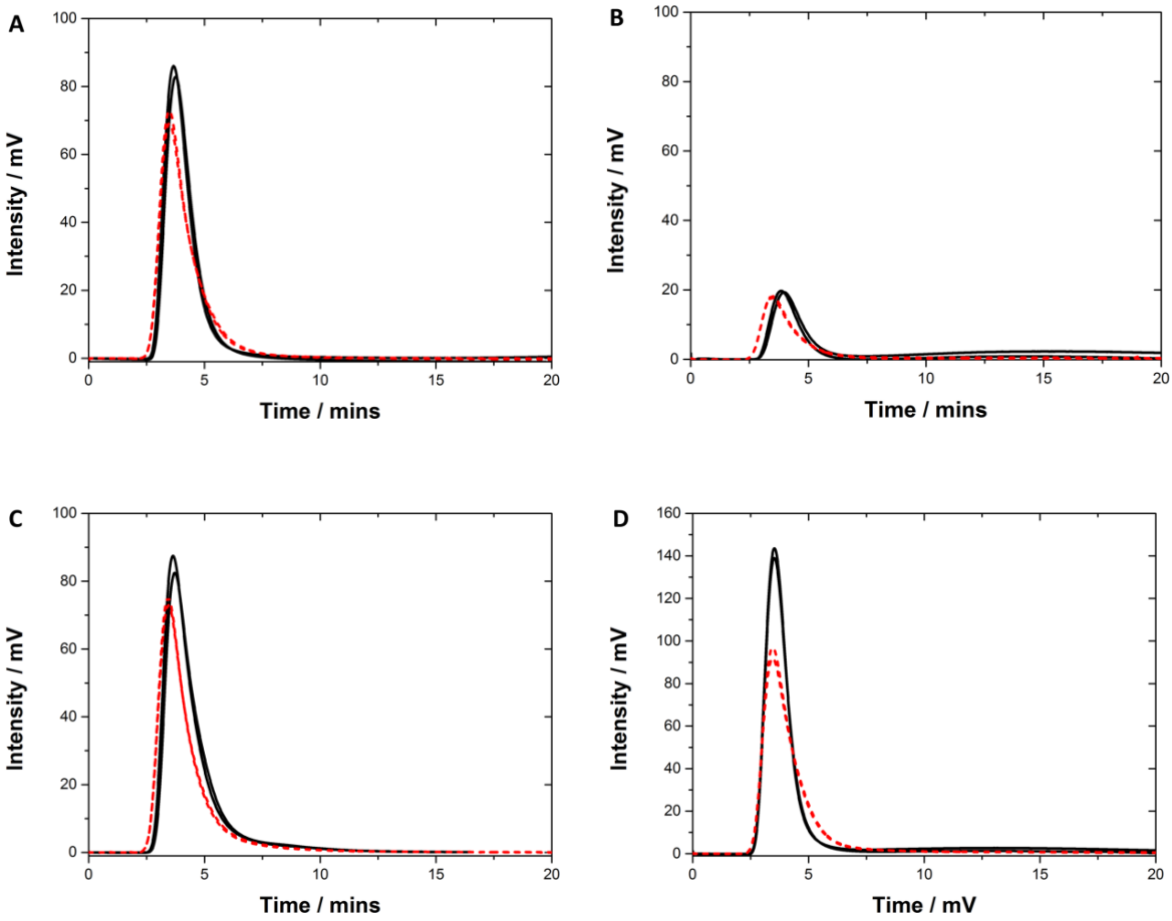

Figure A3.2: Chromatograms of 0.05 mM (A) Diclofenac free acid, (B) Aceclofenac, (C) PABA and (D) mixture of all three, using a column filled with NINs (dashed red line) and DINs (continuous black line). Mobile phase UP H_2O with 10% ACN and 5 mM NaCl, flow rate of 0.1 mL min^{-1}, A, B + D recorded at 275 nm, C recorded at 325 nm

Table A3.1: Retention times and peak areas calculated from HPLC chromatograms

		Retention time / mins	Peak area / mV min
Diclofenac free acid	NINs	3.485	6,932,883
	DINs	3.715	7,072,067
Aceclofenac	NINs	3.465	1,733,410
	DINs	3.91	1,714,416
PABA	NINs	3.435	7,257,334
	DINs	3.47	10,557,807
Mixture	NINs	3.455	9,154,903.5
	DINs	3.53	10,085,770.5

As can be seen in the above table, the retention time for each solution is slightly larger when using the column filled with DINs as opposed to that with NINs, which could be explained by an interaction of the drug molecules with DINs and not with NINs. The peak area remains relatively constant for Diclofenac FA and Aceclofenac, however it becomes much larger for PABA and the mixture in the results with DINs. One could deduce that these results mean there is an interaction between the drugs and the silica nanoparticles, however variations in the column packing between NINs and DINs mean these results are not entirely accurate. Several attempts were made to try optimise the column loading process, but due to time restraints other techniques were considered. Consequently the focus shifted to capillary electrophoresis to attempt the same aim, i.e. the characterisation of the Diclofenac – DINs interaction.

Capillary Electrophoresis experiments with NINs and DINs as pseudo-stationary phases

As with HPLC, Capillary electrophoresis (CE) was used in this research with the aim of comparing the interaction of the drug molecules (which are anionic) with the DINs [190,201]. In HPLC the affinity of the drug molecules to the stationary phase of the HPLC column was investigated, thereby allowing differences between the drug molecules interactions with DINs to be studied. However, with CE, the interactions are analysed by measuring changes in the electrophoretic mobility (μ_{ep}) of the drug molecules through the capillary, in the presence and absence of the nanoparticles. The technique involved filling a capillary with a buffer solution at a certain pH (which also may contain the NINs or DINs), applying a high voltage to generate an electric field, which then causes the anionic drug molecules to move through the capillary. Electroosmotic flow is the motion of the buffer solution through the capillary under the influence of the electric field, however the velocity at which the drug molecules move is not equal to this as it depends on their charge, size and interaction with the components in the capillary. All these factors are taken into account in the following equation and the overall electrophoretic mobility, μ_{ep}, of the drug molecules calculated. This value was then used to compare the interaction of the drugs with the DINs. This equation describes the relationship between μ_{ep}, μ_{app} (apparent mobility) and μ_{EOF} (electroosmotic mobility).

$$\mu_{app} = \mu_{EOF} + \mu_{ep} \quad (1)$$

Rearranging this equation to focus on the calculation of the μ_{ep} gives:

$$\mu_{ep} = \mu_{app} - \mu_{EOF} \quad (2)$$

The μ_{EOF} was obtained by calculating the μ_{app} for a neutral molecule (such as DMSO in these experiments). Neutral molecules do not have a μ_{ep} and so μ_{EOF} is equal to μ_{app} of DMSO in all these calculations.

$$\mu_{ep} = \mu_{app} - \mu_{app\,(DMSO)} \quad (3)$$

The apparent mobility depends on the migration time (t_m) of the drug molecules, amongst other experimental parameters (separation voltage ΔV, total length of capillary L, and effective length l) and was calculated using the following equation:

$$\mu_{app} = \frac{L.l}{\Delta V.t_m} (4)$$

The experimental parameters were outlined in Chapter 2, Section 2.3. The 10mM stock solutions of Diclofenac free acid, Aceclofenac, PABA and the mixture were in EtOH. Three BGE's were used:

1. 10 mM Borate buffer @ pH 9
2. 10 mM Borate buffer @ pH 9 with 0.5 g L^{-1} NINs
3. 10 mM Borate buffer @ pH 9 with 0.5 g L^{-1} DINs.

The first electropherogram below (Figure A3.3) shows DMSO in BGE 1, with a retention time of 2.9 minutes. As mentioned previously, it is a neutral molecule whose purpose is to measure the electroosmotic flow (EOF).

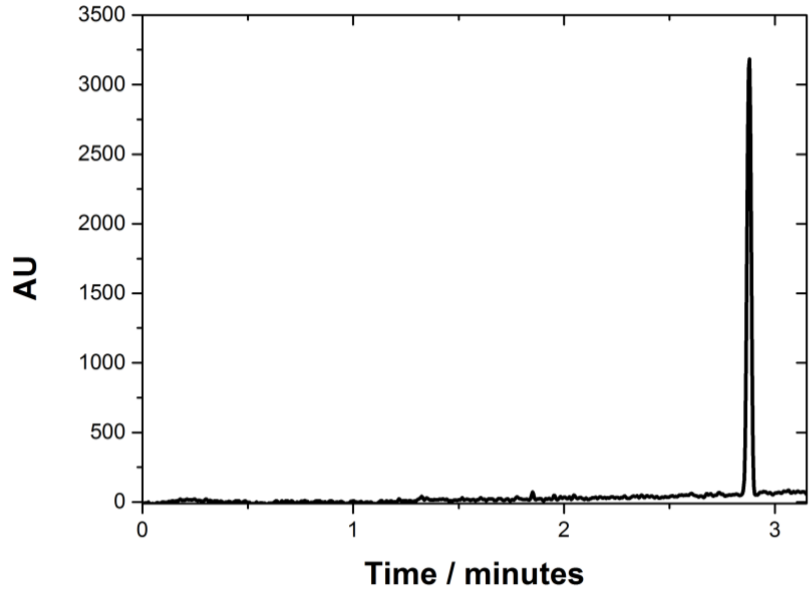

Figure A3.3: Electropherogram of 0.005% DMSO in BGE 1. ΔV = 20 kV, inj. 5 s

The following figures show the electropherograms that were obtained for Diclofenac FA alone (A3.4), NINs in BGE (A3.5) and Diclofenac FA injected into the BGE containing NINs (A3.6).

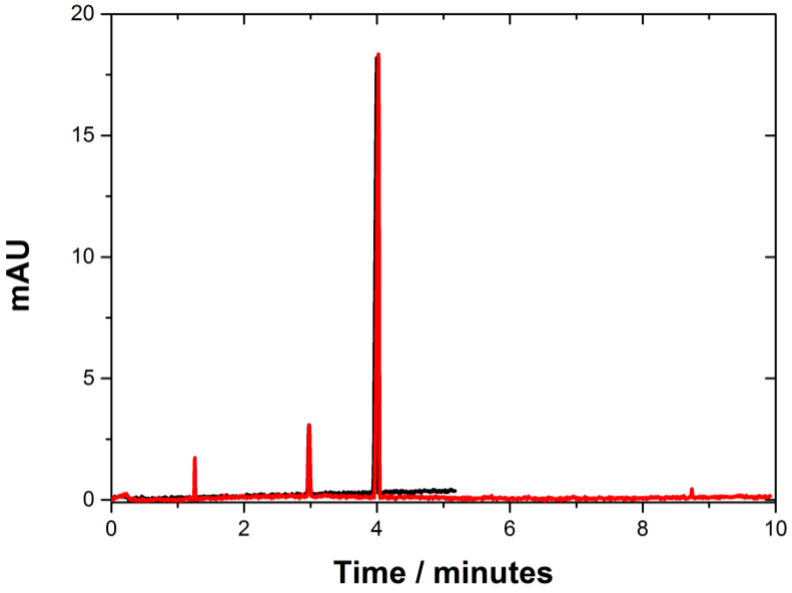

Figure A3.4: Electropherogram of 0.1 mM Diclofenac FA with 0.005% DMSO in BGE 1 (run 1 = black line, run 2 = red line). ΔV = 20 kV, inj. 5 s

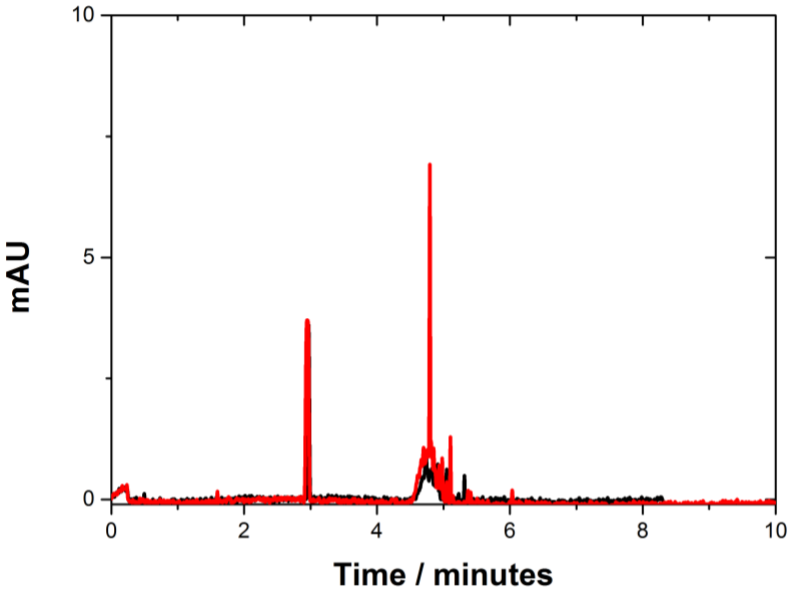

Figure A3.5: Electropherogram of 0.005% DMSO in BGE 2 (run 1 @ inj. 5 s = black line, run 2 @ inj. 10 s = red line). ΔV = 20 kV

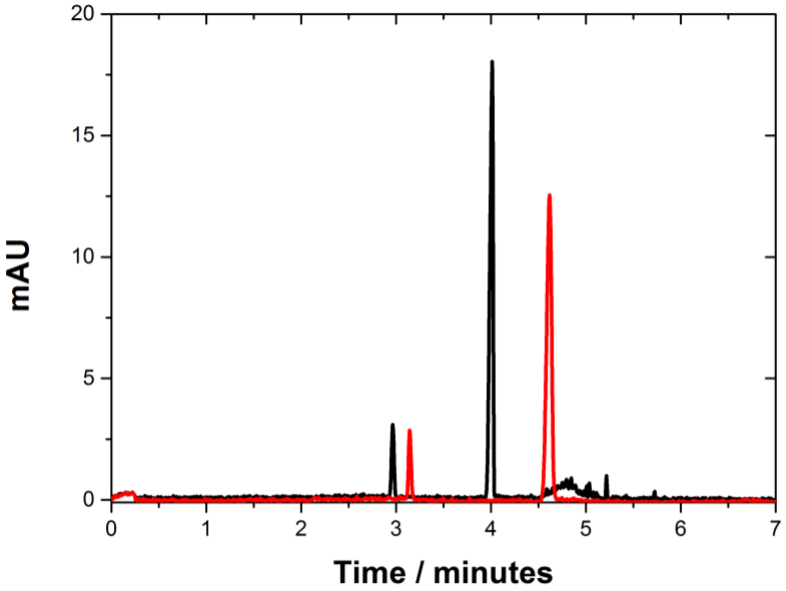

Figure A3.6: Electropherogram of 0.1 mM Diclofenac FA with 0.005% DMSO in BGE 2 (run 1 = black line, run 2 = red line). ΔV = 20 kV, inj. 5 s

The peak for Diclofenac FA is clear to see in Figure A3.4 at 4 minutes and it is very reproducible. A grouping of small peak between 4.5 and 5 minutes in Figure A3.5 represents the NINs, as proved by the increase in peak height when the injection time is changed from 5 to 10 seconds (black to red line). The result from the combination of both Diclofenac and NINs in the capillary is shown in Figure A3.6. Run 1 shows no change in the peak height or position of Diclofenac, and only a slightly longer retention time for the NINs. However in Run 2, the peak positions of both DMSO and Diclofenac are shifted and no peak is seen for NINs. It should be also said that the retention time for DMSO remains constant at 2.9 minutes in all electropherograms, except for run 2 in Figure A3.6, when it shifts to 3.15 minutes.

Figure A3.8 shows the electropherograms that were obtained for DINs in BGE and Figure A3.9 shows the results for Diclofenac FA injected into the BGE containing DINs. To note the experiments were performed on a different day to those above and thus the retention time for DMSO and Diclofenac just very slightly increased, by ~0.1 minutes (Figure A3.4 Vs A3.7).

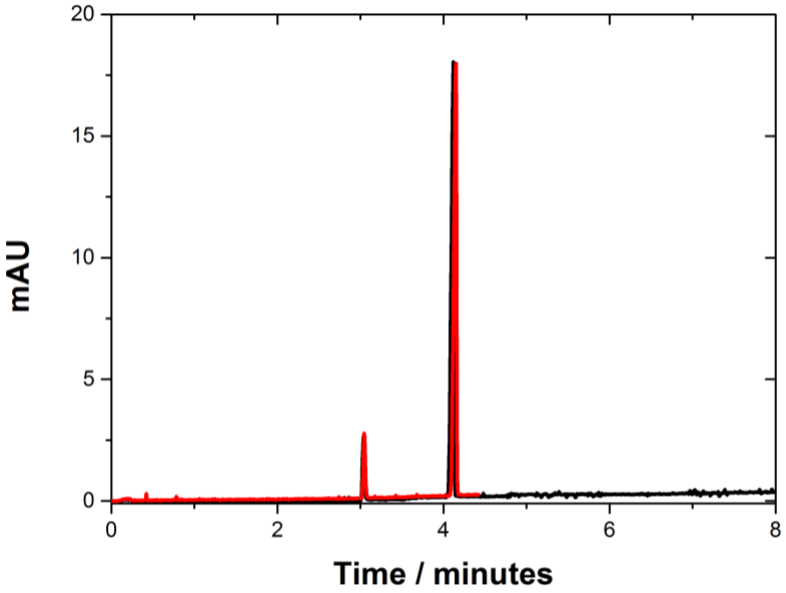

Figure A3.7: Electropherogram of 0.1 mM Diclofenac FA with 0.005% DMSO in BGE 1 (run 1 = black line, run 2 = red line)

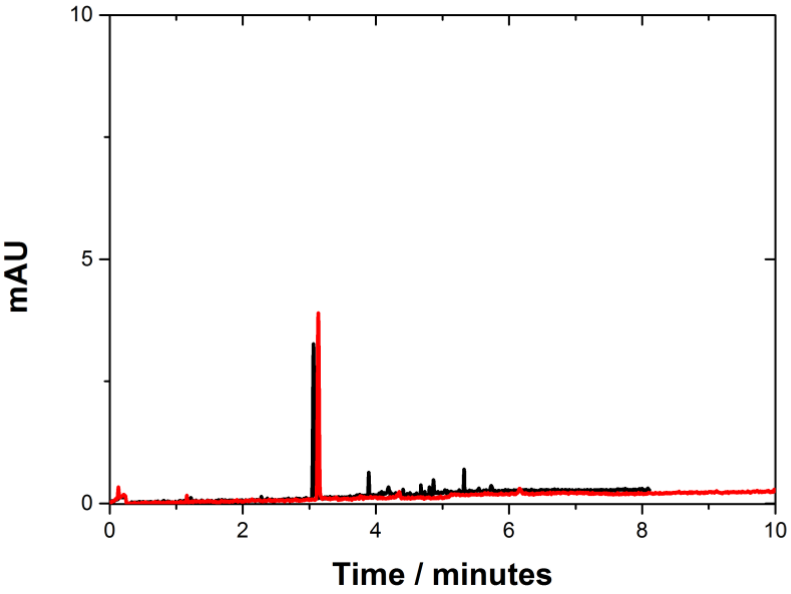

Figure A3.8: Electropherogram of 0.005% DMSO in BGE 3 (run 1 = black line, run 2 = red line)

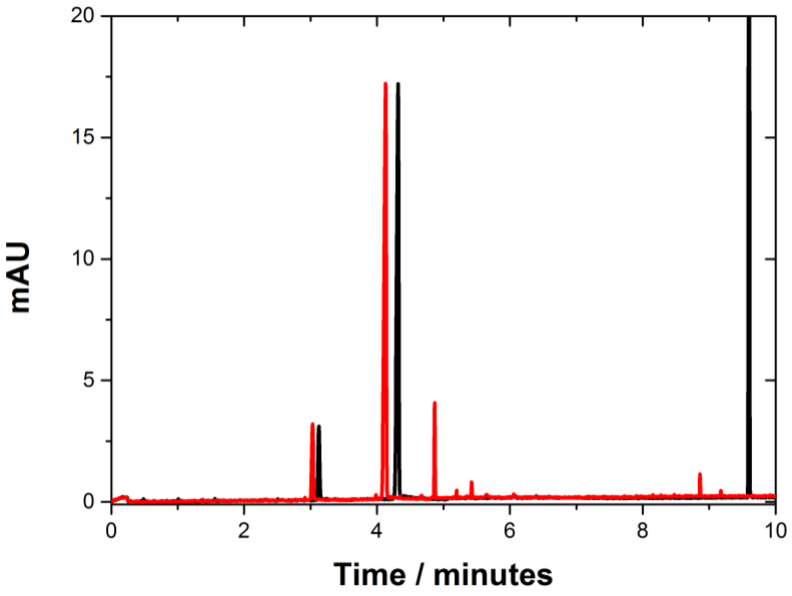

Figure A3.9: Electropherogram of 0.1 mM Diclofenac FA with 0.005% DMSO in BGE 3 (run 1 = black line, run 2 = red line). ΔV = 20 kV, inj. 5 s

Figure A3.7 shows the peak for Diclofenac FA at 4.1 minutes and it is very reproducible. A cluster of very small peaks between 3.9 and 5.8 minutes in Figure A3.8 could be due to the DINs, however it is not very reproducible. The result from the combination of both Diclofenac and DINs in the capillary is shown in Figure A3.9. In Run 1 the peak positions of DMSO and Diclofenac are both slightly shifted and no small peaks are visible for DINs. However Run 2 shows no change in the peak height or position of Diclofenac when it is on its own, and some small peaks are present for the DINs. The retention time for DMSO remains approximately constant at 3.05 minutes in all electropherograms.

Based on Figures A3.4 to A3.9, the following table of values of $\mu_{EOF\ (DMSO)}$, μ_{app} and μ_{ep} were calculated.

Table A3.2: $\mu_{EOF\ (DMSO)}$, μ_{app} and μ_{ep} values obtained from CE experiments (units: $m^2\ V^{-1}\ s^{-1}$)

	Run	$\mu_{EOF\ (DMSO)}$ x 10^{-8}	μ_{app} x 10^{-8}	μ_{ep} x 10^{-8}
Diclo	1	8.25 ± 0.057	6.10 ± 0.012	-2.15 ± 0.057
Diclo + NINs	1	8.4	6.2	-2.2
	2	7.9	5.4	-2.5
Diclo + DINs	1	7.9	5.7	-2.2
	2	8.2	6.0	-2.2

Unfortunately, no clear change in the μ_{ep} for Diclofenac FA alone and in the presence of NINs and DINs was obtained. This was expected for NINs as Diclofenac should not interact with them. However with DINs an interaction is expected between the Diclofenac and the imprint cavities in the DINs but from the unchanged μ_{ep} values it would seem that there was no interaction between them. It was possible that the experimental parameters were not optimised for this technique and so this would affect the quality of the results.

SUMMARY:

Ce travail avait pour but d'améliorer la sensibilité et la sélectivité de la détection de solutés à l'interface liquide-liquide (LLI) par l'utilisation de nanoparticules de silice. Les nanoparticules de silices ont été choisies car elle peuvent s'assembler à l'interface entre la phase aqueuse et la phase organique et servir d'aide pour accroître la sensibilité et la sensibilité au soluté visé. Le transfert de solutés ioniques au travers de la LLI peut être détecté par électrochimie et c'est donc par cette méthode que les améliorations ont été suivies. Pour étudier la sensibilité, un colorant cationique a été choisi comme soluté modèle et des expériences électrochimiques et spectrophotométriques ont été faites. Les résultats ont confirmé une forte affinité du colorant cationique pour les nanoparticules de silice, ce qui, combiné avec l'aptitude des nanoparticules à s'adsorber à l'interface résulte en l'accumulation du colorant à l'interface et a pour conséquence une augmentation de la sensibilité de la détection. Pour améliorer la sélectivité de la détection électrochimique, des nanoparticules de silice à empreinte moléculaire d'une molécule médicamenteuse ont été synthétisées. Des mesures spectrophotométriques ont permis la détermination de la constante thermodynamique d'affinité des empreintes pour la molécule cible, cette constante a une très grande valeur, permettant une grande sélectivité des empreintes. La détection électrochimique à la LLI du soluté cible est très fortement impactée par la présence des nanoparticules à empreinte moléculaire.

This research aimed to improve the sensitivity and selectivity of analyte detection at the liquid-liquid interface (LLI), by the use of silica nanoparticles. Silica nanoparticles were chosen as they can assemble at the interface between an aqueous and organic phase and they serve as an aid to enhance sensitivity and selectivity of a target analyte. The transfer of the ionic analyte across the LLI can be detected by electrochemistry and this is how the improvements were followed. To study the sensitivity, a cationic dye was chosen as a model analyte and electrochemical and spectroscopic experiments performed. Results confirmed a strong affinity for the cationic dye to the silica nanoparticles, which combined with the ability of the silica to adsorb at the interface, resulted in an accumulation of the cation at the LLI and so an increase in sensitivity of detection was achieved. In order to improve selectivity, molecularly imprinted silica nanoparticles were synthesised using a chosen drug molecule. Spectroscopic experiments allowed the determination of a large affinity constant value, proving a strong selectivity of the imprinted silica for its target analyte. The electrochemical analyte detection of the imprint drug molecule was shown to be greatly impacted by the imprinted silica nanoparticles.